Catalytic conversion of bio-derived platform molecules into useful chemicals *via* selective oxidation

Leandro Ardemani

Doctor of Philosophy

Aston University

November 2015

Aston University

Catalytic conversion of bio-derived platform molecules into useful chemicals *via* selective oxidation.

Leandro Ardemani, Doctor of Philosophy, 2015

Green Chemistry regards the design of products and processes that minimise the use and generation of hazardous substances. Heterogeneous catalysis facilitates such energy and atom efficient processes, affording simple and low cost product isolation methods, and catalytic materials that can be easily recovered and reused.

This thesis reports on the selective aerobic oxidation of 5-hydroxymethyl-2-furufural (HMF), a potential platform chemical that may be derived from cellulose, into 2,5-furandicarboxylic acid (FDCA) over noble metal nanoparticles dispersed on a solid base support. FDCA has been touted as a potential replacement for polyethyleneterephtalate (PET) and is also an interesting synthetic building block.

Au nanoparticles are extremely active and selective oxidation catalyst for a range of environmental and fine chemical transformations, however they require a homogeneous base, such as NaOH, to work. Au NPs dispersed on hydrotalcites (HT), anionic microporous clays, have shown promise in HMF oxidation to FDCA, hydrotalcite acting as both the support and the source of base. However, key questions remained regarding the nature of active site, potential role of homogeneous contributions and importance of reaction basicity upon activity and selectivity.

Kinetic profiling of HMF and its intermediates HMFCA and FFCA over Na-free Au/MgAl HT catalysts highlight the role of base in achieving high FDCA yields. The order of reaction in Au, in oxygen and in HMF were found, determination of the Arrhenius E_a for the R-OH and the R-CHO functions allowed to find the rate-determining step. *Ex situ* and *operando* XAS were performed to detect Au oxidation state and Au chemical environment in the catalyst, enlighting the true active site during the selox. Eventual changes in Au oxidation state were investigated to find how the precursor $HAuCl_4$ evolves during the calcination.

As the reaction was found to be pH-sensitive and as the calcination of HTs convert them into stronger bases, the impact of calcination temperature was studied; also a comparison between calcination and calcination rehydration protocols was done.

The incorporation of Pd into Au catalysts improved activity and lifetime for these AuPd bimetallic formulations. AuPd NPs were prepared *via* DP method on HT support, varying Au:Pd ratio, then kinetic studies for the selox of HMF to FDCA were carried out, followed by accurate characterisations.

Key words: gold, palladium, hydrotalcite, green chemistry, HMF.

Acknowledgements

This thesis would not have been possible without the help and support of many people, to whom I am extremely grateful.

To start, I would like to thank Professor Adam Lee and Professor Karen Wilson for supervising and guiding me through this PhD. I am grateful for your support. I thank the EPSRC for funding this project, and also the School of Chemistry at Cardiff University and the EBRI at Aston University for providing me with the facilities to carry out my research.

Several of the results in this thesis were obtained with the assistance of some very helpful people. Thank you to Dr. Jinesh Cherukattu Manayil, for his great support throughout my PhD and for helping me to improve the Na-free protocol for the preparation of hydrotalcites. Thank you to Dr. Christopher Parlett and Dr. Mark Isaacs for carrying out XPS and TEM analysis for me, and for helping me understanding more about XPS and XAS analysis. Thank you to Dr. Amin Osatiashtiani, for his support during my first year with HPLC analysis. All of your guidance has been a holy hand! Thanks to Dr. Giannantonio Chibin, the beam line scientist at Diamond who helped me in obtaining EXAFS data, thanks to Dr. Georgios Kyriakou to help me running XAS experiments, thanks to Dr. Robert Jenkins, Dr. Robert Evans and Dr. Khalid Doudin for their help using the NMR.

To all of the past and current members of the Cardiff Surface Chemistry and Catalysis group, and to the Aston EBRI ones: thank you for have been with me, for working in the lab, the parties, lunches, dinners and the nights spent out together! Thanks to Brunella Barbero, Lucia Frattini, Dr. Andreia Machado, Akihiro Hayashi, Dr. Vannia Cristina dos Santos, Dr. Lee Durndell, Dr. Tai Zhijun, Dr. James Bennett, Dr. Takayoshi Hara, Daijiro Kizawa, Dr. Violaine Mendez, Dr. Parminder Sandhu, Jim Hunns, Mariano Tapia Reche, Dr. Lachlan Ciddor, Dr. Priscilla Johnson, Scott Board, Trofimovaite Rima, Dr. Hongsheng Huang, Dr. Ângela Silva, Nazrizawati Ahmad Tajuddin, Hessam Jahangiri, Andrés Miròn Garcia, Anabel Montano Gomez, Rebeca S.V, Dr. Santosh Kumar, Tim Miller.

To all of my other friends, who supported me from Italy: thanks for always telling me "do never give up!". Davide Parma, Riccardo Riccardi, Laura D'Incà, Dr. Roberto and

Dr. Christian Ferioli, Claudio Scurati, Dr. Mario Marola, Davide Coslovi, Maria Teresa Falcone, Giacomo Lari, Giulia Lotti, Prof. Paolo Chiesa, Francesco Englaro, Maurizio Cerioni, Gaspare Coscarella, Dr. Natasha Spadafora, Dr. Giuseppe Perelli, Federica Tucci, Stella Cutini, Giulia and Beatrice Messina. To a new group of faithful friends: Romina De Mola, Floriana Daga, Deborah D'Arrigo, Dorina Polinari, Valentina Vita, Alessandra Poiana, Matteo Dell'Aglio, Gianpaolo Sacconi, Antonella Stara, Antonella Mura, Sara Tau, Elisa Quinale, Elisa Vergani, Anna Iossa, Melania Rivoli, Gemma Distefano, Stefano Abarth, Anna Lisa Murè, Luciana Piazzolla, Stefano Shakak, Lawrence Campagnoli, Lucio Maneschi, Domenico Capasso, Irene Scaini, Lisa Costa. We are Survivors!

To my fantastic Mum and Dad: you have been here, always next to me since I have left Italy for this adventure. I would not be here if it was not for your great support. Words cannot really express my gratitude for all you have done for me. And to Vincenza Avellina, who has been with me for three years, in my hearth.

Some of the research reported in this manuscript has been published in a peer reviewed journal article, which is referenced below:

Solid base catalysed 5-HMF oxidation to 2,5-FDCA over Au/hydrotalcites: fact or fiction?

Leandro Ardemani, Giannantonio Cibin, Andrew J. Dent, Mark A. Isaacs, Georgios Kyriakou, Adam F. Lee, Christopher M. A. Parlett, Stephen A. Parry and Karen Wilson.

List of contents

List of abbreviations

At. %	Atomic percent
Acac	Acetyl acetonate
BET	Brunauer-Emmet-Teller adsorption theory
BINAP	(2,2'-bis(diphenylphosphino)-1,1'-binaphthyl)
CHT	Calcined hydrotalcite
CHT-RW	Calcined hydrotalcite, rehydrated in water
CHTHotw	Calcined hydrotalcite, rehydrated in hot water
CHTSubw	Calcined hydrotalcite, rehydrated in subcritical water
CHTVap	Calcined hydrotalcite, rehydrated in vapour phase
DFT	Density functional theory
DRIFTS	Diffuse reflectance infrared Fourier transform spectroscopy
DTGA	Differential thermogravimetric analysis
EDX	Energy dispersive X-Ray
EXAFS	Extended X-ray absorption spectroscopy

FDCA	2,5-furandicarboxylic acid
FFCA	5-formyl-2-furancarboxylic acid
FWHM	Full width half maximum
HAADF	High angle annular dark field
HMF	5-hydroxymethyl-2-furfural
HMFCA	5-hydroxymethyl-2-furancarboxylic acid
HPLC	High performance liquid chromatography
HT	Hydrotalcite
LDH	Layered double hydroxide
ICP-OES	Inductively coupled plasma optical emission spectroscopy
MIBK	Methyl isobutyl ketone
NMR	Nuclear magnetic resonance
PGM	Platinum group metals
ppm	parts per million
RPM	Revolutions per minute
RT	Room temperature
Selox	Selective oxidation
SEM	Scanning electron microscopy
STEM	Scanning transmission electron microscopy
TEM	Transmission electron microscopy
TGA	Thermal gravimetric analysis
TOF	Turn over frequency
TPD	Temperature programmed desorption
wt. %	Weight percent
XANES	X-ray absorption near edge structure
XAS	X-ray absorption spectroscopy
XPS	X-ray photoelectron spectroscopy
XRD	X-ray diffraction
XRF	X-ray fluorescence spectroscopy

List of tables and schemes

List of figures

Chapter 1

Introduction

List of contents

1.1 The role of heterogeneous catalysis for "green" chemistry

The rising cost, decreasing availability and environmental impact of fossil fuels have generated increasing interest in the production of sustainable alternative energy and chemical feedstocks[1]. In the case of organic chemicals, renewable biomass is a potential candidate to supply this need[2, 3]. Therefore, Green Chemistry has evolved into an underpinning philosophy for the chemicals industry, advancing the design and use of products and processes that minimise the use and generation of hazardous substances, and promoting a transition from chemistry based upon fossil fuel resources to new technologies utilising bio-derived sustainable feedstocks[1, 2, 4-8].

Heterogeneous catalysis is one of the most important supports of green chemistry[1, 8]; the research and development of new catalysts, catalytic systems, new chemical products and processes that reduce or eliminate the use and generation of hazardous substances lead to reach important results for human health and environmental protection[4], facilitating such energy and atom efficient processes, affording simple and low cost production and isolation methods and catalytic materials that can be easily recovered and re-used[9], giving thus economic, social and environmental benefits. The interesting challenge of Green Chemistry is to provide a more stable and secure supply of feedstocks, an environmentally beneficial reduction in the carbon footprint of chemicals and liquid fuels, and a more stable and profitable agricultural economy, minimising waste[2].

1.1.1 Definition of catalyst and its components

1.1.1.1 Catalysts, promoters, supports and pore networks

A catalyst[10] is a substance that increases the rate at which a chemical reaction occurs, without itself being significantly consumed during the reaction, providing a new reaction pathway that proceeds *via* an alternative mechanism, through a distinct transition state that facilitates the reaction because of its lower activation energy barrier. A reagent forms, indeed, an intermediate complex with the catalyst, from which the product is formed and leaves the catalyst unaltered. It is worth underscoring that the process does not overrule the thermodynamic equilibrium, but it accelerates the kinetics by enhancing the rate at which the equilibrium is reached[10].

Catalysis can be divided into two subdivisions. A catalytic reaction is said to be homogeneous when both reagents and catalyst are in the same phase, as for the common case of soluble metal complexes in liquid phase reactions. Active and selective homogeneous catalysts are commonly investigated, with improvements obtained *via* careful adjusting of new ligands and the auxiliary chemicals used.

Nevertheless, their use is still far to be ideal and sometimes presents inconveniences for an industrial scale: their recovery and reuse require purifications, which lead to either loss of catalytic active component and/or further costs for industrial processes. Again, homogeneous catalysts can contaminate products and this is not tolerable, especially for pharmaceutical industries, where high quality and purity is a necessary requirement for human health and most homogeneous catalysts particularly toxic, even in minimal quantities.

Although these are the most important reasons to consider homogeneous catalysts sometimes environmentally and economically unjustificable for large industrial scale applications[11], there are some industrial processes where homogeneous catalysis is profitably used, when high selectivity is crucial. The Noyori[12] asymmetric hydrogenation uses different BINAP-Ru homogeneous catalysts for the enantioselective hydrogenation[13, 14] of olefins, ketones, aldehydes and imines; this enantioselective hydrogenation is largely used for the production of several drugs and medicines[15], such as antibiotics and antipsychotic agents.

Another interesting industrial application of homogeneous catalysis is for the olefin metathesis[16], used to prepare higher olefins from α-olefins. The most important industrial process for the olefin metathesis is the SHOP (Shell higher olefins process)[17], in which linear α-olefins are produced *via* ethylene oligomerisation, using Ni-phosphine complex; then, olefin metathesis produces higher olefins, using Schrock[18] (Mo-complexes) or Grubbs[19] (Ru-complexes) catalysts.

A catalytic reaction is said to be heterogeneous when the catalyst is in a different phase, such as a solid catalyst and liquid/gas reagents, being the recovery of the catalyst facilitated at the end of the catalytic process itself, either by filtration, centrifugation or decantation and reducing both economical and environmental impact. Nevertheless, the nature of the active sites is usually less well understood; for this reason, studying the actual site of action and subsequent catalyst deactivation, specifically under operating conditions, is also an interesting subject.

A heterogeneous catalyst is made of several components: active sites, support and promoters[10]. The catalytic surface is always heterogeneous, because its chemical and physical properties are different, depending on which region is considered; this implicates that active sites are in determined points of the catalyst surface where the reaction actually occurs.

A support, usually a porous solid or a high polymer, immobilises the active phase (e.g. metal nanoparticles) and makes easier the separation of the products from the catalyst itself. Then, promoters increase the activity and or selectivity of a catalyst. Promoters can be deposited onto an already supported catalyst or alternatively they can be simultaneously deposited onto the support along with the active species. The promoter can exist as either adatom sites, very small particles of up to a few atoms which do not form multiple layers, or as multilayer sites either positioned on the catalyst or the support, although they must be in close proximity to the active sites. The role of promoters is not fully understood and thus has led to the speculation of numerous effects:

a) The promoters actively block some of the active sites. Decomposition is favoured at either surface vacancies present on the active metal face or on large flat surfaces. These sites are blocked by the promoter, reducing poisoning of the active sites.

b) Oxygen absorbed to the promoters can facilitate the cleaning of the catalyst surface, removing impurities that could cause poisoning.

c) The promoters cause an electronic modification of the surface, altering the strength of adsorption/desorption.

d) The promoters and active species form an alloy that has higher activity/selectivity.

Pore networks in catalysts and their supports play a key role for the mass transport of substrates to active sites within the catalyst bulk, and are important for a high activity of catalytic materials. According to the average pore diameters, materials can either be defined as microporous (pore size < 2 nm), mesoporous (2-50 nm) or macroporous (> 50 nm)[20].

1.1.1.2 Deactivation of catalysts

Deactivation can be split into four main different types[21, 22]: the first is poisoning[23] of the active sites *via* the adsorption of strongly bound chemisorbed species. A poison is an impurity in the feed that reacts selectively on the catalytic sites stopping their activity and the way to regenerate them is to destroy the poison with an adequate treatment, such as the removal of sulfur via hydrogenation to give H_2S.

The second is fouling[24] due to powders, coke or polymers that block the active sites or support and the way to regenerate the catalyst is combustion with air enriched or impoverished of O_2. Then, the sintering (agglomeration)[25, 26] is a physical irreversible process that reduces the surface area and might be due to crystallyte growth either of the support or of the dispersed metal or both of them. The fourth is metal leaching[27-29], that is a cleavage and a consequential lost of the active species and/or the promoter from the support into the reaction solution. Then, mechanical degradation and solid state transformation (reduction of surface oxidation state)[25, 26] also play a role in the loss of active phase.

1.1.1.3 Kinetic pathways and activation energy

In theory, reactions would be 100 % selective to the desired products[30], nevertheless in practice this is seldom the case. Therefore, as important as activity is, selectivity of a catalytic system can be an important deciding factor on whether this catalyst can be implemented on an industrial scale[31]. The overall selectivity of a catalyst, under reaction conditions, is determined by the relative occurrence of various possible reaction pathways. The formation of undesired products rather than the preferable one, from identical or differing transition states, is counterproductive[32].

If a reaction can occur with a catalyst[10] in the heterogeneous phase or without it in the homogeneous one, the effect of a catalyst is to give an alternative reaction pathway with lower activation energy, which is easier to overcome **(Scheme 1.1).** As said before, while the catalyst lowers the activation energy, by forming a different activated complex on its surface at the transition state, it does not change the energies of the original reactants or products. Rather, the reactant energy and the product energy remain the same and only the activation energy is lowered.

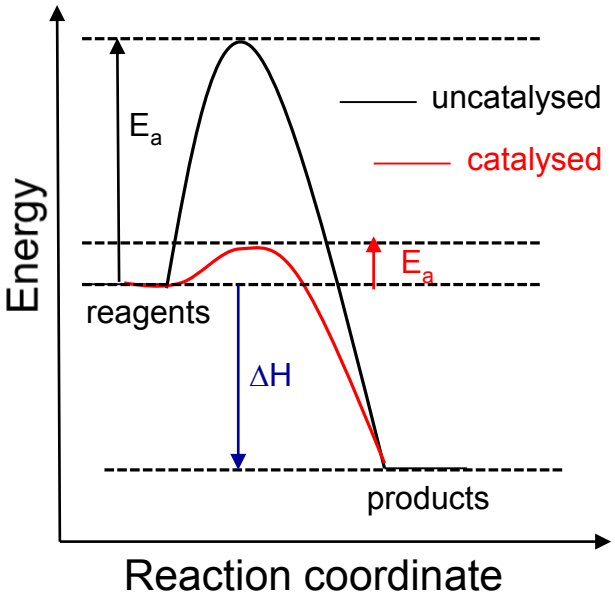

Scheme 1.1: the reaction pathway with and without the catalyst; E_a indicates the activation energy.

Activation energy barriers of by-product formation must be similar to the favourable product, with the degree to which they form being relative to how close they are[33]. This occurs due to several reaction pathways that an adsorbed intermediate can undergo and is responsible for the simultaneous formation of side products.

Any modification of the active surface during the reaction will result in changes to the activation energy barriers towards possible products, and thus shift selectivity to a parallel reaction[33]. Controlling desired product selectivity requires a varied approach to enhance activity because the rate determining step might not necessarily be the step that decides selectivity.

Consecutive reactions, which is the case of selox of HMF in this thesis work, where the major product can further react to form more thermodynamically stable product(s) might be either desired or disconcerting. When selectivity towards an intermediate of these possible products is desired, the use of a catalyst that will not form unwanted by-products is crucial, allowing kinetic control. When the desired product is at the end of the possible reaction pathway, the use of a catalyst that can undergo all the predicted steps, without following parallel pathways and without stopping to the first intermediate, help to achieve high yields of desired products[32]. These selectivity influencing factors depend on surface structure, adsorbate induced restructuring, reaction intermediates and surface composition[33].

1.2 Production and selective oxidation of 5-hydroxymethylfurfural

1.2.1 Production of HMF

Several raw materials have been studied for new green processes in the last years, especially sugars, glycerol and vegetable oils, giving the attention to the production of biofuels, green polymers and fine chemical intermediates. 5-hydroxymethyl-2furufural (HMF)[1, 3, 6, 8, 34] belongs to a class of biomass-derived oxygenated organic chemicals and it is one of the many promising potential platform chemicals for biorenewable chemicals production. HMF is a waste product from sugars **(Figure 1.1)** and it has been successfully synthesized by dehydration of glucose, fructose and cellulose[35-38]; this important relatively new platform molecule might be transformed into several high value products. 2,5-furandicarboxylic acid (FDCA) is an interesting monomer for the synthesis of a new biodegradable polymer[39] that might replace polyethyleneterephtalates, then it is also an interesting building block for other polymers[1, 5, 6, 8, 40].

Figure 1.1: left – sugar crops, natural source of HMF and right – an example of application of biodegradable polymers for daily use.

A process to synthesize HMF starts from glucose, which is extracted from cellulose, isomerised to fructose[41] via base catalysts and dehydrated in the aqueous phase using either HCl or an acidic ion-exchange resin or auto-catalytic formation in DMSO; then the HMF product is continuously extracted into an organic phase (methylisobutylketone) modified with

2-butanol, giving 80% HMF selectivity at 90% fructose conversion, from 10 to 50 wt % fructose)[42].

Other synthesis are well known[3], and one of them is based on heterogeneous strong acid ion exchange resins in methyl isobutylketone, which allow the dehydration of D-fructose to 5-hydroxymethyl-2-furancarboxaldehyde at mild temperature and pressure[43]. Then, metal chloride containing ionic liquids ($CuCl_2$ and $CrCl_2$) dissolved in 1-ethyl-3-methylimidazolium chloride ([EMIM]Cl) at temperatures of 80–120 °C collectively catalyzed the single-step process of converting cellulose to HMF with an unrefined 96 % purity among recoverable products at 55 % HMF yield[44], giving also sugars or sugar-derivatives.

It is worth mentioning two interesting works recently published by our research group[45, 46] about bifunctional heterogeneous sulfonated zirconia catalysts for HMF production from glucose in water solvent. Mesoporous silica SBA-15 was grafted with ZrO_2 film with various thickness, followed by sulfation. Sulfated zirconia films prepared with S/Zr < 0.18 appeared chemically stable through the conversion from glucose to 5-HMF; glucose isomerization to fructose was achieved via base or Lewis acid sites, while subsequent dehydration of fructose to HMF was possible because of sulfated Brønsted acid sites. These catalysts showed 3-fold enhancement in HMF productivity per gram of Zr and exhibit excellent hydrothermal stability at temperatures as high as 170 °C, showing promises for further applications in biomass processes.

1.2.2 Selective oxidation of HMF

HMF oxidation into FDCA was examined using stoichiometric oxidants[1, 40], such as $KMnO_4$, or homogeneous metal salts (Co/Mn/Zn/Br)[47] under high pressure (70 bar, in air) or vanadyl-pyridine complexes[48]. To bypass problems due to the homogeneous catalysts (toxicity, harsh working conditions, purification and recycling), heterogeneous catalysts were studied and afforded FDCA *via* HMF oxidation with molecular oxygen.

Supported Pt/C or Pt/Pb/C catalysts were first demonstrated to work[1, 40, 49] with the aid of homogeneous base at high pH (pH = 14) resulting in near quantitative FDCA yield. Direct synthesis of FDCA from fructose has been also tried using a solid acid and PtBi/C in water/MIBK, affording 25 % FDCA yield with 50 % selectivity[40]. Although high conversion with excellent FDCA selectivity (99 %) was obtained from fructose in the presence of

Co(acac)–SiO_2 bi-functional catalyst, this reaction was performed under harsh conditions (433 K, 20 bar)[50].

The oxidation of HMF over Pt/Al_2O_3 catalysts was also investigated by Vinke and co-authors[51] at lower pH (pH = 9). Although FDCA was eventually formed, the intermediate product 5-formyl-2-furancarboxylic acid (FFCA) was observed, while the intermediate product 5-hydroxymethylfuran-2-carboxylic acid (HMFCA) appeared at higher pH.

Recently, three noticeable improvements were reported, using Au supported catalysts for aqueous HMF oxidation. Gorbanev and co-authors[40] demonstrated that commercial Au/TiO_2 could oxidise HMF into FDCA in 71 % yield at near room temperature. Pasini and co-authors[5] obtained good results, at higher temperature (95 °C) using the bimetallic Au-Cu/TiO_2 that gave FDCA in 99 % yield. Then, Casanova and co-authors[6] showed Au/CeO_2 nanocrystalline was more active and selective, giving FDCA in 96 % yields at room temperature.

However, these catalysts require addition of homogeneous base (1–20 equiv. NaOH) that is suspected to play a role in the deactivation of these catalysts, and high oxygen pressure (10–20 bar). Then, a decrease in the catalytic activity and selectivity is shown after 2-5 catalytic cycles and, in the most of cases, the HMF/Au bulk molar ratio required for a full and selective conversion was quite low (100-640).

An interesting and innovative heterogeneous catalytic system was tested by Gupta *et al.*[8] and these authors tried the selective oxidation with Au supported on hydrotalcite as the solid base, giving FDCA in high selectivity and nearly quantitative conversion. This was the first catalyst that worked at ambient pressure and the first attempt to use a heterogeneous source of base instead of the usual NaOH. This showed the way forward to a new recyclable catalyst, even if the HMF/Au bulk molar ratio used was still too low (40).

Another remarkable work was carried out by Davis and co-authors[1, 52, 53], who compared the activity of commercial Pt, Pd and Au NPs supported on TiO_2 or C at room temperature and 10-20 bar of O_2. Even if the HMF/M ratio, where M is one of the named metals, was higher (6700) than all the other tried experiments, the selectivity in FDCA decreased (Pt = 79 %, Pd = 71 % and Au = 8 %). This work clearly showed a big difference between Pt and Au activity, giving a decrease for Au as the amount of loaded metal decreases. Nevertheless, Pt and Pd

catalysts lose the activity and the yield decreases after 4 cycles, and Davis Au NPs were larger than 10 nm and tested without an adequate amount of base.

This research project aims to study and develop heterogeneous catalysts for the selective oxidation of 5-hydroxymethylfurufural (HMF) into 2,5-furandicarboxylic acid (FDCA) using an heterogeneous catalytic system made of Au or AuPd nanoparticles supported onto hydrotalcites[54], a class of synthetic anionic clays.

1.3 Supported Au NPs for selox

Gold in its bulk state has been thought to be catalytically inert and the most noble of the elements, until in the 1980's Haruta and Hutchings understood its important role in catalysis and its activity, when divided to the nanoscale[55, 56]. Haruta[57, 58] disclosed the unexpected capability of gold NPs as the most promising catalyst for the oxidation of CO at temperatures as low as – 76 °C, while Hutchings[59], working on vapour phase hydrochlorination of acetylene, found that gold would have been the most active catalyst for this reaction and his further studies supported his initial predictions[60-62].

The oxidation of primary alcohols to aldehydes or to carboxylic acids is an important process for the synthesis of highly valuable intermediates[63]. Different substrates[64, 65], such as alcohols[66, 67], polyols[67], aldehydes and sugars[68, 69], have been oxidised using gold nanoparticles as a naked sol[65, 70] or supported on solid[64, 65, 69, 71-74], the most common ones being carbon, TiO_2 or CeO_2[75-77].

The need for a homogeneous base[52], such as NaOH, in the aerobic selective oxidation of sugars, alcohols and aldehydes, carried out over supported Au catalysts, is a serious and not environmental friendly limitation[78] of this catalytic system, as the final product requires acidification with HCl to get the free acid from the disodic salt and purification. These steps increase the operating cost of the industrial process and produce additional salt byproducts, which are of no added value and may have a negative environmental impact.

This already explained need of NaOH has been recognised as an essential component for supported Au catalysts since initial studies carried out by Prati and Rossi[67, 74], in which these authors demonstrated that supported Au NPs can be very effective for the selox of 1,2 propanediol to lactic acid, by oxidation of the primary alcohol group rather than the secondary one, which might have been expected to be more reactive. Carrettin and co-workers[9] and

Hutchings and co-workers[79] also demonstrated that glycerol cannot be oxidised in absence of base over Au catalysts.

The use of gold for manufacturing new catalytic systems[56] was affected by the high variation of the catalytic results, depending on the preparation method employed related to the support used[80] and to gold particle morphology and metal support interactions, both crucial to modify activity and selectivity of a catalyst.

Recent mechanistic studies carried out by Davis and co-workers[52, 53, 81] on gold catalysts have shown the essential role of hydroxide ions during the selective oxidation of alcohols. Hydroxide ions facilitate the initial deprotonation of alcohols, which are weak acids (pKa = 14–18), since a gold catalyst, by itself, cannot deprotonate the hydroxyl group in alcohols.

Rossi, Prati and co-workers tried to explain[64, 65, 82, 83] this need of base and to understand their catalytic system made of pre-formed Au sol deposited onto different solid supports; the oxidation of the aldehydic group in sugars is reported as a significant example. **Scheme 1.2** shows the proposed mechanism of oxygen molecular activation for gold catalysts on the basis of the promoting effect of liquid base on the aldehydic carbon and the formation of hydrogen peroxide as a reaction product.

Scheme 1.2: proposed mechanism *via* gem-diol for the selective oxidation of the aldehydic carbon of glucose using Au nanoparticles, from references 64, 65, 82 and 83.

The critical point is represented by electron-rich gold species, formed by the hydrated glucose anion and gold surface atoms, which are supposed to activate molecular oxygen *via* nucleophilic attack. An efficient nucleophilic behaviour is determined by the electronic properties of the nanometric gold particles (d < 10 nm). In the dioxogold intermediate, either $Au^{+}{-}O_2^{-}$ or $Au^{2+}{-}O_2^{2-}$ were proposed[64, 65, 83] as a bridge for the two electrons-transfer from glucose to dioxygen and peroxidic-like species have been supposed as a reaction intermediate during dihydrogen oxidation to water on a gold catalyst.

One of the aims of this thesis was to study if it was possible to replace the homogeneous base with a heterogeneous one, the solid being both the support and the source of base. Also, EXAFS experiments were carried out either to verify or to prove wrong the proposed mechanism by Rossi and Prati, analysing Au oxidation state and its chemical environment during the aerobic selox of HMF *in situ*.

1.4 Hydrotalcites and mixed MgAl oxides as the catalytic support and the source of solid base

Hydrotalcites (HTs), with the general formula $[M^{2+}_{(1-x)}M^{3+}_{x}(OH)_2]^{x+}(A_{x/n})^{n-} \cdot y\ H_2O$, belong to a class of anionic clays named layered double hydroxides (LDH)[54, 84, 85]. Their structure is composed of positively charged brucite-like hydroxide layers, in which some octahedrally coordinated M^{2+} cations have undergone isomorphous substitution by M^{3+} ones. Counter anions A^{n-}, commonly carbonates, reside in the interlayer space to balance the residual positive charges[54, 86, 87], although intercalation of sulfate[88], nitrate[89] and various organic anions[90] have been reported in the literature. An example of hydrotalcite structure is shown in **Figure 1.2**.

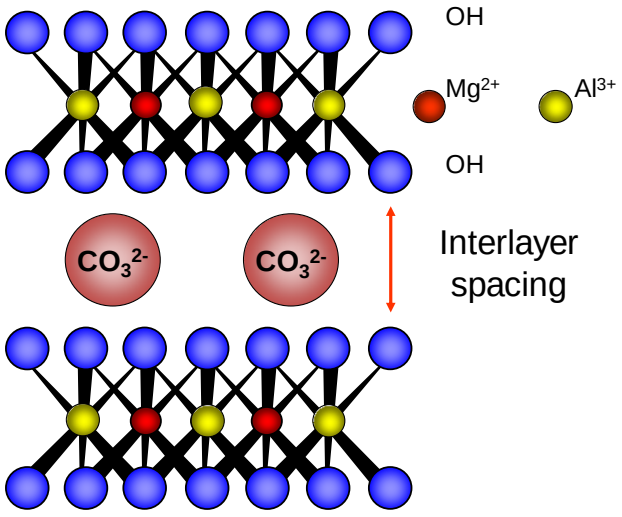

Figure 1.2: a schematic representation of the layered double hydroxide structure of a MgAl hydrotalcite[91, 92].

Hydrotalcites find a wide use as catalysts for aldol reactions or for transesterification of bio-oils[54, 85, 92-94], but they have also found applications as in flame retardants or antacids[54]. They have good anion exchange capacity[95] and are therefore used in applications such as the removal of anions from wastewater supplies[96].

This thesis focuses on MgAl hydrotalcites, in which M^{2+} is Mg^{2+} and M^{3+} is Al^{3+}, with a generic formula of $[Mg_{(1-x)}Al_x(OH)_2]^{x+}(CO_3)_{x/n}^{2-} \cdot y\ H_2O$. Variations in the Al content, reported as x = Al/(Al+Mg), are known to modify the base properties of these materials, with stable pure HT structures reported to form for compositions in the range $0.20 < x < 0.33$[54, 86,

[97]. For these values, the Al^{3+} ions in the brucite-like sheet remain distant one from the other, because of the repulsion of their positive charges.

According to Brindley and Kikkawa[97], for x values lower than 0.33, the Al octahedra are not neighbouring and HT structure is stable. For higher values of x, the increased number of Al octahedra results in the formation of $Al(OH)_3$ bayerite or gibbsite and, in the same way, lower values of x lead to a higher Mg octahedra content in the brucite-like sheets, with concomitant phase separation of $Mg(OH)_2$ brucite or $Mg_5(CO_3)_4(OH)_2{\cdot}4(H_2O)$ hydromagnesite[91, 92, 97, 98]. These considerations will be proved and discussed in **Chapter 3.**

It is also important to note that conventional preparative routes, such as those reported by Cavani and co-workers[54] or Géraud and co-workers[99], involve co-precipitation induced by alkali hydroxides and carbonates, which presents problems of alkali contaminants in the finished catalyst. In this case, the removal of contaminants is often incomplete, the catalyst might leach and afford homogeneous contributions to the observed catalysis[92, 100].

Based on previous work conducted by Cantrell and co-workers[92], or Géraud and co-workers[99], an alkali-free route was chosen to prepare Na-free hydrotalcites, using $(NH_4)_2CO_3$ and NH_4OH as the precipitation agents, at pH values of 9.3-9.5. High pH values generally facilitate greater incorporation of Mg into the hydrotalcite structure, due to increased solubility of $Mg(OH)_2$ compared to $Al(OH)_3$ and increase the basic strength of the solid base[101].

Gupta and co-workers[8] previously employed hydrotalcites obtained *via* alkali precipitation routes as both a support and solid base for Au nanoparticles, resulting in significant HMF oxidation and high 2,5-furandicarboxylic acid (FDCA) yields. In this work a hydrotalcite with a nominal Mg:Al molar ratio of 5 was reported as the most active, however the actual composition was not quantified and such a high Mg:Al ratio is not generally accepted as possible for pure phase HTs, as mentioned before[54].

Calcination of hydrotalcites at temperatures between 450–500 °C is known to result in the loss of interlayer carbonate anions and the concomitant formation of mixed metal oxides[53, 54, 92, 102]. Subsequent rehydration of such mixed metal oxides can promote re-regeneration of the parent layered double hydroxide structure, the so-called "memory effect"[54, 86, 94, 103, 104], in which hydroxide anions replace the original carbonates within the interlayers, provided that the calcination temperature remains below around 550 °C[94]. Rehydration of thermally generated

periclase-like Mg-(Al)-O is critical for the production of Brønsted base sites within hydrotalcites and their associated solid base catalysis[84, 105-107].

Our group have previously demonstrated the utility of calcined-rehydrated hydrotalcites as solid bases for the transesterification of triglycerides in biodiesel production,[92-101] however the corresponding 48 h vapour phase rehydration protocol is time-consuming, and the impact of calcination temperature on base properties has not been systematically investigated to date[108].

1.5 Supported AuPd NPs for selox

The oxidation of alcohols and polyols to carbonyls has been widely studied using supported heterogeneous Pd catalysts[1, 52, 53, 109-114] in aqueous[109] and organic solvents[66, 109, 115]. Our research group has shown that high surface area (300 $m^2.g^{-1}$) mesoporous alumina[116] or mesoporous silica[115, 117, 118], such as surfactant-templated SBA-15 (a high surface area support with hexagonally packed, p6mm, parallel mesopore channels (950 $m^2.g^{-1}$), and two high surface area cubic silica supports with three-dimensional interpenetrating mesopore networks, SBA-16, Im3m, ($m^2.g^{-1}$) and KIT-6, Ia3d, (940 $m^2.g^{-1}$)), potentially linked via micropores[117, 118], were able to stabilise atomically highly dispersed Pd^{2+} centres, that exhibit exceptional activity toward the aerobic selox of allylic alcohols, being PdO the true active site for the oxidative dehydrogenation.

These materials were found to be highly selective (70-80 %) to the allylic aldehyde with the remaining products due to decarbonylation, breaking the C-O bond and hydrogenation, due to surface hydrogen arising from the oxidative dehydrogenation mechanism. However, PdO can undergo *in situ* reduction to Pd^0 during alcohol selox[117-119] and does not carry on the second step required for HMF selox, the oxidation of the aldehyde to carboxylic acid.

To overcome these issues, our research group[66, 120] and several other authors[55, 79, 109, 121] tested bimetallic AuPd NPs catalysts for the selox of different alcohols and polyols. Also, Hutchings and co-authors[55, 79, 122] found this alloy to be very active for direct synthesis of H_2O_2 from hydrogen and oxygen, either prepared *via* deposition-precipitation, or *via* impregnation, or *via* sol immobilisation.

Different routes are known in literature to prepare AuPd NPs and different kind of structured nanoparticles can be obtained[123]. Mainly, polymer-stabilised bimetallic alloys can

be obtained following co-reduction of mixed ions precursors, while successive reduction of two metal salts can be considered an adequate method to prepare core-shell bimetallic nanoparticles. For this purpose, the presence of an adequate polymer for NPs stabilisation is crucial, being PVP or PVA the most common used, and the order in which precursors are reduced may yield Au-core/Pd-shell, Pd-core/Au-shell or cluster-in-cluster particles[123].

Several old methods were reported for the reduction of precursor ions to metallic NPs; Schmid and co-authors[124], for example, prepared ligand-stabilised (p-$H_2NC_6H_4SO_3Na$) AuPd NPs by successive reductions, using citrate. PVP-stabilised AuPd bimetallic particles were prepared from their salts by alcohol reduction method by Toshima and co-authors[123], under refluxing of alcohol solutions of metal ions: alcohols work as a solvent and as reductants, being oxidised into aldehyde or ketone during the preparation.

Nevertheless, AuPd NPs, with a better control of particle size distribution, small sizes and higher catalytical activity have been prepared by deposition-precipitation[55, 79] at pH = 10, using NH_3, wet impregnation[79] or sol immobilisation on inorganic supports[74, 121], with or without the addition of polymers as stabilisers. The deposition-precipitation was chosen for this thesis work, because it was used also to prepare Au NPs and therefore offered a good comparison between NPs obtained using similar procedures.

Positive synergic effects, both geometric and electronic between Au and Pd have been found to increase not only catalytic activity, yields and selectivity, but also catalytic lifetime under mild reaction conditions[66, 109]. Prati and co-authors reported in their works[109] that, in the presence of a homogeneous base, such as NaOH, the activity of all these catalysts was enhanced; in this thesis work, AuPd NPs were deposited-precipitated on HT as both the support and the source of solid base and tested as catalysts for the selox of HMF to FDCA.

1.6 Reaction scheme for the selox of HMF

The selective oxidation of HMF proceeds through three steps[8] (**Scheme 1.3**). In the presence of O_2, supported Au nanoparticles and NaOH, the final product is actually the disodic salt of FDCA and not the free acid but, in order to simplify the discussion, the reagent and the products will be indicated as HMF (5-hydroxymethyl-2-furfural), HMFCA (5-hydroxymethyl-2-furancarboxylic acid), FFCA (5-formyl-2-furancarboxylic acid) and FDCA (2,5-furandicarboxylic acid) and the carboxylic group as the free acid instead of sodium salt.

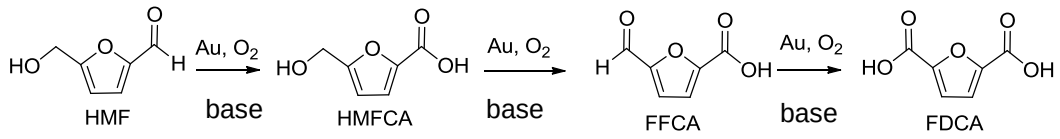

Scheme 1.3: selective oxidation of HMF to FDCA from reference 8.

1.7 Thesis Aims

Based on the previous studies reported in the literature, this PhD focuses its attention on understanding how the catalytic system, made of Au nanoparticles supported on solid bases, works for the selective oxidation of HMF. As reported by Gupta and co-authors[8], their hydrotalcites obtained *via* alkali route have a nominal Mg/Al ratio of 5 and have shown a high activity, both for the conversion and selectivity to FDCA. Nevertheless, these authors did not characterise accurately their hydrotalcites and, as well-known by Cavani and co-authors[54] and also reported by Cantrell and co-authors[92], such high Mg/Al ratio is not accepted for pure phase hydrotalcites and contaminations of NaOH and/or $Mg(OH)_2$ in the HT-phase might affect their results. One of the first goals of this project was to understand if the catalytic system described by Gupta and co-authors[8] is really heterogeneous or partially homo- and partially heterogeneous, focusing the attention on the role of NaOH and $Mg(OH)_2$ contaminations in the prepared hydrotalcite and consequentially the role of pH for this selective oxidation.

All the articles previously cited reported that when Au supported on carbon or TiO_2 is used as the catalyst for the selective oxidation of HMF, the reaction does not work without the addition of a homogeneous base and high NaOH/substrate ratios were necessary to oxidise both the R-OH and the R-CHO to R-COOH.

Furthermore, the selective oxidation of the aldehydic group is easier than the alcoholic one using this catalytic system but, to date, a systematic study of how important is the pH in this reaction and a systematic direct comparison between Na-free hydrotalcites as the heterogeneous base and NaOH as the homogeneous one have not been performed yet, together with the effect of alkali contaminations or phase impurities in the hydrotalcites on the selective oxidation of HMF.

The use of hydrotalcite as the support and the heterogeneous solid base allows the reaction to work at ambient pressure, even if a temperature of 90 °C is still required for the oxidation of the –OH group, and it was thought by Gupta and co-authors[8] to be the way to get the free carboxylic acid instead of its alkaline or alkaline-earth salt, without further purifications. Au nanoparticles dispersed on hydrotalcites (HT)[8], anionic microporous clays with a layered double hydroxide structure, have shown promise in HMF oxidation to FDCA, however key questions remain regarding the nature of active site[6], potential role of homogeneous and Na impurities contributions[1], and importance of reaction basicity upon activity and selectivity[5]. The incorporation of Pd into Au catalysts to provide a series of AuPd NPs, from Au-rich to Pd-rich alloys and its effect in enhancing Au catalytic activity were studied to improve the catalyst and FDCA yields.

1.8 References

1. S. E. Davis, L. R. Houk, E. C. Tamargo, A. K. Datye and R. J. Davis, *Catalysis Today*, 2011, **160**, 55-60.
2. R. A. Sheldon, *Catalysis Today*, 2011, **167**, 3-13.
3. B. F. M. Kuster, *Starch - Stärke*, 1990, **42**, 314-321.
4. P. T. Anastas, M. M. Kirchhoff and T. C. Williamson, *Applied Catalysis A: General*, 2001, **221**, 3-13.
5. T. Pasini, M. Piccinini, M. Blosi, R. Bonelli, S. Albonetti, N. Dimitratos, J. A. Lopez-Sanchez, M. Sankar, Q. He, C. J. Kiely, G. J. Hutchings and F. Cavani, *Green Chemistry*, 2011, **13**, 2091-2099.
6. O. Casanova, S. Iborra and A. Corma, *ChemSusChem*, 2009, **2**, 1138-1144.
7. O. Casanova, S. Iborra and A. Corma, *Journal of Catalysis*, 2009, **265**, 109-116.
8. N. K. Gupta, S. Nishimura, A. Takagaki and K. Ebitani, *Green Chemistry*, 2011, **13**, 824-827.
9. S. Carrettin, P. McMorn, P. Johnston, K. Griffin, C. J. Kiely and G. J. Hutchings, *Physical Chemistry Chemical Physics*, 2003, **5**, 1329-1336.
10. P. D. P. Atkins, *Oxford University Press, 5th edition*, 2009, 459.
11. J. H. Clark, D. J. Macquarrie, J. H. Clark and D. J. Macquarrie, *Chemical Society Reviews*, 1996, **25**, 303.
12. R. Noyori, T. Ohkuma, M. Kitamura, H. Takaya, N. Sayo, H. Kumobayashi and S. Akutagawa, *Journal of the American Chemical Society*, 1987, **109**, 5856-5858.
13. K. Mashima, K.-h. Kusano, N. Sato, Y.-i. Matsumura, K. Nozaki, H. Kumobayashi, N. Sayo, Y. Hori and T. Ishizaki, *The Journal of Organic Chemistry*, 1994, **59**, 3064-3076.
14. M. Kitamura, T. Ohkuma, S. Inoue, N. Sayo, H. Kumobayashi, S. Akutagawa, T. Ohta, H. Takaya and R. Noyori, *Journal of the American Chemical Society*, 1988, **110**, 629-631.
15. R. Noyori, *Angewandte Chemie International Edition*, 2002, **41**, 2008-2022.
16. J. C. Mol, *Journal of Molecular Catalysis A: Chemical*, 2004, **213**, 39-45.
17. W. Keim, *Angewandte Chemie International Edition*, 2013, **52**, 12492-12496.

18. R. R. Schrock, J. S. Murdzek, G. C. Bazan, J. Robbins, M. DiMare and M. O'Regan, *Journal of the American Chemical Society*, 1990, **112**, 3875-3886.
19. S. T. Nguyen, L. K. Johnson, R. H. Grubbs and J. W. Ziller, *Journal of the American Chemical Society*, 1992, **114**, 3974-3975.
20. K. S. W. Sing, D. H. Everett, R. A. W. Haul, L. Moscou, R. A. Pierotti, J. Rouquerol and T. Siemieniewska, in *Handbook of Heterogeneous Catalysis*, Wiley-VCH Verlag GmbH & Co. KGaA, 2008.
21. C. H. Bartholomew, *Applied Catalysis A: General*, 2001, **212**, 17-60.
22. J. A. Moulijn, A. E. van Diepen and F. Kapteijn, *Applied Catalysis A: General*, 2001, **212**, 3-16.
23. J.-D. Grunwaldt, M. Caravati and A. Baiker, *The Journal of Physical Chemistry B*, 2006, **110**, 25586-25589.
24. A. F. Lee, Z. Chang, P. Ellis, S. F. J. Hackett and K. Wilson, *The Journal of Physical Chemistry C*, 2007, **111**, 18844-18847.
25. B. M. Choudary, Lakshmi, B.M. and Lakshmi, S.P., *Catalysis Today*, 2000, **57**, 17.
26. H. Yang, X. Han, Z. Ma, R. Wang, J. Liu and X. Ji, *Green Chemistry*, 2010, **12**, 441-451.
27. R. A. Sheldon, Arends, I. and Dijksman, A., *Catalysis Today*, 2000, **57**, 157.
28. V. Polshettiwar and R. S. Varma, *Green Chemistry*, 2010, **12**, 743-754.
29. T. Mallat and A. Baiker, *Chemical Reviews*, 2004, **104**, 3037-3058.
30. J. H. Clark, *Green Chemistry*, 1999, **1**, 1-8.
31. G. A. Somorjai and K. McCrea, *Applied Catalysis A: General*, 2001, **222**, 3-18.
32. F. Zaera, *Catal Lett*, 2003, **91**, 1-10.
33. G. A. Somorjai and J. Y. Park, *Angewandte Chemie International Edition*, 2008, **47**, 9212-9228.
34. S. K. R. Patil, J. Heltzel and C. R. F. Lund, *Energy & Fuels*, 2012, **26**, 5281-5293.
35. J. N. Chheda, G. W. Huber and J. A. Dumesic, *Angewandte Chemie International Edition*, 2007, **46**, 7164-7183.
36. D. Mercadier, L. Rigal, A. Gaset and J.-P. Gorrichon, *Journal of Chemical Technology and Biotechnology*, 1981, **31**, 489-496.
37. C. Moreau, R. Durand, S. Razigade, J. Duhamet, P. Faugeras, P. Rivalier, P. Ros and G. Avignon, *Applied Catalysis A: General*, 1996, **145**, 211-224.
38. J. N. Chheda, Y. Roman-Leshkov and J. A. Dumesic, *Green Chemistry*, 2007, **9**, 342-350.
39. A. Gandini, A. J. D. Silvestre, C. P. Neto, A. F. Sousa and M. Gomes, *Journal of Polymer Science Part A: Polymer Chemistry*, 2009, **47**, 295-298.
40. Y. Y. Gorbanev, S. K. Klitgaard, J. M. Woodley, C. H. Christensen and A. Riisager, *ChemSusChem*, 2009, **2**, 672-675.
41. A. Ranoux, K. Djanashvili, I. W. C. E. Arends and U. Hanefeld, *ACS Catalysis*, 2013, **3**, 760-763.
42. Y. Roman-Leshkov, J. N. Chheda and J. A. Dumesic, *Science*, 2006, **312**, 1933-1937.
43. H. Zhao, J. E. Holladay, H. Brown and Z. C. Zhang, *Science*, 2007, **316**, 1597-1600.
44. Y. Su, H. M. Brown, X. Huang, X.-d. Zhou, J. E. Amonette and Z. C. Zhang, *Applied Catalysis A: General*, 2009, **361**, 117-122.
45. A. Osatiashtiani, A. F. Lee, D. R. Brown, J. A. Melero, G. Morales and K. Wilson, *Catalysis Science & Technology*, 2014, **4**, 333-342.
46. A. Osatiashtiani, A. F. Lee, M. Granollers, D. R. Brown, L. Olivi, G. Morales, J. A. Melero and K. Wilson, *ACS Catalysis*, 2015, **5**, 4345-4352.
47. W. Partenheimer and Vladimir V. Grushin, *Advanced Synthesis & Catalysis*, 2001, **343**, 102-111.

48. O. C. C. Navarro, A.C.; Chornet, S.I., *Top Catal*, 2009, **52**, 304.
49. P. Verdeguer, N. Merat and A. Gaset, *Journal of Molecular Catalysis*, 1993, **85**, 327-344.
50. U. S. M. L. Ribeiro, *Catal. Commun.*, 2003, **4**, 83-86.
51. P. v. D. Vinke, H.E.; van Bekkum, H., *Elsevier, New York*, 1990, 147.
52. S. E. Davis, B. N. Zope and R. J. Davis, *Green Chemistry*, 2012, **14**, 143-147.
53. S. E. Davis, A. D. Benavidez, R. W. Gosselink, J. H. Bitter, K. P. de Jong, A. K. Datye and R. J. Davis, *Journal of Molecular Catalysis A: Chemical*, 2014, **388–389**, 123-132.
54. F. Cavani, F. Trifirò and A. Vaccari, *Catalysis Today*, 1991, **11**, 173-301.
55. S. Meenakshisundaram, E. Nowicka, P. J. Miedziak, G. L. Brett, R. L. Jenkins, N. Dimitratos, S. H. Taylor, D. W. Knight, D. Bethell and G. J. Hutchings, *Faraday Discussions*, 2010, **145**, 341-356.
56. L. Prati and A. Villa, *Catalysts*, 2011, **2**, 24.
57. M. Haruta, T. Kobayashi, H. Sano and N. Yamada, *Chemistry Letters*, 1987, **16**, 405-408.
58. M. Haruta, N. Yamada, T. Kobayashi and S. Iijima, *Journal of Catalysis*, 1989, **115**, 301-309.
59. G. J. Hutchings, *Journal of Catalysis*, 1985, **96**, 292-295.
60. B. Nkosi, N. J. Coville and G. J. Hutchings, *Journal of the Chemical Society, Chemical Communications*, 1988, 71-72.
61. B. Nkosi, N. J. Coville and G. J. Hutchings, *Applied Catalysis*, 1988, **43**, 33-39.
62. B. Nkosi, N. J. Coville, G. J. Hutchings, M. D. Adams, J. Friedl and F. E. Wagner, *Journal of Catalysis*, 1991, **128**, 366-377.
63. R. A. a. K. Sheldon, J.K., *Academic Press, New York.*, 1981.
64. C. D. Pina, E. Falletta and M. Rossi, *Chemical Society Reviews*, 2012, **41**, 350-369.
65. C. Della Pina, E. Falletta, L. Prati and M. Rossi, *Chemical Society Reviews*, 2008, **37**, 2077-2095.
66. A. F. Lee, C. V. Ellis, K. Wilson and N. S. Hondow, *Catalysis Today*, 2010, **157**, 243-249.
67. L. Prati and M. Rossi, *Journal of Catalysis*, 1998, **176**, 552-560.
68. M. Comotti, C. D. Pina and M. Rossi, *Journal of Molecular Catalysis A: Chemical*, 2006, **251**, 89-92.
69. M. Comotti, C. Della Pina, E. Falletta and M. Rossi, *Journal of Catalysis*, 2006, **244**, 122-125.
70. M. Comotti, C. Della Pina, R. Matarrese and M. Rossi, *Angewandte Chemie International Edition*, 2004, **43**, 5812-5815.
71. C. Bianchi, S. Biella, A. Gervasini, L. Prati and M. Rossi, *Catal Lett*, 2003, **85**, 91-96.
72. S. Biella, L. Prati and M. Rossi, *Journal of Catalysis*, 2002, **206**, 242-247.
73. N. Dimitratos, A. Villa, C. L. Bianchi, L. Prati and M. Makkee, *Applied Catalysis A: General*, 2006, **311**, 185-192.
74. L. Prati and G. Martra, *Gold Bulletin*, 1999, **32**, 96-101.
75. A. Abad, P. Concepción, A. Corma and H. García, *Angewandte Chemie International Edition*, 2005, **44**, 4066-4069.
76. A. Corma and M. E. Domine, *Chemical Communications*, 2005, 4042-4044.
77. A. Abad, A. Corma and H. García, *Chemistry – A European Journal*, 2008, **14**, 212-222.
78. B. Zope, S. Davis and R. Davis, *Topics in Catalysis*, 2012, **55**, 24-32.
79. G. L. Brett, Q. He, C. Hammond, P. J. Miedziak, N. Dimitratos, M. Sankar, A. A. Herzing, M. Conte, J. A. Lopez-Sanchez, C. J. Kiely, D. W. Knight, S. H. Taylor and G. J. Hutchings, *Angewandte Chemie*, 2011, **123**, 10318-10321.

80. M. Haruta, *Catalysis Today*, 1997, **36**, 153-166.
81. B. N. Zope, R. J. Davis, *Topics in Catalysis*, 2012, **55**, 24-32.
82. P. Beltrame, M. Comotti, C. Della Pina and M. Rossi, *Applied Catalysis A: General*, 2006, **297**, 1-7.
83. M. Comotti, C. Della Pina, E. Falletta and M. Rossi, *Advanced Synthesis & Catalysis*, 2006, **348**, 313-316.
84. M. J. Climent, A. Corma, S. Iborra, K. Epping and A. Velty, *Journal of Catalysis*, 2004, **225**, 316-326.
85. D. G. Evans and R. C. T. Slade, in *Layered Double Hydroxides*, eds. X. Duan and D. G. Evans, Springer Berlin Heidelberg, Berlin, Heidelberg, 2006, pp. 1-87.
86. A. Vaccari, *Catalysis Today*, 1998, **41**, 53-71.
87. V. R. L. Constantino and T. J. Pinnavaia, *Inorganic Chemistry*, 1995, **34**, 883-892.
88. S. Miyata and A. Okada, *Clay Clay Min.*, 1977, **25**, 14-18.
89. O. Marino and G. Mascolo, *Thermochim. Acta*, 1982, **55**, 377-383.
90. W. T. Reichle, *Journal of Catalysis*, 1985, **94**, 547-557.
91. J. I. Di Cosimo, V. K. Díez, M. Xu, E. Iglesia and C. R. Apesteguía, *Journal of Catalysis*, 1998, **178**, 499-510.
92. D. G. Cantrell, L. J. Gillie, A. F. Lee and K. Wilson, *Applied Catalysis A: General*, 2005, **287**, 183-190.
93. W. T. Reichle, *Journal of Catalysis*, 1985, **94**, 547-557.
94. W. T. Reichle, S. Y. Kang and D. S. Everhardt, *Journal of Catalysis*, 1986, **101**, 352-359.
95. A. Vaccari, *Catalysis Today*, 1998, **41**, 53-71.
96. L. Lv, P. Sun, Z. Gu, H. Du, X. Pang, X. Tao, R. Xu and L. Xu, *Journal of Hazardous Materials*, 2009, **161**, 1444-1449.
97. G. W. Brindley and S. Kikkawa, *American Mineralogist*, 1979, **64**, 836-843.
98. J. S. Valente, F. Figueras, M. Gravelle, P. Kumbhar, J. Lopez and J. P. Besse, *Journal of Catalysis*, 2000, **189**, 370-381.
99. E. Géraud, S. Rafqah, M. Sarakha, C. Forano, V. Prevot and F. Leroux, *Chemistry of Materials*, 2008, **20**, 1116-1125.
100. J. M. Fraile, N. García, J. A. Mayoral, E. Pires and L. Roldán, *Applied Catalysis A: General*, 2010, **387**, 67-74.
101. J. J. Woodford, J.-P. Dacquin, K. Wilson and A. F. Lee, *Energy & Environmental Science*, 2012, **5**, 6145-6150.
102. S. Abelló, F. Medina, D. Tichit, J. Pérez-Ramírez, X. Rodríguez, J. E. Sueiras, P. Salagre and Y. Cesteros, *Applied Catalysis A: General*, 2005, **281**, 191-198.
103. E. Angelescu, O. D. Pavel, R. Bîrjega, M. Florea and R. Zăvoianu, *Applied Catalysis A: General*, 2008, **341**, 50-57.
104. V. Dávila, E. Lima, S. Bulbulian and P. Bosch, *Microporous and Mesoporous Materials*, 2008, **107**, 240-246.
105. A. Corma, S. B. A. Hamid, S. Iborra and A. Velty, *Journal of Catalysis*, 2005, **234**, 340-347.
106. M. J. Climent, A. Corma, S. Iborra and J. Primo, *Journal of Catalysis*, 1995, **151**, 60-66.
107. M. J. Climent, A. Corma, S. Iborra and A. Velty, *Journal of Catalysis*, 2004, **221**, 474-482.
108. Y. Xi and R. J. Davis, *Journal of Catalysis*, 2009, **268**, 307-317.
109. N. Dimitratos, A. Villa, D. Wang, F. Porta, D. Su and L. Prati, *Journal of Catalysis*, 2006, **244**, 113-121.
110. M. Besson and P. Gallezot, *Catalysis Today*, 2000, **57**, 127-141.

111. A.-B. Crozon, M. Besson and P. Gallezot, *New Journal of Chemistry*, 1998, **22**, 269-273.
112. T. Mallat and A. Baiker, *Catalysis Today*, 1994, **19**, 247-283.
113. P. Vinke, D. d. Wit, A. T. J. W. de Goede and H. v. Bekkum, in *Studies in Surface Science and Catalysis*, eds. P. Ruiz and B. Delmon, Elsevier, 1992, vol. Volume 72, pp. 1-20.
114. P. Gallezot, *Catalysis Today*, 1997, **37**, 405-418.
115. Y.-S. J. Lee, Y.; Chung, Y-D.; Lim, K-Y.; Whang, C-N.; Oh, S-J., *Journal of the Korean Physical Society*, 2000, **37**, 451-455.
116. S. F. J. Hackett, R. M. Brydson, M. H. Gass, I. Harvey, A. D. Newman, K. Wilson and A. F. Lee, *Angewandte Chemie International Edition*, 2007, **46**, 8593-8596.
117. C. M. A. Parlett, D. W. Bruce, N. S. Hondow, A. F. Lee and K. Wilson, *ACS Catalysis*, 2011, **1**, 636-640.
118. C. M. A. Parlett, A. F. Lee, K. Wilson, D. W. Bruce, N. S. Hondow, M. A. Newton, *CHEMCATCHEM*, 2013, **5**, 939-950.
119. A. F. Lee and K. Wilson, *Green Chemistry*, 2004, **6**, 37-42.
120. J. Naughton, A. F. Lee, S. Thompson, C. P. Vinod and K. Wilson, *Physical Chemistry Chemical Physics*, 2010, **12**, 2670-2678.
121. A. Villa, N. Janjic, P. Spontoni, D. Wang, D. S. Su and L. Prati, *Applied Catalysis A: General*, 2009, **364**, 221-228.
122. J. K. E. D. I. Enache, P. Landon, B. Solsona-Espriu, A. F. Carley, A. A. Herzing, and C. J. K. M. Watanabe, D. W. Knight and G. J. Hutchings, *Science*, 2006, **311**, 362.
123. N. Toshima and T. Yonezawa, *New Journal of Chemistry*, 1998, **22**, 1179-1201.
124. G. Schmid, H. West, J.-O. Malm, J.-O. Bovin and C. Grenthe, *Chemistry – A European Journal*, 1996, **2**, 1099-1103.

Chapter 2

Experimental

List of contents

2.1 Catalyst preparation

2.1.1 Parent hydrotalcite synthesis

Hydrotalcites were synthesised using the alkali-free co-precipitation method of Cantrell and co-workers[1], with some modifications, from aqueous dilute solutions. Briefly, an Atlas Syrris pump-syringe with two addition channels was used instead of conventional addition funnels, in order to have a better repeatability; 1 M solutions of $Mg(NO_3)_2\ 6H_2O$ (Sigma-Aldrich, 98.0 – 102.0 %) and $Al(NO_3)_3\ 9H_2O$ (Sigma-Aldrich, ≥ 98 %) were separately prepared in de-ionised H_2O, then mixed in a volumetric flask to get 100 ml of a new solution, having Mg/Al = 3 as the theoretical molar ratio (pump 1). 100 ml of a 2 M buffer aqueous solution of $(NH_4)_2CO_3$ (Sigma-Aldrich Fluka, 30-33 % NH_3 basis) and NH_4OH (Fisher NH_4OH, NH_3 solution, 35 wt. %) at pH = 9 was prepared and charged into another volumetric flask (pump 2). The addition rate was set up to be 1 mL/min, the pH was monitored using a Jenway 3510 pH meter and kept constant in the range of 9.3-9.5 by adding concentrated NH_4OH when necessary (35 wt. % NH_3 aqueous solution).

The two solutions were added dropwise in parallel and simultaneously at room temperature into a 2 L Radleys Ready reactor **(Figure 2.1)**, pre-filled with 300 ml of de-ionised water and under stirring (300 rpm); the white hydrogel formed was left to age overnight at T = 65 °C, washed with H_2O until the pH was as close to the neutral as possible, then dried in a vacuum oven overnight at T = 100 °C. High pH values generally facilitate greater incorporation of Mg into the hydrotalcite structure, due to increased solubility of $Mg(OH)_2$ compared to $Al(OH)_3$ and increase the basic strength of the solid base[2].

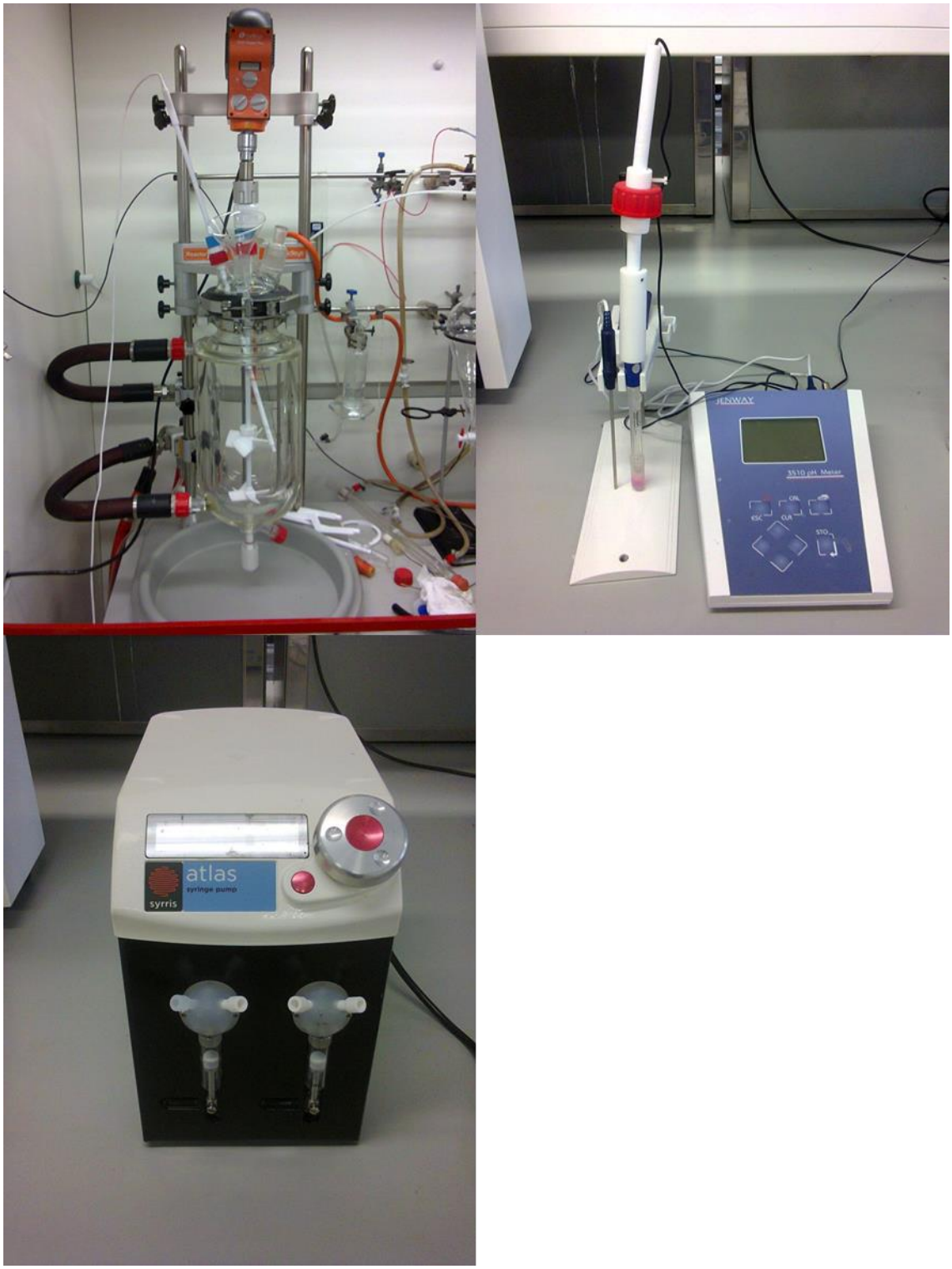

Figure 2.1: top left – Radleys Ready reactor, top right – Jenway 3510 pH meter with equipped electrode for Radleys Ready reactor and bottom left – Atlas Syrris pump-syringe.

2.1.2 Typical preparation of Au/HT or Au/CHT catalysts

The deposition-precipitation method was chosen to prepare a series of gold catalysts, respectively 0.5, 1, 2, 5 and 10 wt. % Au. This method allowed to prepare Au nanoparticles supported onto HT, following the procedure described by Gupta and co-authors[3]. Briefly, an adequate amount of aqueous solution of $HAuCl_4\,3H_2O$ (Alfa Aesar, ≥ 99.99 %, Au = 49.5 wt. %), having a concentration of [Au] = 10 or 20 $mg.mL^{-1}$, was dissolved in 40 ml H_2O under stirring, then 1 g of hydrotalcite was added, followed by concentrated NH_4OH (35 wt. % NH_3 aqueous solution), until the pH was monitored to be 10 (0.6 - 0.8 mL base solution added).

The reaction was left under stirring at room temperature for 6 h, then under reflux for 30 min. The yellow-orange solid was filtered off, washed through with H_2O until neutral pH was determined with a pH indicator, then calcined under O_2 (always used in this thesis work pure at 99.995 %) in a tube furnace for 4 h at T = 200 °C. The final catalysts were purple and this change in colour was first empirical evidence that Au^0 nanoparticles were formed, due to their associated surface plasmon resonance[4, 5].

To support gold on mixed oxides, the same procedure was followed, but the calcination temperatures used were 300, 400 or 500 °C respectively.

2.1.3 Typical preparation of Au/CHT and rehydrated

The prepared catalyst described in **Chapter 2.1.2**, 2 wt. % Au supported on HT, was divided in six separated batches. The calcination followed by reconstruction of the hydrotalcite phase in H_2O was systematically studied in different conditions, to optimise the preparation procedures. Two different calcination temperatures were tested, respectively 300 or 450 °C and three rehydration methods were tested: vapour phase[6, 7], water in subcritical conditions at 120 °C in pressured flasks[8] or simply hot water at 100 °C [9].

In order to explain each procedure and to help distinguish the batches, samples are labelled according to the following nomenclature: CHT-XXX-YYY, where XXX is the calcination temperature and YYY is the rehydration protocol. Oxygen and nitrogen purity is 99.995 %.

- CHT300Vap: calcined hydrotalcite at 300 °C for 4 h in O_2, cooled down under N_2 until RT and then rehydrated in water-wet N_2, at RT, for 48 h. The flow was held at 20 ml/min using a gas regulator.

- CHT300Subw: calcined hydrotalcite at 300 °C for 4 h, then rehydrated in water, under pressure, in Ace™ round-bottomed flasks, at 120 °C in subcritical conditions for 6 h.

- CHT300Hotw: calcined hydrotalcite at 300 °C for 4 h, then rehydrated in boiling water at ambient pressure and for 6 h.

The same three procedures were used to prepare the analogous CHT 450 °C series. CHT-RW represents the general family of rehydrated materials, as distinguished from the parent hydrotalcites.

After this screening, a range of gold loadings spanning 0.5, 1, 2, 5 and 10 wt. % were supported on HT as described above, calcined at 450 °C for 4 h and subsequent water vapour phase rehydration under wet N_2 for 48 h, as described above.

2.1.4 Typical preparation of AuPd/hydrotalcites

The deposition-precipitation method[3] was chosen to prepare a series of AuPd/HT catalysts. The total amount of metal was chosen to be 1 wt. %, while the chosen molar ratios were $Au_{95}Pd_5$, $Au_{90}Pd_{10}$, $Au_{80}Pd_{20}$, $Au_{70}Pd_{30}$ and $Au_{60}Pd_{40}$. Briefly, an adequate amount of aqueous solution of $HAuCl_4$ 3 H_2O (Alfa Aesar, ≥ 99.99, Au = 49.5 wt. %), having a concentration of [Au] = 10 $mg.mL^{-1}$, and of aqueous solution of $PdCl_2$ having [Pd] = 5.5 $mg.mL^{-1}$ (Alfa Aesar $PdCl_2$ mother solution, Pd 20-25 w/w) were dissolved in 40 mL H_2O under stirring, then 1 g of hydrotalcite was added, followed by concentrated NH_4OH (35 wt. % NH_3 aqueous solution), until the pH was monitored to be 10 (0.6 - 0.8 mL base solution added).

The reaction was left under stirring at room temperature for 6 h, then under reflux for 30 min. The white solid was filtered off, washed through with H_2O until neutral pH, calcined under O_2 in a tube furnace for 4 h at T = 200 °C and then reduced under H_2 at the same temperature for 4 h. The final catalysts were grey and this change in colour was first empirical evidence that AuPd metal nanoparticles were formed[10].

2.1.5 Preparation of 2 wt. % Au on C and of 1 wt. % Pd/HT

Rossi's[11] and Prati's[12] methods were chosen to prepare a supported Au sol on carbon[13]; 2 g of carbon (Johnson Mattey, carbon support) was washed under stirring at 500 rpm with 20 mL HNO_3 6M (diluted in de-ionised water from HNO_3 70 wt. % Fisher Scientific), to remove ash and inorganic salts, which might plug carbon micropores, poison the catalyst and not guarantee constant properties even from batch to batch[14]. After filtration, carbon was washed with deionised water until pH = 7 and dried in the oven at T = 100 °C.

A solution of $HAuCl_4$ having [Au] = 20 mg/mL was prepared as described in **Chapter 2.1.2**, then 1 mL of this was diluted in a 1 L beaker in deionised H_2O 500 mL. Glucose (D-(+)-Glucose, Sigma-Aldrich, > 99.5 %) was then added as a stabiliser and pH adjusted to 2.6 using HCl 1M, (diluted in de-ionised water from HCl 37 wt. % Fisher Scientific), then 5 mL of a freshly prepared aqueous solution of reductant, $NaBH_4$ 0.1 M ($NaBH_4$ Sigma-Aldrich 98 %) were added to the solution. The colour changed from yellow to red ruby-mahogany and this was a first indicator that a sol made of Au^0 nanoparticles was formed, due to their associated surface plasmon resonance[4, 5].

Pre-treated carbon was added as the support immediately after the described change in colour and left under stirring for 1 h. The catalyst was filtered off, washed through with H_2O until neutral pH and dried in the oven at 80 °C overnight. The same method was follow under identical conditions to support 1 wt. % Pd colloid on 1 g of HT, starting from a $PdCl_2$ aqueous solution having [Pd] = 5.5 $mg.mL^{-1}$.

2.2 Support and catalyst characterisation

2.2.1 Elemental analysis

Bulk Au and Pd loadings, together with Mg and Al contents for the HT, CHT and CHT-RW series were determined by MEDAC Analytical and Chemical Consultancy Service LTD. Samples were digested in *aqua regia* (a mixture of HCl:HNO_3 = 3:1) and diluted in aqueous 10 wt. % HNO_3 until the sample was not clear, prior analysis on a Varian Vista MPX ICP-OES.

ICP-OES is a type of emission spectroscopy based on an inductively coupled plasma, which is used to produce excited atoms and ions that emit electromagnetic radiations at a

wavelength characteristic of particular elements. The plasma torch is made of three concentric quartz tubes[15] and a coil of a radio-frequency generator surrounds a part of it. Argon is used to generate the plasma and its flame temperature reaches 10,000 °C. When the torch is turned on, an intense electromagnetic field is generated within the coil by the high power radio-frequency signal flowing through it (i.e. 27 or 40 MHz) and cages the plasma. The Ar gas is ignited by a Tesla coil that generates a discharge arc through the gas flow and initiates the ionisation process; after that, the Tesla unit is switched off; the Ar flow feeds plasma, being ionized by the strong magnetic field. A peristaltic pump sends the solution, usually metal ions in 10 wt. % HNO_3, to a nebuliser and then inside the plasma, where it collides with electrons, ionized gas and it breaks into charged ions itself. Thus, sample atoms break up in ions, lose electrons and recombine in the plasma, generating radiations at the characteristic wavelength of the involved element, analysed in an adequate optical chamber. Calibration curves, obtained *via* different concentration standards, allow quantification of the unknown concentration in the analysed solution. **Figure 2.2** shows a schematic illustration of ICP instrument[16].

Figure 2.2: inset top left – ionised Ar plasma flame; main – a scheme illustrating the difference between ICP-AES and ICP-MS analysis system, from reference 16.

When ICP was not available, samples were analysed by XRF spectroscopy on a Horiba XGT-7000 X-ray analytical microscope fitted with a rhodium X-ray tube operating at 50 kV, a nickel filter, a spot size of 1.2 mm and a silicon detector. Bombardment of a sample with sufficiently high energy X-rays facilitates ejection of a core electron. The "hole" in the lower energy shell decreases atomic stability, which is overcome by the relegation of a high energy shell electron to the hole[17]; this process generates excess energy, which is emitted as a secondary X-ray photon, whose energy is characteristic. The secondary X-ray is described by the electron shell transition, i.e. L → K is Kα while M → K is Kβ. Fluorescence is thus described as the phenomenon of radiation absorption, which may be followed by radiative emission at a different energy, as shown in **Figure 2.3**

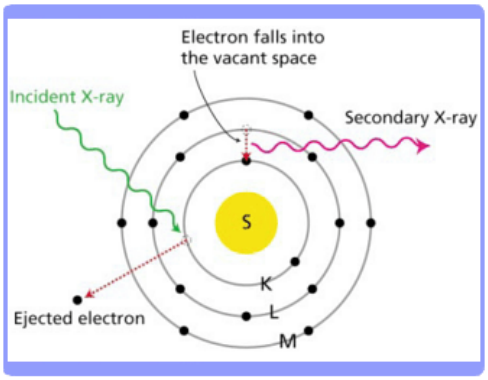

Figure 2.3: an illustrative representation of X-ray fluorescence mechanism.

2.2.2 Powder X-ray diffraction

During the first part of this thesis work at Cardiff University, *ex-situ* X-ray diffraction (XRD) patterns were recorded on a Panalytical X'pert Pro diffractometer fitted with an X'Celerator detector, using a Cu K_α (1.54 Å, 8.04 KeV) source with a nickel filter, calibrated against a Si standard, wide angle patterns were collected over a range of 2θ = 5-80° or 5-100° (step size 0.02°, scan speed 0.020° s^{-1}). During the second part of this work at Aston University, X-ray diffraction patterns were recorded on a Bruker d8 Advance XRD fitted with a LYNX eye high speed strip detector, patterns were obtained between 5 and 100 degrees and a step size of 0.02 degrees and 1 second per step. *In-situ* XRD patterns were performed using an Anton-Paar XRK-900 cell and Bronkhorst EL-Flow mass flow controllors, O_2 (99.995 %) was used for the calcination ramp.

A tungsten filament is electrically heated (40 KV, 40 mA) and emits e^-, which are fired on a Cu anode. Cu K_α (1.54 Å, 8.04 KeV) X-ray photons, generated via the demotion of a high energy shell electron to a lower vacancy, in the copper anode, are fired at a homogeneous powder sample, at a sufficient energy to allow bulk characterisation. Sample homogeneity guarantees that, for a randomly organised powder specimen, there will be enough material correctly orientated to allow constructive interference from crystal planes[18]. This arises from elastic scattering of the photons which if in-phase[19], as shown in **Figure 2.4**, results in constructive interference.

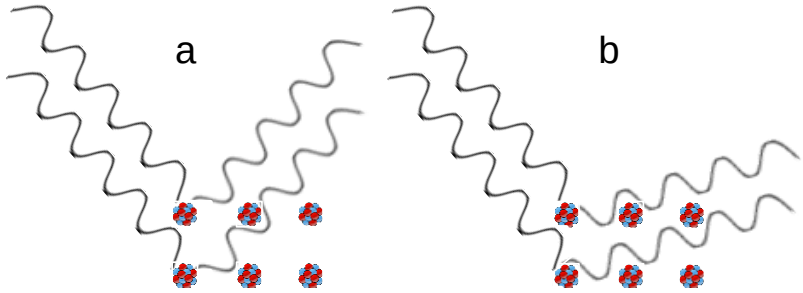

Figure 2.4 a) constructive and b) deconstructive interference of X-ray photons[20].

Interaction of X-rays with the sample, in the specific case with atoms in the crystallographic groups, creates secondary "diffracted" beams (actually generated in the form of cones) of X-rays related to interplanar spacings in the crystalline powder, according to a mathematical relation, Bragg's Law, that must apply when constructive interference occurs **(Equation 2.1)**. For set refraction angles, the distance between scatterers must be equal to an integer multiplied by the X-ray wavelength[19]. **Figure 2.5** illustrates X-ray diffraction from a crystalline material.

$$\mathbf{2d\sin\theta = n\lambda} \qquad \textbf{Equation 2.1}$$

Whereas n = order of interference (integer) λ = incident wavelength of the X-rays, d = interplanar lattice spacing generating the diffraction and θ = diffraction angle; λ and d are usually measured in Å.

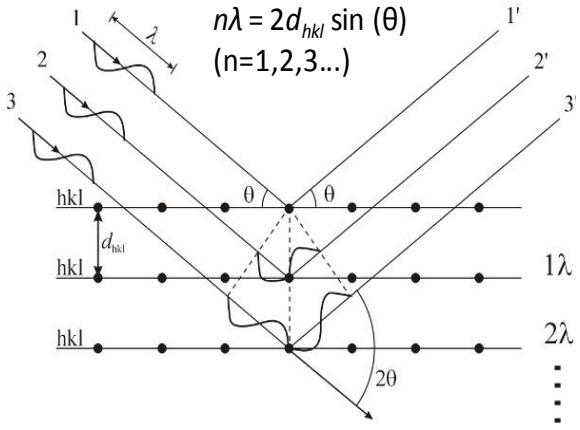

Figure 2.5: Schematic illustrating Bragg's X-ray and the relationship between lattice spacing and constructive interference.[20]

Around 3 % of the incident X-ray photons will be elastically scattered and diffracted by the crystal planes, while the other 97 % leave the crystal as transmitted radiation. The angle of the X-rays is altered and as a 2θ value is reached where constructive interference can occur for the crystal phase being examined, the diffracted X-rays are recorded by the detector, giving rise to characteristic diffraction patterns unique to individual materials.[18, 19] Diffraction peaks only occur if long range order is present (crystalline materials or ordered porosity), with a minimum detectable crystallite size of ~2 nm.[19, 21]

As it will be discussed later in **Chapter 3.2.3.2**, page 81, for a hydrotalcite mineral, existing in the polytype form named rombohedral 3R[6], with 3R stacking of the brucite layers, the interlayer spacing *d* can be calculated from measuring the peak position of the d_{003} reflection from the XRD pattern and then with the **Equation 2.2.**

$$d = d_{003} = \frac{\mathbf{n\,\lambda}}{\mathbf{2\,\sin\,\theta}} \qquad \textbf{Equation 2.2}$$

The lattice parameter *a*, related to the unit cell[6], was calculated using the d(110) XRD peak position, with the **Equation 2.3.**

$$a = 2\,d_{110} \qquad \textbf{Equation 2.3}$$

The lattice parameter *c*, that corresponds to three times the interlayer spacing *d* between two consecutive layers[22], was calculated using the d(003), d(006) and d(009) XRD peak position, with the **Equation 2.4**

$$c = d_{003} + 2\ d_{006} + 3\ d_{009} \qquad \textbf{Equation 2.4}$$

Peak width increases with decreasing particle size, due to incomplete cancelling of scattered X-rays close to the peak maxima. This happens because the refraction from the next lattice plane, when just off the maxima, is only slightly out of phase and cancels weakly. In larger crystals the combination of multiple refractions overcome this, whereas the limited number of lattice planes in small crystals diminishes this effect.[18, 19] The peak width can therefore be utilised for particle size determination by the Scherrer Equation **(Equation 2.5)**[23] and in this specific case it was used either for Au or for AuPd NPs.

$$\mathbf{PS_{av} = \frac{k\lambda}{\left(\sqrt{(B^2 - S^2)}\cos\theta\right)}} \qquad \textbf{Equation 2.5 –} \text{ Scherrer equation}$$

Whereas PS_{av} = average particle size (Å); B = FWHM of diffraction peak; S = 0.15 (systematic broadening caused by diffractometer); k = 0.9 (constant).

2.2.3 Nitrogen porosimetry

N_2 porosimetry was undertaken on a Quantachrome Nova 1200 porosimeter **(Figure 2.6)** using NovaWin analysis software, version 11.03. Samples were degassed at 120 °C for 2 h prior to N_2 adsorption. Adsorption/desorption isotherms were recorded at – 196 °C (liquid nitrogen temperature). BET surface areas were calculated over the relative pressure range 0.01-0.2 where a linear relationship was observed. Micropore analysis was undertaken using an Autosorb porosimeter, at lower relative pressures of 0.015-0.2, using ASiQwin, version 3.1 analysis software, pore diameters and volumes were calculated applying the DFT method and using the fitting model for N_2 at – 196 °C on carbon (slit pores, QSDFT equilibrium mode), because it was capable of giving the best fitting with experimental data.

Figure 2.6: Quantachrome Nova 1200 porosimeter connected with a computer for data analysis.

In physisorption there is a van der Waals interaction (dipole to dipole attractions)[17, 24] between the adsorbate and the substrate; in this specific case, N_2 adsorption, recorded at –196 °C, results from London forces[17], and are due to induced temporary dipoles. These interactions have a long range but are weak, and the energy released when a particle is physisorbed is of the same order of magnitude as the enthalpy of condensation. This small energy can be absorbed as vibrations of the lattice and dissipate as thermal motion, so a molecule bouncing across the surface will gradually lose its energy and adsorb on it in a process named accommodation[25].

The enthalpy of physisorption is in the region of 20 kJ mol^{-1}, but this small enthalpy change does not lead to bond breaking, so a physisorbed molecule does not change its nature, even if it might be distorted by the presence of the surface. N_2 physisorption occurs at temperatures below its boiling point,[24] due to the weak enthalpy of adsorption, and this permits multilayer adsorption, as the enthalpy of vaporisation (condensation) from adsorbate–adsorbate interactions is near in value to the enthalpy of adsorption and non-selective to sites of physisorption[26].

For a spontaneous process, the free Gibbs energy must be negative. Adsorption, at constant temperature and pressure, results in a decrease in system entropy, because the translational freedom of the adsorbate is reduced when it is adsorbed, thus enthalpy of adsorption must be negative (that means the process is exothermic)[17] to satisfy the negative condition of free Gibbs energy (exoergic) to occur[24, 27].

Isotherms are generated by the static volumetric technique,[26] N_2 is incrementally dosed and the amount adsorbed (under dynamic equilibrium, when rate of adsorption = rate of desorption) at a given pressure and constant temperature recorded. The isotherm type and its shape divulge information regarding the adsorbents. There are six classifications of isotherm, according to the IUPAC, shown in **Figure 2.7 – left**[28, 29].

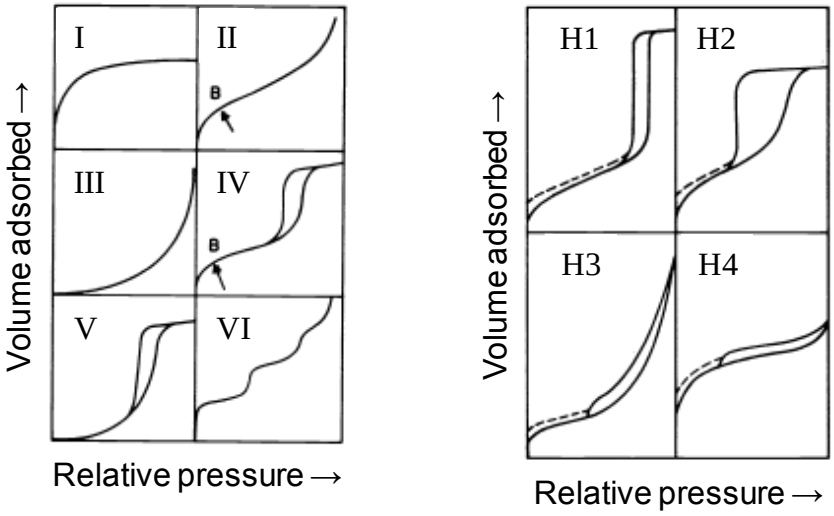

Figure 2.7 – Common adsorption isotherms and hysteresis types, from reference 28. B indicates the monolayer.

Type I represents microporous materials where a strong interaction between adsorbate and adsorbent occurs from their close proximity within micropores, type II is typical for either nonporous or macroporous materials; the unusual type III occurs when adsorbate interactions are greater than those with the surface. Hysteresis observed in types IV and V is indicative of mesoporous supports, while type VI indicates consecutive adsorbate layer formation due to uniform surface.

Hysteresis, visible in isotherm types IV and V, presents as four types, as shown in **Figure 2.7 – right** and occurs because of differences in condensation (adsorption) and evaporation (desorption) within mesopores;[26] adsorption occurs from the pore wall inwards.

The neighbourhood between adsorbate and pore wall improves the attractive interactions, leading to capillary condensation, and therefore there is a much sharper increase in the volume of gas adsorbed compared to non-porous materials.

Desorption, instead, occurs from the liquid surface at pore openings, where there is a strong interaction,[26] lowering the pressure that gas evaporation occurs relative to the condensation process. Hysteresis shape reveals further information: type H1 is shown for uniform pore sizes, while H2 represents non-uniformity ink bottle pore shapes. In the case of non-uniform pores, adsorption (condensation) will occur at the narrowest part of the pore and not fill the wider cross section until the vapour pressure has increased sufficiently. On desorption however, no evaporation will occur until the vapour pressure relating to evaporation from the widest cross-section of the pore has been reached, giving this much wider hysteresis loop[30]. Slit shaped pores produce H3 and H4[29].

Total surface areas were calculated using the BET equation **(Equation 2.6)**[31] that arises as a development of the Langmuir theory to accommodate multilayer formation via an additional parameter, c. If the initial adsorbed layer can act as a substrate for further (for example, physical) adsorption, then, instead of the isotherm levelling off to some saturated value at high pressures, it can be expected to rise indefinitely.

This accounts for differences between the strength of mono- and multilayer interactions, with a low value indicating a stronger interaction between adsorbate molecules than with the surface (adsorbent), and an opposite behaviour for high values.[29] Surface areas are determined from the monolayer volume, assuming N_2 molecules close pack and each occupies 0.162 nm^2 **(Equation 2.7).**[24, 26, 29]

$$\frac{\mathbf{P}}{\mathbf{V_a(P_0-P)}} = \frac{\mathbf{1}}{\mathbf{V_m C}} + \frac{\mathbf{C-1}}{\mathbf{V_m C}}\left(\frac{\mathbf{P}}{\mathbf{P_0}}\right) \qquad \textbf{Equation 2.6 – BET (linear)}$$

$$\mathbf{V_m} = \frac{\mathbf{1}}{\mathbf{(Gradient+Intercept)}}$$

$$\mathbf{c} = \left(\frac{\mathbf{Gradient}}{\mathbf{Intercept}}\right) + \mathbf{1}$$

$$\mathbf{Sa} = \frac{\mathbf{V_m \sigma N_a}}{\mathbf{mv}} \qquad \textbf{Equation 2.7}$$

Whereas P = pressure, P_0 = saturation pressure, V_a = volume adsorbed, V_m = monolayer volume, C = multilayer adsorption parameter, S_a = surface area; σ = N_2 area (0.162 nm^2); N_a = Avogadro number; m = sample mass; v = gas molar volume.

Micro- and mesoporosity were assessed using the DFT method,[32, 33] and the fitting model for N_2 at 77 K on carbon for slit pores. The QSDFT equilibrium gave the best agreement with experimental data. These classical models are limited in the scope of their applicability: the Kelvin equation is valid for mesopores[26] and the HK method[34] is valid for micropores; furthermore, it has been demonstrated that these pore-filling models do not provide a realistic description of adsorption in micropores[35, 36]. The DFT pore-filling model, instead, describes adsorption over the entire range of pore sizes and treats experimental isotherms as the summation of sorbate uptake, at a given pressure, in pores of variable size H. **Equation 2.8** is the resulting integral equation of the isothermal adsorption for distributed pore size.

$$Q(p) = \int dH q(p,H) f(H) \qquad \textbf{Equation 2.8}$$

Whereas Q(p) is the total amount of adsorbate per gram of adsorbent at pressure p in pores H, distributed over the entire micro – meso – macro range; q(p,H) is the Kernel function and describes the adsorption isotherm for an ideally homoporous material characterised by pore width H as quantity of adsorbate per m^2 of pore surface and f(H) is the pore surface area distribution function as a function of H. An accurate description of the DFT function has been described by Dombrowski and co-authors[32] and by Occelli and co-authors[33] and it is not the main aim of this thesis work; nevertheless it is worth mentioning that **Equation 2.8** can be simplified as a summation of the numerical values of f(H) and re-written as **Equation 2.9**:

$$\sum_i q(p,H_i) f(H_i) \qquad \textbf{Equation 2.9}$$

Whereas Q(p) is an experimental adsorption isotherm interpolated onto a vector p of pressure points, $q(p,H_i)$ is a matrix of values for quantity adsorbed per square meter, each row calculated for a value of H, at pressures p, and $f(H_i)$ is the solution vector that represents the area of surface in the sample characterised by each pore width H_i. Using the set of hybrid models constructed described by Occelli and co-authors[33], as the function $q(p,H_i)$ and the

experimental adsorption isotherm for the function Q(p), **Equation 2.9** can be solved for the distribution vector $f(H_i)$ and gives distributions of pore area and pore volume as a function of pore width.

2.2.4 SEM and TEM Electron microscopy

2.2.4.1 Scanning electron microscopy

Scanning electron microscopy (SEM) images were recorded on a Carl Zeiss Evo-40 SEM, operating at a wavelength of 12.3 pm, 10 kV, at Cardiff University or on a Carl Zeiss EVO MA15 variable pressure W SEM with Oxford Instruments AZtecEnergy EDX system with 80mm X-Max SDD detector- secondary and backscattered imaging, EDX elemental mapping and line scans plus CZ STEM detector at University of Leeds. Samples were supported on aluminium stubs using adhesive carbon tape and gold sputter coated to reduce charging.

An electron beam is emitted from an electron gun fitted with a tungsten filament cathode. Tungsten is normally used because it has the highest melting point and lowest vapour pressure of all metals and can be heated for electron emissions; the electron beam is then focused through a series of electromagnetic lenses onto the sample. These electrons hit the sample and lose energy through interactions occurring in multiple ways, generating high energy backscattering electrons, secondary electrons through inelastic scattering and X-ray radiation. In secondary electron imaging (SEI) mode, SEM images are formed by detection of these secondary electrons that result from the displacement of a K orbital (1s) electron.[37]

The low energy, ~50 eV, of the secondary electrons means that their escape is impeded and therefore the technique is surface sensitive. Scanning coils within the microscope allow the electron beam to raster over a sample. Image contrast is generated from the morphology of the sample: surfaces at right angles to the beam are brightest and as surfaces tilt towards being parallel to the beam increasingly darker areas are observed. This allows the production of a 3-D image of the sample surface. **Figure 2.8** shows a schematic explanation about the working principles of a SEM microscope[42].

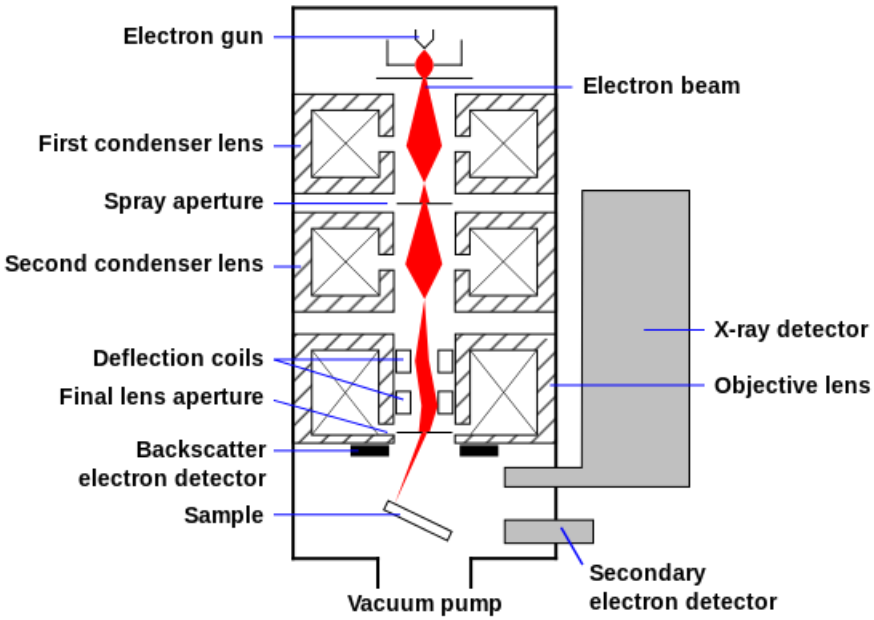

Figure 2.8: a scheme showing the operating principle of an SEM microscope, from reference 42.

The Everhart-Thornley detector[38] with its light-guide and highly efficient photomultiplier is the most frequently used detector in SEMs for secondary electrons and it consists of a scintillator inside a Faraday cage, inside the specimen chamber of the microscope. A low positive voltage is applied to the Faraday cage to attract the low-energy secondary electrons. The scintillator generates a high positive voltage (10,000 eV) to accelerate the incoming electrons to it, where they can be converted to light photons. Their direction is then focused to the light-guide by a metal coating on the scintillator acting as a mirror. In the light pipe the photons travel outside of the microscope's vacuum chamber to a photomultiplier tube for amplification.

BSE detectors[39] are usually either of scintillator or of semiconductor types. High atomic number elements backscatter electrons more strongly than low atomic number ones, therefore appear brighter in the image and BSE are used to detect contrast between areas with different chemical compositions. When all parts of the detector are used to collect electrons symmetrically about the beam, atomic number contrast is produced. By collecting back-scattered electrons from one side above the specimen using an asymmetrical, directional BSE detector, a strong contrast is produced and generates illumination of the interested region from that side. Semiconductor detectors can be made in radial segments that can be switched in or out to control the type of contrast produced and its directionality. Backscattered electron

detectors are positioned above the sample in a toroid type arrangement, concentric with the electron beam, maximising the solid angle of collection.

In the most of cases, a Field Emission Scanning Electron Microscope is used to image the surface structures or near-surface structures of a specimen, nevertheless a Scanning Transmission Electron Microscope detector (STEM) allows to detect also transmitted electrons. Specimens need to be ultra-thin to be penetrated easily by the electron beam. The 1-channel a-STEM[40] is optimised to the scattering behaviour of electrons in STEM mode and provides improved low kV response and higher sensitivity. Bright field (BF) and dark field (DF) signals can be clearly separated, allowing electrons scattered at higher angles to be detected by the annular dark field (ADF) or the high angle annular dark field (HAADF) segment.

2.2.4.2 Transmission electron microscopy

High resolution TEM/STEM (HAADF) images were recorded on a JEOL 2100F FEG STEM operating at 200 keV and equipped with a spherical aberration probe corrector (CEOS GmbH) and a Bruker XFlash 5030 EDX, with analysis carried out at the University of Birmingham.

Samples were prepared by dispersion in methanol and drop casted onto a copper grid coated with a holey carbon support film (Agar Scientific Ltd). Images were analysed using the software ImageJ 1.41, above 100 nanoparticles per sample were measured in different sites of interest to get an average particle size distribution.

For TEM analysis, the electron beam that is transmitted through the sample, with and without interaction generates 2-D representative images of the sample[37]. STEM can be considered as a combination of both SEM and TEM, allowing a converged electron beam to raster across the sample, generating HAADF images, commonly referred to as Z contrast.

Bright or dark field images are produced from high angle scattering of the beam by the atoms nucleus: the higher the atomic mass of the element, the stronger it diffracts and thus appears brighter[41]. High resolution of heavier elements or clusters on lower molecular weight substrates is possible; nevertheless, if the specimen thickness is excessive, high angle scattering from low atomic mass species increases because of multiple scattering processes[41]. **Figure 2.9** shows a schematic picture of TEM microscope[42].

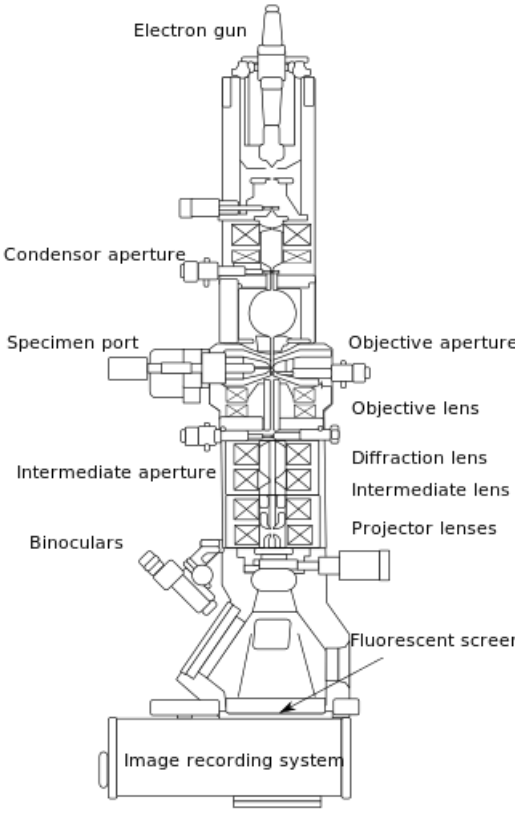

Figure 2.9: a scheme showing the operating principle of a TEM microscope, from reference 42.

2.2.4.3 Energy dispersive X-ray analysis

Samples were analysed using Oxford INCA energy EDX analysis software linked to the SEM with a 30 mm two light element capable atmospheric twin window (ATW) detector. EDX measures the X-ray radiation produced as the electron beam is fired at the sample. The electron beam excites ground state electrons in atoms of the sample, which are then ejected from the atom. As an electron from a higher energy shell moves to fill the hole left by the ejected electron, the difference in energy between the higher energy shell and lower energy shell is released as an X-ray. Measurement of these X-rays provides information about the atomic structure of the sample, as the energy of the X-rays are characteristic of the element from which they were emitted.[39]

The X-ray penetration depth is about 10 μm.[43] Therefore, EDX is a bulk technique when compared to the 1-3 nm penetration depth through XPS analysis. The atomic ratios calculated via EDX analysis in this study are considered bulk ratios, with those calculated from XPS surface ratios.

2.2.5 Thermal gravimetric analysis

Thermal gravimetric analysis (TGA) was performed on a Stanton Redcroft STA-780 thermal analyser fitted with a temperature programmer, DC amplifier and balance control **(Figure 2.10)**. Samples (10-12 mg) were placed into an alumina crucible on a two plate balance, together with a reference alumina crucible containing around 15 mg of pre-treated and inert γ-alumina. Samples were heated to 700 ºC at a calcination ramp of 10 ºC min^{-1} under O_2 gas flow, set up to be 20 mL min^{-1} and controlled *via* mass flow controller. The mass of the analysed sample was monitored with increasing temperature and differential thermal analysis (dTGA) was followed *via* computer, using PicoLog recording software.

TGA allows monitoring changes in mass of a sample when heated under gases. This analysis was used to follow and identify the loss of water in the hydrotalcite interlayers, the loss of hydroxyl groups and of carbonates, decomposed *via* gas production. Differences between the temperature of the sample and that of the inert reference material are measured during heating process.

Figure 2.10: a photo showing Stanton Redcroft STA-780 thermal analyser.

2.2.6 Diffuse reflection infrared Fourier transform spectroscopy (DRIFTS)

Ex and *in situ* DRIFTS analysis were performed on a Thermo Scientific Nicolet IS50 FT-IR with Smart Collector accessory, ever-glo mid/near infrared source and mercury cadmium telluride (MCT-A) photon detector at -196 °C, cooled by liquid N_2 **(Figure 2.11).** *Ex situ* analysis were carried out at room temperature, then a temperature programmable, gold-coated *in-situ* cell, interfaced to electronic mass flow controllers via a gas manifold permitted the following treatment. A calcination ramp (5 °C/min) under flowing O_2 (20 ml min^{-1}) was set up from room temperature up to 500 °C, spectra were acquired from 4000 to 400 cm^{-1} wavenumbers with a resolution of 4. Thus, changes in the HT morphology were followed as a function of calcination temperature.

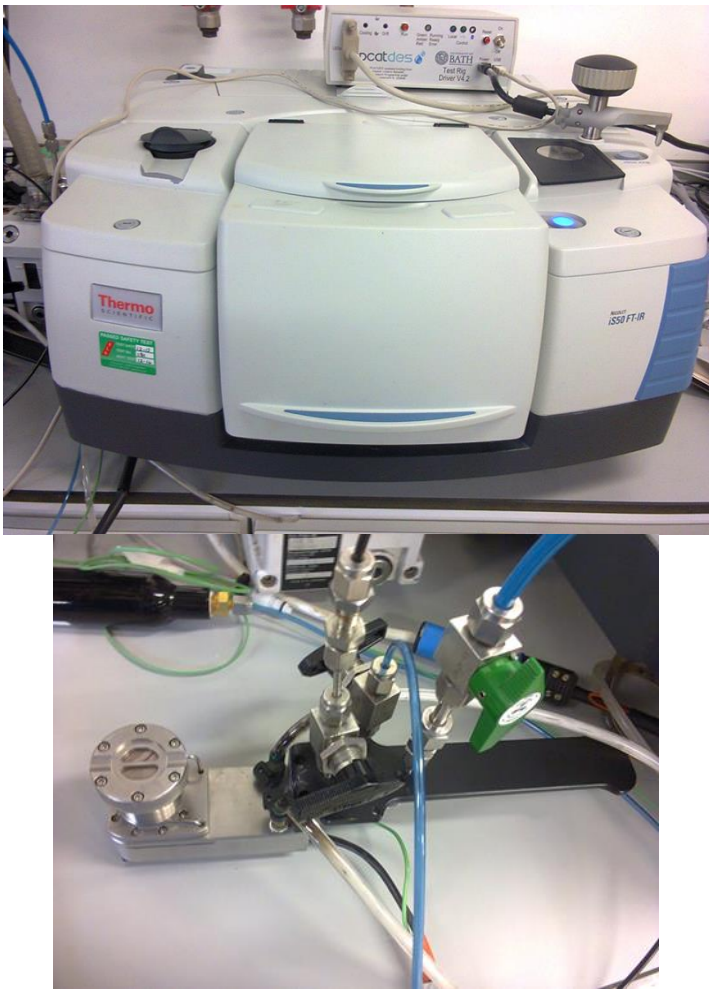

Figure 2.11: top – Thermo Scientific Nicolet IS50 FT-IR instrument, bottom – *in situ* cell.

Diffuse reflectance orientation focuses infrared radiation onto the sample **(Figure 2.12)**[44, 45]; photons are partially reflected by it and the remaining photons are transmitted through it, in different directions. Reflected signal originates both from the surface and bulk, the latter by reflection of photons that transmits through the surface. Random orientation in powder sample generates multiple scattering angles, so a parabolic mirror is required to focus the reflected beam maximising detection[19].

A molecule can vibrate in many ways and each way is called "vibrational mode". A vibrational mode in a molecule is "IR active" when it is associated with changes in the dipole. A permanent dipole is not necessary, as only a change in dipole moment is required[19, 25]. Molecular vibrations, either stretching or bending, are excited by the adsorption of photons of an appropriate energy, causing the dipole moment of the molecule to pulse.

Figure 2.12: top – scheme showing FTIR spectrophotometer, from reference 44 and bottom – different FTIR detection types, from reference 45.

2.2.7 CO_2 titration and TPD (Temperature programmed desorption)

CO_2 pulse chemisorption, followed by temperature programmed desorption (TPD) of the CO_2 saturated samples were carried out on a Quantachrome ChemBet3000 system, using a thermal conductivity detector. The catalyst sample being tested (~ 25 mg) was placed into a quartz U-shaped chemisorption cell, plugged with quartz wool and connected to the ChemBet. A furnace was set-up with a thermocouple inside the quartz cell, in parallel with the sample. **Figure 2.13** illustrates the ChemBet system set-up.

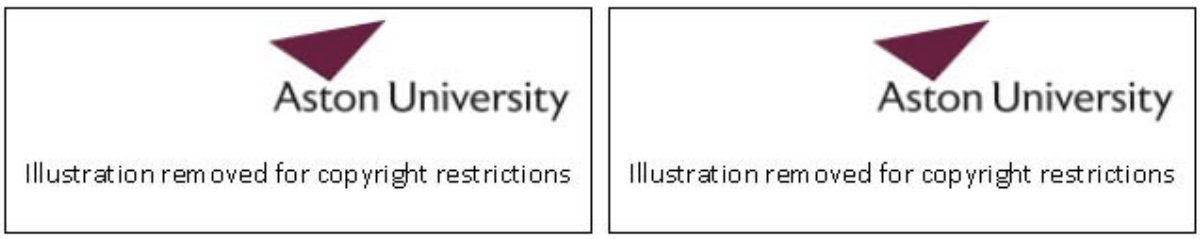

Figure 2.13: a) the ChemBet 3000 instrument and b) a schematic representation of the chemisorption cell set-up.

The sample was outgassed at 120 ºC for 2 h under He (20 mL min^{-1}), then it was cooled to 40 ºC; analyses were carried out at this temperature to avoid fluctuations in room temperature affecting the results. CO_2 gas was pulsed through the cell and over the sample in 50 μL doses; a part of this gas was adsorbed on the sample, a part was released and recorded on a computer when reaching the detector. The analysis was considered finished once 3 peaks of the same height and counts had been recorded by the detector, meaning that the sample was saturated, and all of the CO_2 was travelling through the system instead of being adsorbed on the sample. The sample was then heated up to 550 ºC at 10 ºC min^{-1} under a flow of He to desorb the CO_2.

Calibration was done injecting three pulses of CO_2 in an empty tube, knowing the volume of CO_2 injected; the peak area corresponded to a known amount of CO_2 and therefore by measuring the TCD/ID peak areas of unknown samples, the amount of CO_2 desorbing can

be determined. Therefore, as CO_2 is already present in bulk hydrotalcites, titrations are less accurate than TPD analysis and some sites are blocked; CO_2 contribute determined by TGA analysis was subtracted from TPD results to get a more accurate base site distribution.

CO_2 is an acidic probe molecule and it is assumed that each molecule of CO_2 adsorbs onto one base site on the hydrotalcite, forming a bicarbonate species with the hydroxide anions or surface hydroxyl groups[1, 2, 46, 47]. The number of CO_2 molecules desorbed from the surface during a TPD experiment gives therefore the number of base sites per mass of sample analysed. The CO_2 can adsorb as an acidic probe molecule to base sites of hydrotalcites in several ways, as monodentate, bidentate or bicarbonate anions, detected through IR studies[46]. **Figure 2.14** illustrates these different CO_2 species.

Figure 2.14: Adsorbed CO_2 species on a basic solid, and the associated IR signals, taken from Debecker and co-workers[48].

The monodentate carbonate anion adsorbs to low coordinate oxygen atoms and therefore accounts for strong basic sites[47, 49, 50], while the bidentate anion forms at intermediate strength acid-base pairs[50], such as Mg^{2+}-O^{2-}. Bicarbonate anions form at weakly basic surface hydroxyl groups in Mg rich hydrotalcites[51].

2.2.8 X-ray photoelectron spectroscopy

XPS quali- and quantitative analysis was performed on a Kratos Axis HSi X-ray photoelectron spectrometer fitted with a charge neutraliser and magnetic focusing lens

employing Mg K_α monochromated radiation (1253.6 eV) **(Figure 2.15)**. Spectral fitting was performed using CasaXPS version 2.3.15. Binding energies were corrected to adventitious C 1s at 284.6 eV, Au 4f peaks were fitted using a common peak shape determined from a Au standard and the Mg 2s contribution, which falls in the same region, was subtracted. Errors were estimated by varying a Shirley background across reasonable limits.

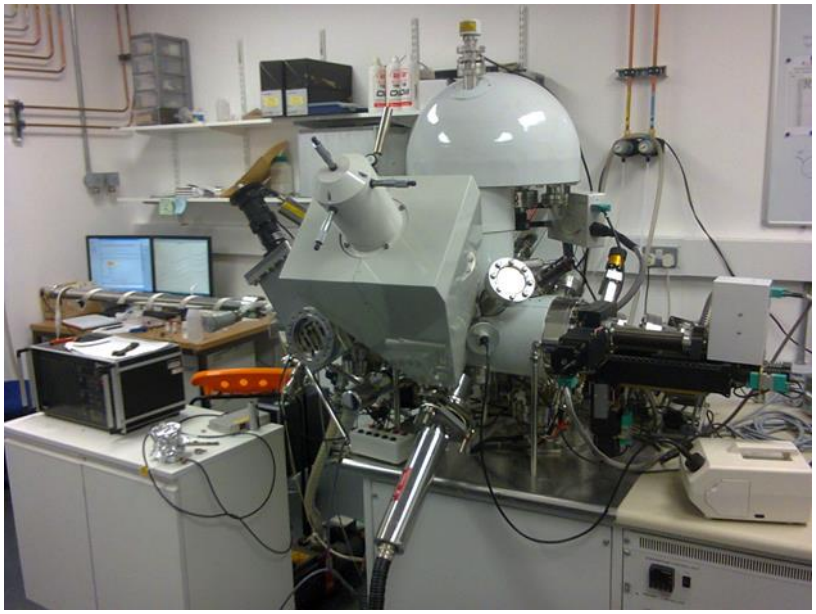

Figure 2.15: a photo of the Kratos Axis HSi X-ray photoelectron spectrometer.

In XPS instruments, X-rays are generated by bombarding a metallic anode with high-energy electrons. The energy of the emitted X-rays depends on the anode material and beam intensity depends on the electron current striking the anode and its energy.

XPS gives information on elemental composition, oxidation state, and local elemental environment of the sample. XPS is a surface-sensitive analysis, due to the short distance (1-3 nm) that a photoelectron can escape from (1-3 nm). The low escape depth is due to interactions between the ejected photoelectron and electrons of other atoms imparting short electron mean free path values over the electron energy range of 0-1000 eV.[52]

X-rays routinely employed are Mg Kα (1253.6 eV) and Al Kα (1486.6 eV) which due to their low energy, relative to XAS, are classed as soft X-rays.[53] The incident X-ray source excites a core electron, which is emitted as a photoelectron, when adequate energy is

supplied[17, 53]. A schematic representation of this photoelectron emission can be seen in **Figure 2.16**[19, 52].

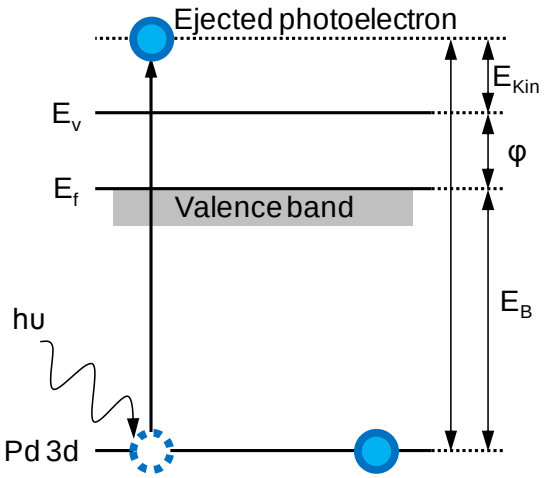

Figure 2.16: Schematic explanation of photo-ionisation, illustrating how a photo-electron is generated and ejected. (E_{Kin} = photo-electron kinetic energy; hν = photon energy (Planck's constant multiplied by frequency); E_b = electron binding energy; φ = work function; E_f = Fermi level; E_v = vacuum level)

The ejected photoelectron has a discrete kinetic energy, characteristic of the element and its chemical environment. Quantification of kinetic energy, and the intensity of photoelectrons at this energy, generates an XPS spectrum. Spectra are plotted as a function of the binding energy, which obeys the following mathematic relationship (**Equation 2.10**).

$$\mathbf{E_{kin} = h\nu - E_b - \varphi_{sp}} \quad \textbf{Equation 2.10}$$

Whereas E_{kin} = Photoelectron kinetic energy; hν = photon energy; E_b = electron binding energy; φ_{sp} = spectrometer work function.

Work function relates to the energy required to eject an electron at the Fermi level into the vacuum, i.e. the ionisation potential[19]. For conducting samples, an electrical connection between the sample and spectrometer aligns their Fermi levels. For insulating samples, e.g. silica, charge referencing is required[19]. This is achieved by systematically shifting binding energies by a common value, usually adventitious carbon at 284.6 eV, so that a known peak is aligned at its correct value. This justifies uniform shifts in binding energies

to higher values due to an increasing positive charge at the analyte surface; charge neutralisers can help to compensate this problem.

To detect electrons, a hemispherical analyser with a magnetic field is used. Electrons emitted from the sample travel across a column, in which focusing lens help keeping a straight pathway, then across a magnetic field in the hemispheric analyser and are detected by one of the five channeltrons analysers, according to their kinetic energy.

Oxidation state and the local elemental environment influence creates shifts in photoelectron binding energy of an element[19, 52]. As the oxidation state of an atom increases, the binding energy increases, due to the greater attractive force of the nucleus felt by fewer electrons. The binding energy of an electron is related to the electronegativity of adjacent atoms. Electrons ejected from orbitals having an angular momentum (l > 0, i.e. p, d and f orbitals) are affected by spin coupling between orbital angular momentum (l) and electron spin magnetic fields (m_s) and their sum is equal to total angular momentum (j). This interaction might give a valid contribute or not, because m_s can be anti-clockwise (+½) or clockwise (-½) and thus two values for j exist. This spin coupling results in peak doublets (spin-orbital splitting)[19], with predetermined ratios equal to $2j + 1$; for 2p orbitals $l = 1$ and thus $j = 3/2$ and $1/2$. The area ratio of the two spin orbit peaks will be 2:1, corresponding to 4 electrons in the $2p_{3/2}$ orbital and 2 electrons in the $2p_{1/2}$ orbital.

The number of components fitted to an XP spectrum must be justified with the number of environments that the element is found within the sample. In this thesis work, for example, magnesium was found as mixed MgAl oxides or MgAl hydrotalcite, so the Mg 2p peak was fitted with 2 different components with differing binding energies, peak areas and FWHMs.

2.2.9 XAS – XANES and EXAFS

XAS (X-ray adsorption spectroscopy) – X-ray adsorption near edge structure (XANES) and extended X-ray adsorption fine structure (EXAFS) measurements were made on beamline B18 of the Diamond Light Source in fluorescence mode, using a Si(111) double crystal monochromator and 9-element Ge solid state detector; Au L_{III} edge (11919 eV) spectra were acquired. *In situ* thermal decomposition of the catalyst precursor was followed in a bespoke "Sankar" pellet furnace under flowing oxygen (10 $ml.min^{-1}$ O_2) between 25-

500 °C. *Operando* measurements were made in a bespoke PTFE cell with Kapton windows on a catalyst reaction mixture (250 mg 2 wt. % Au/HT, 1 mmol HMF, 60 ml H_2O) recirculated from an external oxygenated round bottom flask (10 $ml.min^{-1}$ O_2) between room temperature and 90 °C; spectra were processed using Athena and Artemis software within the IFEFFIT software suite. **Figure 2.17** shows an example of *in situ* experimental setup[54], while **Figure 2.18** shows a schematic of the B18 beam line.

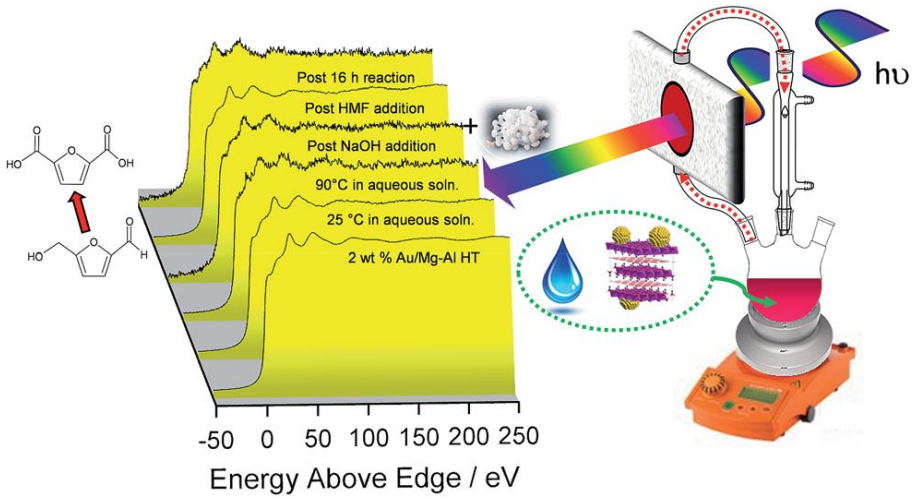

Figure 2.17: operando Au LIII-edge XAS of a 2 wt. % Au/HT catalyst during aqueous phase selective aerobic oxidation of HMF; catalytically active, metallic gold nanoparticles are unaffected by hot water or NaOH addition. Image published in reference 53.

Figure 2.18: The design of B18 beamline at "Diamond", based on three main optical elements: a collimating mirror, a water-cooled double crystal monochromator and a focusing mirror.

The first element is a water-cooled, vertically collimating Si mirror, which is placed at 20 m from the source. It is coated with Cr and Pt stripes and is able to cover the whole energy range from 2 to 35 keV. The fixed exit double crystal monochromator is water cooled and allows run fast scanning. It has two sets of crystals, Si(111) and Si(311), that can be translated horizontally under vacuum to allow a rapid configuration change.

A double toroidal mirror, coated with Cr and Pt, is placed at 25 m from the source to focus the two beam branches horizontally and vertically onto the sample. The position of this mirror is also fixed in the vertical and horizontal directions while a pair of smaller plane mirrors for harmonics rejection is placed in the Experimental Hutch. They are inserted in the beam path for low energy (<11 keV) operations.

The in-air section of the table can be used for experiments between 4 and 35 keV and it is equipped with ionization chambers for transmission mode measurement and intensity monitoring and a high rate fluorescence 9 element Ge solid state detector system with Portable Vortex detector.

Ex situ spectra of the powder catalyst samples mounted in a stainless steel washer were acquired, XANES and EXAFS spectra were normalised, background subtracted, and fitted, using the Athena and Artemis components of the IFEFFIT software suite respectively, recording Au foil, $Au(OH)_3$, Au_2O_3, $HAuCl_4$, PdO and Pd foil as standards.

XAS involves the generation of photoelectrons, but instead of evaluating these directly the technique assess their influence on the adsorption of subsequent X-ray photons[19]. The technique is an X-ray photon in X-ray photon out measurement, which eliminates the need for ultra-high vacuum systems, allowing characterisation of materials under atmospheric conditions and the option of *in situ*/*operando* investigations[55]. When the adsorption of an X-ray photon bears sufficient energy, greater than the binding energy of the electron, it ejects an electron as a photoelectron[56]. Electrons from a shell close to the nucleus are generally targeted, which results in increasingly energetically demanding transformations.

In the case of Au, the L_{III} edge (2p electrons) is commonly studied, with adsorption occurring at 11919 eV for Au. Ejection of a photoelectron results in excitation of the probed atom by the unfilled electron orbital, which affects subsequent X-ray photon adsorption. This excited state can be stabilised by fluorescence, by 'electron hole' shifting or by adsorption of scattered photoelectrons, including backscattering of the original. The scattering of photoelectrons by their neighbouring atoms induces a multitude of effects[19], both constructive and deconstructive in regards to photon absorption.

The resulting spectra show bulk information regarding both electronic and local geometry. Typically photon energies are varied from ~300 eV below to ~1000 eV above the adsorption edge, this being the minimum energy at which X-ray photon absorption occurs and generate photoelectrons[19].

The first 100 eV or so after the adsorption edge is named the XANES region and gives information about oxidation state, due to both photoelectrons and valence electron interactions; a result of the relatively low photoelectron kinetic energy which occur because of the close proximity between incident X-rays and electron binding energy.

The EXAFS region extends up to ~1000 eV or as far as oscillations are detectable; these photoelectrons possess higher kinetic energy, because of the increasing incident X-ray energy, which allow them to propagate further. These scattering of the photoelectrons by surrounding atoms result and allow local geometry to be understood. For the EXAFS, the

interesting signals are the oscillations well above the absorption edge, and define the EXAFS fine-structure function χ(E) as in the **Equation 2.11**:

$$\chi(E) = \frac{\mu(E) - \mu_0(E)}{\Delta\mu_0(E)} \qquad \textbf{Equation 2.11}$$

where μ(E) is the measured absorption coefficient, $\mu_0(E)$ is a smooth background function representing the absorption of an isolated atom, and $\Delta\mu_0$ is the measured jump in the absorption μ(E) at the threshold energy E_0. EXAFS is best understood in terms of the wave behaviour of the photo-electron created in the absorption process. It is therefore common to convert the x-ray energy to *k*, the wave number of the photo-electron, which has dimensions of 1/distance and is defined as in the **Equation 2.12:**

$$k = \sqrt{\frac{2m(E-E_0)}{\hbar^2}} \qquad \textbf{Equation 2.12}$$

where E_0 is the absorption edge energy, m is the electron mass and ħ is the reduced Planck constant or Dirac constant. The primary quantity for EXAFS is then χ(k), the oscillations as a function of photo-electron wave number, and χ (k) is often referred to as "the EXAFS", it is oscillatory and decays quickly with k. To emphasize the oscillations, χ(k) is often multiplied by a power of k, typically k^2 or k^3.

The different frequencies apparent in the oscillations in χ(k) correspond to different near neighbour coordination shells, which can be described and modelled according to the EXAFS equation **(Equation 2.13).**

$$\chi(k) = \sum_j \frac{N_j f_j(k) e^{-2k^2\sigma_j^2}}{k R_j^2} \sin[2kR_j + \delta_j(k)] \qquad \textbf{Equation 2.13}$$

where f(k) and δ(k) are scattering properties of the atoms neighbouring the excited atom, N is the number of neighbouring atoms, R is the average scattering distance to the neighbouring atom, and σ^2 is the Debye-Waller disorder factors, the mean square fluctuation in the neighbour distance. D-W factor accounts for thermal and structural disorder and generally

governs the ”melting” of the XAFS oscillations with respect to increasing temperature and their decay with respect to increasing photoelectron energy.

The EXAFS equation allows determination of N, R and σ^2 knowing the scattering amplitude f(k) and phase-shift δ(k). Furthermore, since these scattering factors depend on the Z of the neighbouring atom, EXAFS is also sensitive to the atomic species of the neighbouring atoms. An example of typical XAS spectrum for FeO, taken from Ravell and Newville[57, 58] is shown in **Figure 2.19,** while **Figure 2.20** shows the mathematic functions applied:

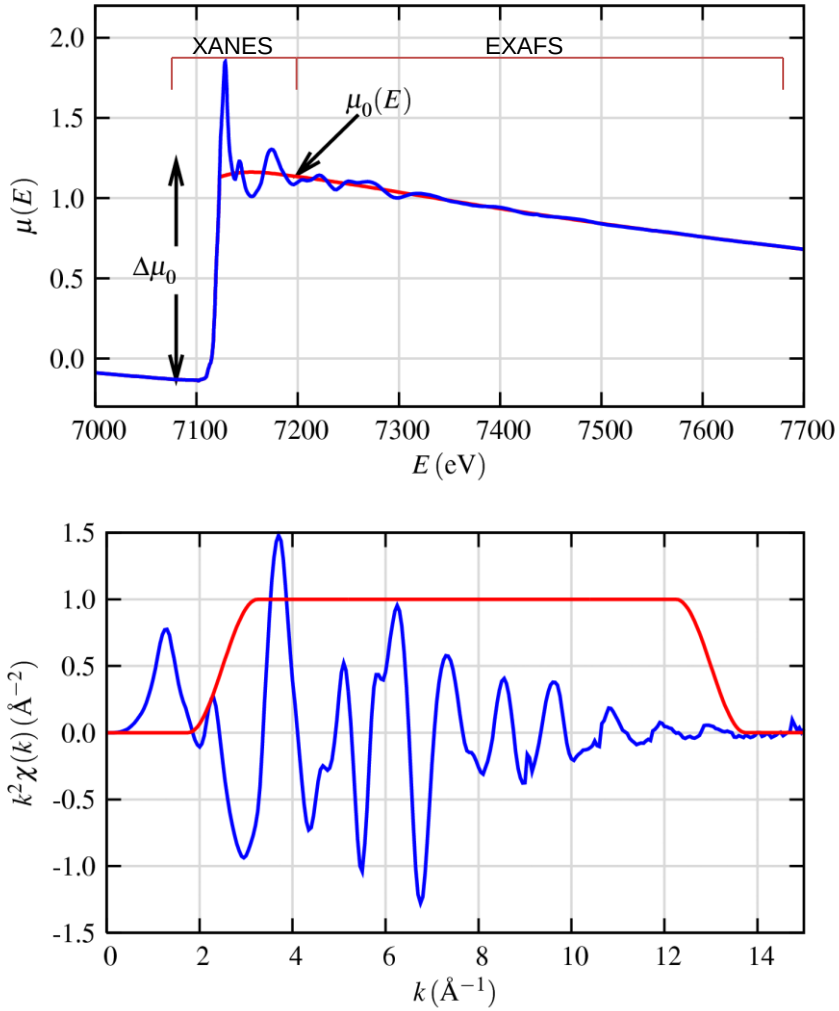

Figure 2.19: from reference 52 and 53, top – XAFS μ(E) for FeO; measured XAFS spectrum is shown with the XANES and EXAFS regions identified, μ(E) is shown with smooth background function, $\mu_0(E)$, and the edge-step, $\Delta\mu_0(E_0)$. Bottom – the EXAFS weighted by k^2 amplifies the oscillations at high k. The window Function shows that it will be multiplied by $k^2\chi(k)$ before doing a Fourier transform.

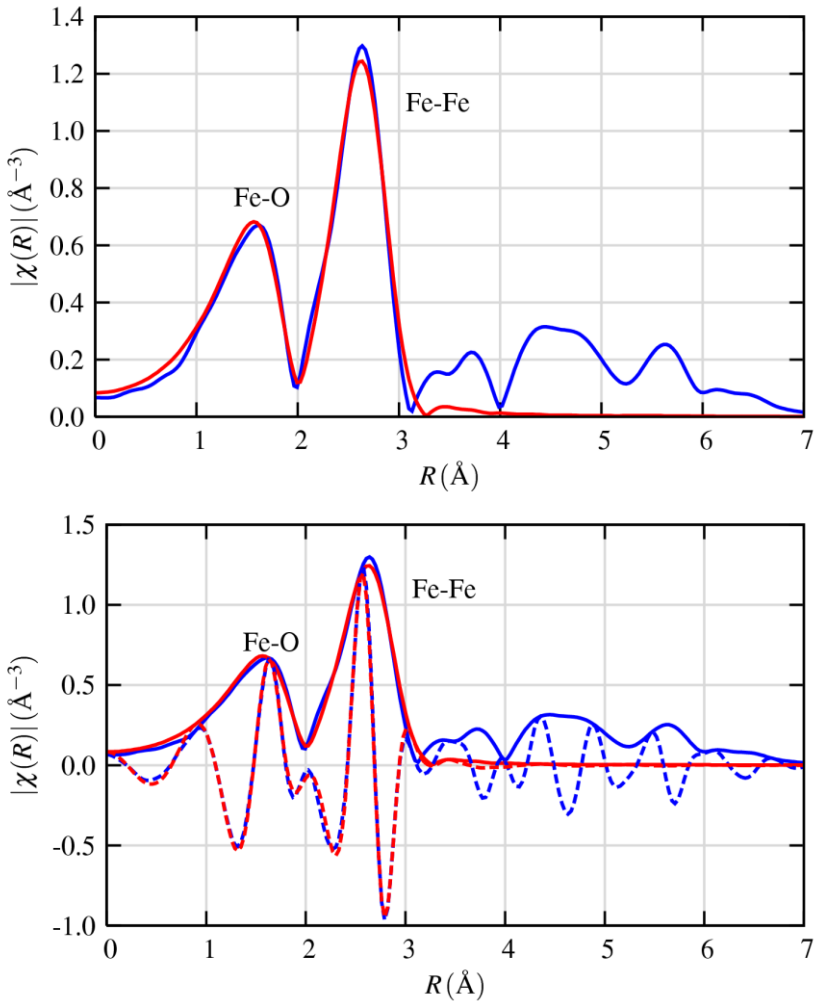

Figure 2.20: from reference 52 and 53, the Fourier Transformed XAFS, χ(R). Top – the magnitude |χ(R)|, but as the Fourier transformed XAFS is a complex function, with both real and imaginary parts, the bottom figure shows the Real part of χ (R) together with |χ(R)|.

2.2.10 Nuclear Magnetic Resonance

Nuclear Magnetic resonance experiments were performed on a Bruker AVANCE 300 spectrometer, equipped with a 5 mm broadband dual probe. Nuclear Magnetic Resonance is a physical phenomenon in which nuclei in a magnetic field absorb and re-emit electromagnetic radiation, in the range of radio frequencies. This frequency depends on the strength of the magnetic field and the magnetic properties of the isotope of the studied atoms, ^{1}H and ^{13}C being the most common nuclei.

Many atomic nuclei have a property called spin and they behave as if they were spinning; any atomic nucleus that has either odd mass, odd atomic number or both has a quantised spin angular momentum and a magnetic moment[59]. For each nucleus with spin, the number of allowed spin states is quantised and determined by its nuclear spin quantum number *I*. For each nucleus, this number *I* is a physical constant and there are $2I + 1$ allowed spin states ranging from $+ I$ to $- I$ and fit into the sequence shown in **Equation 2.11**

$$+ I, (I - 1), \ldots (- I + 1), - I \qquad \textbf{Equation 2.11}$$

Spin states are not of equivalent energy when they are in an applied magnetic field, because the nucleus is a charged particle[59], and any moving charge generates a magnetic field of its own. A nucleus has therefore a magnetic moment μ generated by its charge and spin; the spin might be clockwise (+ ½) or anticlockwise (– ½) both pointing in opposite directions. In the case of ^{1}H nuclei, they can be in one or the other orientations, with respect to the applied magnetic field, being the spin (+ ½) at lower energy, as it is aligned with the applied field, and (– ½) at higher energy, since it opposes to the applied field[59, 60].

NMR phenomenon occurs[59, 60] when nuclei aligned in an applied field absorb energy and change their spin orientation with respect to the applied field. This energy absorption is quantised and it must be equal to the energy difference between the two states involved, according to **Equation 2.12** and it is a function of the strength of the applied magnetic field B_0: the stronger the field is, the higher the energy difference between the two states is.

$$E_{abs} = (E_{-\frac{1}{2}\text{ state}} - E_{+\frac{1}{2}\text{ state}}) = h\nu \qquad \textbf{Equation 2.12}$$

Each nucleus has a different ratio of magnetic moment to angular moment because of each has a different mass and charge; this is called magnetogyric ratio γ and allows calculation of the energy dependence on the magnetic field, considering that the magnetogyric ratio is quantised in units of $h/2\pi$ **(Equation 2.13)**

$$\Delta E = \gamma \frac{h}{2\pi} B_0 = h\nu \qquad \textbf{Equation 2.13}$$

Solving **Equation 2.13** allows us to find the Larmor frequency of the absorbed energy **(Equation 2.14):**

$$\nu = \frac{\gamma}{2\pi} B_0 \qquad \textbf{Equation 2.14}$$

When the magnetic field increases, the Larmor frequency increases and so the higher the difference between the two spin levels is. The nuclear magnetic momentum, instead, is given by the **Equation 2.15**:

$$\mu = \gamma I \frac{h}{2\pi} \qquad \textbf{Equation 2.15}$$

where γ is the magnetogyric momentum, *I* is the nuclear spin quantic number, h is the Planck constant.

Not all the protons in a molecule show resonance at the same frequency, as they are surrounded by electrons, in different electronic (magnetic) environments, therefore there is a variation in the valence-shell electron density from a proton to another and protons are shielded by the surrounding electrons[59]. When a magnetic field is applied, the valence electrons of the protons are forced to circulate and this phenomenon is called local diamagnetic current; this current opposes the applied magnetic field and this effect is called diamagnetic shielding or diamagnetic anisotropy. Each proton in a magnetic field is therefore shielded from the applied magnetic field to an extent related to and directly proportional to the electron density surrounding it[59, 60].

Each proton is in a different chemical environment and has a different amount of electronic shielding, which results in a different resonance frequency; differences in frequency are very low, in the range of ppm, hence it is very difficult to measure precisely exact frequencies. An internal standard, tetramethylsilane $(CH_3)_4Si$, abbreviated as TMS, is used as reference, as its protons are most shielded than those of most other compounds, and its signal is the "zero". When another compound is measured, the resonance of its protons are reported as how far, in Hertz, they are shifted from those of TMS.[59, 60]

As this shift depends on the strength of the applied magnetic field, and as different instruments are available nowadays (300, 400, 500 and 600 MHz are the most common), a standardisation in measurements is required to have similar data for comparisons, by dividing the shift in Hz of a given proton by the frequency in MHz of the instrument and obtaining a field-independent measure, called chemical shift (δ) and expressed in ppm. **(Equation 2.16)**

$$\delta = \frac{\text{shift in Hz}}{\text{spectrometer frequency in MHz}}$$ **Equation 2.16**

Modern instruments work as pulsed Fourier – Transform NMR: a pulse of energy excites all magnetic nuclei in the molecule; when this pulse is discontinued, the excited nuclei lose energy and return to their original spin state, or relax. Since the molecules contain many different nuclei, their emissions generate a time-domain free induction decay (FID) signal. The Fourier transformation converts signals from time-domain to frequency-domain and separate each of the individual components, easily understandable. Chemical shifts, obtained as explained above because of different chemical environments, give information about different types of protons, carbons or other analysed nuclei; in this thesis work, main attention was put on protons. The integration of the area under each spectrum peak gives information about how many protons fall in that ppm range and allow quantification[59, 60].

It is not aim of this thesis to explain all the phenomena influencing chemical shifts, as tables and textbooks are available[59, 60], but it is worth focusing attention on the spin-spin splitting. In organic molecules, each type of protons rarely gives a single resonance peak; an example can be made when considering the spectrum for 1,1,2-trichloroethane **(Scheme 2.1).**

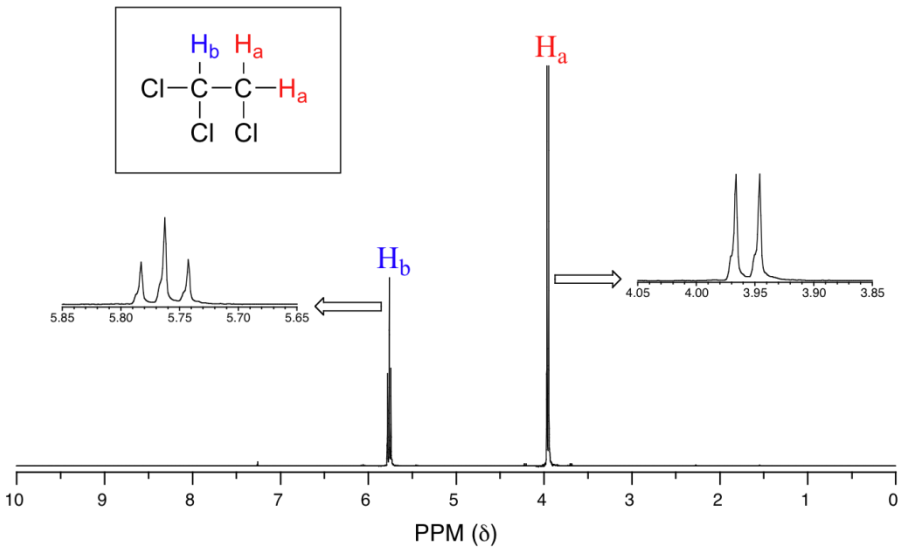

Scheme 2.1: ^{1}H NMR spectrum of 1,1,2-trichloroethane.

On the basis of the information explained before, a prediction would be two resonance peaks with a ratio of 2:1. Nevertheless, the signal at 3.96 ppm, corresponding to the two H_a protons, is split into two sub-peaks of equal height and area; this is referred to as a doublet.

The H_b signal at 5.76 ppm, instead, is split into three sub-peaks, being the middle peak higher than the two other outside, the integration of each sub-peak giving the middle peak twice that of each of the outside peaks; this is called a triplet[59].

The reason of this spin-spin splitting phenomenon can be explained by the so-called (n + 1) rule: each proton is influenced by the number of equivalent protons (n) on the carbon atoms next to the one to which is bonded, and its resonance peak is split into (n+1) components. Considering the H_a signal in **Scheme 2.1**, a simple explanation can be done: each of these protons is shielded by nearby valence electrons and is also influenced by the small magnetic field generate by its neighbour H_b. In some molecules, the magnetic moment of H_b is aligned with B_0 and in some others it is aligned in the opposite direction, therefore the chemical shift of protons H_a is influenced by the direction of the spin in proton H_b or, in other words, it is said H_a protons are coupled to H_b, resulting in a doublet for H_a and in a triplet for H_b. **Scheme 2.2** shows how protons can be shielded or de-shielded and helps understand the explanation[59].

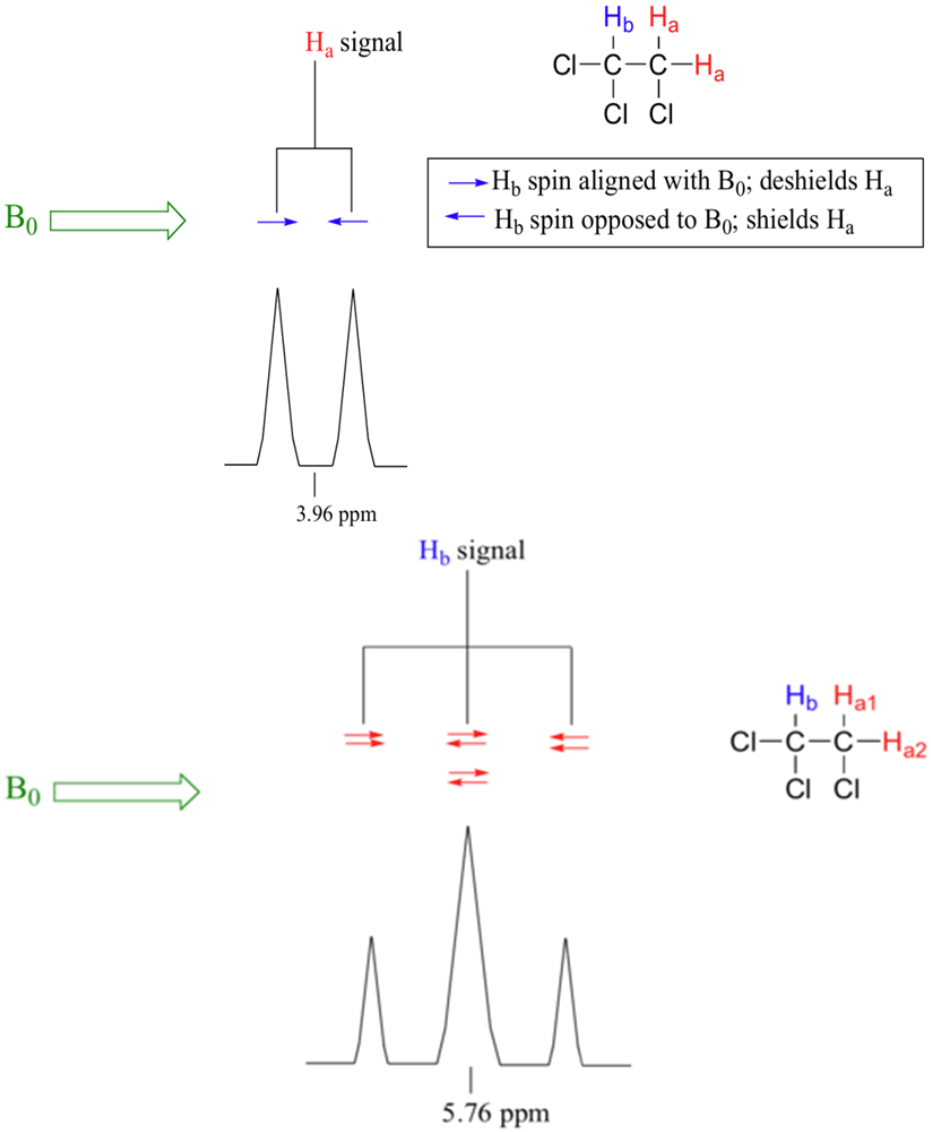

Scheme 2.2: an example of doublet and triplet for the 1,1,2-trichloroethane, showing shielding and de-shielding effects.

2.2.11 HPLC and HPLC analysis protocol

Quali- and quantitative analysis were carried out in duplicate, with values averaged, on an HPLC Agilent Technologies 1200 Series Infinity, equipped with UV-visible light and refractive index detectors **(Figure 2.21)**. The column was a Zorbax Hilic plus 4.6x100 mm, 3.5µm (p/n: 959961-901). To protect the column, a guard cartridge in a guard column Rx-SIL Guard 4.6x12.5 (p/n 820950-919) was used.

Figure 2.21: a photo showing an HPLC Agilent Technologies 1200 Series Infinity, equipped with UV-visible light and refractive index detectors

A gradient was necessary to get the best peak resolution, the mobile phase was prepared choosing HPLC grade acetonitrile (Fisher Scientific, ≥ 99.99 %) as the eluent A and the eluent B was prepared by dissolving in HPLC grade water a buffer of 50 mM CH_3COONH_4 (Sigma-Aldrich, ≥ 98.0 %) and the pH was adjusted to 5.2, adding the needed amount of glacial CH_3COOH (Sigma-Aldrich, ≥ 99.7 %) and the column was working at a temperature of 20 °C.

Table 1 shows the gradient variation as the time analysis increases: from 0 to 5 minutes, the percentage of A decreases and B increases until the desired set-point, then the new concentrations are kept constant for a minute, to ripristinate gradually the initial values; the analysis is complete in 10 minutes.

Table 1: gradient of eluents for HPLC analysis

Time	% A CH_3CN	% B aqueous pH = 5.2
0	95	5
5	60	40
6	60	40
6.5	95	5

HILIC (hydrophylic interaction chromatography) uses polar columns, made of non-bonded silica, optimised for hydrophilic interaction systems. It works in an organic/aqueous mobile phase, using a water layer on the silica sorbent, then acetonitrile is the weak solvent with increasing aqueous composition being used to elute more polar analytes.

Calibration curves were prepared using the method of external standards at the following concentrations: 1 mM, 2 mM, 5 mM and 7 mM in the aqueous mobile phase B. For the selective oxidation of HMF, four standards were used, respectively HMF (Sigma-Aldrich ≥ 99.0 %) (retention time = 1.2 min, UV wavelength = 282 nm), HMFCA (Sigma-Aldrich, (r.t. = 3.0 min, UV wavelength = 260 nm), FFCA (Tokyo Chemical Industry, ≥ 98.0 %) (r.t. = 4.2 min, UV wavelength = 282 nm) and FDCA (Alfa Aesar, ≥ 98.0 %) (r.t. = 5.2 min, UV wavelength = 260 nm). The flow rate was 1.2 ml/min, the injected volume 1μL and the temperature 20 °C.

2.3 Selox reactions

2.3.1 HMF, HMFCA and FFCA selective oxidations

2.3.1.1 HMF, HMFCA and FFCA reaction profiles and kinetic study tuning the [NaOH]

All the reactions were performed using a Radleys reactor **(Figure 2.22)**, into 3-neck round bottom flasks equipped with condensers, using 25 mg of catalyst, either 0.1 mmol of HMF (Sigma-Aldrich ≥ 99.0 %) (12.61 mg) or of HMFCA (Sigma Aldrich, ≥ 99.0 %) (14.23 mg) or of FFCA (Tokyo Chemical Industry, ≥ 98.0 %) (14.16 mg), T = 90 °C, V = 6 ml H_2O and ν O_2 = 15 ml/min, under stirring at 500 rpm, sufficient to eliminate external reagent diffusion limitations. In order to slow down the reaction, kinetic studies for HMF and FFCA were performed using 0.2 instead of 0.1 mmol. The catalyst used for this study was the 2 wt.

% Au/HT and it was tested either alone or after the addition of a pre-determined amount of NaOH (Fisher Scientific, 98.3 %) to the reaction mixture for Na:Mg molar ratios of 0.1, 1, 5, 10, 20 and 50, respectively 2.85×10^{-2}, 2.85×10^{-1}, 1.43, 2.85, 5.7 and 14.3 mmol. Reactions were sampled (0.3 mL) at adequate intervals and diluted (1 mL) with aqueous mobile phase B at pH = 5.2 described in **Chapter 2.2.11**, for the acquisition of activity and selectivity profiles.

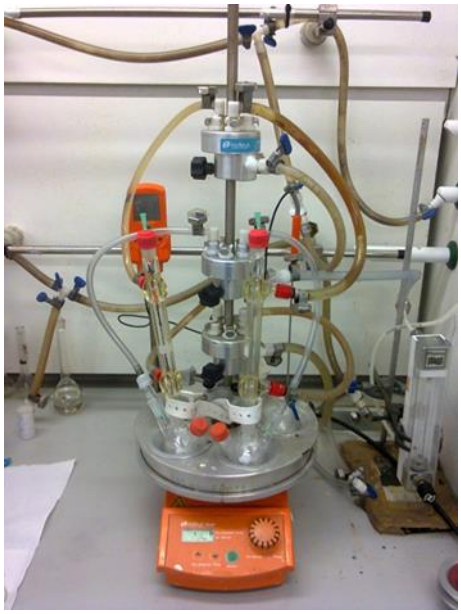

Figure 2.22: Radleys reactor, fitted with 3-neck round bottom flasks equipped with condensers and oxygen line for selox reactions.

2.3.1.2 HMF, HMFCA, FFCA selox, standard protocol for Au reaction profiles

All the reactions were performed using a Radleys reactor, into 3-neck round bottom flasks equipped with condensers, using 25 mg of catalyst, either 0.1 mmol of HMF (12.61 mg) or of HMFCA (14.23 mg) or of FFCA (14.16 mg), T = 90 °C, V = 6 ml H_2O and ν O_2 = 15 ml/min, under stirring at 500 rpm, sufficient to eliminate external reagent diffusion limitations. Catalysts used for this study were varied in the range of 0.5-10 wt. % Au/HT, tested either alone or after the addition of [NaOH] 1M to have pH = 14. Reactions were sampled (0.3 mL) at adequate intervals and diluted (1 mL) with aqueous mobile phase B at pH = 5.2 described in **Chapter 2.2.11**, for the acquisition of activity and selectivity profiles.

2.3.1.3 HMF, HMFCA, FFCA selox, standard protocol for Au kinetic studies

All the reactions were performed using a Radleys reactor, following the standard protocol described in **Chapter 2.3.1.2** with a minor modification: in order to allow monitoring the reaction and take more data points in the first minutes, kinetic studies for HMF and FFCA were performed using 0.2 instead of 0.1 mmol. Catalysts used for this study were varied in the range of 0.5-10 wt. % Au/HT, tested either alone or after the addition of [NaOH] 1M to have pH = 14. Reactions were sampled (0.3 mL) at adequate intervals and diluted (1 mL) with aqueous mobile phase B at pH = 5.2 described in **Chapter 2.2.11**, for the acquisition of activity and selectivity profiles.

2.3.1.4 Mass transfer limitations

The role of stirring rate was studied for the 2 wt. % Au/HT; standard reaction protocol described in **Chapter 2.3.1.2** was followed, with stirring rates varied (100-700 rpm). As no significant dependence of the reaction profile upon stirrer speed was revealed, no evidence for external diffusion limitations was found in these experiments and 500 rpm was chosen as the optimal speed. This conclusion was supported by tests using three different charges of the 2 wt. % Au/HT catalyst for 5-HMF selox of 10, 50 and 100 mg. A linear increase in the conversion and a slope of 1 on the associated bi-logarithm plot of Ln[cat] vs. Ln r, confirmed that reaction was not under external diffusion control, as it will be shown in details in **Chapter 3.2.4.1**.

2.3.1.5 HMF and HMFCA selox, standard protocol for AuPd reaction profiles or kinetic studies

All the reactions were performed using a Radleys reactor, following either the protocol described for standard reactions in **Chapter 2.3.1.2** or the one for kinetic reactions in **Chapter 2.3.1.3**. Catalysts used for this study were prepared varying the AuPd ratio, respectively $Au_{90}Pd_{10}$, $Au_{80}Pd_{20}$, $Au_{70}Pd_{30}$ and $Au_{60}Pd_{40}$, having a total amount of 1 wt. % metal; 2g mg of catalyst were tested either alone or after the addition of [NaOH] 1M to have pH = 14. Reactions were sampled (0.3 mL) at adequate intervals and diluted (1 mL) with aqueous mobile phase B at pH = 5.2 described in **Chapter 2.2.11**, for the acquisition of activity and selectivity profiles.

2.3.2 Heterogeneity of the active site – the Sheldon test

The Sheldon test[61] consists in a hot filtration of the heterogeneous catalyst to determine if, after its removal, any homogeneous contribution affects the reaction and confirm the heterogeneity of the active species. The standard reaction protocol described in **Chapter 2.3.1.2** was followed for the 2 wt. % Au catalyst, samples were taken and analysed with HPLC as described in **Chapter 2.2.11**. After 1 h, the hot mixture was filtered off and the catalyst was removed. The reaction was left on-going for other two h, but no reaction occurred in the absence of catalyst, suggesting that Au nanoparticles do not leach from the support to the homogeneous phase. When the catalyst was added back to the reaction, the conversion restarted.

2.3.3 Role of oxygen on HMF selox

HMF selox was scaled-up by a factor of 10, reaction conditions were therefore chosen as follow: 1 mmol of HMF, 60 ml of H_2O, 250 mg of catalyst, T = 90 °C and 500 rpm. A "Parr 5500 series, 316 stainless steel autoclave" (100 mL volume), fitted with a magnetically driven impellor (≤ 1500 rpm agitation) and dip-tube sampling system for kinetic analysis was used to find the order of reaction in O_2 **(Figure 2.23** and **Figure 2.24)**; the reaction was tested at 1, 5 and 10 atm of oxygen.

Figure 2.23: a photo of the Parr 5500 series, 316 stainless steel autoclave used for high pressure reactions.

Figure 2.24: top – scheme showing the head fittings for the autoclave; bottom – scheme showing the autoclave parts and the internal part, in which also the stirrer is visible.

2.3.4 Order of reaction in HMF for HMF selox and Arrhenius parameters

The standard reaction protocol described in **Chapter 2.3.1.2** was followed for the 2 wt. % Au catalyst, with some minor modifications: in order to find the order of reaction for HMF: different quantities of HMF, respectively 0.1, 0.2 and 0.5 mmol, were tested.

The same standard reaction protocol was tested for HMF and HMFCA selox at four different temperatures, respectively 25, 40, 60 and 90 °C. Kinetic constants were determined and a plot of the logarithm of kinetic constants for HMF or for HMFCA vs. 1/T allowed estimation of the Arrhenius activation energy E_a.

2.3.5 Recycle testing

Catalyst reusability was assessed for 3 consecutive reactions. The catalyst was reactivated by calcination at 200 °C for 4 h in oxygen (10 mL/min, ramp rate 10 °C min^{-1}) and reaction conditions were scaled up as follow, to get enough catalyst for each step: 1^{st} test) 0.6 mmol of HMF, 36 ml of H_2O, 151 mg of 2 wt. % Au/HT. 2^{nd} test) 0.3 mmol of HMF, 18 ml of H_2O, 78 mg of 2 wt. % Au/HT. 3^{rd} test) 0.1 mmol of HMF, 6 ml of H_2O, 25 mg of 2 wt. % Au/HT; all reactions were carried out at T = 90 °C, 15 ml/min O_2 and 500 rpm.

2.3.6 Selox of 2-furfuryl alcohol and 2-furaldehyd to 2-furoic acid, standard protocols

All the reactions were performed using a Radleys reactor, following the standard protocol described in **Chapter 2.3.1.2** for reaction profiles (0.1 mmol either of 2-furfuryl alcohol, 98.6 mg, or of 2-furaldehyde, 96.4 mg) or for kinetic studies (as above, but 0.2 mmol). This model reaction was studied to help distinguish the effects of gold and of NaOH on the alcohol and on the aldehyde function. The catalyst used for this model reaction was 2 wt. % Au/HT, tested either alone or after the addition of [NaOH] 1M to have pH = 14. Reactions were sampled and analysed as described in **Chapter 2.2.11**, with a minor modification: the solvent used to separate the compounds was pure HPLC grade acetonitrile.

2.4 References

1. D. G. Cantrell, L. J. Gillie, A. F. Lee and K. Wilson, *Applied Catalysis A: General*, 2005, **287**, 183-190.
2. J. J. Woodford, J.-P. Dacquin, K. Wilson and A. F. Lee, *Energy & Environmental Science*, 2012, **5**, 6145-6150.
3. N. K. Gupta, S. Nishimura, A. Takagaki and K. Ebitani, *Green Chemistry*, 2011, **13**, 824-827.
4. Y. Sun and Y. Xia, *Analytical Chemistry*, 2002, **74**, 5297-5305.
5. S. K. Ghosh and T. Pal, *Chemical Reviews*, 2007, **107**, 4797-4862.
6. F. Cavani, F. Trifirò² and A. Vaccari, *Catalysis Today*, 1991, **11**, 173-301.
7. J. S. Valente, F. Figueras, M. Gravelle, P. Kumbhar, J. Lopez and J. P. Besse, *Journal of Catalysis*, 2000, **189**, 370-381.
8. T. Hibino and A. Tsunashima, *Chemistry of Materials*, 1998, **10**, 4055-4061.
9. Y. Xi and R. J. Davis, *Journal of Catalysis*, 2009, **268**, 307-317.
10. S. Sarina, H. Zhu, E. Jaatinen, Q. Xiao, H. Liu, J. Jia, C. Chen and J. Zhao, *Journal of the American Chemical Society*, 2013, **135**, 5793-5801.
11. M. Comotti, C. D. Pina and M. Rossi, *Journal of Molecular Catalysis A: Chemical*, 2006, **251**, 89-92.
12. L. Prati and G. Martra, *Gold Bull*, 1999, **32**, 96-101.
13. C. Della Pina, E. Falletta, L. Prati and M. Rossi, *Chemical Society Reviews*, 2008, **37**, 2077-2095.
14. C. L. Bianchi, S. Biella, A. Gervasini, L. Prati and M. Rossi, *Catal Lett*, **85**, 91-96.
15. R. H. Rezaaiyaan, G. M.; Anderson, H.; Kaiser, H.; Meddings, B., *Applied spectroscopy*, 1982, **36**, 627-631.
16. *http://teamd.lbl.gov/chem-analysis.html*.
17. G. A. Somorjai and Y. Li, *Introduction to surface chemistry and catalysis*, John Wiley & Sons Inc, Hoboken, 2010.
18. C. Hammond, *Basics of Crystallography and Diffraction*, Oxford University Press, New York, 2001.
19. J. W. Niemantsverdriet, *Spectroscopy in catalysis*, John Wiley & Sons, 2007.
20. Katholieke Universiteit Leuven Nuclear solid state group, 2010, **X-ray diffraction – Bruker D8 Discover**, [online] Available at: <http://fys.kuleuven.be/iks/nvsf/experimental-facilities/x-ray-diffraction-2013-bruker-d2018-discover> [Accessed March 2012].
21. N. Pernicone, *Cattech*, 2003, **7**, 196-204.
22. V. Rives, *Materials Chemistry and Physics*, 2002, **75**, 19-25.
23. P. Scherrer, *Gottinger Nachrichten*, 1918, **2**, 98.
24. R. P. H. Gasser, *An introduction to chemisorption and catalysis by metals*, Oxford University Press, New York, 1985.
25. P. D. P. Atkins, J., *Oxford: Oxford University press*, 2009, **5th edition** 459.
26. P. A. Webb and C. Orr, *Analytical Methods in Fine Particle Technology*, Micromeritics, Norcross, 1997.
27. P. Atkins, *Oxford: Oxford University press*, 2001, **3rd ed**.
28. K. S. W. Sing, L. Moscou, R. A. Pierotti, J. Roquerol and T. Siemieniewska., *Pure Appl. Chem.*, 1985, **57**, 603-619.
29. F. Rouquerol, J. Rouquerol and K. S. W. Sing, *Adsorption by powders & porous solids: principles, methodology and applications*, Academic Press, Bodmin, 1999.
30. J. W. McBain, *J. Am. Chem. Soc.*, 1935, **57**, 699-700.

31. S. Brunauer, P. H. Emmett and E. Teller, *J. Am. Chem. Soc.*, 1938, **60**, 309-319.
32. R. J. Dombrowski, D. R. Hyduke and C. M. Lastoskie, *Langmuir*, 2000, **16**, 5041-5050.
33. M. L. Occelli, J. P. Olivier, A. Auroux, M. Kalwei and H. Eckert, *Chemistry of Materials*, 2003, **15**, 4231-4238.
34. G. Horvath and K. Kawazoe, *Journal of Chemical Engineering of Japan*, 1983, **16**, 470-475.
35. C. M. Lastoskie, N. Quirke and K. E. Gubbins, in *Studies in Surface Science and Catalysis*, eds. W. A. S. W. Rudziński and G. Zgrablich, Elsevier, 1997, vol. Volume 104, pp. 745-775.
36. P. I. Ravikovitch, G. L. Haller and A. V. Neimark, *Advances in Colloid and Interface Science*, 1998, **76–77**, 203-226.
37. T. G. Rochow and P. A. Tucker, *Introduction to microscopy by means of light, electrons, X rays, or acoustics*, Springer, New York, 1994.
38. T. E. Everhart and R. F. M. Thornley, *Journal of Scientific Instruments*, 1960, **37**, 246.
39. J. Goldstein, *Scanning electron microscopy and X-ray microanalysis*, Springer, 2003.
40. http://www.zeiss.com/microscopy/en_de/products/scanning-electron-microscopes/upgrades/1-channel-astem.html#introduction.
41. R. A. J. G. Keyse, P.J. and Lorimer, G.W., *Guilford: Bios Scientific Publishers*, 1998.
42. Taken from Wikipedia 25-09-2015.
43. B. C. R., E. C. A. and W. S., *Encyclopedia of Materials Characterization: Surfaces, Interfaces, Thin Films*, Gulf professional publishing, 1992.
44. *http://faculty.sdmiramar.edu/fgarces/LabMatters/Instruments/FTIR/FTIR.htm*.
45. F. Zaera, *Chemical Society Reviews*, 2014, **43**, 7624-7663.
46. J. I. Di Cosimo, V. K. Díez, M. Xu, E. Iglesia and C. R. Apesteguía, *Journal of Catalysis*, 1998, **178**, 499-510.
47. S. Abelló, F. Medina, D. Tichit, J. Pérez-Ramírez, X. Rodríguez, J. E. Sueiras, P. Salagre and Y. Cesteros, *Applied Catalysis A: General*, 2005, **281**, 191-198.
48. D. P. Debecker, E. M. Gaigneaux and G. Busca, *Chemistry – A European Journal*, 2009, **15**, 3920-3935.
49. S. Abelló, F. Medina, D. Tichit, J. Pérez-Ramírez, J. C. Groen, J. E. Sueiras, P. Salagre and Y. Cesteros, *Chemistry – A European Journal*, 2005, **11**, 728-739.
50. V. K. Diez, C. R. Apesteguia and J. I. Di Cosimo, *Journal of Catalysis*, 2003, **215**, 220-233.
51. R. Philipp and K. Fujimoto, *Journal of Physical Chemistry*, 1992, **96**, 9035-9038.
52. I. Chorkendorff and J. W. Niemantsverdriet, *Concepts of modern catalysis and kinetics*, Wiley-VCH, Mörlenbach, 2003.
53. R. Richards, ed., *Surface and Nanomolecular Catalysis*, CRC Press, Boca Ranton, 2006.
54. L. Ardemani, G. Cibin, A. J. Dent, M. A. Isaacs, G. Kyriakou, A. F. Lee, C. M. A. Parlett, S. A. Parry and K. Wilson, *Chemical Science*, 2015, **6**, 4940-4945.
55. M. A. Newton and W. van Beek, *Chemical Society Reviews*, 2010, **39**, 4845-4863.
56. D. Macquarrie, *Applied Organometallic Chemistry*, 2005, **19**, 696-696.
57. B. R. a. M. Newville, *Journal of synchrotron radiation* 2005, **12**, 537-541.
58. http://xraypy.github.io/xraylarch/xafs/index.html.
59. G. M. P. Lampman, D.L.; Kriz, G.S. and Vyvyan, J.R., *International Edition*, 2010, **4th edition**.
60. J. G. Clayden, N.; Warren, S. and Wothers, P., *Oxford* 2001.
61. A. Corma, D. Das, H. García and A. Leyva, *Journal of Catalysis*, 2005, **229**, 322-331.

Chapter 3

On the role of base in the Au/hydrotalcite catalysed oxidation of 5-HMF

List of contents

3.1 Introduction

A range of oxygenated substrates, such as alcohols[1, 2], polyols[2], aldehydes and sugars[3, 4], have been oxidised using gold nanoparticles, either as naked stabilised sols[3, 5] or dispersed on solid supports[6-9]. This chapter explores the aerobic selective oxidation of 5-hydroxymethyl-2-furfural[10] (5-HMF) catalysed by Au nanoparticles on a MgAl hydrotalcite solid base support[11].

The common requirement for basicity[12, 13] in the aerobic selective oxidation of alcohols and aldehydes in aqueous solvent represents a serious and environmentally unfriendly limitation[14, 15] of this catalytic system, since the final product requires neutralisation and purification. The presence of a homogeneous base, usually NaOH, has been recognised as an essential component for supported Au catalysts since initial studies carried out by Prati and Rossi[2]; recent mechanistic studies by Davis and co-workers[12, 14, 16] have further highlighted the essential role of hydroxide ions during the selective oxidation of alcohols over gold. However, the exact role of base and gold has yet to be clarified, and hence the nature of the catalytically active species and reaction mechanism require elucidation.

Hydrotalcites, with the general formula $[M^{2+}_{(1-x)}M^{3+}_{x}(OH)_2]^{x+}(A_{x/n})^{n-} \cdot y\ H_2O$, belong to a class of anionic clays named layered double hydroxides (LDH)[17, 18]. Their structure is composed of positively charged brucite-like hydroxide layers, in which some octahedrally coordinated M^{2+} cations have undergone isomorphous substitution by M^{3+} ones. Counter anions A^{n-}, commonly carbonates, reside in the interlayer space to balance the residual positive charges[19]. An example of hydrotalcite structure is shown in **Figure 3.1**.

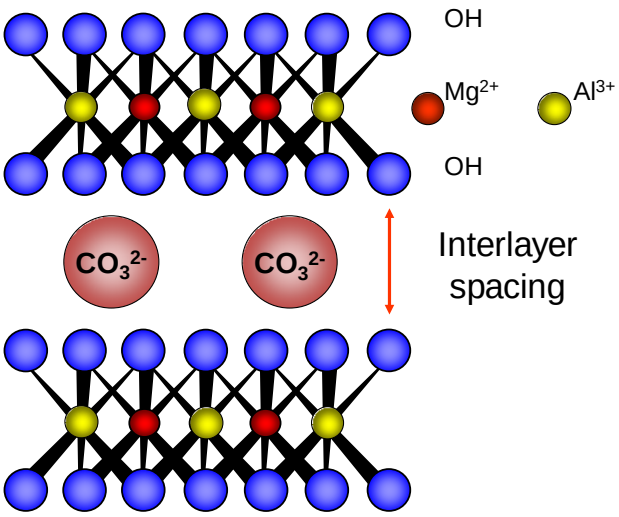

Figure 3.1: a schematic representation of the layered double hydroxide structure of a MgAl hydrotalcite[20].

Gupta and co-workers[11] previously employed hydrotalcites obtained *via* alkali precipitation routes as both a support and solid base for Au nanoparticles, resulting in significant 5-HMF oxidation and high 2,5-furandicarboxylic acid (FDCA) yields. In this work a hydrotalcite with a nominal Mg:Al molar ratio of 5 was reported as the most active, however the actual composition was not quantified and such a high Mg:Al ratio is not generally accepted as possible for pure phase HTs, as mentioned before[17].

In order to quantitatively assess the role of basicity in the aerobic selective oxidation of 5-HMF, this chapter explores the role of solution pH and a heterogeneous alkali-free MgAl HT support in regulating Au catalysis. Subsequently, the influence of gold loading was studied to further elucidate the role of gold in each step of the cascade oxidations, and the nature of the gold active species examined via XPS and *in-situ* XAS.

3.2 Results and discussion

3.2.1 Typical preparation of Mg_3Al HT

Hydrotalcites were synthesised following the procedures described before in **chapter 2.1.1.**

3.2.2 Typical preparation of Au/HT and Au/mixed oxides

Au/hydrotalcites and Au/CHT (mixed oxides) were synthesised following the procedures described **chapter 2.1.2** and **chapter 2.1.3**, respectively.

3.2.3 Characterisation of hydrotalcite and Au/hydrotalcites

Bulk elemental analysis was performed to determine the actual Au content and Mg:Al ratio, and the structural properties of materials examined by powder X-ray diffraction (XRD), N_2 porosimetry and electron microscopy. SEM was also used to study the support morphology, and TEM to measure the average Au particle size. IR, TGA, XPS, XAS and CO_2 TPD analysis were also performed to investigate the oxidation state and acid properties of the hydrotalcite support and Au nanoparticles. ^{1}H NMR was used to follow changes in 5-HMF upon NaOH addition to understand the reaction mechanism.

3.2.3.1 Elemental analysis

XPS, EDX and ICP analysis were conducted on the parent hydrotalcite and Au/HTs to quantify their bulk and surface compositions. Gold loadings are reported in **Table 3.1**.

Table 3.1: elemental analysis of Au/HTs.

Nominal Au loading / wt%	EDX / wt%	ICP / wt%	XPS / wt%
Parent HT	-	-	-
0.5	0.7 ± 0.04	0.5 ± 0.005	0.3 ± 0.02
1	1.3 ± 0.03	0.9 ± 0.007	0.9 ± 0.01
2	2.6 ± 0.05	1.9 ± 0.004	1.9 ± 0.03
5	4.9 ± 0.07	4.5 ± 0.008	6.8 ± 0.05
10	9.6 ± 0.06	9.6 ± 0.006	10.2 ± 0.08

Table 3.2 summarises surface elemental compositions of the same catalysts and hydrotalcite support.

Table 3.2: surface elemental analysis of Au/HTs by XPS.

0.5 wt.% AuHT	Element / wt.%	1 wt.% AuHT	Element / wt.%	2 wt.% AuHT	Element / wt.%
Mg	27.5	Mg	26.2	Mg	26.0
Al	8.2	Al	7.0	Al	9.3
O	59.4	O	60.5	O	57.9
C	3.4	C	4.2	C	3.7
Cl	1.2	Cl	1.1	Cl	1.3
Au	0.3	Au	1.0	Au	1.9

5 wt.% AuHT	Element / wt.%	10 wt.% AuHT	Element / wt.%	Parent HT	Element / wt.%
Mg	26.4	Mg	21.9	Mg	27.7
Al	7.6	Al	8.5	Al	8.3
O	54.3	O	54.3	O	60.5
C	3.8	C	3.7	C	3.5
Cl	1.1	Cl	1.4	Cl	-
Au	6.8	Au	10.2	Au	-

The average Mg:Al atomic ratio was 3.0 ± 0.2 by both EDX and XPS, consistent with the nominal ratio in the synthesis. However, this high Mg content was achieved via a substantial modification of the Na-free method described by Cantrell[20] and Woodford[21], wherein both authors observed that the actual bulk and surface ratios were lower than the nominal targets, as a result of increasing the pH from 7.6-8.0 to 9.3-9.5[17].

3.2.3.2 Ex situ XRD analysis

Ex situ powder XRD were run on the parent HT and Au/HTs. The parent HT exhibited reflections at 11.2° (*d* 003), 22.4° (*d* 006), 34.2° (*d* 009), 38.3° (*d* 015), 44.6° (*d* 018), 60.1° (*d* 110), 61.3° (*d* 113) and 64.7° (*d* 116) **(Figure 3.2)**, consistent with literature values for this material[17, 22, 23].

In contrast to Woodford and co-authors[21], no Mg and Al oxide or carbonate impurities were detected for these Mg_3Al hydrotalcites prepared at pH 9.3-9.5. Volume-averaged crystallite sizes were determined as 7.2 nm from the 11.2° peak applying the Scherrer equation[24]. These small crystallite sizes indicate that the extended porous network arises from agglomeration or fusion of these nanocrystalline platelets.

The intensity of Au peaks, that usually are visible at 38° (*d* 111), 44° (*d* 200), 65° (*d* 220) and 78° (*d* 311), increased with Au loading[25, 26]; nevertheless, these peaks overlap with HT ones and are not visible for low gold loading, necessitating background subtraction of the parent HT contribution. Peak fitting of the resultant gold reflection reveals an increase in Au particle size with loading.

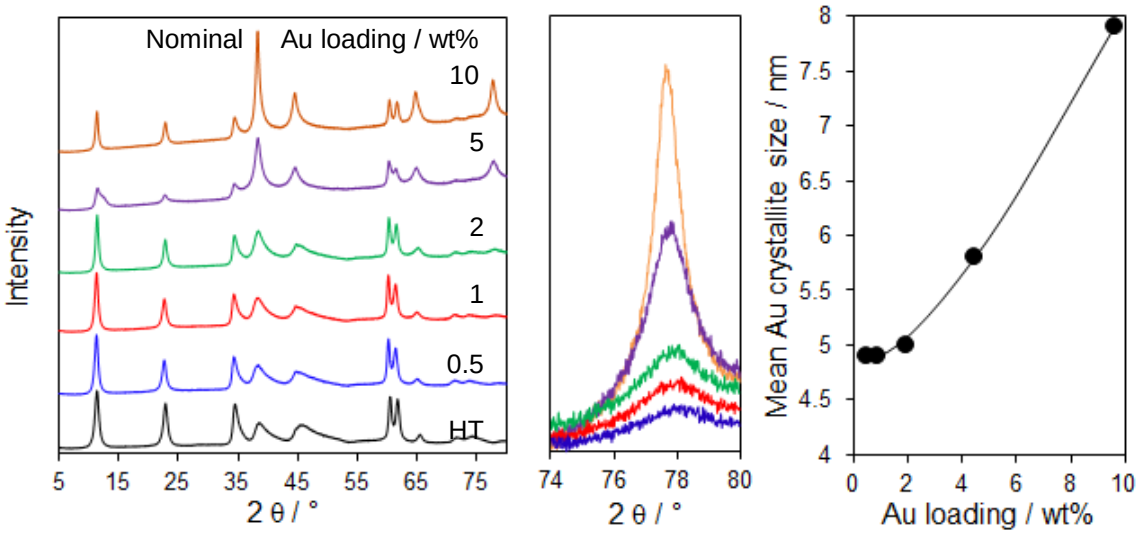

Figure 3.2: left – X-ray diffractograms of Au/HT catalysts, middle – evolution of Au reflection, and right – evolution of Au particle size with loading from line broadening of the 78° reflection by Scherrer analysis.

Powder XRD patterns were phase corrected using the software EVA, interlayer spacing *d* and lattice parameters *a* and *c* subsequently calculated for different Au loadings, showing good agreement with literature values[17, 20, 27]. Results are shown in **Table 3.3** below.

Table 3.3: Structural parameters of Au/HTs from powder XRD.

Catalyst	Interlayer spacing *d* / Å	Lattice parameter *a* / Å	Lattice parameter *c* / Å
Parent hydrotalcite	7.70 ± 0.01	3.053 ± 0.001	23.164 ± 0.001
0.5 wt.% Au	7.78 ± 0.01	3.071 ± 0.001	23.447 ± 0.001
0.9 wt.% Au	7.86 ± 0.01	3.071 ± 0.001	23.567 ± 0.001
1.9 wt.% Au	7.86 ± 0.01	3.074 ± 0.001	23.607 ± 0.001
4.5 wt.% Au	7.90 ± 0.01	3.074 ± 0.001	23.640 ± 0.001
9.6 wt.% Au	7.94 ± 0.01	3.076 ± 0.001	23.671 ± 0.001

A mineral having the ideal formula $Mg_6Al_2(OH)_{16}CO_3 \cdot 4\ H_2O$ can exist in two different polytypes, as the brucite-like sheets can stack one on the other in two different symmetries: the so-called hydrotalcite, having the 3R rombohedral[17] symmetry and the so-called manasseite, having the 2H hexagonal one, according to Cavani and co-authors[17]. For clarity, if the three-fold axis of the OH group between the HT interlayers can be named ABC, the stack may follow the sequence BC-CA-AB-BC including three sheets per unit cell (rombohedral 3R symmetry) or the sequence BC-CB-BC (hexagonal 2H symmetry). For a hydrotalcite model with rombohedral 3R[17] stacking of the brucite layers, the interlayer spacing *d* can be calculated from measuring the peak position of the d_{003} reflections from the XRD pattern and then with the **Equation 3.1.**

$$d = d_{003} = \frac{n\,\lambda}{2\,\sin\theta} \qquad \textbf{Equation 3.1}$$

The lattice parameter *a*, related to the unit cell, was calculated using the d(110) XRD peak position[17] with the **Equation 3.2.**

$$a = 2\,d_{110} \qquad \textbf{Equation 3.2}$$

The lattice parameter *c*, that corresponds to three times the interlayer spacing *d* between two consecutive layers[28], was calculated using the d(003), d(006) and d(009) XRD peak position, with the **Equation 3.3**

$$c = d_{003} + 2\,d_{006} + 3\,d_{009} \qquad \textbf{Equation 3.3}$$

Vegard's law states that at a constant temperature, a linear relationship exists between a crystal lattice parameter of an alloy and the concentration of the constituent elements[29-31]. Cavani and co-authors[17] plotted HT lattice parameters as a function of Al/(Al+Mg) ratio, taking them from different authors in the literature and shown in **Figure 3.3**, showing that linear relationships for pure HT phases are valid in the range of $0.2 \leq x \leq 0.33$, whereas x = Al/(Al+Mg). In terms of Mg/Al ratio, these values can be written as $2 \leq Mg/Al \leq 4$.

The experimental value (marked in red in **Figure 3.3**) was obtained in this thesis work for parent HT Mg/Al = 3.0 and it corresponds to 0.25; lattice parameter *a* was found to be 3.053 Å, showing a good agreement with literature values[17].

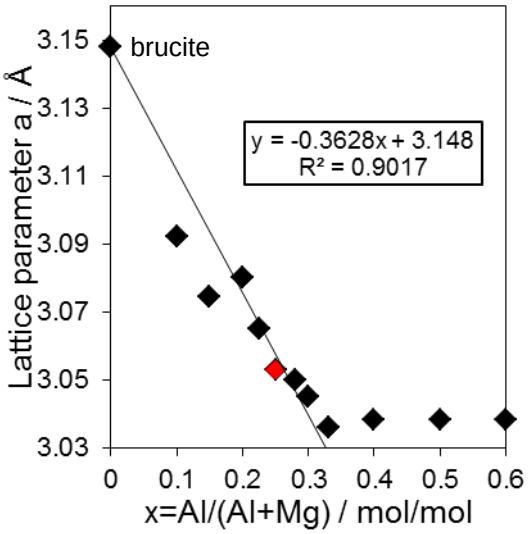

Figure 3.3: lattice parameter *a* as a function of the Al content, x, for HT materials, from reference 17. The experimental point for this thesis work is marked in red: experimental lattice parameter gave 0.25 using the Vegard's law and confirmed a pure phase Mg/Al = 3 for the obtained HT.

The parameter *a* decreases when the aluminium content x increases[17], within the range of pure HTs, because the Al^{3+} radius is smaller than Mg^{2+}, thus satisfying Vegard's law, while it remains constant outside the range.

3.2.3.3 N_2 Porosimetry

N_2 adsorption-desorption isotherms[32, 33] for the parent hydrotalcite and Au/HTs are shown in **Figure 3.4**. The isotherms have been offset for clarity.

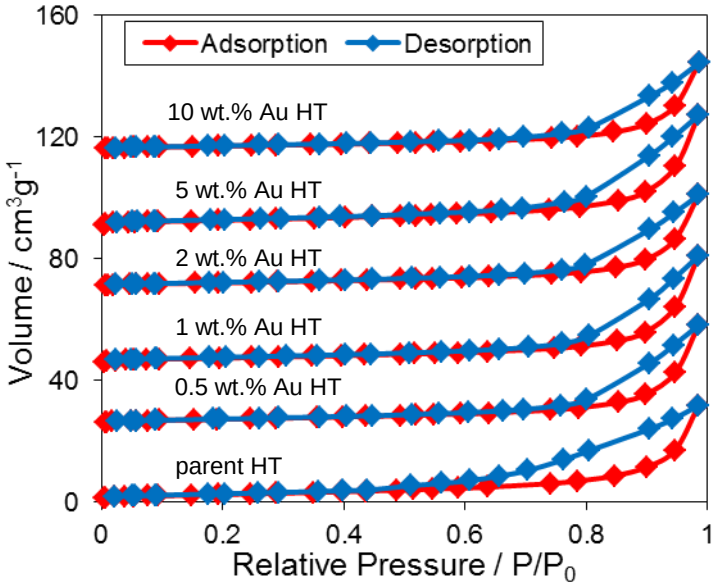

Figure 3.4: N_2 adsorption-desorption isotherms for Au/HTs.

The parent hydrotalcite exhibits a type II H3 isotherm, that is retained in all the Au/HTs, and is consistent with microporous crystallites with interplatelet mesoporous voids and slit type pores[34]. Following Au deposition and 200 °C calcination the Au/HTs exhibit smaller hysteresis loops than the parent HT. A reduction in the hysteresis may suggest that pores are more accessible[35] after calcination at 200 °C, due to an expansion of interplatelet mesoporous voids and a removal of water from interlayers[19, 36]. **Table 3.4** reports BET surface areas for the parent hydrotalcite and Au/HTs, with values in accordance with the literature[20].

Table 3.4: Surface areas of HT and Au/HTs determined by N_2 porosimetry.

	BET surface area / m^2g^{-1}
Parent HT	95 ± 9.5
0.5 wt.% AuHT	88 ± 8.8
1 wt.% AuHT	88 ± 8.8
2 wt.% AuHT	90 ± 9.0
5 wt.% AuHT	91 ± 9.1
10 wt.% AuHT	75 ± 7.5

A more accurate pore analysis was carried out over the parent HT, using a QuantaChrome Autosorb instrument and N_2 at 77 K as the gas for the analysis. **Figure 3.5 – left** shows the resulting mesopore size distribution, obtained using the DFT method[37] and the fitting model for N_2 at 77 K on carbon for slit pores and a QSDFT equilibrium; **Figure 3.5 – right** shows good agreement between the model and experimental data. The average mesopore diameter was 8.2 nm, similar to values from previous works[32], and attributed to intercrystallite voids, with a total pore volume of 0.814 $cm^3.g^{-1} \pm 0.024$.

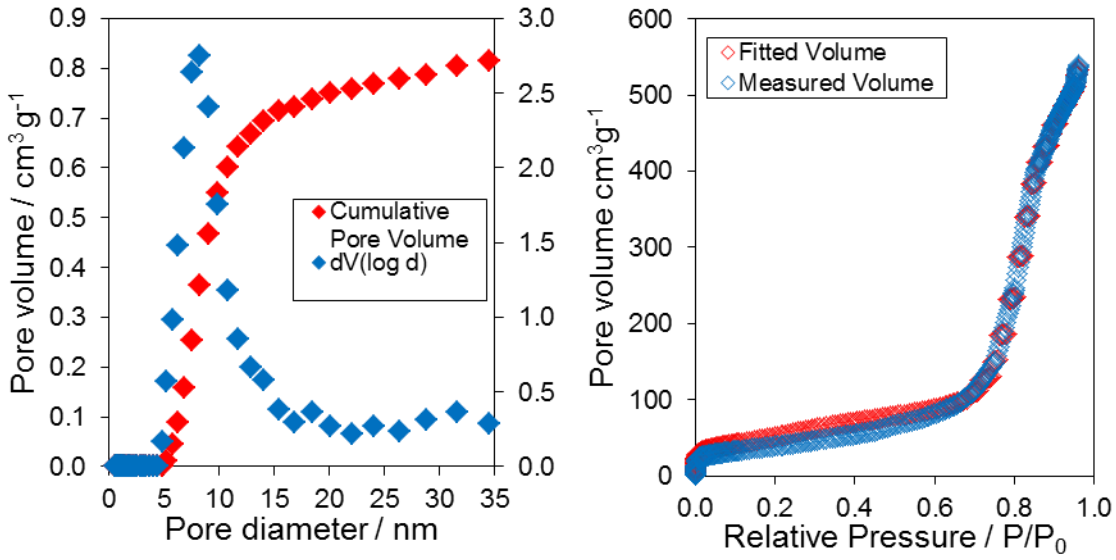

Figure 3.5: left – pore diameter vs. pore volume and its derivative function for Mg_3Al hydrotalcite, right – fitted vs. measured volume shows a good agreement for the selected mathematical model.

3.2.3.4 SEM, TEM and Au particle size distribution

An SEM image was obtained for the parent HT and TEM images were obtained for Au/HTs, with **Figure 3.6** illustrating the morphology of the parent material.

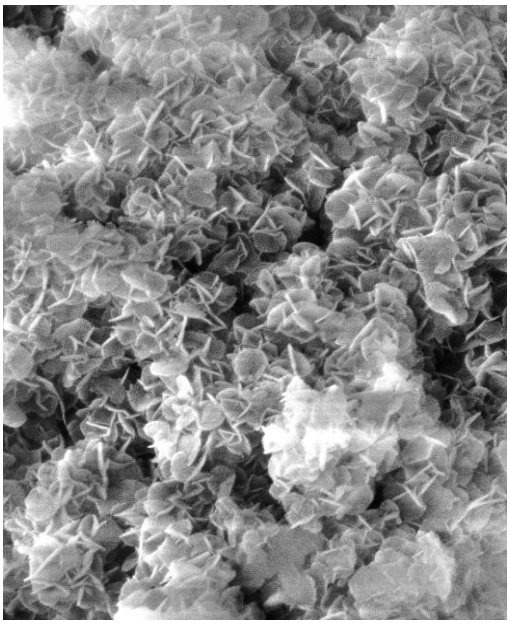

Figure 3.6: SEM micrograph of parent Mg_3Al HT, showing characteristic sand rose morphology.

According to the nature of the charge-compensating counter-anion in the interlayers, or when an excess of NH_4OH is used, the co-precipitation method might yield poor surface area manasseite, instead of the desired high surface area hydrotalcite[17, 38], as already mentioned in **Chapter 3.2.3.2.** Large and well-defined (around 200 nm up to 1 μm) compact particles fused together are clearly visible,[20, 21, 39] showing the characteristic hydrotalcite sand-rose morphology and confirming the rombohedral 3R crystal system[17, 38].

Dark/bright field (S)TEM images of the Au/HT series are shown in **Figure 3.7**

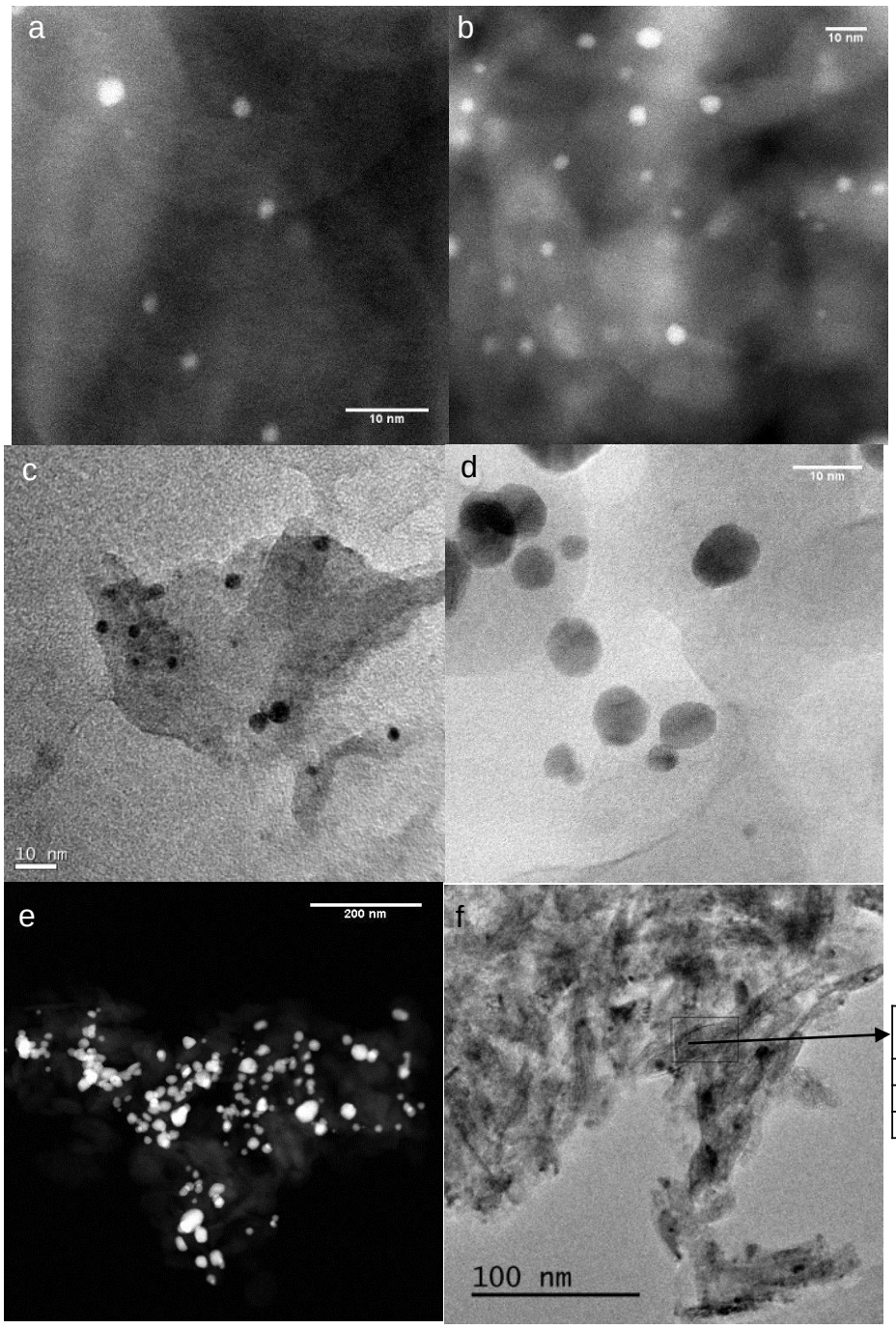

Element	EDX / atom%	XPS / atom%
Mg	15.3	16.8
Al	5.0	5.6
Mg:Al	3.0	3.0

Figure 3.7: Dark and bright field (S)TEM images of (a) 0.5 wt. %, (b) 1 wt. %, (c) 2 wt. %, (d) 5 wt. % and (e) 10 wt% Au/HT; (f) image of 2 wt. % Au/HT highlighting hydrotalcite nanosheets. EDX and XPS confirmed Mg_3Al composition.

ImageJ software was used to measure the particle size distribution for each material, 100 NPs were measured for each sample and results are shown in **Figure 3.8**. The mean particle size increased with gold loading, resulting in a trend similar to that observed by XRD. Particles appear to be very well dispersed for the 0.5, 1 and 2 wt. % Au/HT, growing and agglomerating at higher loadings to give a broad range of size.

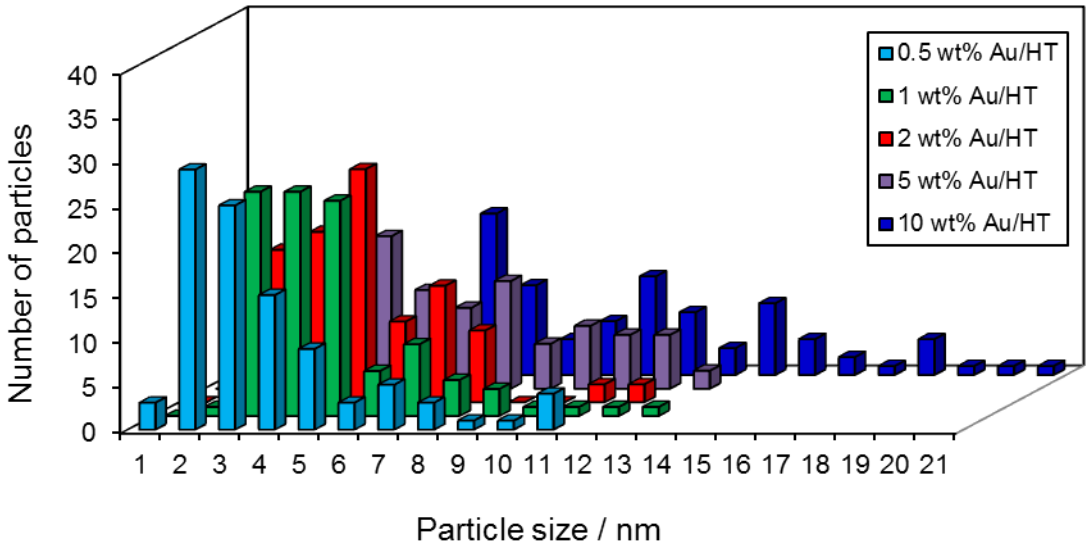

Figure 3.8: particle size distributions for Au/HT obtained by counting 100 NPs per sample using ImageJ software and counting 100 NPs per sample; mean particle size increases with gold loading.

3.2.3.5 Ex situ DRIFT spectra

Ex situ DRIFT spectra **(Figure 3.9 – left)** compare the uncalcined parent hydrotalcite and 2 wt. % Au/HT calcined at 200 °C; the peak assignment was made according to that reported by Meliàn-Cabrera and co-authors[40] and Davis and co-authors[36]. At 3800-2500 cm^{-1} the OH stretching is clearly visible for both the parent hydrotalcite and the 2 wt. % Au/HT as a broad band. The shoulder at 3080 cm^{-1} is characteristic of layered HTs, arising from hydrogen bonding between water molecules and CO_3^{2-} groups within the interlayer region. The OH bend of physisorbed water is visible at 1590 cm^{-1}, while the two bands at 1497 cm^{-1} and 1331 cm^{-1} are due to the stretching of CO_3^{2-} in the interlayer region.

Deposition-precipitation of Au, followed by calcination, caused interlayer water removal and a carbonate rearrangement, evidenced by the absence of the previous shoulder in the OH region at 3080 cm^{-1} and the 1590 cm^{-1} bend, and emergence of two new peaks corresponding to C=O at 1508 cm^{-1} and to C-O at 1338 cm^{-1} in **Figure 3.9 –** left**.** No significant changes were seen in ATR spectra as a function of Au loading (**Figure 3.9 –** right).

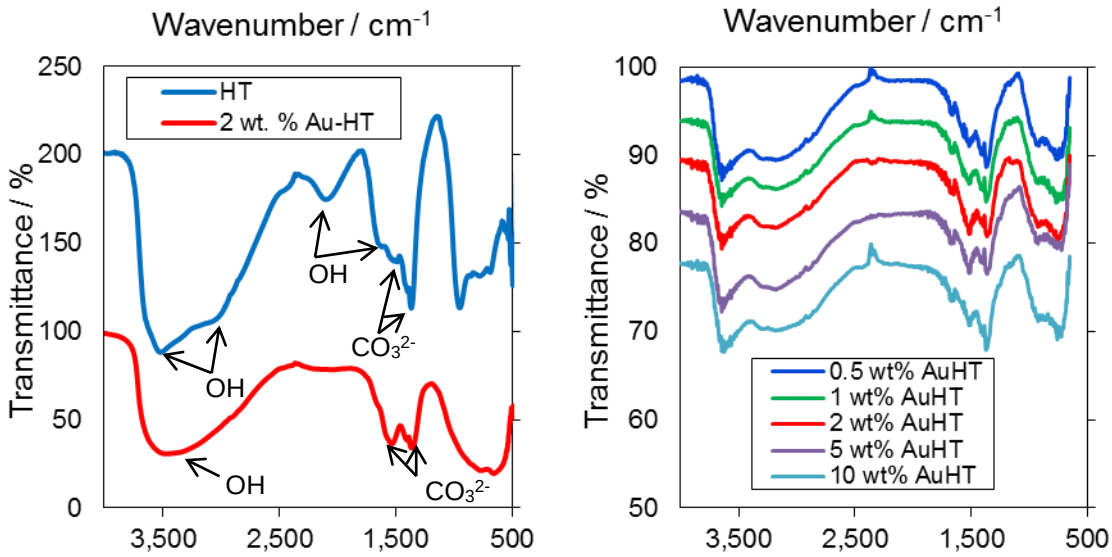

Figure 3.9: left **–** DRIFT spectra of parent uncalcined HT and 2 wt. % AuHT calcined at 200 °C, right – ATR spectra of 0.5, 1, 2, 5 and 10 wt. % Au on HT calcined at 200 °C.

Scheme 3.1 below[40] illustrates the proposed changes in HT morphology during calcination up to 150 °C.

Scheme 3.1: schematic of carbonate rearrangement and interlayer water removal for calcined HT from reference 40.

3.2.3.6 CO_2 titration and TPD

CO_2 pulse chemisorption and following TPD analysis were used to determine the base site density and strength for different Au/HTs. CO_2 is an acidic probe molecule, and it is assumed that each molecule of CO_2 adsorbs onto one base site on the hydrotalcite, forming a bicarbonate species with the hydroxide anions or surface hydroxyl groups[21, 39, 41].The impact of Au loading on basicity was explored in **Figure 3.10 –** left.

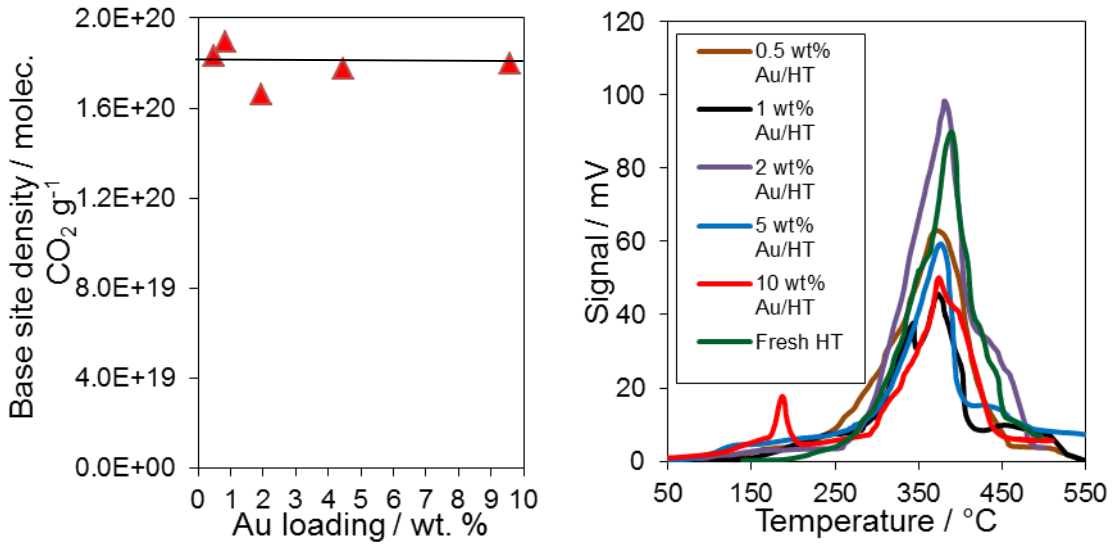

Figure 3.10: left – base site densities as a function of Au loading in Au/HT materials and right – base site strength for the same materials, all values from CO_2 TPD.

Since the same hydrotalcite and thermal treatment was employed in every case, the resulting TPD profiles were similar for Au loadings, and the base site densities almost identical as summarised in **Table 3.5.**

Table 3.5: Base site density and peak desorption temperature for Au/HTs.

Au/HT / wt. %	Number of base sites / g^{-1}	Desorption peak max T / ºC
0.5	1.83×10^{20}	367 ± 0.2
1	1.90×10^{20}	367 ± 0.2
2	1.66×10^{20}	380 ± 0.2
5	1.77×10^{20}	383 ± 0.2
10	1.79×10^{20}	371 ± 0.2

The desorption peak maxima all fell between 370-380 °C, attributed to medium strength base sites **(Figure 3.10 –** right**).** The 10 wt. % Au/HT material also exhibited a low concentration of weak base sites at 180 °C, attributed to weak bicarbonate species bound to surface hydroxyls in the lattice.

3.2.3.7 Surface chemical analysis

XPS analysis was carried out on the Au/HT series. The Mg 2p spectra **(Figure 3.11)** was fitted by a single chemical environment containing the spin-orbit 2p doublet (separation = 0.28 eV), with binding energies of 49.80 eV and 50.08 eV (NIST database[42] 50.40 eV for $MgAl_2O_4$ spinel, 49.5-49.9 eV for hydrotalcite phase, Cantrell and co-authors[20]).

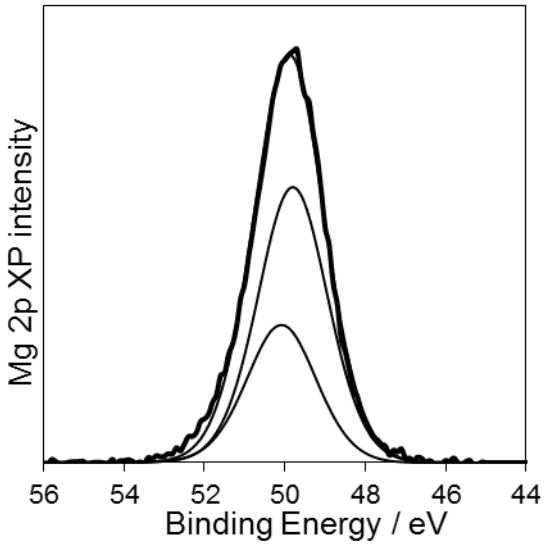

Figure 3.11: High resolution Mg 2p XP spectra for 2 wt. % Au/HT showing a single chemical state assigned to pure HT.

The Al 2p spectra **(Figure 3.12)** was likewise fitted by a single chemical environment containing the spin-orbit 2p doublet (doublet separation = 0.41 eV), with binding energies of 73.52 eV and 73.93 eV (NIST database[42] 74.10 eV for $MgAl_2O_4$ spinel, 73.50 for hydrotalcite phase, Creasey and co-authors[43]).

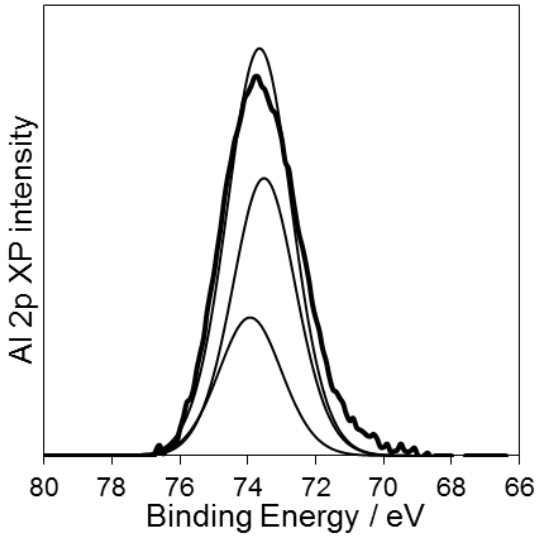

Figure 3.12: High resolution Al 2p XP spectra for 2 wt. % Au/HT showing a single chemical state assigned to pure HT.

Shifts in the Mg and Al binding energies relative to the literature are attributed to the different Mg:Al ratio, being 3 for the catalysts prepared in this thesis, and 2 for literature materials[20, 21, 43] and the NIST database[42]. The observation of a single HT phase agrees with XRD results **(see Chapter 3.2.3.2.).**

The O 1s spectra **(Figure 3.13)** comprised two distinct chemical components: one attributed to the O^{2-} of HT and carbonates with a binding energy of 531.42 eV, (NIST database[42] 531.50 eV for $MgAl_2O_4$ spinel and for $MgCO_3$), and the second one attributed to hydroxyls with a lower binding energy of 529.25 eV. (NIST database[42] 530.9 eV for $Mg(OH)_2$, 529.3-530.9 eV for OH in hydrotalcite phase, Cantrell and co-authors[20]).

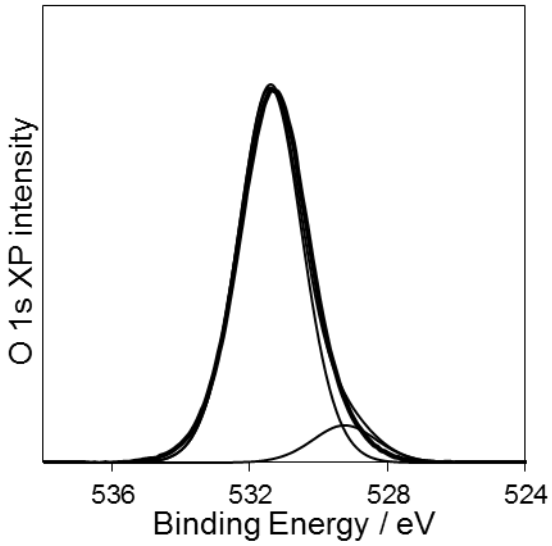

Figure 3.13: high resolution O 1s XP spectrum of 2 wt. % Au/HT highlighting the high binding energy CO_3^{2-} and low binding energy OH^- states.

The C 1s spectrum **(Figure 3.14)** was likewise fitted by two chemical states: one at 284.6 eV due to adventitious carbon, and one at 288.99 eV due to carbonate (NIST database[42] 289.40 for $MgCO_3$).

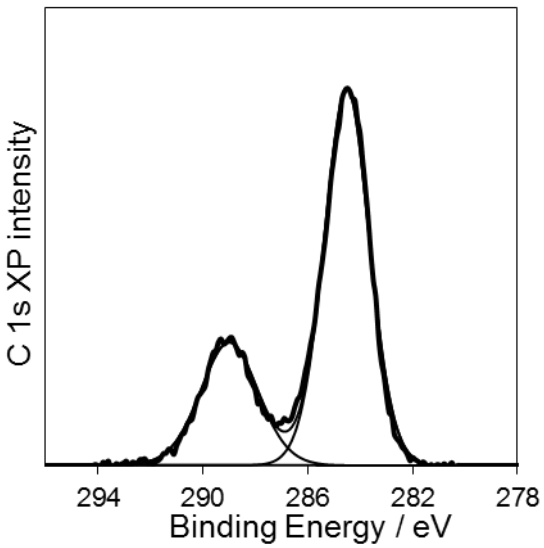

Figure 3.14: high resolution C 1s XP spectrum of 2 wt. % Au/HT highlighting the high binding energy CO_3^{2-} and low binding energy adventitious carbon states.

The Cl 2p spectrum **(Figure 3.15)** comprised a single 2p doublet (separation = 1.60 eV) with binding energies of 198.3 and 196.8 eV (NIST database[42] $NaAuCl_4$ 198.80 eV), arising from residual chlorine due to trace of NH_4Cl during the synthesis, even following catalyst washing and low temperature calcination.

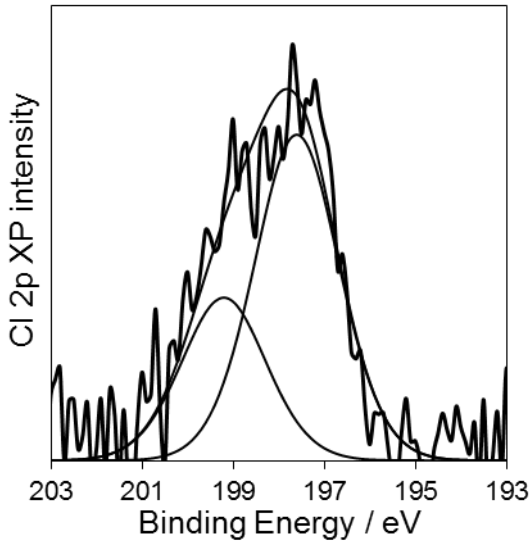

Figure 3.15: high resolution Cl 2p XP spectrum, highlighting residual chloride for 2 wt. % Au/HT.

The Au 4f spectrum **(Figure 3.16)** could only be adequately fitted by two separate chemical species, a single Au 4f chemical state (doublet separation = 3.70 eV) and an additional overlapping Mg 2s state whose fitting and subtraction permitted quantification of the gold species. The Au 4f binding energies of 83.21 eV and at 86.92 eV were consistent with the presence of metallic gold (NIST database[42] $CsAuCl_4$ (Au^{3+}) 87.5-91.2 eV, Au foil 84.0-88.0 eV).

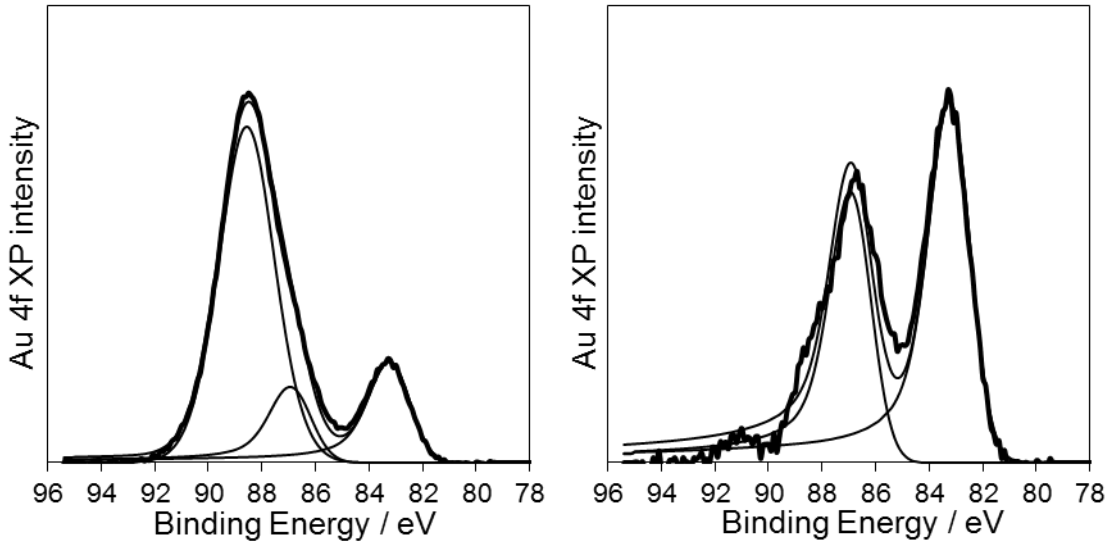

Figure 3.16: high resolution Au 4f XP spectra of 2 wt. % Au/HT (left) before and (right) after subtraction of the overlapping Mg 2s component.

Au 4f XP spectra were subsequently compared as a function of gold loading on hydrotalcite as shown in **Figure 3.17**.

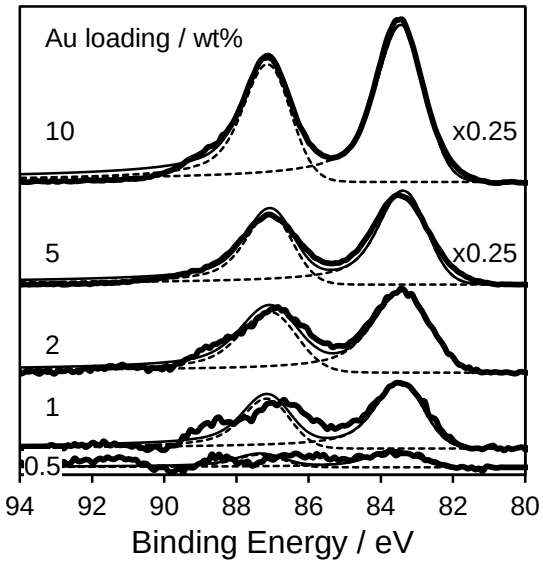

Figure 3.17: High resolution Au 4f XP spectra of Au/HTs as a function of Au loading. The weak peak for 1 wt. % Au comes from the Mg 2s subtraction.

A common experimental shift of 0.6 eV to lower binding energy relative to Au foil was found across the loading series, with all materials consistent with the presence of metallic gold; Radnik and co-authors[44] attributed this shift to the presence of gold nanoparticles instead of gold foil and their average value was found to be 0.4–0.6 eV.

These authors proposed that such shift to lower binding energy might be related to different effects, such as a difference in the formal oxidation state or band structure of Au nanoparticles. Complementary *ex* and *in* situ XANES measurements described later in this thesis (see **Chapter 3.2.3.8**) confirm the presence of gold in a formal Au^0 oxidation state after calcining at 200 °C for Au/HT.

The lower coordination number of Au surface atoms has also been proposed by Radnik and co-authors[44] to account for the observed binding energy shift relative to bulk gold. Initial state effects depend on the orbital energy of the emitted electron, while final state effects reflect relaxation (reabsorption) of the photoexcited system. For small particles < 2 nm, low-coordination surface atoms such as those at edge and corners dominate, and a change of initial state is expected, due to not efficient overlapping of Au orbitals, while for particles > 3 nm, as is largely the case in this thesis, final state contributions may be more significant, particular on poorly conductive HT supports. EXAFS measurements (see **Chapter 3.2.3.8**) confirmed that the Au-Au nearest neighbour coordination number varied between 10.2 and 11.4 across the Au/HTs, and hence was indeed lower than the bulk value of 12, supporting the hypothesis of Radnik and co-authors[44].

3.2.3.8 Operando XAS studies on the Au oxidation state

Au L_{III}-edge (11.9 keV) fluorescence XAS measurements[45, 46] were recorded *in situ* to study the thermochemical transformation of the $HAuCl_4$ catalyst precursor over the Mg_3Al hydrotalcite (post NH_4OH addition) in order to identify the active gold species and optimise its synthesis. The catalyst precursor was studied within an environmental (Sankar) reaction cell at Diamond Light Source. The precursor was heated under air flow at 2 °C/min from 25 °C to 500 °C. XANES spectra of the as-prepared material was consistent with the presence of a Au(III) salt[45, 47-49], most likely a mix of $Au(NH_3)_4(OH)_3$ and around 10% of $Au(OH)_3$.

Heating to 65 °C under flowing air initiated precursor decomposition and the concomitant appearance of Au_2O_3, which remained stable to ~110 °C before decomposing to metallic Au. Complete decomposition of both the $Au(NH_3)_4(OH)_3$ precursor and Au_2O_3 to metallic gold required calcination > 170 °C as shown in **Figure 3.18**[50].

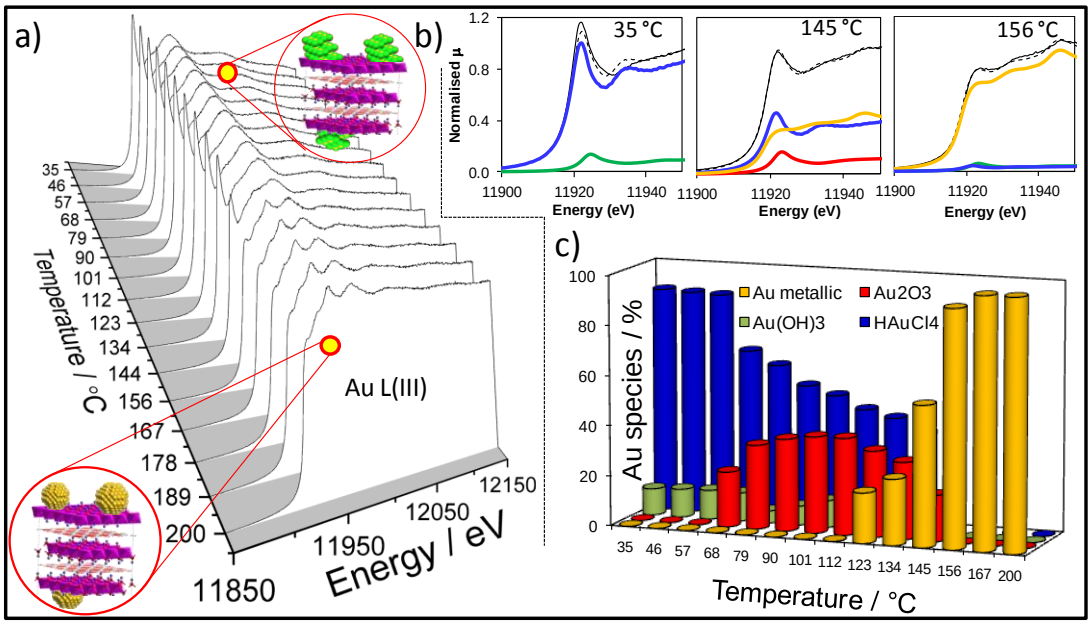

Figure 3.18 *In-situ* Au L_{III} XANES during thermal processing of the $HAuCl_4$/Mg-Al HT precursor a) waterfall plot showing thermal evolution of normalised XANES spectra; b) representative least squares fitted XANES spectra to reference gold species; c) quantitative thermal evolution of fitted Au species.

An *operando in situ* XAS study was subsequently performed of the thermally processed 2 wt.% Au/HT material, in order to identify the nature of the gold active sites during 5-HMF oxidation. A 1.96 wt. % Au/HT sample was placed within a bespoke PTFE trickle-bed, recirculating cell, held in place using carbon fibre wadding; the catalyst was charged with oxygenated aqueous solution from an external reservoir and heated to 90 °C. On reaching reaction temperature, first 1 M NaOH, and subsequently 0.1 mmol of 5-HMF, were added to the reservoir and the reaction operated for 16 h during spectral acquisition.

Despite such high pH, the XANES spectra remained unperturbed following NaOH or 5-HMF addition,[51] confirming that gold remained in its metallic form during the selective oxidation of 5-HMF, with no evidence of $Au(OH)_3$ or Na-Au intermetallics detected as might arise due to either gold leaching or Na chemisorption and alloying (**Figure 3.19**).

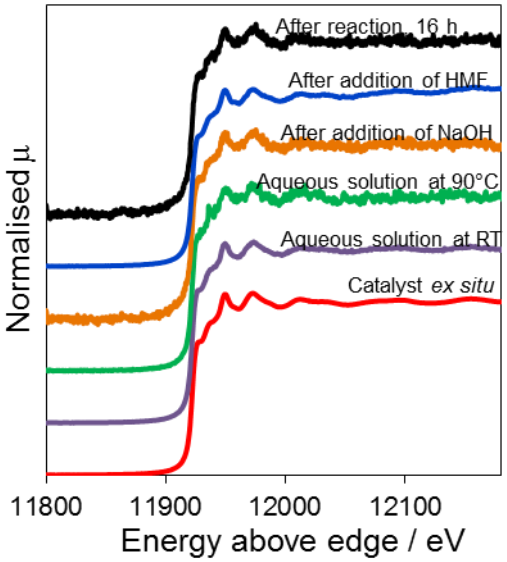

Figure 3.19: Au L_{III} edge (11.9 keV) *in situ* XANES spectra for the aerobic selective oxidation of HMF, as a function of reaction conditions. No changes were visible in the Au^0 oxidation state. 2 wt. % Au catalyst used for this experiment.

These results confirm that gold nanoparticles do not sinter or leach even after 16 h reaction and that NaOH directly promotes oxidation without influencing the electronic or structural properties of gold. This is consistent with reported isotope-labelling and DFT studies[6, 12], which suggest that hydroxyls adsorbed at the edge of Au clusters are the critical surface species participating in the catalytic cycle, lowering the barriers to C-H and O-H dissociation[52] and removing surface hydride.

Ex situ measurements of the same catalyst were run and the EXAFS region of Au foil standard was fitted to its Fm-3m space group[53]. This enabled amplitude factors, interatomic distances of the neighbouring scatters (coordination shell distances), and Debye-Waller disorder factors to be determined, identifying only Au-Au coordination shells. The resulting K^3 weighted and Fourier transformed fits are presented in **Figure 3.20,** with their corresponding coordination numbers, interatomic distance and Debye-Waller factors recorded in **Table 3.6**.

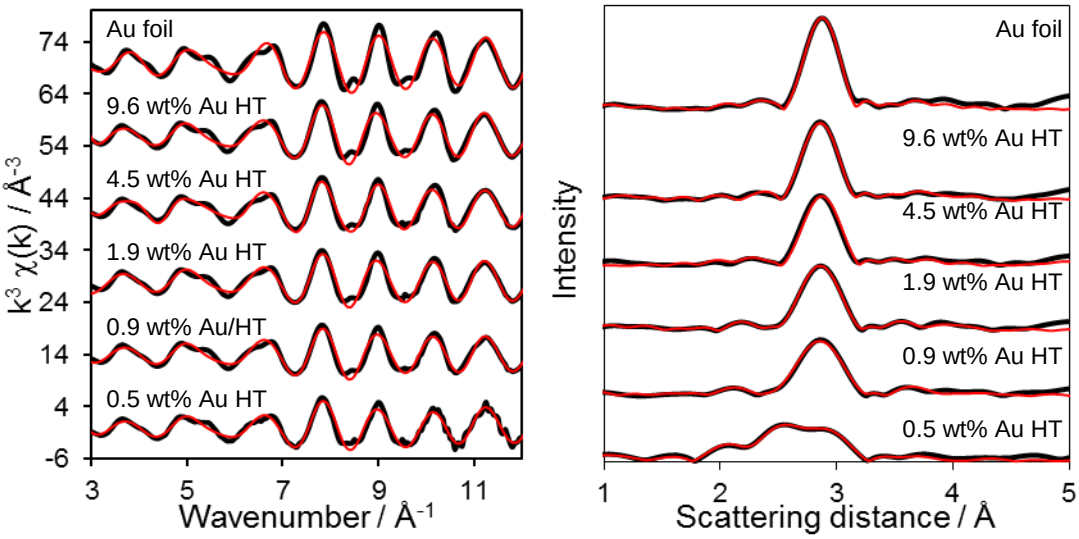

Figure 3.20: (left) Au L_{III}-edge k^3-weighted EXAFS spectra and (right) Fourier transformed spectra of Au/HT catalysts as a function of Au loading.

Table 3.6: Au L_{III}-edge EXAFS fitting parameters for Au/HT catalysts, calcined at T = 200 °C in air.

Au loading / wt%	Scattering pair	Coordination number	Scattering distance / Å	σ / Å²	Fit factor
Au foil	Au-Au	12	2.86 (±0.02)	0.0083 (±0.0005)	2.56
	Au-Au	6	4.04 (±0.03)	0.0159 (±0.0051)	
0.5	Au-Au	10.2 (±0.3)	2.85 (±0.03)	0.0089 (±0.0016)	7.26
0.9	Au-Au	10.5 (±0.2)	2.85 (±0.03)	0.0089 (±0.0010)	6.98
1.9	Au-Au	10.6 (±0.1)	2.85 (±0.03)	0.0084 (±0.0008)	1.94
4.5	Au-Au	11.1 (±0.1)	2.86 (±0.02)	0.0086 (±0.0006)	5.12
9.6	Au-Au	11.4 (±0.1)	2.85 (±0.03)	0.0083 (±0.0006)	7.33

Figure 3.21 shows the mean Au nanoparticle diameters estimated from TEM, XRD and EXAFS first shell coordination numbers employing the model proposed by Jentys[54], showing excellent agreement between these different local and averaging analytical methods.

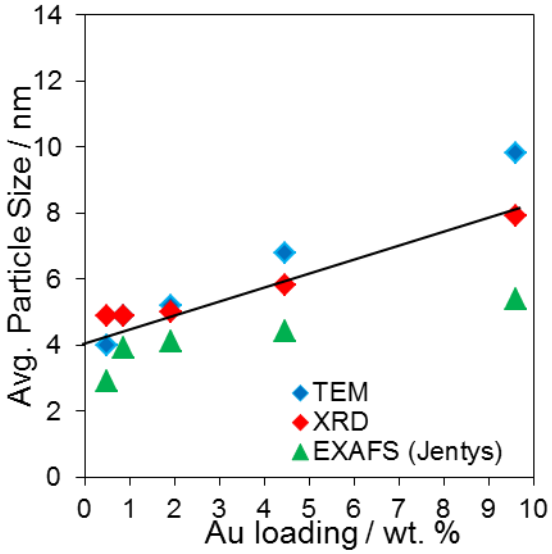

Figure 3.21: Measured (TEM) and calculated (XRD and EXAFS) mean particle sizes gold nanoparticles as a function of Au loading in Au/HTs.

3.2.3.9 ^{1}H NMR studies of HMF ± NaOH

As the preceding *operando* XAS analysis showed that liquid NaOH does not affect the Au oxidation state, ^{1}H NMR studies were undertaken to investigate the role of soluble base upon the HMF substrate[55]. It is worth remembering that in the absence of α–hydrogens, NaOH does not react with aldehydes through the aldol reaction, but rather an equilibrium exists between the aldehyde and its hydrated 1,1 gem-diol form[56]. Rossi and co-workers[57] have proposed the gem-diol as the reactive species in gold catalysed selective oxidation of aldehydes and sugars under basic conditions[58]. In order to demonstrate the formation of this postulated reactive intermediate, ^{1}H NMR spectra of HMF in D_2O was recorded before and after NaOH addition **(Figure 3.22** and **Figure 3.23).**

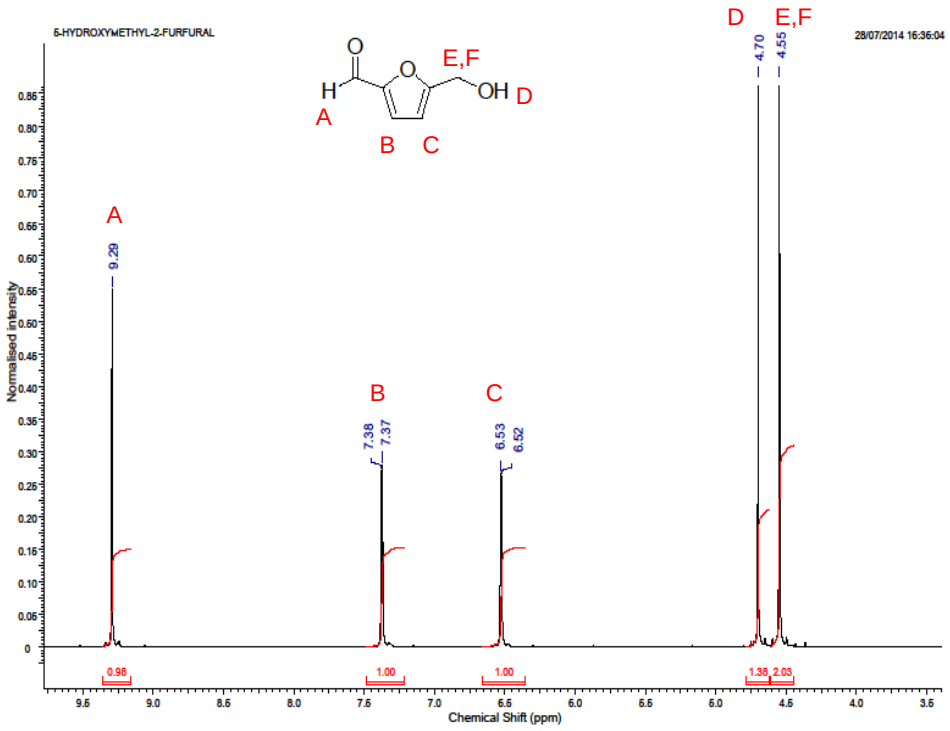

Figure 3.22: ^{1}H NMR spectra of HMF. δ_H (300 MHz, D_2O): A) 9.3 ppm (s, 1H, –CHO); B) 7.4 ppm (d, 1H, aromatic –CH near R–CHO, J = 3.477), C) 6.5 ppm (d, 1H, aromatic –CH near R–OH, J = 3.48); D) 4.7 ppm (s, 1H, –OH and water); E, F) 4.5 ppm (s, 2H, R–CH_2).

As H_2O is visible at 4.7 ppm, this signal was attributed to the exchange of R-OH moieties with D_2O. A NaOH pellet was subsequently added to the same NMR tube, to produce a 0.1 M aqueous solution in D_2O at pH = 13 and a spectrum was acquired immediately. Such concentration was chosen to prevent side reactions in the absence of catalyst. The ^{1}H NMR spectrum in **Figure 3.23** reveals interesting changes in the molecule after the NaOH addition: both the aldehydic CHO (A) and the adjacent aromatic H (B) appear broader and weaker, indicative of an anionic species forming and of chemical equilibrium, in which bonds are breaking and forming[59, 60].

A low concentration of a new compound is visible in the NMR spectrum, as the equilibrium favours the aldehyde form, and spectra analysis has shown this is the 1,1 gem-diol forming; experimental data agree with the NMR prediction (see spectra in **Figure 3a.1** and **Figure 3a.2** Appendix).

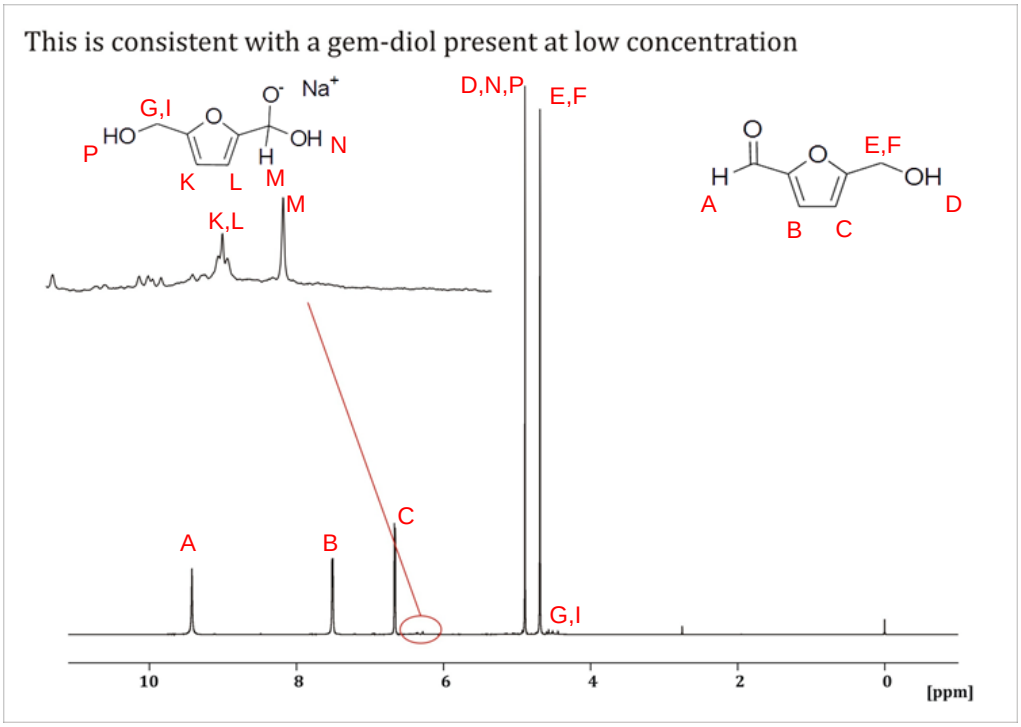

Figure 3.23: ^{1}H NMR spectra of HMF + NaOH. Hydrogens A, B, C, D, E and F for HMF attributed as in **Figure 3.22**. δ_H HMF gem-diol (300 MHz, D_2O): K, L) 6.2 ppm (d, 2H, aromatic –CH, J = 3.46), M) 6.1 ppm (s, 1H, aldehyde that became gem-diol); N, P) 4.7 ppm (s, 3H, –OH and water); G, I) 4.5 ppm (s, 2H, R–CH_2).

Nevertheless, 1,1-geminal diols, also known as hydrates, are not stable enough to be isolated, as the equilibrium shifts back to starting materials[56]; also, the molecule can undergo to subsequent Cannizzaro disproportion[61], as it happened in the absence of catalyst after 20-30 minutes, to yield a 1:1 mixture of an alcohol, respectively 2,5-dihydroxymethylfuran (DHMF) and the Na salt of HMFCA **(Figure 3.24).** A spectra of HMFCA standard is available in the Appendix, **Figure 3a.3**, together with DHMF prediction, **Figure 3a.4**.

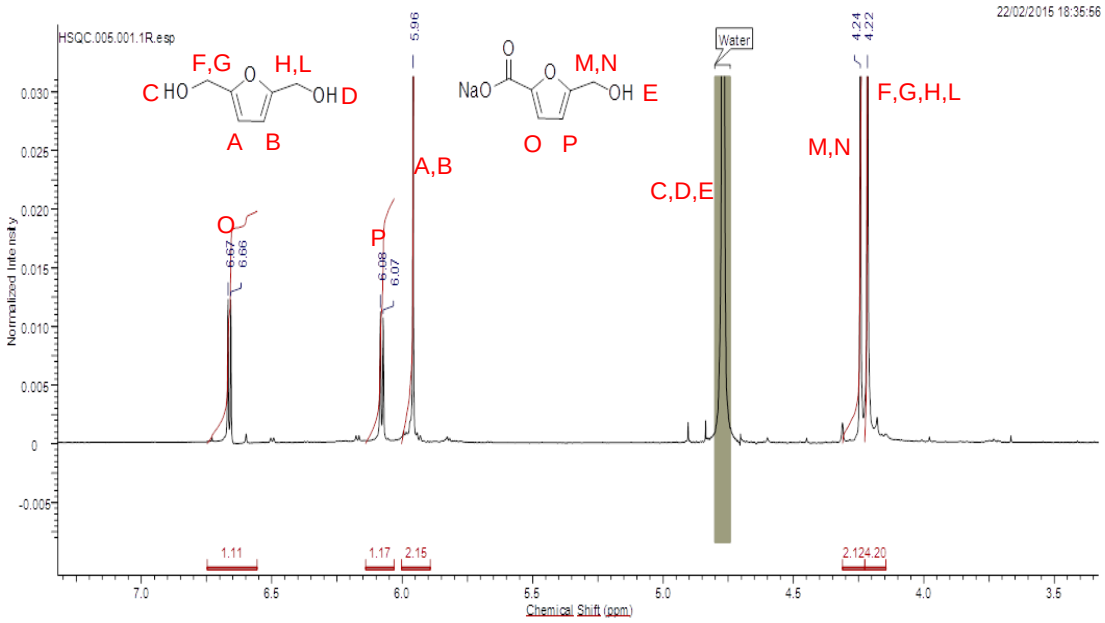

Figure 3.24: ^{1}H NMR spectra of HMFCA sodic salt + DHMF. δ_H DHMF (300 MHz, D_2O): A, B) 5.9 ppm (s, 2H, aromatic –CH); C, D) 4.7 ppm (s, 2H, –OH and water), F, G, H, L) 4.22 ppm (s, 4H, two for $–CH_2$). δ_H HMFCA sodic salt (300 MHz, D_2O): O) 6.7 ppm (d, 1H, aromatic –CH near –COONa), P) 6.1 ppm (d, 1H, aromatic –CH near the R–OH); E) 4.7 ppm (s, 2H, –OH and water), M, N) 4.24 ppm (s, 2H, $–CH_2$).

It is widely reported that prolonged exposure of 5-HMF to aqueous NaOH results humin production[62, 63], hence it is likely that Au NPs are crucial to rapidly oxidise the 1,1 gem-diol product to the desired 2,5-FDCA in order to avoid humins.

3.2.4 Au/HT catalysed aerobic selective oxidation of 5-HMF

3.2.4.1 Diffusive or chemical regime?

Preliminary tests were performed using the 2 wt. % Au/HT material to determine whether aqueous phase 5-HMF oxidation was rate-limited by external mass transport effects prior to a detailed kinetic analysis of the reaction network. **Figure 3.25** revealed no significant dependence of the reaction profile upon stirrer speed, and hence no evidence for external diffusion limitations in these experiments was seen, and 500 rpm was chosen as the optimal speed.

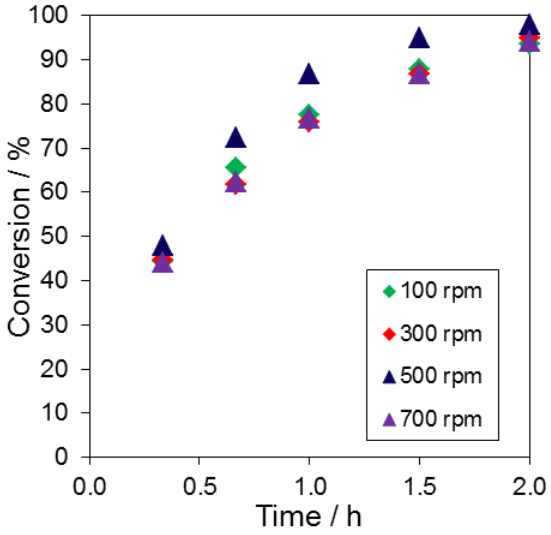

Figure 3.25: reaction profiles for the aqueous phase selox of 5-HMF by 2 wt. % Au/HT as a function of stirring rate. Reaction conditions: 0.1 mmol of HMF, 25 mg of catalyst, V = 6 ml of H_2O, ν O_2 flow = 15 ml min^{-1}, T = 90 °C, different stirrer speeds.

This conclusion was supported by tests using three different charges of the 2 wt. % Au/HT catalyst for 5-HMF selox of 10, 50 and 100 mg. A linear increase in the conversion and a slope of 1 on the associated bi-logarithm plot of Ln[cat] vs. Ln r **(Figure 3.26)**, confirmed that reaction was not under external diffusion control.

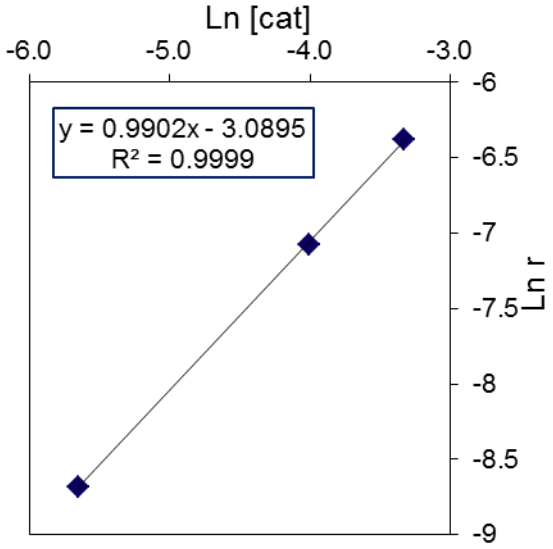

Figure 3.26: Bi-logarithm plot of Ln [cat] vs. Ln [rate] for the aqueous phase selox of 5-HMF by 2 wt. % Au/HT as a function of catalyst charge. Reaction conditions: 0.1 mmol of HMF, 10, 50 or 100 mg of catalyst, V = 6 ml of H_2O, ν O_2 flow = 15 ml min^{-1}, T = 90 °C, 500 rpm.

3.2.4.2 The effect of solution pH on the aerobic selox of HMF, HMFCA and FFCA

Systematic reactions were subsequently carried out to understand the impact of pH (via tuning the [NaOH]) upon 5-HMF selox. **Scheme 3.2** shows the reaction pathway for the aerobic selective oxidation of 5-HMF to 2,5-FDCA over Au/HTs.

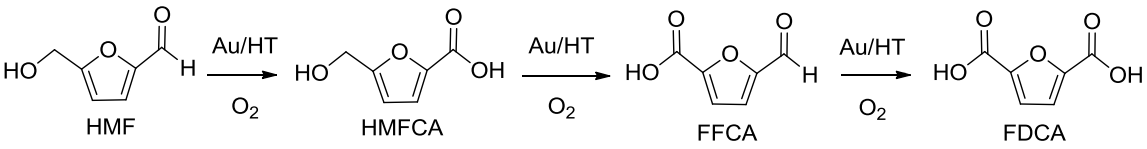

Scheme 3.2: the aerobic selective oxidation of HMF to FDCA.

The catalyst used for this study was the 2 wt. % Au/HT. Reaction conditions were as follows: 25 mg of catalyst, 0.1 mmol of HMF in order to have HMF/Au = 40 (mol/mol), T = 90 °C, V = 6 ml H_2O and ν O_2 = 15 ml/min. This catalyst was tested either alone in solution, or after the addition of a pre-determined amount of NaOH to the reaction mixture for Na:Mg molar ratios of 0.1, 1, 5, 10, 20 and 50 **(Figure 3.27** and **3.28)**.

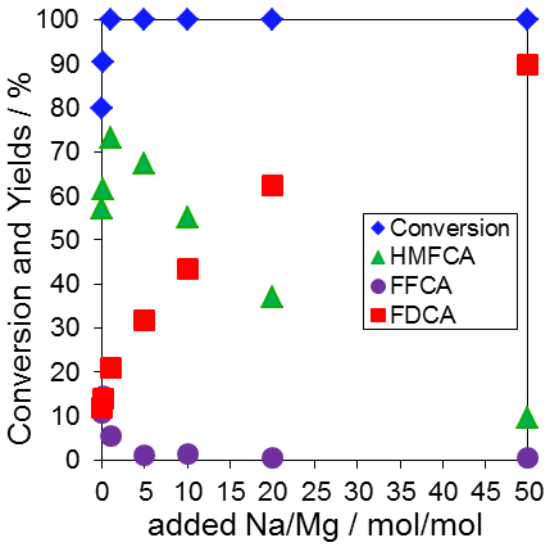

Figure 3.27: influence of NaOH addition on the aqueous phase selox of 5-HMF by 2 wt. % Au/HT after 7 h. Reaction conditions: 25 mg of catalyst, 0.1 mmol of HMF in order to have HMF/Au = 40 (mol/mol), T = 90 °C, V = 6 ml H_2O and ν O_2 = 15 ml/min. Amount of added NaOH / mmol = no addition, 2.85×10^{-2}, 2.85×10^{-1}, 1.43, 2.85, 5.7 and 14.3 mmol.

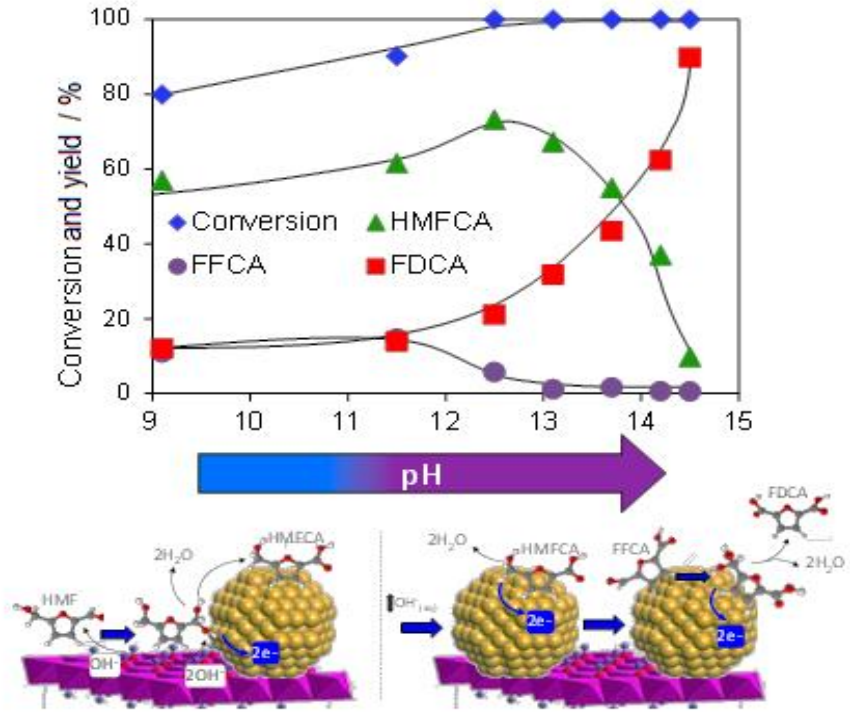

Figure 3.28: main – influence of pH on the aqueous phase selox of 5-HMF by 2 wt.% Au/HT after 7 h; inset – postulated pH dependent reaction mechanism[50]. Reaction conditions as in **Figure 3.27.**

The measured pH of the reaction before the addition of NaOH was 9, due to the intrinsic basicity of the hydrotalcite support. Even a minor amount of added NaOH was enough to increase 5-HMF conversion, although a large [NaOH] was necessary to increase the yield of desired 2,5-FDCA product. It is important to note that two control tests confirmed Rossi and Prati's earlier work[2], namely that 5-HMF could not be activated over Au NPs supported on either carbon or silica under base-free conditions. The following control reactions also yielded no 5-HMF conversion: $H_2O + O_2$; $H_2O + O_2$ + HT.

Soluble base thus appears essential for the efficient activation of 5-HMF and HMFCA formation for this particular 5-HMF:surface gold ratio; the highest pH delivers the highest FDCA yield. Note that this conclusion is not generally valid, as will be shown in **Chapter 3.2.4.4.**

In order to elucidate the origin of this striking pH sensitivity, comprehensive kinetic mapping of all the individual steps in the reaction pathway was carried out, using the same 2 wt. % Au/HT catalyst in the absence or presence of NaOH (6 mmol, pH 14). Results are summarised in **Scheme 3.3** below, which highlights the principal role of NaOH is to accelerate HMF oxidation to HMFCA, at least partially through suppressing the dehydration of the reactively – formed geminal diol intermediate[50].

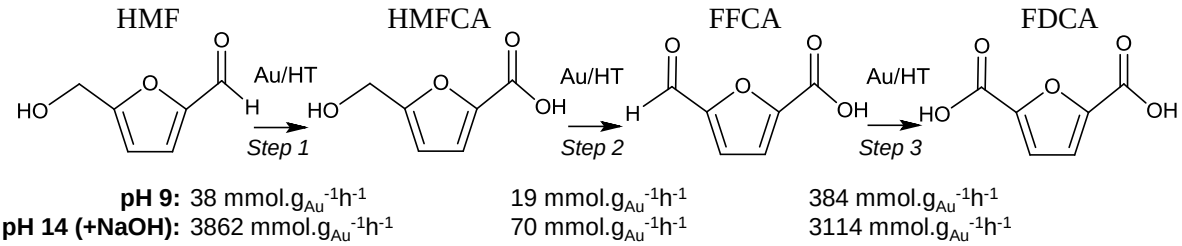

Scheme 3.3: impact of NaOH on kinetics for the aerobic selective oxidation of HMF over 2 wt. % Au/HT and kinetic constant experimentally determined.

In accordance with previous literature, which holds that alcohols are oxidised more slowly than aldehydes over Au[58, 64], the step HMFCA → FFCA exhibited the slowest rate with/without additional NaOH; however, the aldehyde oxidation in step 1 and 3 exhibited the strongest NaOH dependencies.

3.2.4.3 The effect of NaOH on the aerobic selox of 2-furfuryl alcohol and 2-furfural

A model reaction, the aerobic selective oxidation of 2-furfuryl alcohol and 2-furfural to 2-furoic acid, was chosen to isolate and understand the differences between the NaOH contribution to the selective oxidation of the alcohol function and the aldehyde one. The catalyst studied was 2 wt. % Au on HT with and without extra added NaOH and the reaction is shown in **Scheme 3.4.**

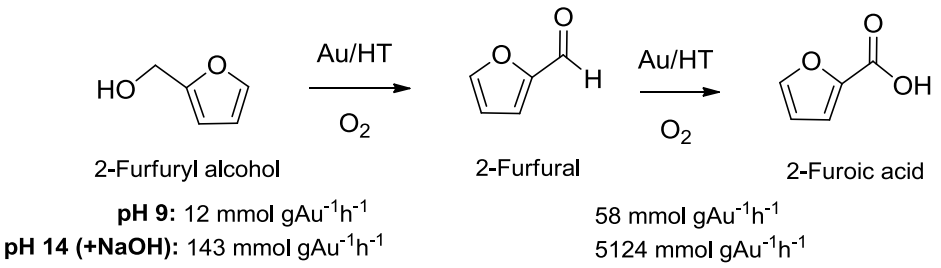

Scheme 3.4: two-steps aerobic selective oxidation of 2-furfuryl alcohol to 2-furfural and to 2-furoic acid.

Reaction conditions were identical to the previously described ones for the aerobic selective oxidation of HMF. As expected, the NaOH contribution was essential to accelerate the oxidation of the alcohol function of 2-furfuryl alcohol, remarking the importance of pH also for the model reaction. The selective oxidation of 2-furaldehyde was already fast at pH = 9 and further proof that the rate-determining step is the oxidation of R-OH function.

Figure 3.29 summarises and compares all the results for the selox of HMF, HMFCA, FFCA, 2-furfuryl alcohol and 2-furaldehyde.

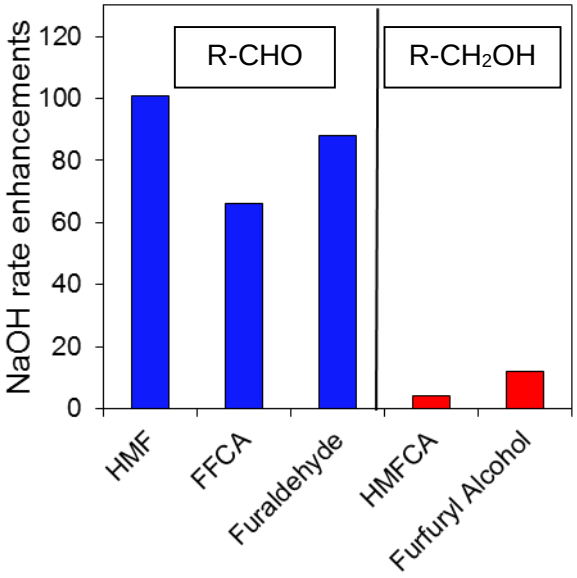

Figure 3.29: comparative NaOH rate enhancements for the selective aerobic oxidation of furanic aldehydes versus alcohols over a 2 wt. % Au/HT catalyst. Reaction conditions: 25 mg of catalyst, 0.2 mmol of R-CHO or 0.1 mmol of R-OH, T = 90 °C, V = 6 ml H_2O and ν O_2 = 15 ml/min. Amount of added NaOH = 6 mmol, pH = 14.

3.2.4.4 The effect of different Au loading on the aerobic selox of HMF and HMFCA

A series of different Au loadings, respectively 0.5, 1, 2, 5 and 10 wt. %, were supported on HT, following the previously described deposition-precipitation procedure[11] and reactions were carried out with and without extra added NaOH as described in **Chapter 3.3.2.** The raw and complete reaction profiles without extra added base are shown in **Figure 3.30** below:

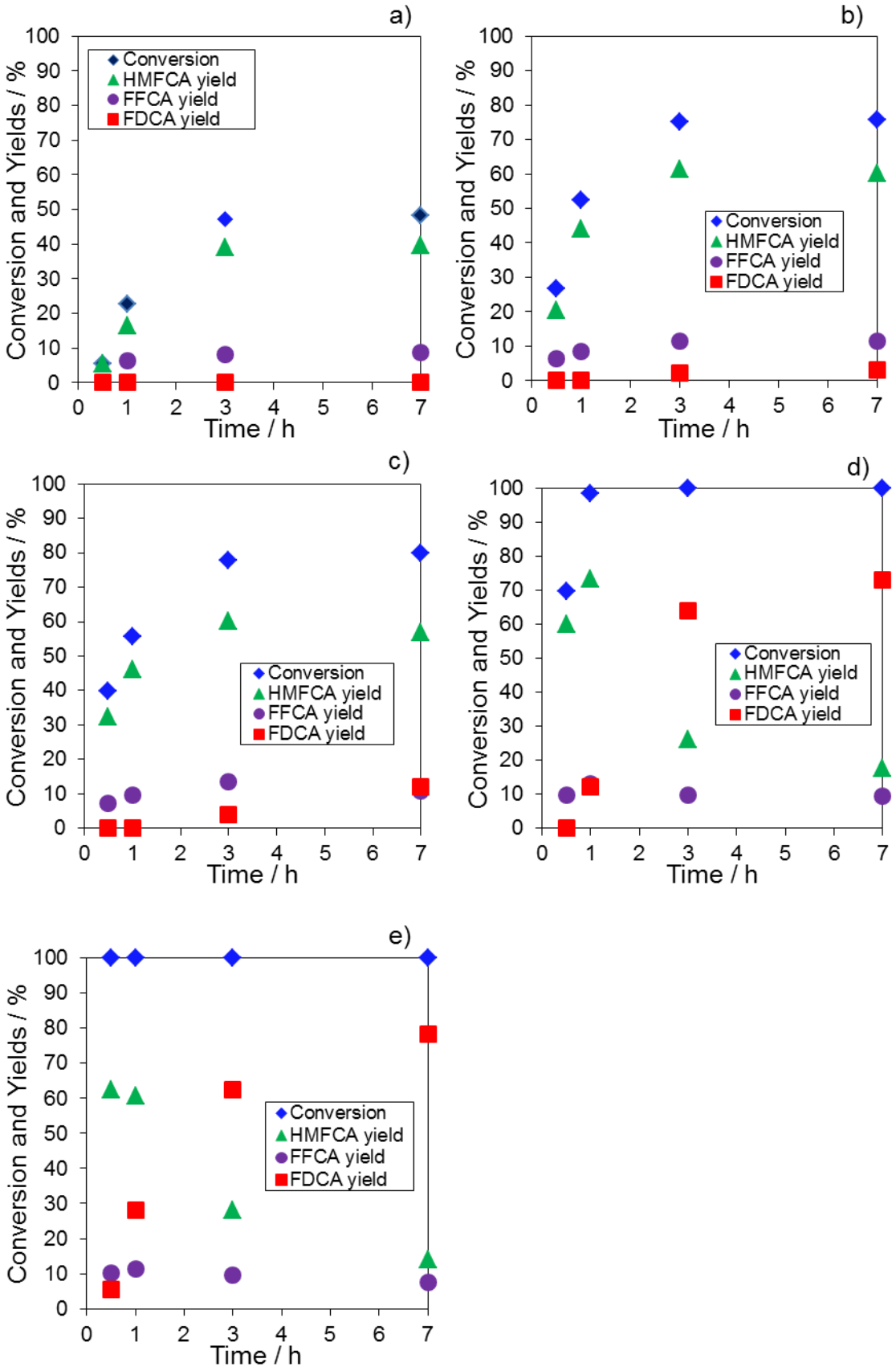

Figure 3.30: reaction profiles for the aerobic selective oxidation of HMF, using different Au loadings and without extra added base at pH = 9 a) 0.5 wt. % Au, HMF/Au

= 160 (mol/mol), b) 1 wt. % Au, 80 (mol/mol), c) 2 wt. % Au, 40 (mol/mol), d) 5 wt. % Au, 16 (mol/mol), and e) 10 wt. % Au, 8 (mol/mol). Reaction conditions: 25 mg of catalyst, 0.1 mmol of HMF, T = 90 °C, V = 6 ml H_2O, 500 rpm and ν O_2 = 15 ml/min.

As the amount of gold increases, conversion and FDCA yields appear to increase, suggesting a positive impact of higher gold loading. The reactions were then repeated in the presence of 6 mmol of NaOH (pH = 14) and all the raw complete reaction profiles are shown in **Figure 3.31**.

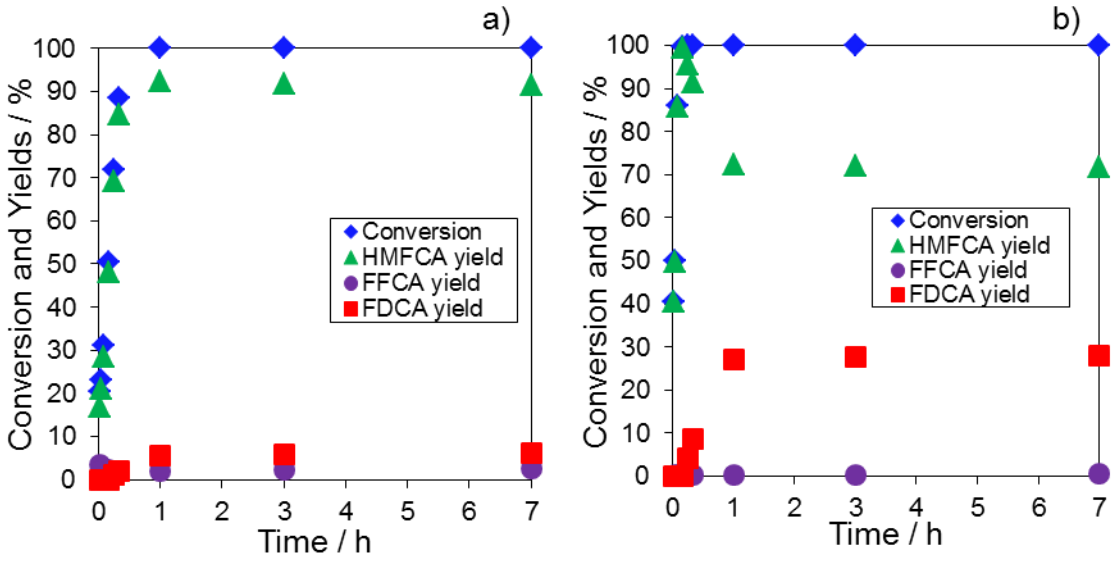

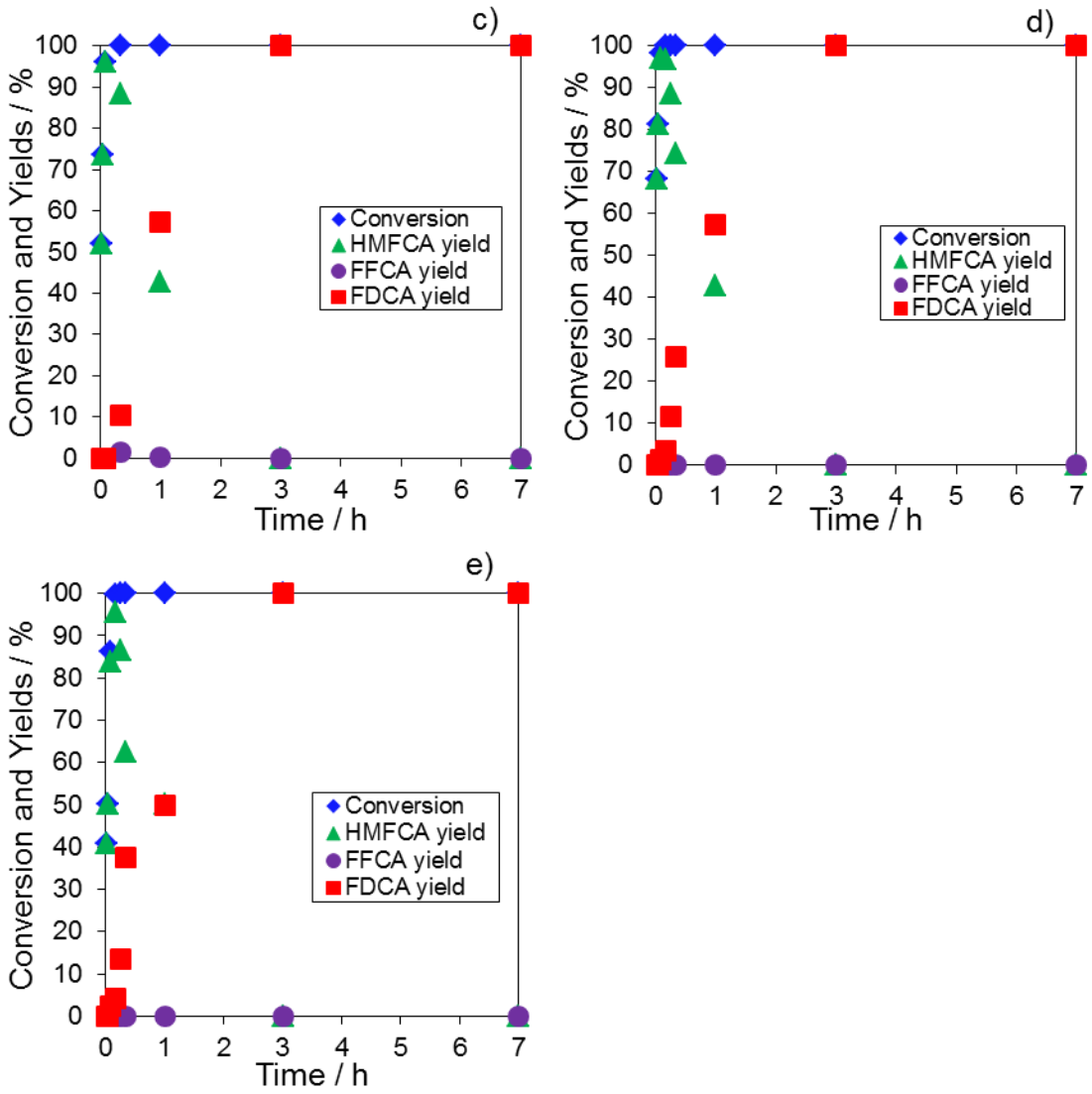

Figure 3.31: reaction profiles for the aerobic selective oxidation of HMF, using different Au loadings and NaOH at pH = 14. A) 0.5 wt. % Au b) 1 wt. % Au c) 2 wt. % Au d) 5 wt. % Au and e) 10 wt. % Au. Reaction conditions and ratios as in **Figure 3.31**, added NaOH = 6 mmol (pH = 14).

In order to better decouple the influence of gold from NaOH on the selective oxidation of the aldehyde and the alcohol function in HMF, additional reactions were performed in the same working conditions on 0.1 mmol of HMFCA. Raw reaction profiles are shown in **Figure 3.32**.

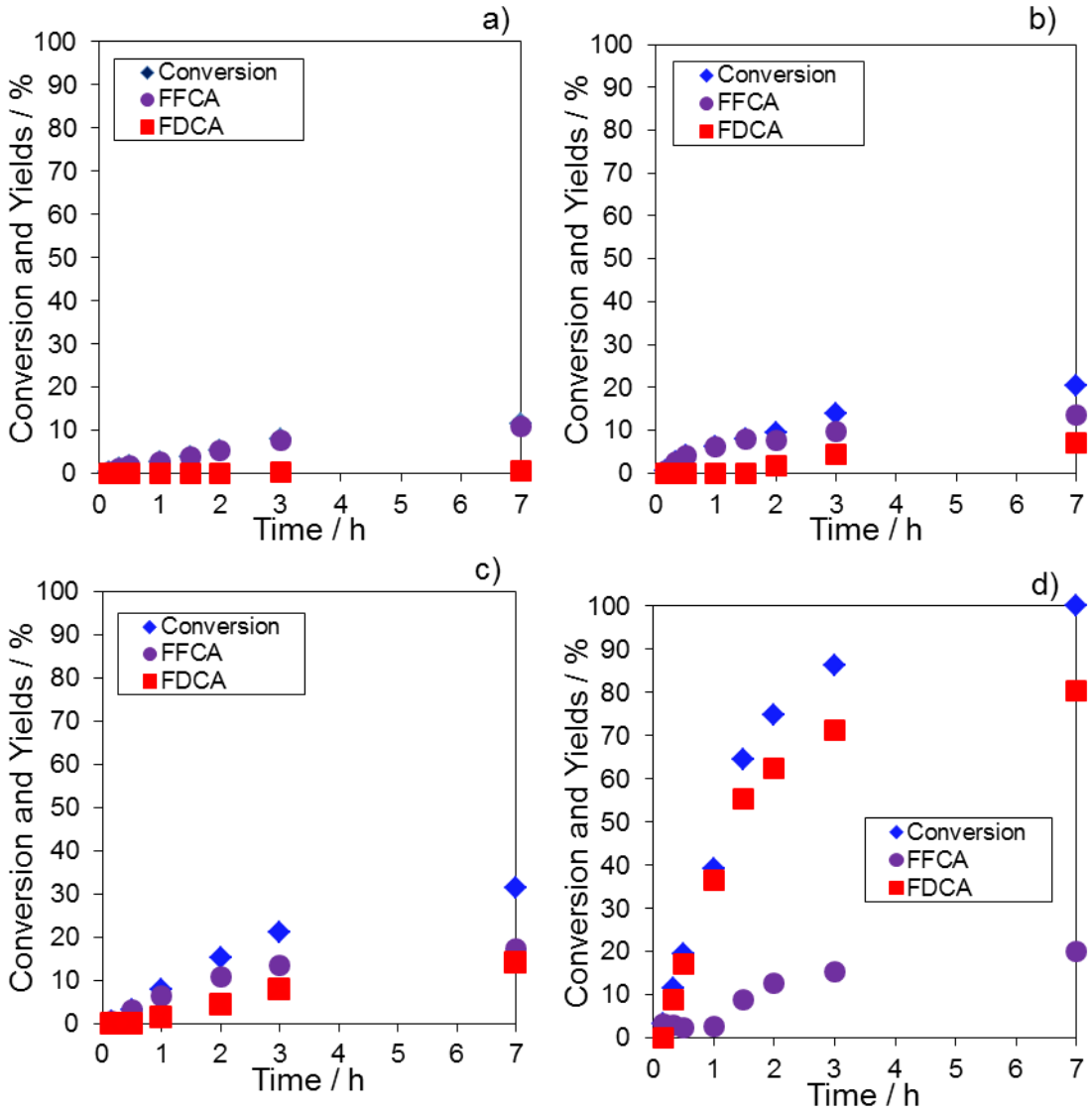
a)
b)
c)
d)
Conversion
FFCA
FDCA
Conversion and Yields / %
Time / h

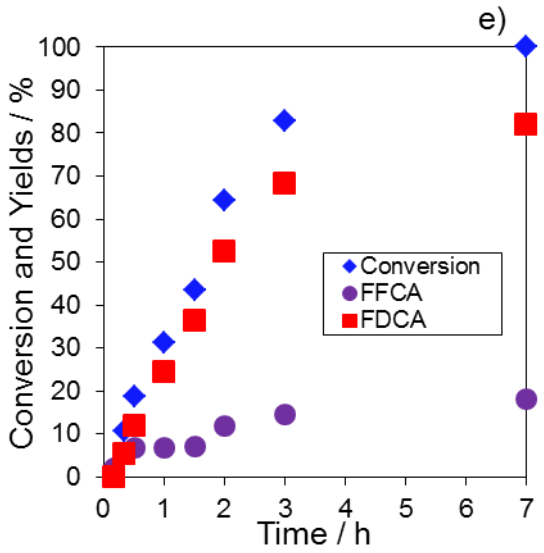

Figure 3.32: reaction profiles for the aerobic selective oxidation of HMFCA using different Au loadings and without extra added base at pH = 9. A) 0.5 wt. % Au, HMFCA/Au = 160 (mol/mol), b) 1 wt. % Au, 80 (mol/mol), c) 2 wt. % Au, 40 (mol/mol), d) 5 wt. % Au, 16 (mol/mol), and e) 10 wt. % Au, 8 (mol/mol). Reaction conditions: 25 mg of catalyst, 0.1 mmol of HMFCA, T = 90 °C, V = 6 ml H_2O and ν O_2 = 15 ml/min.

Also for HMFCA, as the amount of gold increases, conversion and FDCA yields appear to increase, suggesting a positive impact of higher gold loading. The reactions were then repeated in the presence of 6 mmol of NaOH (pH = 14) and all the raw complete reaction profiles are shown in **Figure 3.33**.

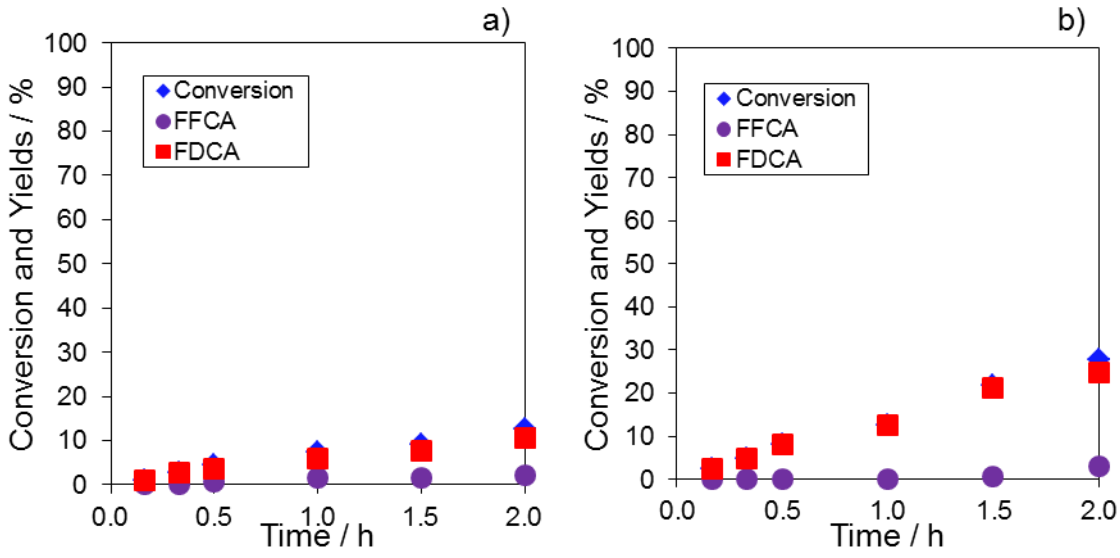

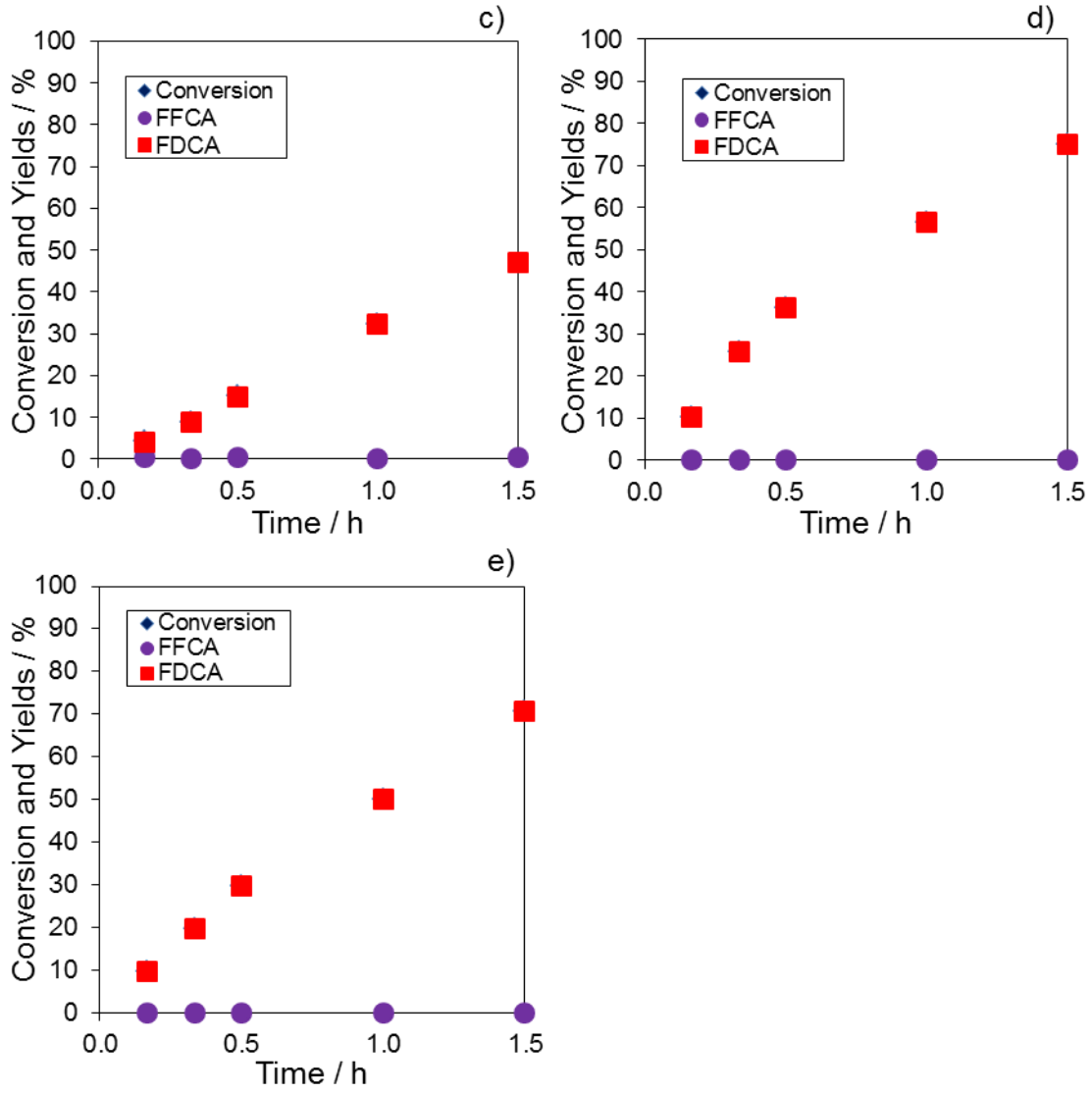

Figure 3.33: reaction profiles for the aerobic selective oxidation of HMFCA using different Au loadings + NaOH at pH = 14. A) 0.5 wt. % Au, b) 1 wt. % Au, c) 2 wt. % Au, d) 5 wt. % Au and e) 10 wt. % Au. Reaction conditions as in **Figure 3.32**, added NaOH = 6 mmol (pH = 14).

A systematic kinetic study to follow any eventual minor impact of NaOH on the conversion of HMF as the gold loading increases was then carried out using an excess of HMF (0.2 mmol instead of 0.1 mmol), in order to slow down the rapid oxidation of HMF to HMFCA. Results for HMF and for HMFCA are shown in **Figure 3.34**, showing 0.5 wt. % Au/HT as the most active catalyst per gram of Au in the presence or absence of NaOH 1M (pH = 14) for the selox of HMF, and showing 5 wt. % Au/HT as the most active for the selox of HMFCA.

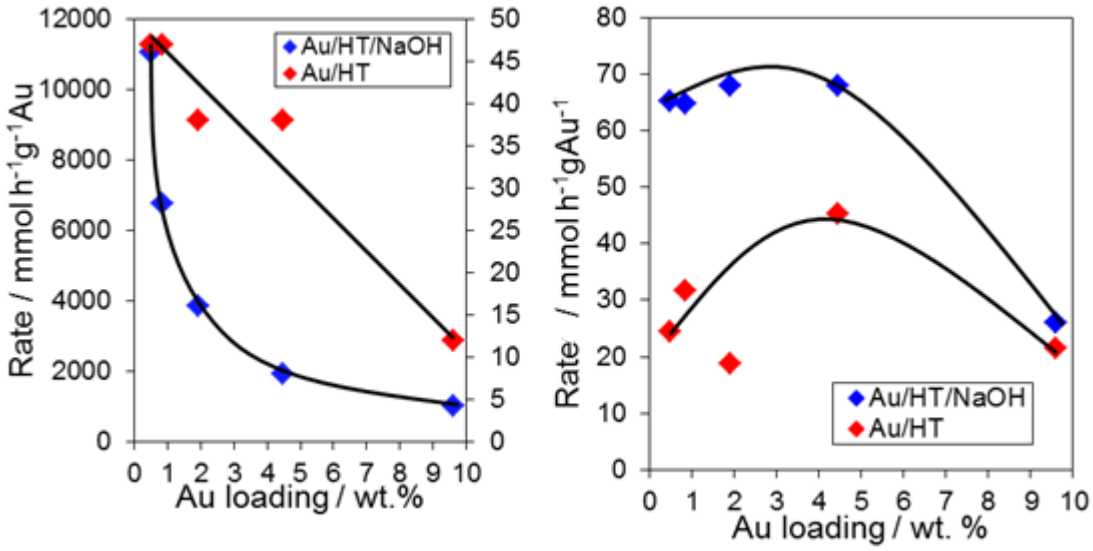

Figure 3.34: left – mass normalised rates of HMF oxidation as a function of Au loading with and without NaOH = 6 mmol (pH = 14) addition. Reaction conditions: 25 mg of catalyst, 0.2 mmol of HMF, T = 90 °C, V = 6 ml H_2O and ν O_2 = 15 ml/min. Right – mass normalised rates of HMFCA oxidation as a function of Au loading with and without NaOH = 6 mmol (pH = 14) addition. Reaction conditions: 25 mg of catalyst, 0.1 mmol of HMFCA, T = 90 °C, V = 6 ml H_2O and ν O_2 = 15 ml/min.

The preceding mass normalised initial rates factor in the total gold present, and hence are only proportional to the density of surface Au active sites. A better parameter for comparing catalyst performance is the Turnover Frequency (TOF), which is problematic for gold since it is hard to implement conventional CO or H_2 chemisorption methods adopted for Platinum Group Metals. A correlation between geometric properties of gold nanoparticles and the bulk amount of gold determined by ICP analysis was therefore used to estimate the Au surface atom density and thereby calculate TOFs. Corma and co-authors[65] estimated the number of external surface Au atoms on the basis of Au mean particle size. In this thesis, the same model is adopted. Assuming that gold nanoparticles can be modelled as an fcc crystal lattice; the number of gold atoms per particle (N_T) was found using the **Equation 3.4:**

$$< d > = 1.105 \times d_{at} \times N_T^{1/3} \qquad \textbf{Equation 3.4}$$

whereas < d > is the mean diameter of gold particle size, determined as an average from XRD, XAS and TEM measurements and d_{at} is the atomic diameter of gold (0.288 nm).

According to the fcc model, one atom is surrounded by 12 neighbour atoms, assuming a full shell close packing model, and N_T is related to the number of shells (m) **(Equation 3.5).** Then, the number of external Au atoms can be estimated using the **Equation 3.6.**

$$N_T = \frac{(10\,m^3 - 15\,m^2 + 11m - 3)}{3} \qquad \textbf{Equation 3.5}$$

$$N_s = 10\,m^2 - 20m + 12 \qquad \textbf{Equation 3.6}$$

$$TOF = \frac{HMF\ rate\ (molecules \times h^{-1})}{n^{\circ}\ of\ Au\ surface\ atoms} \qquad \textbf{Equation 3.7}$$

TOF values were calculated using the **Equation 3.7.** Comotti and co-authors[5] and also Fang and co-authors[66] observed that for particles larger than 6 nm, TOF values deviate from linearity and a sharp cut off is observed above 10 nm. Also in this thesis work the same problem occurred, therefore TOF values were normalised by the fraction of particles below 6 nm, obtained from TEM measurements, and results for Au/HT selox of HMF and HMFCA are shown in **Figure 3.35**.

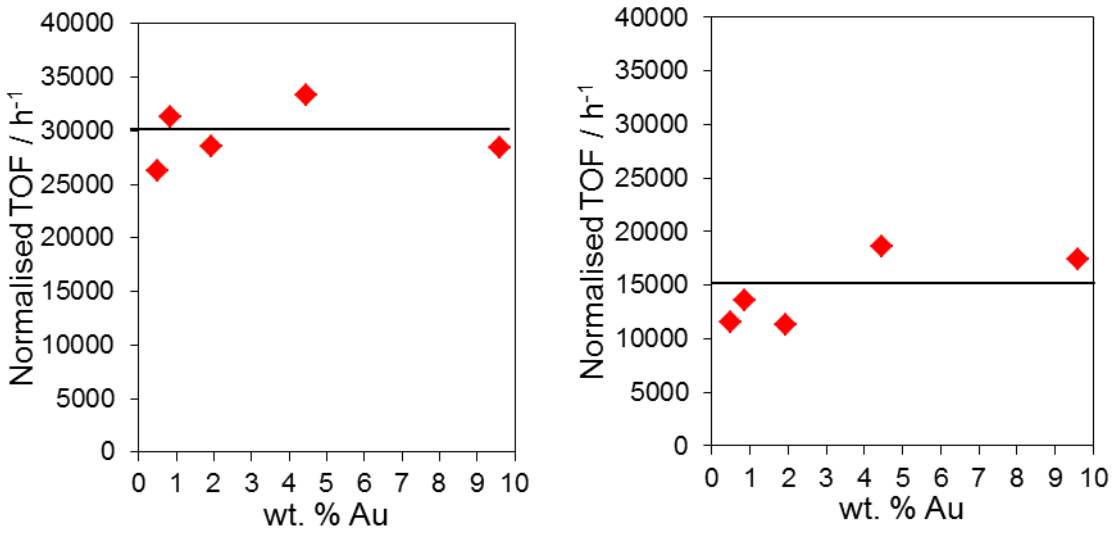

Figure 3.35: left – calculated TOF values for the aerobic selective oxidation of HMF as a function of gold loading, right – TOF values for the aerobic selective oxidation of HMFCA. Reaction conditions: 25 mg of catalyst, 0.2 mmol of HMF, T = 90 °C, V = 6 ml H_2O and ν O_2 = 15 ml/min.

Based on experimental results shown thorough **Chapter 3.2.4.4**, it appears that the overall selective oxidation of HMF to FDCA can be promoted enhancing the rate of surface catalysed geminal diol dehydrogenation in step 1 (HMF/HMFCA) and 3 (FFCA/FDCA) (see **Scheme 3.3** in **Chapter 3.2.4.2**) to corresponding carboxylic acid simply by increasing the gold concentration[50].

Figure 3.36 summarises that higher gold loadings indeed promoted FDCA production (at the expense of HMFCA), with a 78 % yield of the desired dicarboxylic acid, attainable for 10 wt. % Au/HT in the absence of any soluble base[50]. This achievement shows the ability of gold to ameliorate the strong requirement for additional NaOH to drive the two R-CHO oxidation steps (HMF/HMFCA and FFCA/FDCA respectively). It is evident that NaOH rate – enhancements for the selox of HMF fall three-fold as the bulk Au content rises from 0.5 – 10 wt. %, while for the final FFCA oxidation step this enhancement falls 40 – fold over the same gold range.

High FDCA yields are therefore achievable either by using low concentrations of Au in conjunction with a strong soluble base, or high concentrations of Au on a moderate strength solid base.

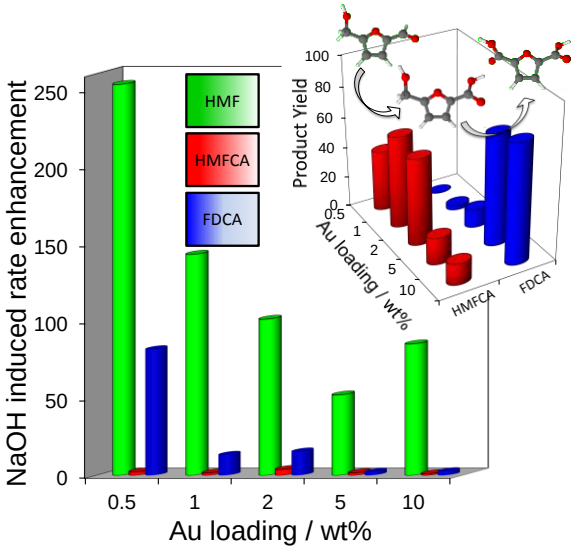

Figure 3.36: (main) impact of Au loading on the sensitivity of individual oxidation steps towards soluble base addition over Au/HT catalysts; (inset) Au loading dependent product selectivity in HMF oxidation in the absence of soluble base. Reaction conditions: 25 mg of catalyst, 0.2 mmol of HMF, T = 90 °C, V = 6 ml H_2O and ν O_2 = 15 ml/min.

3.2.4.5 The effect of $Mg(OH)_2$ and extra added HT on the selective oxidation of HMF

According to Gupta and co-authors[11], a nominal Mg/Al ratio of 5 was declared for the best hydrotalcite chosen as the support for Au NPs but, as shown by Vegard's law in **Chapter 3.2.3.2**, this value is outside the accepted limits for pure phase HT[17]. The following series of experiments was carried out to understand if Gupta's hydrotalcites were affected by contaminations, due to the precipitation and segregation of $Mg(OH)_2$ brucite. The same batch of catalyst used for the tests described in **Chapter 3.3.1** was run with or without the addition of different amounts of $Mg(OH)_2$ from 1 to 4 times the total amount of Mg in the hydrotalcite. **(Figure 3.37).**

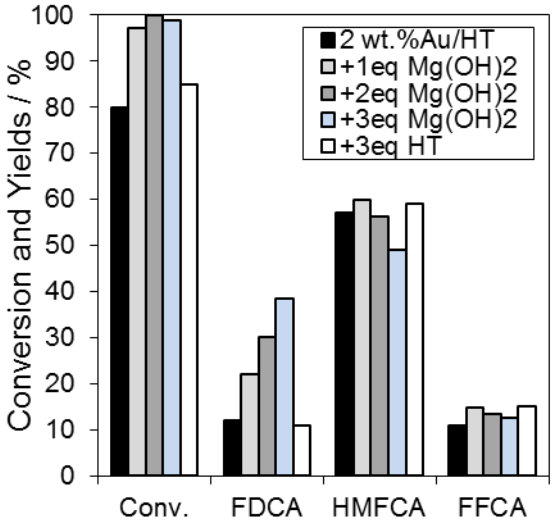

Figure 3.37: the minor impact of extra added HT (+ 75 mg) or $Mg(OH)_2$ (+ 17.5, + 49.8 or + 67.5 mg) on the aerobic selective oxidation of HMF after 7 h. Reaction conditions: 25 mg of catalyst, 0.1 mmol of HMF, T = 90 °C, V = 6 ml H_2O and ν O_2 = 15 ml/min.

Even if the addition of $Mg(OH)_2$ improved both the conversion and the FDCA yield, this enhancement was not as significant as the one obtained with NaOH. The measured pH for all the different quantities of added $Mg(OH)_2$ was 10, as expected by its limited solubility ($K_{ps} = 1.5 \times 10^{-11}$), and this provided further evidence of the effect of pH on this reaction.

The addition of extra hydrotalcite to the catalyst did not improve the conversion or FDCA yield. The pH was found to be always 9, independent by the amount of added

HT, as expected. A blank test with only parent hydrotalcite was performed for the aerobic selective oxidation of HMF and no conversion was obtained.

3.2.4.6 Leaching study

The Sheldon test[67] consists in a hot filtration of the heterogeneous catalyst to determine if, after its removal, any homogeneous contributes affect the reaction and it was performed in the following conditions: 0.1 mmol of HMF, 6 ml H_2O, 25 mg of 2 wt. % Au/HT and 15 ml/min O_2 at T = 90 °C and 500 rpm. Samples were taken and, after 1 h, the hot mixture was filtered off and the catalyst was removed. The reaction was left on-going for other two h, but no reaction occurred in the absence of catalyst, suggesting that Au nanoparticles do not leach from the support to the homogeneous phase. When the catalyst was added back to the reaction, the conversion restarted and results are shown in **Figure 3.38.**

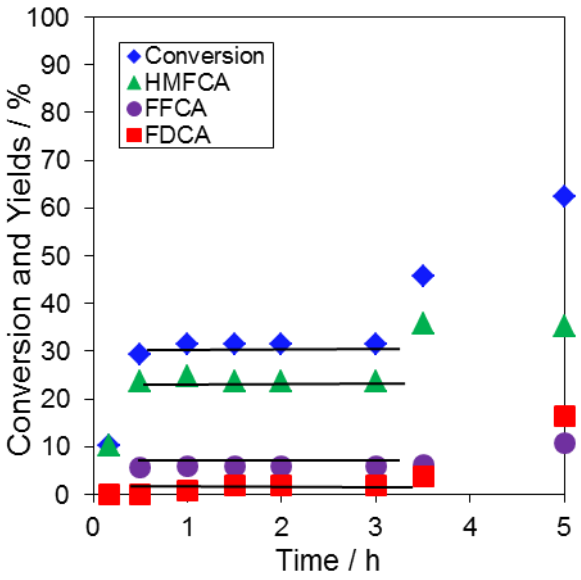

Figure 3.38: Sheldon test showing no reaction after the removal of the catalyst and its restart once that the catalyst was re-added. Reaction conditions: 0.1 mmol of HMF, 6 ml of H_2O, 25 mg of 2 wt. % Au/HT and 15 ml/min O_2, at T = 90 °C and 500 rpm.

The reaction was repeated in the same conditions in parallel, pH was monitored for all the 7 h, showing that it dropped down from 9 to 6.5 during the reaction. ICP analysis was thus carried out to look for Mg, Al and Au in the liquid phase after the filtration. No significant Au and Al was found, 0.012 and 0.029 ppm respectively, but a

Mg leach was detected to be 19 % of the initial amount, suggesting that it might react with formed FDCA, permanently removing Mg as FDCA salts.

The catalyst was then filtered off, washed several times with H_2O, dried in the oven overnight at T = 100 °C, recovered, calcined at 200 °C in oxygen to be reactivated and re-used for three times. Results are shown in **Figure 3.39.** The catalyst maintained activity after three catalytic tests, after thermal treatment prior to re-use, and decreases in yields and selectivity were attributed to the already discussed loss of Mg and of basicity.

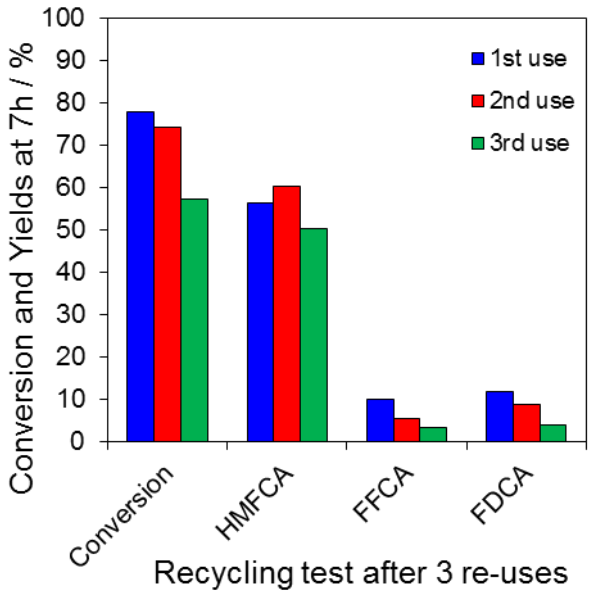

Figure 3.39: recycling test for the aerobic selection of HMF, catalyst 2 wt. % Au/HT at 200 °C. The activity was maintained after three catalytic tests. Reaction conditions: 1st test) 0.6 mmol of HMF, 36 ml of H_2O, 151 mg of 2 wt. % Au/HT. 2nd test) 0.3 mmol of HMF, 18 ml of H_2O, 78 mg of 2 wt. % Au/HT. 3rd test) 0.1 mmol of HMF, 6 ml of H_2O, 25 mg of 2 wt. % Au/HT; all reactions were carried out at T = 90 °C, 15 ml/min O_2 and 500 rpm.

3.2.4.7 EDX and XPS elemental analysis on the spent catalyst

To further understand the effect and the importance of NaOH and high pH on the deactivation of the catalyst, EDX elemental analysis was run on the spent and on the fresh catalysts **(Table 3.7)**, showing that for Na-free HT, a minor leaching of Mg occurs after the reaction. The loss of added NaOH forms the disodic salt of FDCA and prevents Mg leaching.

Table 3.7: comparison between EDX on Na-free fresh catalyst and all the exhausted ones, all data in wt. %.

	Na-Free fresh	Na-Free spent	Na/Mg 0.1	Na/Mg 1	Na/Mg 5	Na/Mg 10	Na/Mg 20
C	10.50	11.83	12.18	8.96	8.59	19.10	6.91
O	59.32	56.97	55.48	59.53	59.46	55.39	57.12
Na	0	0	0.03	0.54	1.74	2.24	6.70
Mg	21.40	21.44	22.29	21.50	21.03	16.53	20.18
Al	7.77	8.64	8.70	8.37	8.26	6.11	7.63
Au	0.97	1.11	1.35	1.08	0.94	0.63	1.45
Mg/Al	2.75	2.48	2.56	2.57	2.54	2.65	2.64

3.2.4.8 Order of reaction and Arrhenius parameters

The selective oxidations of HMF and HMFCA were studied and compared using 25 mg of 0.5, 1, 2, 5 and 10 wt. % Au/HT, in the reaction conditions previously described, in order to find the order of reaction in gold. Plots of the logarithm of initial rates vs. logarithm of gold concentration **(Figure 3.40)** show a linear increase for the first four points and a slope of 1, corresponding to first order of reaction in gold. For catalysts having 10 wt. % of gold, the regime is not linear anymore, suggesting that not all gold but exclusively surface Au atoms participate to the reaction[5], as already discussed in **Chapter 3.2.4.4.**

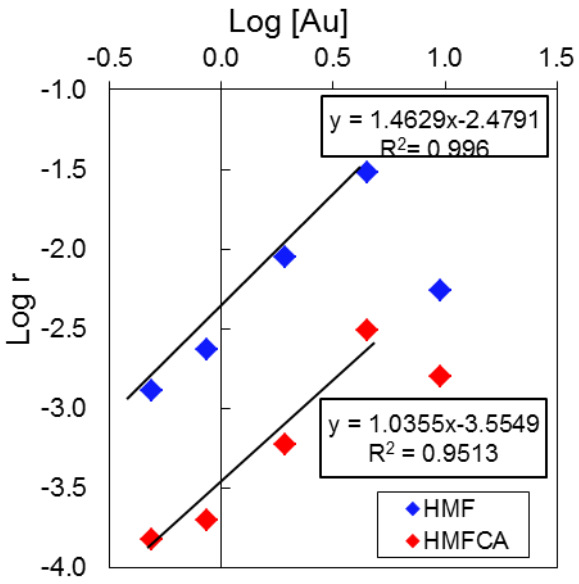

Figure 3.40: order of reaction in gold for the aerobic selective oxidation of HMF (blue) and HMFCA (red). Reaction conditions: 0.1 mmol of HMF, 6 ml of H_2O, 25 mg of catalyst; all reactions were carried out at T = 90 °C, 15 ml/min O_2 and 500 rpm.

To find the order of reaction in HMF, 25 mg of 2 wt. % Au were tested for different quantities of HMF, respectively 0.1, 0.2 and 0.5 mmol, and the relative rate constants were found. A plot of the logarithm of HMF concentrations vs. logarithm of relative rates of reaction **(Figure 3.41)** has shown an order of reaction 1 for HMF.

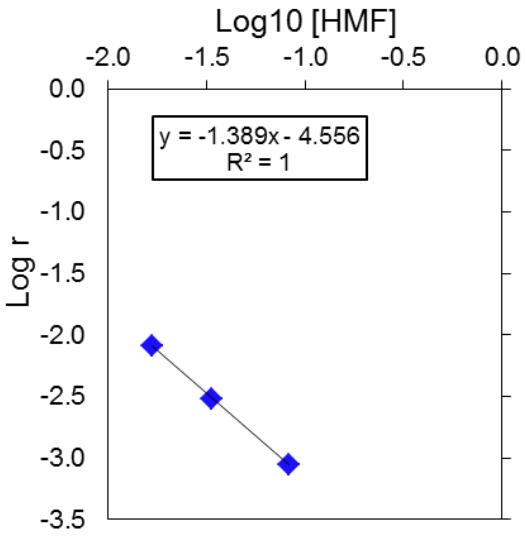

Figure 3.41: aerobic selective oxidation of HMF over Au/HT catalysts, an order of reaction of 1 was found for HMF. Reaction conditions: 0.1, 0.2 or 0.5 mmol of HMF, 6 ml of H_2O, 25 mg of catalyst, T = 90 °C, 15 ml/min O_2 and 500 rpm.

A Parr autoclave was used to find the order of reaction in O_2, the reaction was carried out at 1, 5 and 10 atm. A logarithm plot of the O_2 pressure vs. logarithm of relative rates of reaction **(Figure 3.42)** has shown an order of reaction of 0.5 for O_2, which is consistent with slow activation of oxygen by gold.

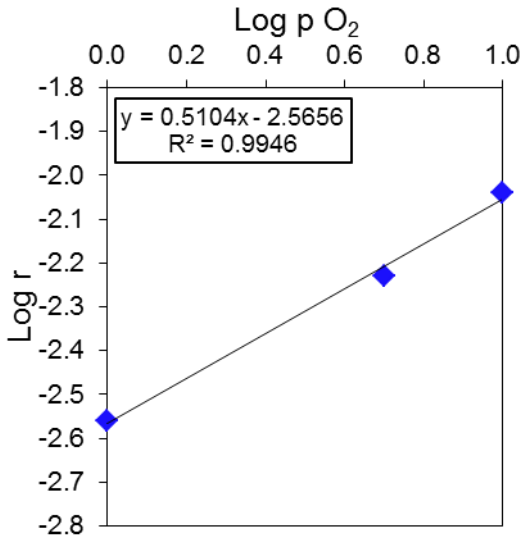

Figure 3.42: a fractionary order of reaction in O_2 for the aerobic selox of HMF over Au/HT catalysts. Reaction conditions: 1 mmol of HMF, 60 ml of H_2O, 250 mg of catalyst, T = 90 °C, 500 rpm and different pO_2 (1, 5 or 10 atm).

To find the Arrhenius activation energy E_a for the selective oxidation of HMF and HMFCA, 25 mg of 2 wt. % Au were tested with 0.1 mmol of HMF or HMFCA, at different reaction temperatures, respectively 25, 40, 60 and 90 °C. Kinetic constants[68] were determined and a plot of the logarithm of k HMF or k HMFCA vs. 1/T **(Figure 3.43)** has given E_a = 32 kJ mol^{-1} for the selox of HMF and E_a = 40 kJ mol^{-1} for the selox of HMFCA; these values agree with what reported by Davis and co-authors[16], even if in this thesis work a higher difference between the alcohol and the aldehyde was found, confirming that the activation of the alcohol is the rate-determining step[50, 58, 64].

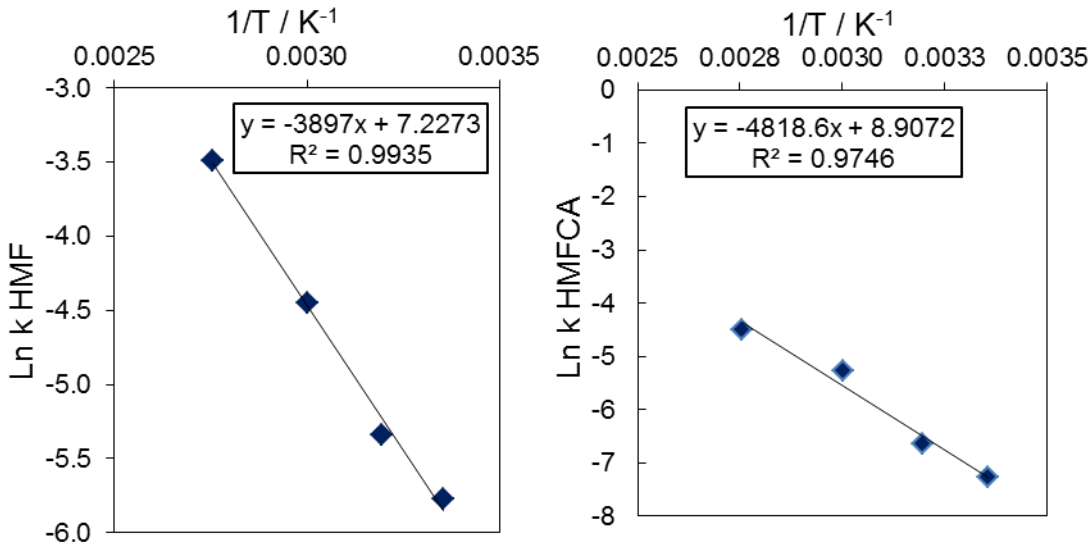

Figure 3.43: Arrhenius E_a for the selox of HMF (left) and for the selox of HMFCA (right). Reaction conditions: 0.1 mmol of HMF, 25 mg of 2 wt. % Au/HT at 200 °C catalyst, V = 6 ml H_2O, 500 rpm and ν O_2 = 15 ml/min. T = 25, 40, 60 or 90 °C.

3.2.5 Proposed reaction pathway

Following the discussion through this Chapter, high FDCA yields have been proved to be achievable either by using low concentrations of Au and a strong soluble base, such as NaOH, or high concentrations of Au on a moderate strength solid base, such as hydrotalcite.

The proposed explanation[50] for the loading dependence of these two catalytic regimes (soluble base ≤ 2 wt. % Au ≤ solid base) is the competitive adsorption between HMF and HMFCA. The HMF:surface Au molar ratio approaches 60:1 for the 0.5 wt. % Au/HT catalyst, hence it is unlikely that the low concentration of gem-diol formed without NaOH can effectively compete for adsorption sites over gold nanoparticles.

NaOH addition promotes and accelerates gem-diol formation[12, 16, 58, 69] from HMF in solution, displacing the HMF adsorption equilibrium and liberating reactive gold surface site for both geminal diol dehydrogenation to HMFCA, and subsequent OH^- mediated oxidative dehydrogenation of HMFCA to FFCA and FFCA hydration/dehydrogenation to FDCA.

In contrast, the HMF:surface Au molar ratio is only 5:1 for the 10 wt. % Au/HT catalyst, and the geminal diol may face significantly less competition from HMF for

vacant gold sites. These hypotheses are supported by the strong non-linear dependence of FDCA production on HMF conversion **(Figure 3.44** main**).** FDCA production requires a threshold HMF conversion > 80 %, indicating that high concentrations of reactively-formed HMFCA, that comes from the first oxidation step, are necessary to compete effectively with unreacted HMF for subsequent oxidation.

FDCA production via the direct aerobic oxidation of HMFCA is, instead, near quantitative and increases linearly with surface Au concentration/conversion, as anticipated for a structure-insensitive reaction in which the reactant coverage is low (weak adsorption or rapid reaction).

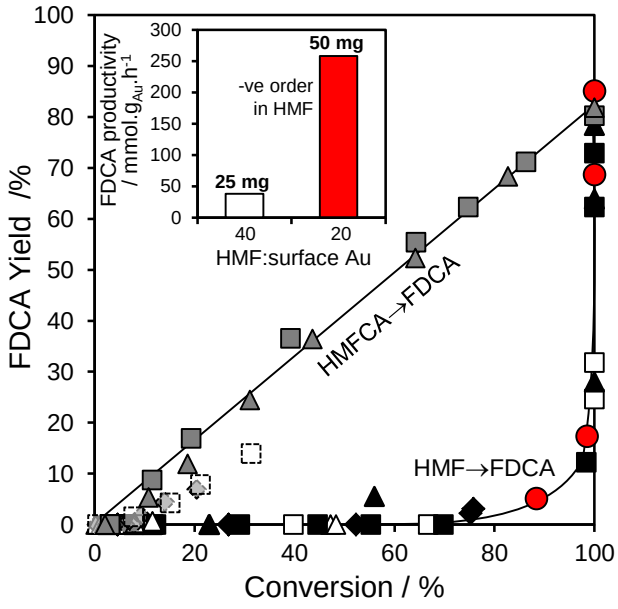

Figure 3.44: FDCA yield as a function of HMF (HMFCA) conversion over 25 mg △ (◬) 0.5 wt. %, ◆(◆) 1 wt. %, □ (⬚) 2 wt. %, ■(■) 5 wt. %, and ▲(▲) 10 wt. % Au/HT catalysts, and 50 mg (●) 2 wt. % Au/HT. Inset shows the FDCA productivity as a function of HMF:surface Au molar ratio for 2 wt. % Au/HT.

Further evidence that strong HMF adsorption site-blocks oxidation of its reactively-formed products is apparent in **Figure 3.44** inset, wherein the HMF:surface Au ratio was varied for the 2 wt. % Au/HT catalyst. In the absence of diffusion limitations, and the presence of available reaction sites, the mass normalised FDCA productivity should be independent of substrate:catalyst ratio, whereas **Figure 3.44** inset reveals that halving the HMF:surface Au ratio imparts a seven-fold increase in FDCA productivity. Reactive gold sites for HMFCA oxidation only become available

for HMF:surface Au ratios below a critical threshold wherein it can effectively compete with adsorption of the parent HMF.

3.3 Conclusions

Hydrotalcites having Mg/Al = 3 molar ratio were prepared using an alkali-free method *via* co-precipitation route. A series of different gold wt. % catalysts were supported on them using the deposition precipitation method and calcined at 200 °C.

Catalysts were tested for the aerobic selective oxidation of HMF to FDCA before or after the addition of an excess of NaOH 1M solution. On increasing of pH, conversion and FDCA yields improved and the reaction was found to be pH-dependent, being the oxidation of alcohol the rate-determining step.

Hydroxide ions facilitate both the activation of the aldehyde function and the initial deprotonation of alcohols, which are well-known to be weak acids (pKa = 14–18), since a gold catalyst, by itself, cannot deprotonate the hydroxyl group of alcohols. The order of reaction for gold, for HMF and for oxygen were experimentally determined and the Arrhenius parameters explained why alcohols react slower than aldehydes under these working conditions, being $E_{a\ R–OH} > E_{a\ R–CHO}$.

The combination of *operando* XAS and detailed kinetic mapping has elucidated the nature of the active sites and mechanism of Au catalysed HMF aerobic selox to FDCA. A delicate balance is revealed between the rate of base catalysed HMF activation and the latter's self-poisoning of requisite metallic gold sites for subsequent oxidation of reactively-formed HMFCA/FFCA intermediates. Hydrotalcite solid base can only drive HMF selox in concert with high concentrations of surface gold, a discovery that has important implications for gold catalysis and cascade oxidations.

3.4 Appendix

It is worth remembering that softwares consider NMR predictions in $CDCl_3$, but D_2O was used in this thesis work to have NaOD. Differences between predictions and experimental data are explained in each spectra below. Spectra prediction was obtained using ChemDraw 12.

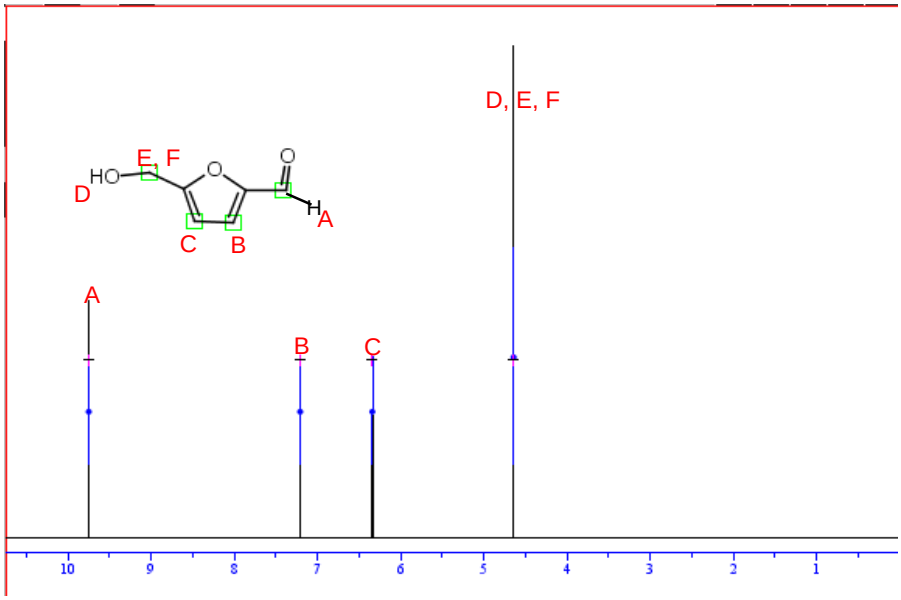

Figure 3a.1: predicted ^1H NMR spectra of HMF. δ_H: A) 9.74 ppm (s, 1H, –CHO); B) 7.20 ppm (d, 1H, aromatic –CH near R–CHO, J = 3.477), C) 6.33 ppm (d, 1H, aromatic –CH near R–OH, J = 3.48); D) 4.64 ppm (s, 1H, –OH); E, F) 4.5 ppm (s, 2H, R–CH_2). Minor shifts appear in experimental data, run in D_2O.

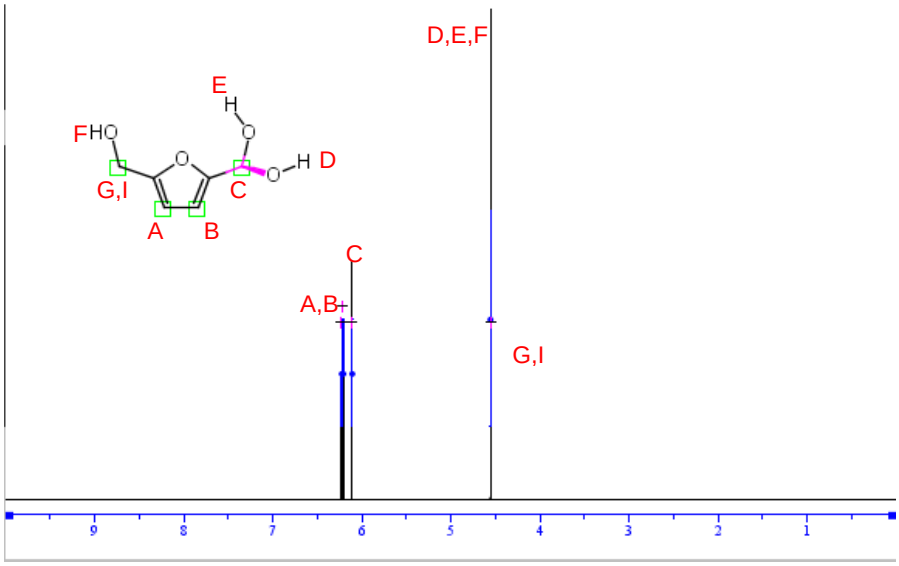

Figure 3a.2: predicted ^{1}H NMR spectra of HMF gem-diol. δ_H: A, B) 6.22 ppm (d, 2H, aromatic –CH, J = 3.46), C) 6.11 ppm (s, 1H, aldehyde that became gem-diol); D, E, F) 4.7 ppm (s, 3H, –OH); G, I) 4.5 ppm (s, 2H, R–CH_2). In D_2O –OH exchange with water.

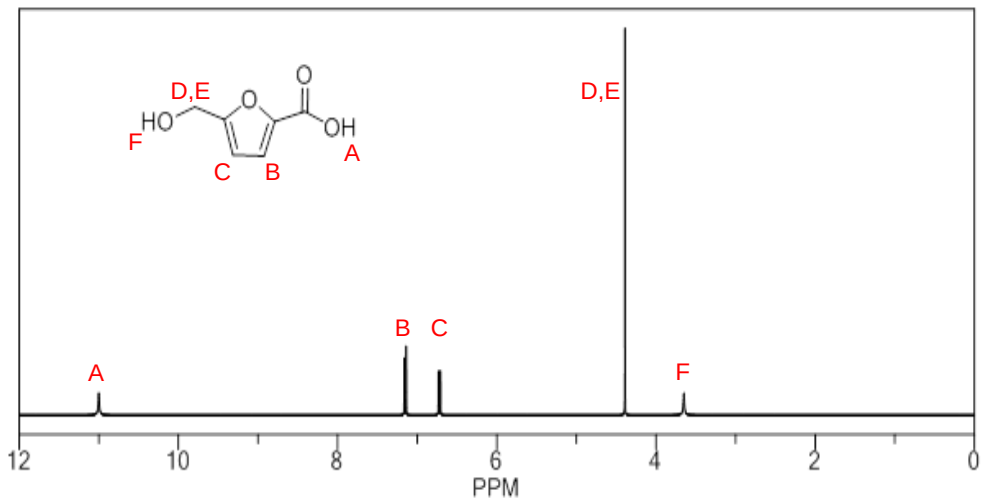

Figure 3a.3: predicted ^{1}H NMR spectra of HMFCA. δ_H: A) 11.0 ppm (s, 1H, R–COOH, B) 7.15 ppm (d, 1H, aromatic –CH near aldehyde, J = 7.5), C) 6.72 ppm (d, 1H, aromatic –CH near alcohol, J = 7.5); D, E) 4.39 ppm (s, 2H, R–CH_2); F) 3.65 ppm (s, 1H, –OH). In D_2O –OH and –COOH exchange with water.

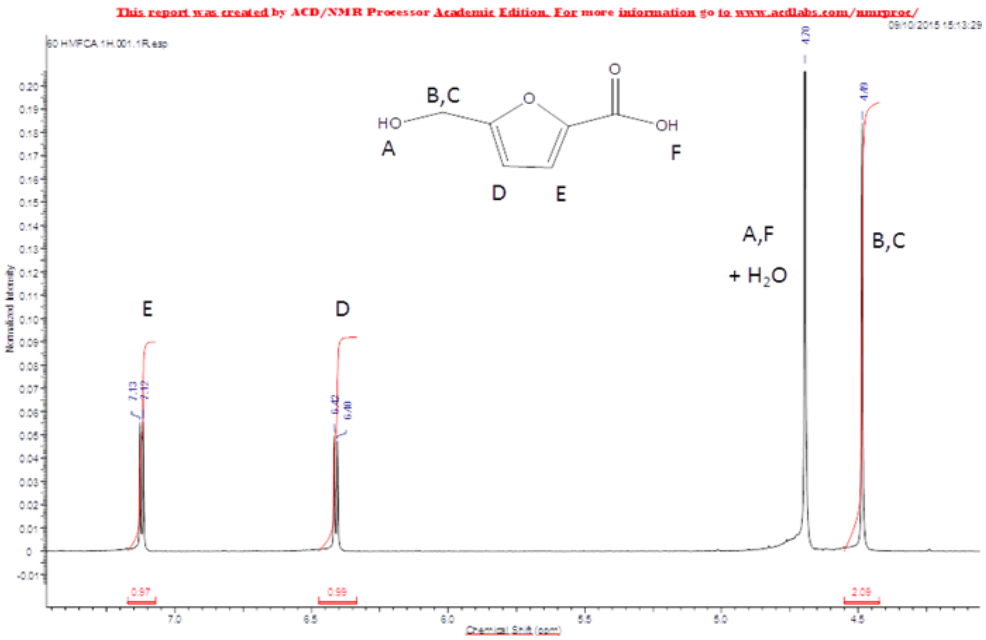

Figure 3a.4: ^{1}H NMR spectra of HMFCA standard. δ_H (300 MHz, D_2O): A, F) 4.70 ppm (s, 2H, R–OH and R–COOH; B, C) 4.49 ppm (s, 2H, R–CH_2), D) 6.42 ppm (d, 1H, aromatic –CH near alcohol, J = 7.52); E) 7.13 ppm (d, 1H, aromatic –CH near carboxylic acid, J = 7.52). In D_2O –OH and –COOH exchange with water.

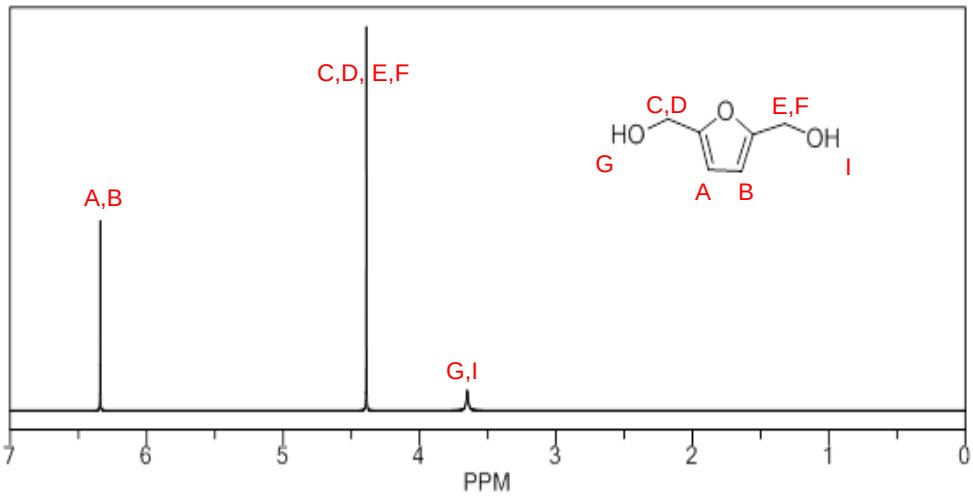

Figure 3a.5: predicted ^{1}H NMR spectra of DHMF. δ_H: A, B) 6.34 ppm (s, 2H, aromatic –CH) C, D, E, F) 4.39 ppm (s, 4H, R–CH_2) G, I) 3.65 ppm (s, 1H, –OH). In D_2O –OH and –COOH exchange with water.

3.5 References

1. A. F. Lee, C. V. Ellis, K. Wilson and N. S. Hondow, *Catalysis Today*, 2010, **157**, 243-249.
2. L. Prati and M. Rossi, *Journal of Catalysis*, 1998, **176**, 552-560.
3. M. Comotti, C. D. Pina and M. Rossi, *Journal of Molecular Catalysis A: Chemical*, 2006, **251**, 89-92.
4. M. Comotti, C. Della Pina, E. Falletta and M. Rossi, *Journal of Catalysis*, 2006, **244**, 122-125.
5. M. Comotti, C. Della Pina, R. Matarrese and M. Rossi, *Angewandte Chemie International Edition*, 2004, **43**, 5812-5815.
6. B. N. Zope, D. D. Hibbitts, M. Neurock and R. J. Davis, *Science*, 2010, **330**, 74-78.
7. C. L. Bianchi, S. Biella, A. Gervasini, L. Prati and M. Rossi, *Catal Lett*, **85**, 91-96.
8. Y. Y. Gorbanev, S. K. Klitgaard, J. M. Woodley, C. H. Christensen and A. Riisager, *ChemSusChem*, 2009, **2**, 672-675.
9. N. Dimitratos, A. Villa, C. L. Bianchi, L. Prati and M. Makkee, *Applied Catalysis A: General*, 2006, **311**, 185-192.
10. O. Casanova, S. Iborra and A. Corma, *ChemSusChem*, 2009, **2**, 1138-1144.
11. N. K. Gupta, S. Nishimura, A. Takagaki and K. Ebitani, *Green Chemistry*, 2011, **13**, 824-827.
12. S. E. Davis, B. N. Zope and R. J. Davis, *Green Chemistry*, 2012, **14**, 143-147.
13. G. L. Brett, Q. He, C. Hammond, P. J. Miedziak, N. Dimitratos, M. Sankar, A. A. Herzing, M. Conte, J. A. Lopez-Sanchez, C. J. Kiely, D. W. Knight, S. H. Taylor and G. J. Hutchings, *Angewandte Chemie*, 2011, **123**, 10318-10321.
14. S. E. Davis, B. N. Zope, R. J. Davis, *Topics in Catalysis*, 2012, **55**, 24-32.
15. S. Carrettin, P. McMorn, P. Johnston, K. Griffin, C. J. Kiely and G. J. Hutchings, *Physical Chemistry Chemical Physics*, 2003, **5**, 1329-1336.
16. S. E. Davis, A. D. Benavidez, R. W. Gosselink, J. H. Bitter, K. P. de Jong, A. K. Datye and R. J. Davis, *Journal of Molecular Catalysis A: Chemical*, 2014, **388–389**, 123-132.
17. F. Cavani, F. Trifirò and A. Vaccari, *Catalysis Today*, 1991, **11**, 173-301.
18. M. J. Climent, A. Corma, S. Iborra, K. Epping and A. Velty, *Journal of Catalysis*, 2004, **225**, 316-326.
19. A. Vaccari, *Catalysis Today*, 1998, **41**, 53-71.
20. D. G. Cantrell, L. J. Gillie, A. F. Lee and K. Wilson, *Applied Catalysis A: General*, 2005, **287**, 183-190.
21. J. J. Woodford, J.-P. Dacquin, K. Wilson and A. F. Lee, *Energy & Environmental Science*, 2012, **5**, 6145-6150.
22. S. K. Sharma, P. K. Kushwaha, V. K. Srivastava, S. D. Bhatt and R. V. Jasra, *Industrial & Engineering Chemistry Research*, 2007, **46**, 4856-4865.
23. P. Liu, Y. Guan, R. A. v. Santen, C. Li and E. J. M. Hensen, *Chemical Communications*, 2011, **47**, 11540-11542.
24. P. Scherrer, *Nachr. Ges. Wiss. Göttingen*, 1918, **26**, 98-100.
25. C. Shimou, L. Yaodong and W. Guozhong, *Nanotechnology*, 2005, **16**, 2360.
26. E. Genty, R. Cousin, C. Gennequin, S. Capelle, A. Aboukaïs and S. Siffert, *Catalysis Today*, 2011, **176**, 116-119.

27. F. Basile, G. Fornasari, M. Gazzano and A. Vaccari, *Applied Clay Science*, 2000, **16**, 185-200.
28. V. Rives, *Materials Chemistry and Physics*, 2002, **75**, 19-25.
29. G. W. Brindley and S. Kikkawa, *American Mineralogist*, 1979, **64**, 836-843.
30. A. R. Denton and N. W. Ashcroft, *Physical Review A*, 1991, **43**, 3161-3164.
31. S. Miyata, *Clays and Clay minerals*, 1980, **28**, 50-56.
32. P. Kuśtrowski, L. Chmielarz, E. Bożek, M. Sawalha and F. Roessner, *Materials Research Bulletin*, 2004, **39**, 263-281.
33. E. P. Barrett, L. G. Joyner and P. P. Halenda, *Journal of the American Chemical Society*, 1951, **73**, 373-380.
34. K. S. W. Sing, L. Moscou, R. A. Pierotti, J. Roquerol and T. Siemieniewska., *Pure Appl. Chem.*, 1985, **57**, 603-619.
35. J. W. McBain, *Journal of the American Chemical Society*, 1935, **57**, 699-700.
36. Y. Xi and R. J. Davis, *Journal of Catalysis*, 2009, **268**, 307-317.
37. P. Kowalczyk, A. P. Terzyk, P. A. Gauden, R. Leboda, E. Szmechtig-Gauden, G. Rychlicki, Z. Ryu and H. Rong, *Carbon*, 2003, **41**, 1113-1125.
38. Q. Wang, Z. Wu, H. H. Tay, L. Chen, Y. Liu, J. Chang, Z. Zhong, J. Luo and A. Borgna, *Catalysis Today*, 2011, **164**, 198-203.
39. S. Abelló, F. Medina, D. Tichit, J. Pérez-Ramírez, X. Rodríguez, J. E. Sueiras, P. Salagre and Y. Cesteros, *Applied Catalysis A: General*, 2005, **281**, 191-198.
40. I. Melian-Cabrera, M. Lopez Granados and J. L. G. Fierro, *Physical Chemistry Chemical Physics*, 2002, **4**, 3122-3127.
41. J. I. Di Cosimo, V. K. Díez, M. Xu, E. Iglesia and C. R. Apesteguía, *Journal of Catalysis*, 1998, **178**, 499-510.
42. A. K.-V. Alexander V. Naumkin, Stephen W. Gaarenstroom, and Cedric J. Powell, *NIST X-ray Photoelectron Spectroscopy Database, Version 4.1 (National Institute of Standards and Technology, Gaithersburg, 2012); http://srdata.nist.gov/xps/*.
43. J. J. Creasey, A. Chieregato, J. C. Manayil, C. M. A. Parlett, K. Wilson and A. F. Lee, *Catalysis Science & Technology*, 2014.
44. J. Radnik, C. Mohr and P. Claus, *Physical Chemistry Chemical Physics*, 2003, **5**, 172-177.
45. X. Chen, W. Chu, D. Chen, Z. Wu, A. Marcelli and Z. Wu, *Chemical Geology*, 2009, **268**, 74-80.
46. P. Haider and A. Baiker, *Journal of Catalysis*, 2007, **248**, 175-187.
47. R. Zanella, L. Delannoy and C. Louis, *Applied Catalysis A: General*, 2005, **291**, 62-72.
48. I. V. Mironov, *Russ. J. Inorg. Chem.*, 2008, **53**, 655-659.
49. S. Ivanova, C. Petit and V. Pitchon, *Applied Catalysis A: General*, 2004, **267**, 191-201.
50. L. Ardemani, G. Cibin, A. J. Dent, M. A. Isaacs, G. Kyriakou, A. F. Lee, C. M. A. Parlett, S. A. Parry and K. Wilson, *Chemical Science*, 2015, **6**, 4940-4945.
51. C. K. Costello, J. Guzman, J. H. Yang, Y. M. Wang, M. C. Kung, B. C. Gates and H. H. Kung, *The Journal of Physical Chemistry B*, 2004, **108**, 12529-12536.
52. C. Shang and Z.-P. Liu, *Journal of the American Chemical Society*, 2011, **133**, 9938-9947.
53. A. W. Hull, *Physical Review*, 1921, **17**, 571-588.
54. A. Jentys, *Physical Chemistry Chemical Physics*, 1999, **1**, 4059-4063.
55. K. R. Vuyyuru and P. Strasser, *Catalysis Today*, 2012, **195**, 144-154.
56. J. G. Clayden, N.; Warren, S. and Wothers, P., *Oxford* 2001.

57. M. Comotti, C. Della Pina, E. Falletta and M. Rossi, *Advanced Synthesis & Catalysis*, 2006, **348**, 313-316.
58. C. Della Pina, E. Falletta, L. Prati and M. Rossi, *Chemical Society Reviews*, 2008, **37**, 2077-2095.
59. P. J. Hore, *Oxford Chemistry Primers*, 1995, **32**.
60. A. D. Bain, *Progress in Nuclear Magnetic Resonance Spectroscopy*, 2003, **43**, 63-103.
61. E.-S. Kang, D. W. Chae, B. Kim and Y. G. Kim, *Journal of Industrial and Engineering Chemistry*, 2012, **18**, 174-177.
62. S. K. R. Patil, J. Heltzel and C. R. F. Lund, *Energy & Fuels*, 2012, **26**, 5281-5293.
63. P. Y. Nikolov and V. A. Yaylayan, *Journal of Agricultural and Food Chemistry*, 2011, **59**, 10104-10113.
64. S. Biella, L. Prati and M. Rossi, *Journal of Molecular Catalysis A: Chemical*, 2003, **197**, 207-212.
65. A. Abad, A. Corma and H. García, *Chemistry – A European Journal*, 2008, **14**, 212-222.
66. W. Fang, J. Chen, Q. Zhang, W. Deng and Y. Wang, *Chemistry – A European Journal*, 2011, **17**, 1247-1256.
67. A. Corma, D. Das, H. García and A. Leyva, *Journal of Catalysis*, 2005, **229**, 322-331.
68. H. Tsunoyama, H. Sakurai, Y. Negishi and T. Tsukuda, *Journal of the American Chemical Society*, 2005, **127**, 9374-9375.
69. C. D. Pina, E. Falletta and M. Rossi, *Chemical Society Reviews*, 2012, **41**, 350-369.

Chapter 4

Impact of thermal processing on Au/hydrotalcite catalysed oxidation of 5-HMF

List of contents

4.1 Introduction

Calcination of hydrotalcites at temperatures between 450–500 °C is known to result in the loss of interlayer carbonate anions and the concomitant formation of mixed metal oxides[1-4]. Subsequent rehydration of such mixed metal oxides can promote re-regeneration of the parent layered double hydroxide structure, the so-called "memory effect"[4-8], in which hydroxide anions replace the original carbonates within the interlayers, provided that the calcination temperature remains below around 550 °C[9]. Rehydration of thermally generated periclase-like Mg-(Al)-O is critical for the production of Brønsted base sites within hydrotalcites and their associated solid base catalysis[10-13].

Our group has previously demonstrated the utility of calcined-rehydrated hydrotalcites as solid bases for the transesterification of triglycerides in biodiesel production,[14-15] however the corresponding 48 h vapour phase rehydration protocol is time-consuming, and the impact of calcination temperature on base properties has not been systematically investigated to date[16].

In this chapter, a 2 wt. % Au/HT material prepared as described in **Chapter 3** (200 °C calcination without rehydration) has therefore been compared with analogues prepared at different calcination temperatures between 300-500 °C wherein mixed Mg_3Al oxides are expected to form in order to identify the optimal calcination temperature. The effect of gold loading and attendant catalytic 5-HMF oxidation was subsequently studied over this optimal hydrotalcite.

Alternative rehydration strategies were then assessed in terms of their effect upon hydrotalcite basicity selective 5-HMF oxidation over a 2 wt. % Au/HT calcined at either 300 or 450 °C. Three rehydration methods were compared: room temperature vapour phase treatment[2, 4, 16] with wet N_2; subcritical water treatment at 120 °C under an autogenous water pressure[17]; and immersion in boiling water at ambient pressure[16]. Synergies between calcination temperature and rehydration protocol were explored in regard of hydrotalcite reconstruction and catalysis.

Finally, the impact of gold loading on hydrotalcite calcined at 450 °C and subject to vapour phase rehydration was explored, in order to identify the optimum synthetic route to Au/HT catalysts for high activity and selectivity in 5-HMF oxidation.

4.2 Results and discussion

4.2.1 Preparation of 2 wt. % Au/HT and Au/mixed oxides

Hydrotalcites were synthesised as previously described in **Chapter 2.1.1** using the alkali-free co-precipitation method of Cantrell and co-workers[14], with some modifications, from diluted metal nitrate solutions. A deposition-precipitation method was employed to prepare 2 wt. % Au/HT or Au/MgAl oxide catalysts as previously described by Gupta and co-authors[18] and as already described in **Chapter 2.1.2.**

The preceding 2 wt. % Au supported on HT catalyst was subsequently divided into two batches: one calcined at 300 °C under oxygen for 4 h; the other one calcined at 450 °C for the same duration, indicated by calcined hydrotalcite (CHT). Each of these batches was sub-divided into three portions and rehydrated in three different ways: vapour phase[2, 4, 16], subcritical water at 120 °C in a pressure flask[17], or boiling in hot water at 100 °C[16], as described in **Chapter 2.1.3**

4.2.2 Preparation of different Au loadings on different calcined and rehydrated hydrotalcites

A range of gold loadings spanning 0.5, 1, 2, 5 and 10 wt. % were supported on HT as described above, calcined at 450 °C for 4 h and subsequent water vapour phase rehydration under wet N_2 for 48 h was conducted.

4.2.3 Characterisation of 2 wt. % Au supported on mixed oxides

4.2.3.1 XRD

Ex situ powder XRD was run on the sample of parent HT calcined at 200 °C and on 2 wt. % Au/CHT at 200, 300, 400 and 500 °C. The parent HT exhibited reflections at 11.2° (*d* 003), 22.4° (*d* 006), 34.2° (*d* 009), 38.3° (*d* 015), 44.6° (*d* 018), 60.1° (*d* 110), 61.3° (*d* 113) and 64.7° (*d* 116). As discussed in **Chapter 3.2.3.2,** no impurities of Mg or Al oxides or carbonates were observed, indicating a pure HT phase[4, 15]. As reported by Corma[10-12] and Cavani[4], calcination converts hydrotalcites into mixed Mg_3Al oxides at above 450 °C, as shown in **Figure 4.1.**

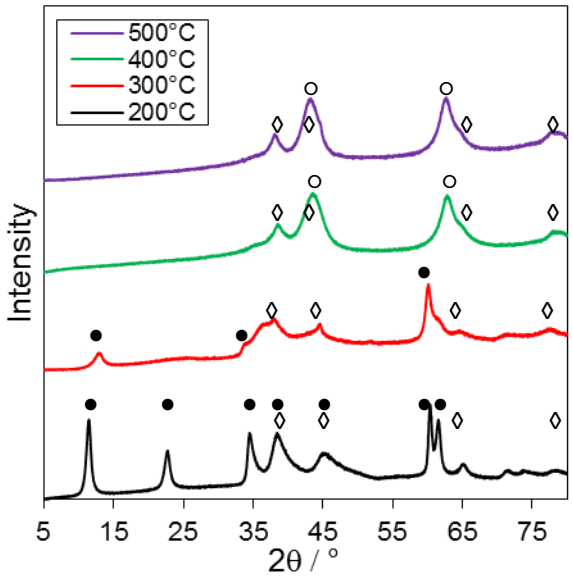

Figure 4.1: XRD patterns of 2 wt. % Au/CHT catalysts as a function of calcination temperature: • hydrotalcite, ○ $Mg_xAl_yO_z$-like phase, ◊ Au.

The nature of these mixed oxides and their formulas have been widely debated in the literature[19]; Reichle and co-authors[9] and Corma and co-authors[13] proposed either $Mg_6Al_2O_8(OH)_2$ or $Mg_6Al_2O_9$ at 300 °C ≤ calcination T ≤ 500 °C.

The *a* value was calculated from the 43.6° (*d* 200 for MgO) reflection in Figure 4.1 and exhibited a common value of 4.184 Å for the materials calcined at 400 °C and 500 °C, very similar to the 4.174 Å reported by Miyata and co-authors[20] and by Rives and co-authors[19], which is less than the 4.214 Å observed for pure MgO[21]. This indicates replacement of Mg^{2+} by smaller Al^{3+} cations in the formation of a mixed $Mg_xAl_yO_z$-like oxide, and consequent lattice contraction, with a likely Mg/Al stoichiometry of 3:1.

Considering **Figure 4.1**, calcination at 300 °C was sufficient to partially transform the initial HT structure into a mixture of hydrotalcite and mixed metal oxide phases. Higher calcination temperatures > 400 °C proved necessary to fully decompose the hydrotalcite structure into mixed Mg_3Al oxides[2, 4]. The peak widths of high temperature calcined samples were also broad, indicating small crystallites[6]. Peak fitting was done on peaks at 43.6° (*d* 200 for MgO) and Scherrer analysis for mixed Mg_3Al oxides has shown very small crystallites, respectively 2.3 nm for materials calcined at 400 °C and 2.1 nm for materials at 500 °C; gold peaks at 38° were clearly visible,

showing nanoparticles of 5.2 nm for the sample at 400 °C and 5.4 nm for the sample at 500 °C.

Vegard's law[1, 2] is an empiric rule and states that the lattice parameters of a solid solution of two constituents is approximately equal to a rule of mixtures of the two constituents' lattice parameters at the same temperature. Vegard's law **(Equation 1)** was used to demonstrate that these obtained Mg_3Al mixed oxides were not a simple physical mixture of MgO and Al_2O_3, as the law is valid when both components A and B have the same crystal structure.

$$a_{A(1-x)Bx} = (1 - x)\, a_A + x\, a_B \qquad \textbf{Equation 1}$$

Whereas $a_{A(1-x)Bx}$ is the lattice parameter of the solution, a_A and a_B are the lattice parameters of the pure constituents, and *x* is the molar fraction of B in the solution. Considering lattice parameters for MgO = 4.214 Å (*d* 200) and for γ-Al_2O_3 = 2.380 Å (which is the most stable alumina phase at 400-600 °C), the Vegard's law becomes

$$a_{A(1-x)Bx} = (0.75 * 4.214) + (0.25 * 2.38) = 3.755 \text{ Å}$$

which is far from the measured 4.184 Å. Therefore, the resulting material is not a physical mixture of magnesium and aluminum oxides.

To further elucidate this phase transformation, *in situ* XRD was carried out of a $HAuCl_4$ precursor supported onto HT as a function of calcination temperature under O_2 between room temperature and 600 °C **(Figure 4.2).**

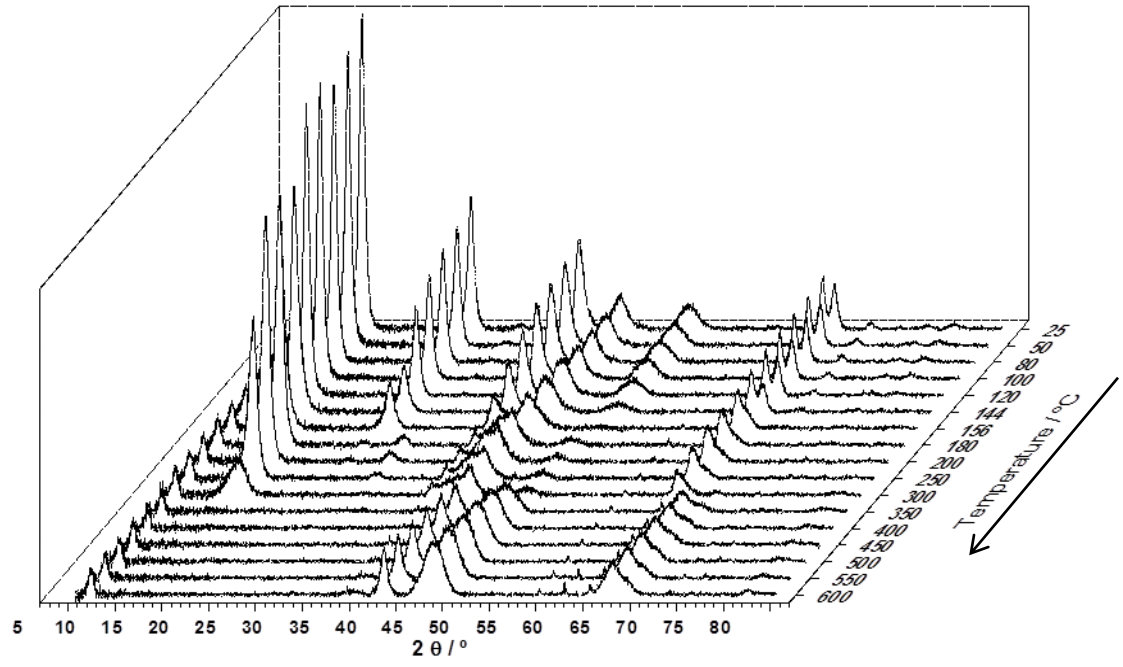

Figure 4.2: *in-situ* XRD patterns for $HAuCl_4$ deposited on HT as a function of calcination temperature.

The characteristic hydrotalcite reflections[20, 22] begin to weaken above 144 °C, although the structure is maintained until 200-250 °C. By 300 °C, a mixture of hydrotalcite and mixed Mg_3Al oxides is observed, likely due to the loss of hydroxyls as indicated by DRIFTS **(see Chpater 4.2.3.4)**, while after 350 °C the material starts losing carbonates, yielding mixed Mg_3Al oxides and being stable until the chosen temperature of 600 °C[23].

As already explained in **Chapter 3.2.3.2**, Au peaks are usually visible at 38° (*d* 111), 44° (*d* 200), 65° (*d* 220) and 78° (*d* 311), however these peaks overlap with the stronger HT reflections and are hence not visible for low gold loadings, necessitating background subtraction of the parent hydrotalcite contribution. The resulting background subtracted Au refelctions **(Figure 4.3)** were fitted in order to estimate the average gold particle size via Scherrer analysis[24], which reveals a monotonic increase in Au particle size with temperature.

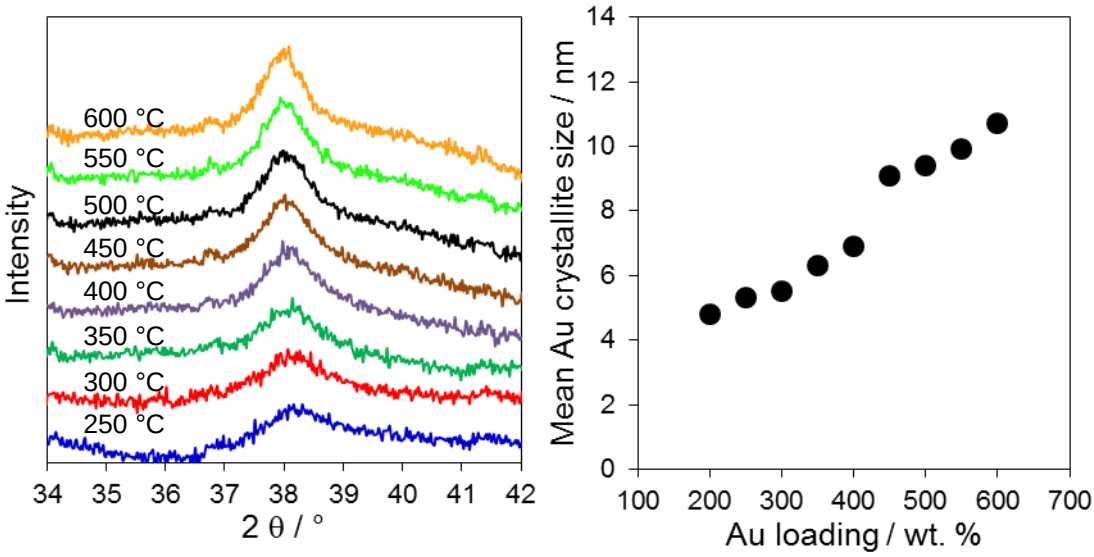

Figure 4.3: left - XRD patterns of 2 wt. % Au/CHT after subtraction of HT component as a function of calcination temperature; right – evolution of Au particle size with loading. The XRD spectra of HT were subtracted from the Au/HT ones and the peak at 38° was fitted using CASA, using GL curves to find the FWHM.

4.2.3.2 N_2 Porosimetry

N_2 adsorption-desorption isotherms[25, 26] for parent hydrotalcite and for 2 wt. % Au supported on CHT at different calcination temperatures are shown in **Figure 4.4**. The parent hydrotalcite exhibited a type II H3 isotherm, consistent with microporous crystallites having interplatelet mesoporous voids and slit type pores[27]. As the calcination temperature increased the isotherms exhibited smaller hysteresis loops than the parent HT indicating a loss of mesoporosity and increased crystallinity.

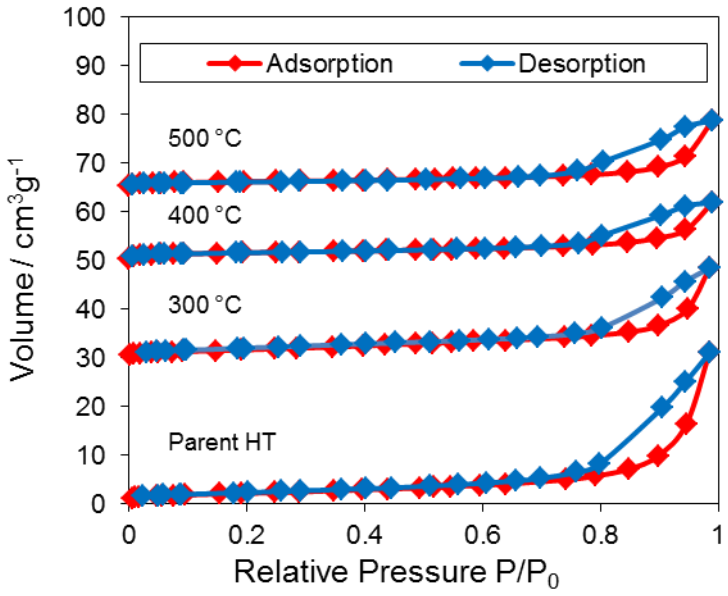

Figure 4.4: N_2 porosimetry isotherms for 2 wt. % Au/CHT as a function of calcination temperature. Isotherms offset for clarity.

Table 4.1 reports the corresponding BET surface areas for the parent hydrotalcite and 2 wt. % Au/CHT materials. No significant differences were detected between the parent HT and catalyst calcined at 200 °C, with areas around 95 $m^2.g^{-1}$ in agreement with literature values[1]. As the calcination temperature increased to 300 °C the surface area increased[1, 2, 6, 19], attributed to removal of interlayer carbonate and unblocking of micropores, reaching a maximum at 400 °C before falling at 500 °C, likely due to particle sintering as discussed in **Chapter 4.2.3.4** and **4.2.3.6**.

Table 4.1: BET surface areas for parent HT and 2 wt. % Au/CHT materials from N_2 porosimetry.

	BET surface area / $m^2.g^{-1}$
Parent HT	95 ± 9.5
2 wt.% AuCHT 200°C	90 ± 9
2 wt.% AuCHT 300°C	122 ± 12.2
2 wt.% AuCHT 400°C	143 ± 14.3
2 wt.% AuCHT 500°C	110 ± 11

4.2.3.3 Thermal analysis

TGA and dTGA profiles for parent HT and 2 wt. % Au/HT can be seen below in **Figure 4.5**; dTGA peak areas were quantified using fitting in Origin software. TGA analysis conducted on the parent HT revealed a three-stage weight loss[2, 20, 28, 29].

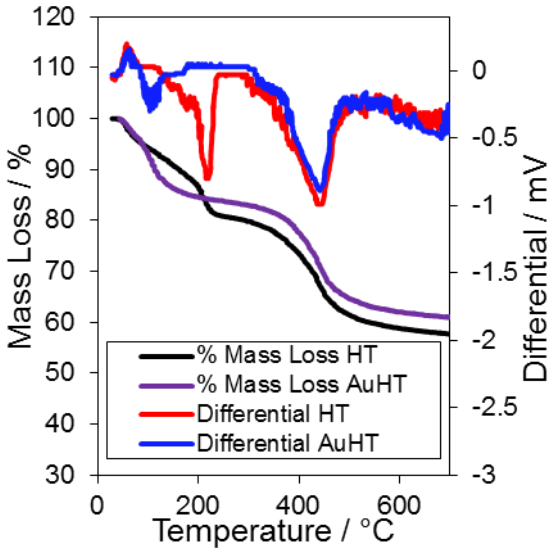

Figure 4.5: Thermogravimetric analysis of Mg_3Al HT as prepared and after Au deposition-precipitation and 200 °C calcination.

A first loss of weight (13.1 wt. % of the initial mass) occurred between 65-220 °C, reaching a maximum at 217 °C. This is attributed to the removal of loosely bound water molecules from the hydrotalcite, trapped in slit-type pores; hence a higher temperature is necessary to desorb water, than the expected 100 °C. A second weight loss (34.3 wt. % of the initial amount) was observed between 330-380 °C, attributed to the loss of hydroxyls.

A final weight loss (45.2 wt. % of the initial amount) is ascribed to the decomposition of interlayer carbonate anions between 400-550 °C, whose loss is anticipated to trigger the formation of mixed Mg_3Al oxides. The principal difference following Au addition was the absence of the physisorbed water desorption at T = 217 °C, suggesting that the thermal activation required to generate Au NPs (200 °C calcination) sufficed to remove all interlayer water. These results and those from bulk elemental analysis in **Chapter 3.2.3.1** were combined together to calculate the experimental chemical formula[4, 30] of parent hydrotalcite before gold deposition-

precipitation, that was found to be $Mg_{5.77}Al_{1.92}(OH)_{15.3}CO_3 \cdot 4.3\ H_2O$, which is in good agreement with the theoretical formula[4, 14] $Mg_6Al_2(OH)_{16}CO_3 \cdot 4\ H_2O$.

4.2.3.4 In situ DRIFTS

Structural changes during calcination of the as-prepared hydrotalcite were further explored through an *in situ* DRIFT study as shown in **Figure 4.6.**

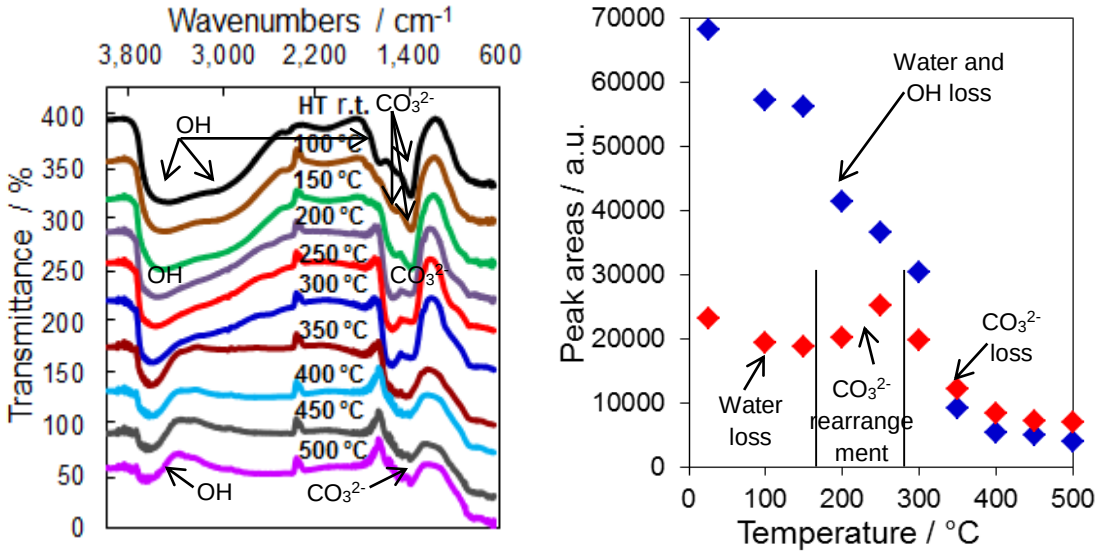

Figure 4.6: left – *in situ* DRIFT spectra of hydrotalcite and 2 wt. % Au/CHT as a function of calcination temperature, spectra offset for clarity. Right – peak areas as a function of calcination temperature, showing a progressive decrease in OH stretching, in blue (loss of water and OH) and a two-step decrease in CO_3^{2-} stretching, in red (rearrangement and loss of carbonates).

As clearly visible, the carbonates' rearrangement[31] at 1497 cm^{-1} and 1331 cm^{-1} starts already at 150 °C and it is complete at 300 °C, the new peaks corresponding to C=O at 1508 cm^{-1} and to C-O at 1338 cm^{-1}, as discussed in **Chapter 3.2.3.5**; for higher temperatures, the carbonate band loses intensity, showing a loss of carbonates at temperatures above 450 °C.

The physisorbed water removal from the interlayers starts at 100 °C and it is complete at 200 °C (loss of the band at 3080 cm^{-1}), while higher temperatures are necessary to remove the OH groups (3800-2500 cm^{-1}). This subsequent structural change begins at 300 °C and it is almost complete at 400 - 450 °C, when mixed Mg_3Al oxides are formed, stable until 500 °C without evident changes[31, 32].

4.2.3.5 Surface basicity

CO_2 chemisorption and subsequent thermal desorption was employed to calculate the surface base site density and strength[1, 3, 15] of the 2 wt. % Au/CHT family as a function of calcination temperature. TPD spectra reveal differences in the total amount of CO_2 adsorbed, and the CO_2 adsorption strength.

All materials were dominated by a desorption peak around 400 C, indicative of moderate solid basicity [1, 15, 33-35], which shifted slightly to higher temperature upon increasing the Au/CHT calcination temperature from 200 °C to 500 °C, indicating a small increase in base strength **(Figure 4.7 – left)**.

However, the 500 °C calcined sample also exhibited a low temperature CO_2 desorption peak around 200 °C, suggesting the presence of some weak base sites accompanies decomposition of the hydrotalcite and formation of mixed Mg_3Al oxides. **Figure 4.7 – right** shows the integrated CO_2 desorption peak areas, which reveals the number of base sites increased with calcination temperature, as previously reported in the literature[36, 37].

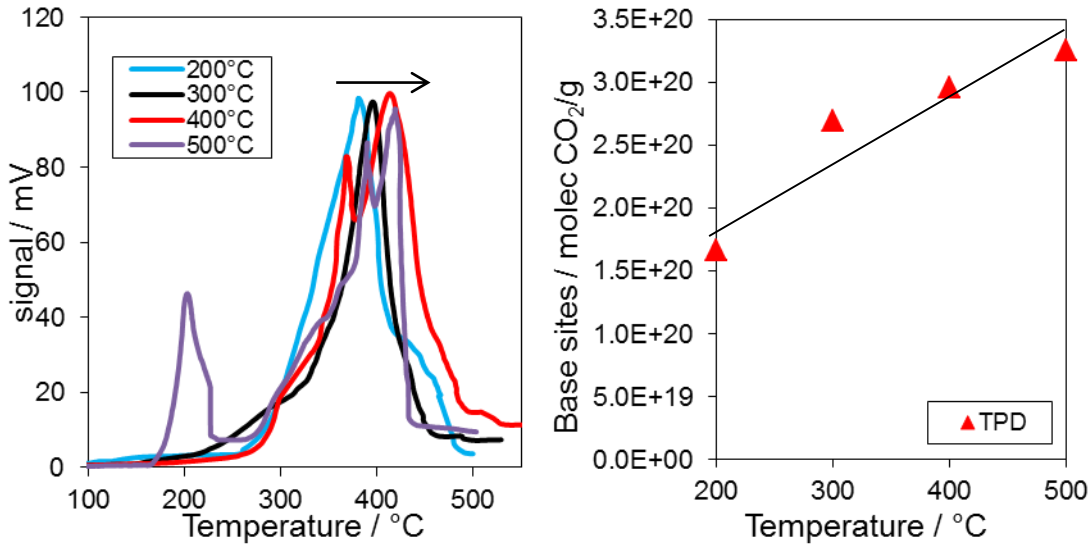

Figure 4.7: left –CO_2 TPD spectra, and right - surface base density determined for 2 wt. % Au/CHT materials as a function of calcination temperature.

TPD data were further analysed to quantify the distribution of weak, medium and strong base sites, assuming that a molecule of CO_2 can bind as bicarbonate species on the surface hydroxyls in lattice (weak sites), or as bicarbonate species on the interlayer anions (medium sites) or as mono- and bidentate species on strong oxides sites[3, 38]. Results are shown in **Table 4.2** and **Table 4.3.**

Table 4.2: base site strength percentage distribution for 2 wt. % Au/HT calcined at different temperatures.

Calcination T / °C	Weak sites / % (200-280 °C)	Medium sites / % (280-380 °C)	Strong sites / % (380-450 °C)
200	-	92.8	7.2
300	-	71.9	28.1
400	-	54.0	46.0
500	23.6	43.9	32.5

Table 4.3: Surface area normalised strong sites for 2 wt. % Au/CHT as a function of calcination temperature, and maximum CO_2 desorption temperature.

Calcination T / °C	Density of strong sites / m^{-2}	T_{max} CO_2 desorption / °C
200	1.26×10^{17}	390
300	9.19×10^{17}	400
400	1.45×10^{18}	420
500	1.04×10^{18}	420

4.2.3.6 Surface analysis

XPS analysis was performed on the parent hydrotalcite and 2 wt. % Au/HT calcined at 200, 300, 400 and 500 °C in order to study the evolution of the HT to mixed Mg_3Al oxide phase. **Figure 4.8 – left** shows the Mg 2p XP region for the parent hydrotalcite, for which a single chemical environment was fitted with a spin-orbit split doublet (separation = 0.28 eV) with binding energies of 50.54 and at 50.82 eV. These were attributed to Mg-OH in hydrotalcite phase, as in **Chapter 3.2.3.8** (NIST database[39] 50.40 eV for $MgAl_2O_4$ spinel, 49.50-49.90 eV for Mg hydrotalcite); the shift was attributed to the different Mg/Al ratio (3 for the analysed sample, 2 for HT in the database).

Figure 4.8 – right shows the Mg 2p XP region for 2 wt. % Au/HT calcined at 200 °C, which required fitting with two distinct chemical environments. The first doublet was attributed to the parent HT phase as discussed above; the second state, with binding energies of 51.02 and 51.30 eV, was attributed to the formation of a mixed Mg_3Al oxide following the loss of physisorbed water within the HT interlayers, due to the proximity of the Al^{3+} cations withdrawing charge from oxygen anions bound to Mg^{2+} centres[2, 22].

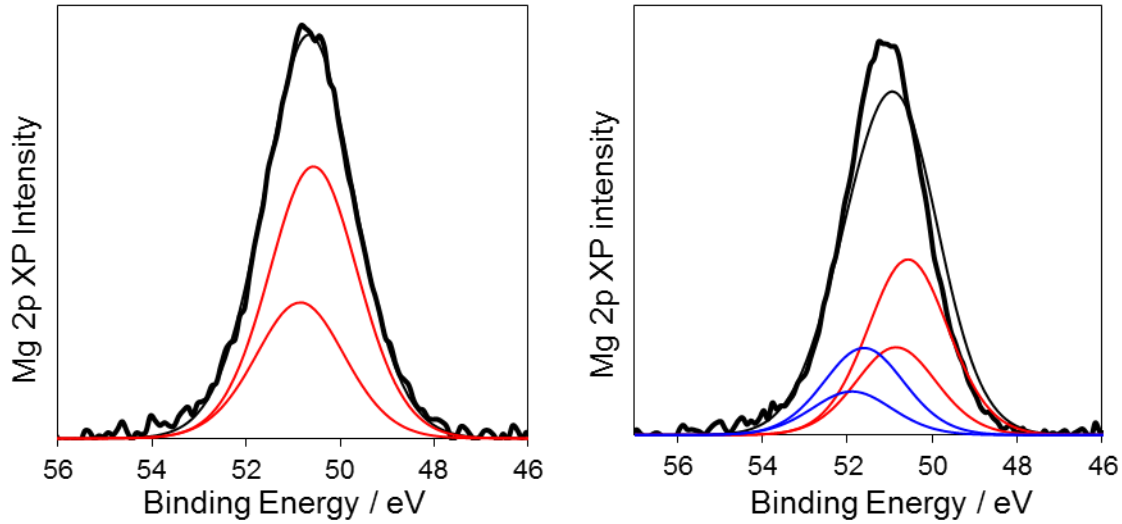

Figure 4.8: High resolution Mg 2p XP spectra of (left) the parent hydrotalcite and (right) 2 wt. % Au/CHT200. HT phase shown in red, mixed Mg_3Al oxide in blue.

Figure 4.9 shows the corresponding Mg 2p XP spectra following 300 °C and 400 °C calcination, in which two chemical environments were likewise fitted, with the intensity of the higher binding energy mixed Mg_3Al oxide state increasing at the expense of the hydrotalcite features with increasing calcination, in accordance with literature reports wherein OH and carbonate decomposition to mixed oxide phases occurs by 400-450 °C[4, 10, 11].

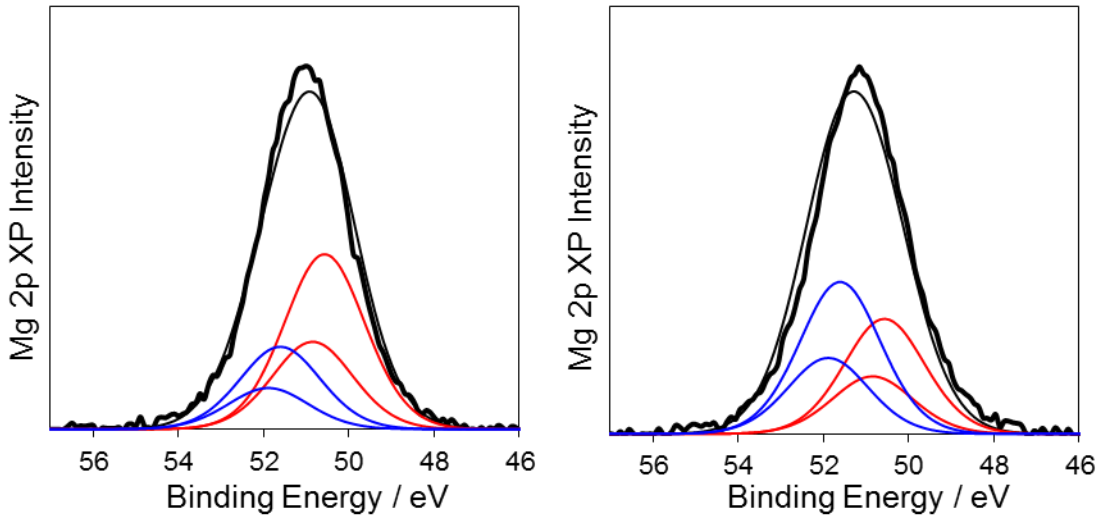

Figure 4.9: High resolution Mg 2p XP spectra for (left) 2 wt. % Au/CHT300 and (right) 2 wt. % Au/CHT400. HT phase shown in red, mixed Mg3Al oxide in blue.

After calcination at 500 °C (**Figure 4.10 – left**) the amount of mixed Mg_3Al oxide was much higher than HT. Temperature dependence intensities of both phases are shown in **Figure 4.10 – right.**

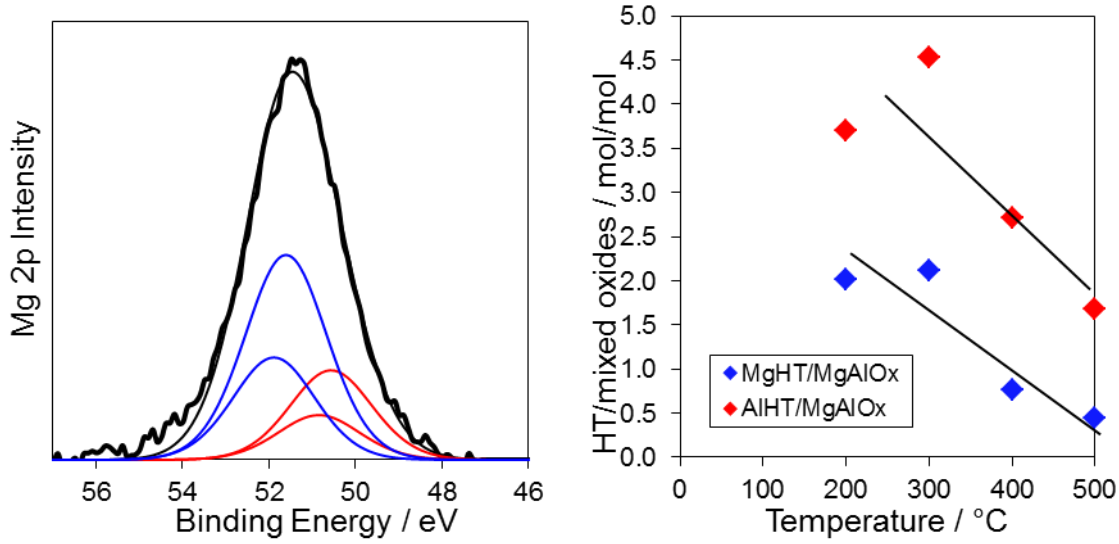

Figure 4.10: left – high resolution Mg 2p XP spectra of 2 wt. % Au/CHT500; right – molar ratio of Mg in HT/Mg in mixed Mg_3Al oxide surface concentrations (in blue) and of Al in HT/Al in mixed Mg_3Al oxide (in red) as a function of calcination temperature.

The Al 2s spectra for the parent hydrotalcite **(Figure 4.11 – left)** was fitted by a single chemical environment, while the Al 2s spectra for CHT at 200 °C **(Figure 4.11 – right)** was fitted by a double chemical environment; the binding energy of 119.68 eV was attributed to HT-like phase and the one of 121.32 eV was attributed to the formation of a mixed Mg_3Al oxide following the loss of physisorbed water within the HT interlayers, due to the proximity of the Al^{3+} cations withdrawing charge from oxygen anions bound to Mg^{2+} centres, as discussed above (NIST database[39] 119.50 eV for Al_2O_3, 119.10 eV for $MgAl_2O_4$; 118.5 eV for HT-phase, Cantrell and co-authors[14]).

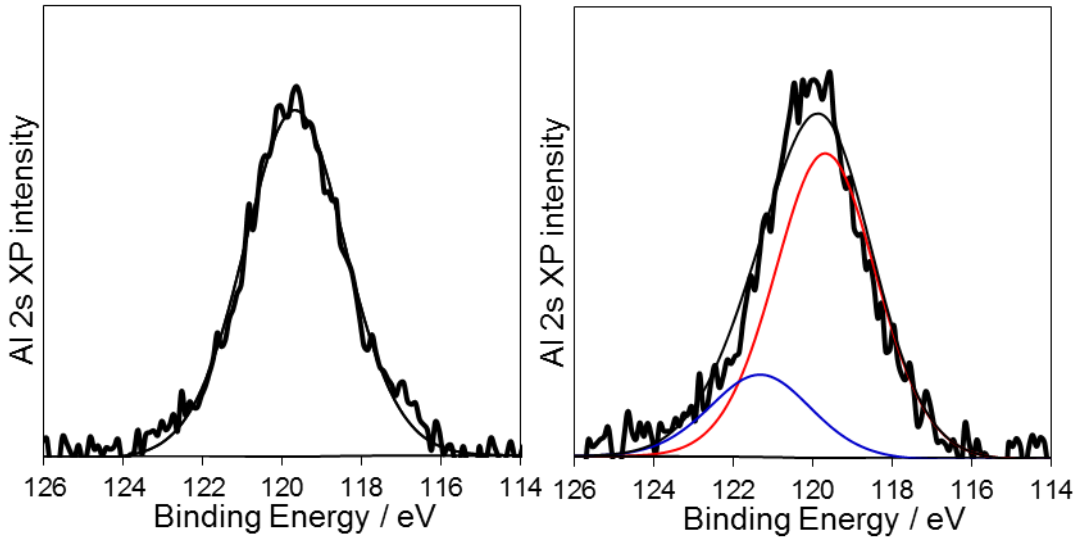

Figure 4.11: high resolution Al 2s XP spectra for parent hydrotalcite (left) and 2 wt. % Au/CHT at 200 °C (right). HT phase shown in red, mixed Mg_3Al oxide in blue.

The Al 2s spectra of CHT at 300 °C **(Figure 4.12 – a)** CHT at 400 °C **(Figure 4.12 – b)** and CHT at 500 °C **(Figure 4.12 – c)** were likewise fitted by a double chemical environment; the amount of Al in Mg_3Al oxides increased with the calcination temperature.

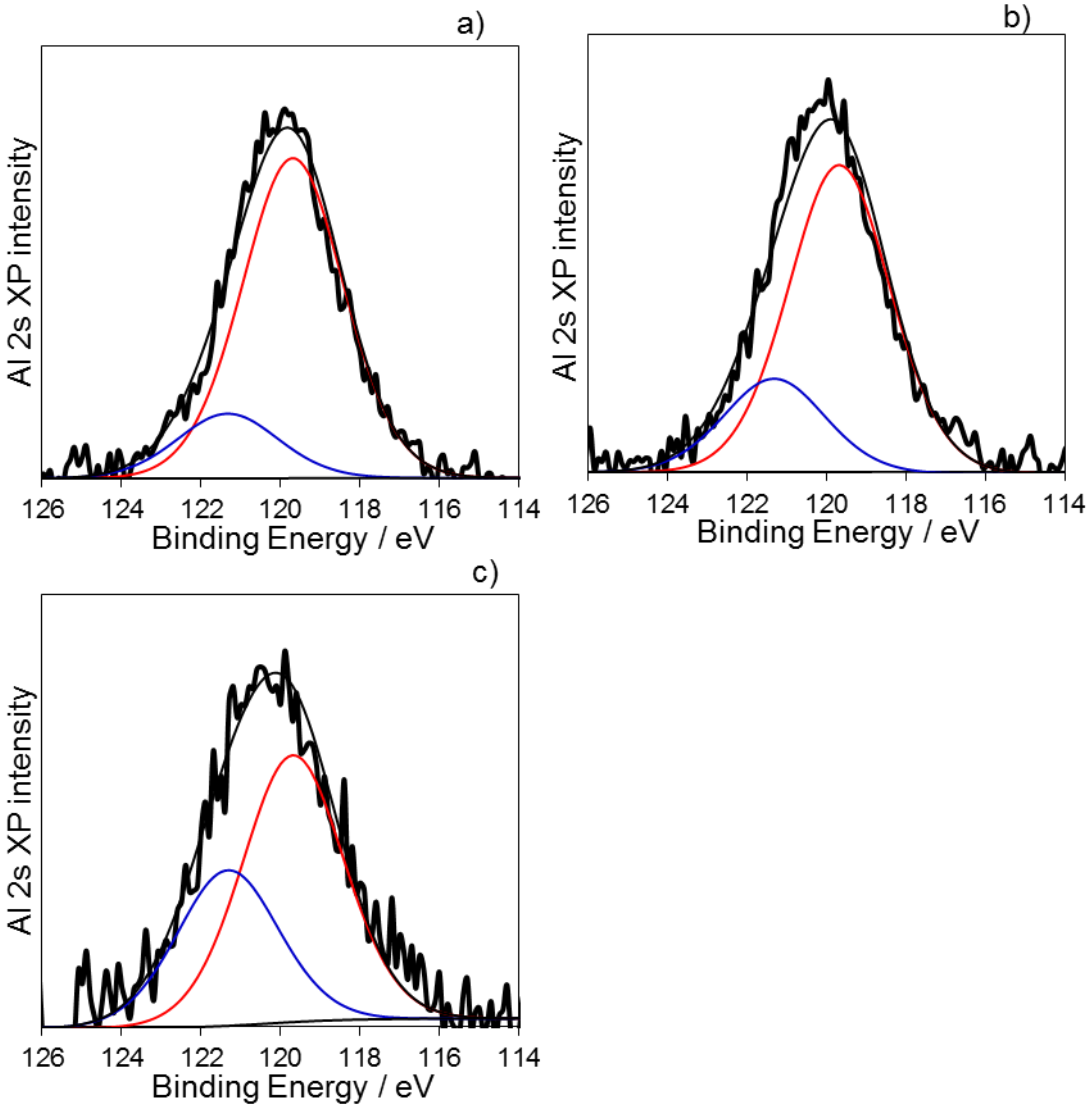

Figure 4.12: high resolution Al 2s XP spectra for a) 2 wt. % Au/CHT at 300 °C, b) at 400 °C and c) at 500 °C. HT phase shown in red, mixed Mg_3Al oxide in blue.

Analysis of the analogous O 1s XP spectra supported the preceding observations of a phase change. The parent HT exhibited two distinct chemical components **(Figure 4.13 – a),** one attributed to the O^{2-} of HT and carbonates[40], with a binding energy of 532.4 eV, and the second one attributed to hydroxyls with a lower binding energy of 531.0 eV (529.3-530.9 eV for OH in hydrotalcite phase, Cantrell and co-authors[14]).

Figure 4.13 – b shows that after calcination at 200 °C, three chemical environments were necessary to fit the O 1s spectra, with the additional state at 529.7 eV binding energy attributed to O^{2-} in a Mg_3Al oxide[41, 42] (NIST database[39] 530.6-529.6

eV for MgO). The intensity of this mixed oxide component increased with calcination temperature (**Figure 4.13 - a-e**).

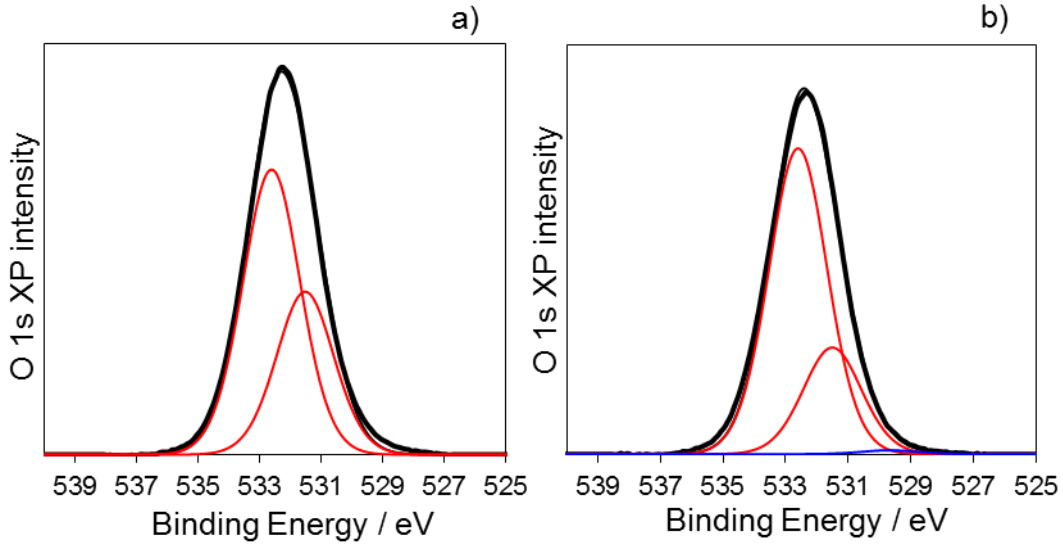

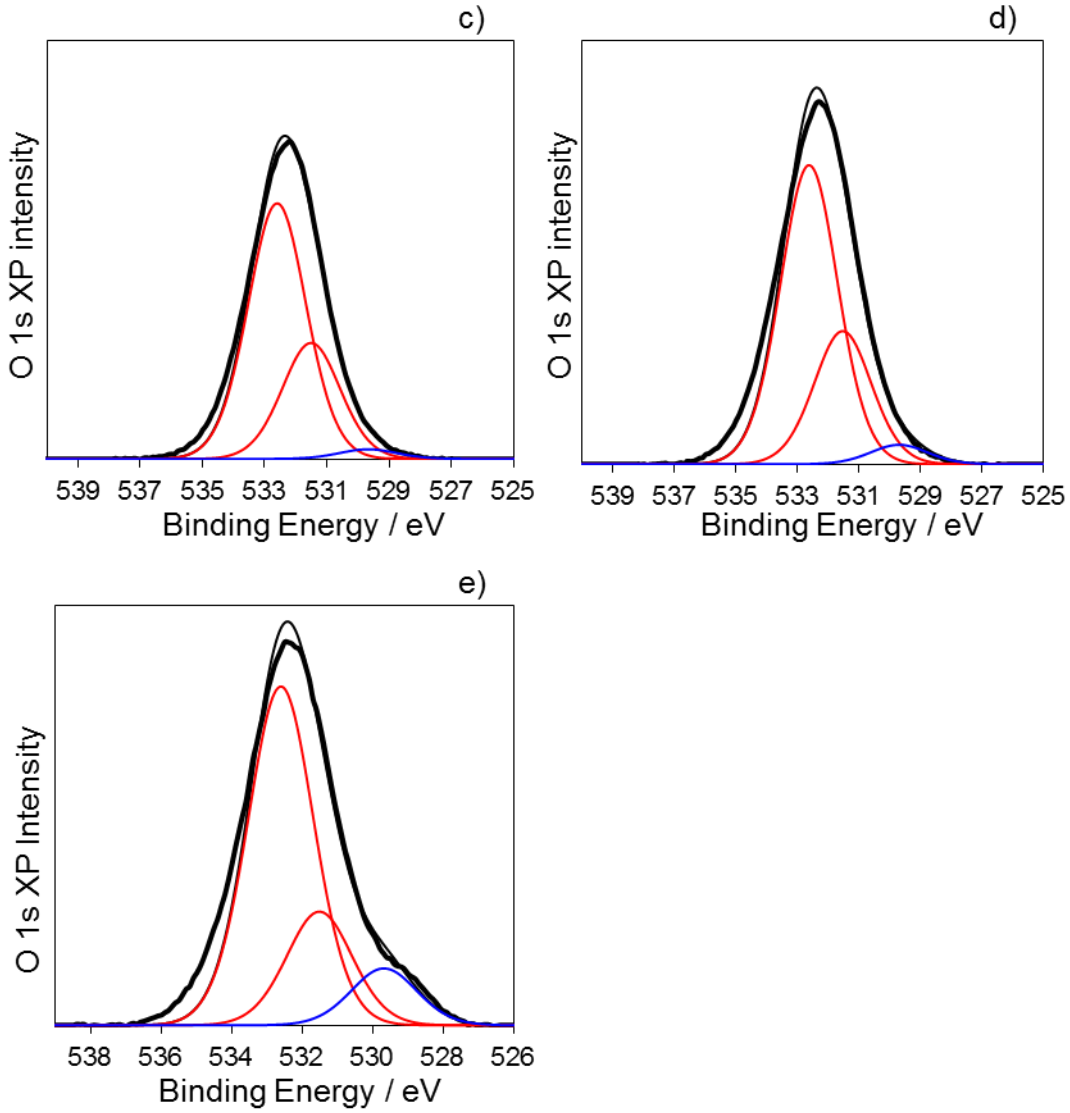

Figure 4.13: High resolution O 1s XP spectra of a) parent HT, b) 2 wt. % Au/CHT200, c) 2 wt. % Au/CHT300, d) 2 wt. % Au/CHT400 and e) 2 wt. % Au/CHT500.

In summary, calcination of Au/HT between 200-400 °C increases the surface area, accompanied by the formation of a mixed metal oxide phase with enhanced solid basicity. Additional calcination to 500 °C begins to lower the surface area and generates a small number of weak base sites, the latter due to segregation of Mg and Al oxide phase, possible at the edges of mixed oxide crystallites[17].

4.2.4 Characterisation of 2 wt. % Au/calcined-rehydrated hydrotalcites

Bulk elemental analysis was performed to determine the actual Au content and Mg:Al ratio, and the structural properties of materials examined by powder X-ray

diffraction (XRD), N_2 porosimetry and electron microscopy. SEM was also used to study the support morphology, and TEM to measure the average Au particle size. IR, TGA, XPS and CO_2 TPD analysis were also performed to investigate the oxidation state and base properties of the hydrotalcite support and Au nanoparticles.

4.2.4.1 Elemental analysis

XPS analysis was run on the parent HT and 2 wt. % Au/calcined-rehydrated hydrotalcites, calcined at either 300 or 450 °C and subsequently rehydrated in the vapour phase, subcritical water or boiling water. **Table 4.4** shows the surface Au loading of calcined and subsequently rehydrated materials.

Table 4.4: surface Au loading of 2 wt. % Au/CHT and Au/CHTrehydrated series, from XPS. In all cases the average Mg:Al atomic ratio was 3.4 ± 0.3.

Nominal 2 wt. % Au loading	XPS / wt. % Au
CHT200	2.1
CHT300	1.9
CHT300Vap	1.6
CHT300Subw	1.3
CHT300Hotw	1.3
CHT450Vap	2.2
CHT450Subw	1.1
CHT450Hotw	1.3

XPS elemental analysis has therefore shown that a gold leach occurred for all the catalysts calcined and rehydrated either in boiling water or in subcritical conditions, which did not happen in the case of calcination and rehydration in vapour phase. During the preparation of those two types of catalysts, the filtered water was visibly pink, indicating that gold was indeed leached under these aggressive conditions. All the resulting catalysts were subsequently tested for 5-HMF selox, however we note here that the most stable and promising material was the CHT450vap for which no leaching occurred. **Table 4.5** presents full surface elemental analysis for the CHT rehydrated materials.

Table 4.5: XPS surface elemental analysis of 2 wt. % Au loading supported on different CHT-RW.

CHT300 Vap	Element / wt.%	CHT300 Subw	Element / wt.%	CHT300 Hotw	Element / wt.%
Mg	25.0	Mg	24.5	Mg	24.4
Al	8.8	Al	7.6	Al	7.6
O	54.0	O	50.9	O	52.8
C	9.2	C	14.6	C	12.9
Cl	1.4	Cl	1.1	Cl	0.8
Au	1.6	Au	1.3	Au	1.3

CHT450 Vap	Element / wt.%	CHT450 Subw	Element / wt.%	CHT450 Hotw	Element / wt.%
Mg	28.4	Mg	24.4	Mg	22.8
Al	8.2	Al	7.9	Al	7.8
O	53.1	O	52.1	O	53.2
C	6.9	C	13.2	C	13.1
Cl	1.2	Cl	1.5	Cl	1.7
Au	2.2	Au	1.1	Au	1.3

Calcined and rehydrated hydrotalcites, in which OH anions replace CO_3^{2-} are also called meixnerite[4, 6, 29, 37] and a detailed discussion on their structure, morphology and properties will be done in **Chapter 4.2.4.2,** while the formulas will be calculated in **Chapter 4.2.4.6.**

4.2.4.2 XRD

Ex situ powder X-ray diffraction was performed on the parent HT and 2 wt. % Au/CHT300vap or Au/CHT450vap materials. The parent hydrotalcite **(Figure 4.12 – left)** exhibited a series of reflections at 11.5° (*d* 003), 23.0° (*d* 006), 34.7° (*d* 009), 38.7° (*d* 015), 45.9° (*d* 018), 60.4° (*d* 110), 60.8° (*d* 113) and 65.4° (*d* 116), as already debated in **Chapter 4.2.3.2.** No impurities of Mg and Al oxides or carbonates were detected for this Mg_3Al hydrotalcite, showing a pure HT phase[2, 4, 19, 28, 43].

As shown in **Figure 4.14**, calcination at 300 °C was sufficient to partially transform the HT structure to a mixture of hydrotalcite and oxide phases, as already described in **Chapter 4.2.3.1**. For both calcination temperatures, vapour phase rehydration proved sufficient to fully reconstruct the parent hydrotalcite phase[22] from

the mixed oxides observed after calcination, with sharper reflections observed for the 450 °C sample, indicating a higher degree of crystallinity in the reconstructed hydrotalcite[10, 16]. When carbonates are replaced by hydroxyl groups in hydrotalcite, the new resulting anionic clay is called meixnerite, for which the reported formula is $Mg_6Al_2(OH)_{18}$ $4H_2O$ [4, 6, 29, 44] and this name was used also in this thesis work to indicate it.

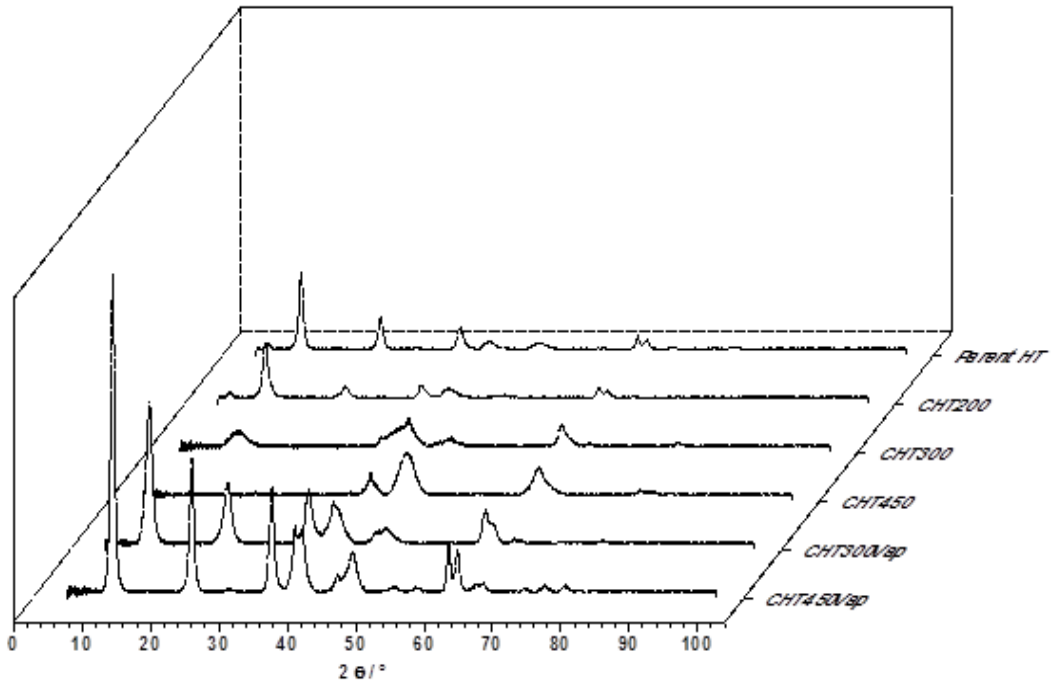

Figure 4.14: *Ex situ* XRD patterns of parent hydrotalcite and 2 wt. % Au/CHT and CHTrehydrated materials.

Powder X-ray diffraction was carried out also on CHT calcined at 300 or at 450 °C and rehydrated in three different ways **(Figure 4.15),** as described in **Chapter 4.2.2.** Rehydration in boiling water or in subcritical water appear to show a better reconstructed HT phase than rehydration in vapour phase, evidenced by more intense reflections which may be due to the presence of atmospheric CO_2 that is intercalated within the HT structure during rehydration in water exposed to air, as opposed to aqueous vapour phase rehydration which was performed under an inert atmosphere.

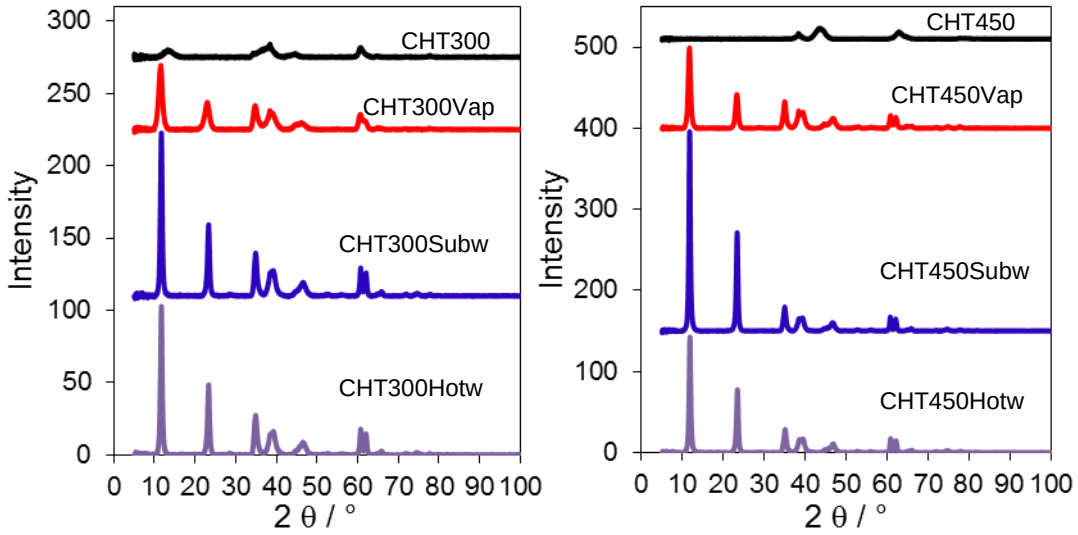

Figure 4.15: *Ex situ* XRD patterns of (left) CHT300 and (right) CHT400 as a function of subsequent rehydration protocol.

Powder XRD patterns were phase corrected using the software EVA, then interlayer spacing *d* and lattice parameters *a* and *c* were calculated for 2 wt. % Au supported on CHT300vap CHT450vap and compared with literature values[1, 4, 45]. Results are shown in **Table 4.6** below.

Table 4.6: interlayer spacing *d* and lattice parameters values for different gold loading on CHT-RW series at 300 and at 450 °C, as determined from powder XRD patterns.

Catalyst	Interlayer spacing *d* / Å	Lattice parameter *a* / Å	Lattice parameter *c* / Å
Parent hydrotalcite	7.70 ± 0.01	3.053 ± 0.001	23.164 ± 0.001
CHT300Vap	7.62 ± 0.01	3.062 ± 0.001	23.179 ± 0.001
CHT450Vap	7.62 ± 0.01	3.043 ± 0.001	23.011 ± 0.001
CHT300Hotw	7.62 ± 0.01	3.050 ± 0.001	23.037 ± 0.001
CHT450Hotw	7.62 ± 0.01	3.043 ± 0.001	23.011 ± 0.001
CHT300Subw	7.62 ± 0.01	3.050 ± 0.001	23.037 ± 0.001
CHT450Subw	7.62 ± 0.01	3.043 ± 0.001	23.011 ± 0.001

For meixnerite materials, the reported literature value[4] for the lattice parameter *a* was 3.046 Å, while for the lattice parameter *c* was 22.93 Å. Values calculated for CHT450vap were closer to the expected ones than values calculated for CHT300vap, confirming that higher calcination temperatures yielded higher removal of CO_2 from the HT interlayers and subsequent major replacement with OH groups. As expected, also the interlayer spacing *d* was lower for meixnerite than for parent hydrotalcite, for the same reason above.

As explained in **Chapter 3.2.3.2**, for a hydrotalcite–like structure with rombohedral 3R symmetry and stacking of brucite layers[4, 46], the interlayer spacing *d* can be calculated from measuring the peak position of the d_{003} reflection from the XRD pattern and then with the **Equation 4.1.**

$$d = d_{003} = \frac{n\,\lambda}{2\,\mathrm{sen}\,\theta} \qquad \textbf{Equation 4.1}$$

The lattice parameter *a,* known as the unit cell parameter, was calculated using the *d*(110) XRD peak position, with the **Equation 4.2.**

$$a = 2\,d_{110} \qquad \textbf{Equation 4.2}$$

For a hydrotalcite – like structure with rombohedral 3R symmetry stacking of brucite layers[4, 16], The lattice parameter *c*, that corresponds to three times the interlayer spacing *d* between two consecutive layers, was calculated using the *d*(003), *d*(006) and *d*(009) XRD peak position, with the **Equation 4.3**

$$c = d_{003} + 2\,d_{006} + 3\,d_{009} \qquad \textbf{Equation 4.3}$$

Volume-averaged HT crystallite sizes were determined using the peak at above 11.5° using the Scherrer equation[24] and results are summarised in **Table 4.7.** As already discussed in **Chapter 3.2.3.2**, small crystallite sizes indicate there is an extended ordered porous architectures formed *via* the agglomeration or fusion of these nanocrystalline platelets[45].

Table 4.7: volume-averaged crystallite size for HT-like materials, obtained *via* Scherrer equation. Crystallite sizes increase after calcination-rehydration, being 7.2 nm for the starting material.

Catalyst	Peak position 2 θ / °	Average crystallite size / nm
CHT300Vap	11.5	7.6
CHT300Subw	11.4	16.1
CHT300Hotw	11.7	17.5
CHT450Vap	11.7	11.7
CHT450Subw	11.7	19.3
CHT450Hotw	11.8	18.4

The reconstructed hydrotalcites have stronger peak intensities, sharper and more symmetric peaks and bigger average crystallite sizes than the parent hydrotalcite, indicating less stacking disorder and less turbostatic disorder[16, 47-49]. As observed by Davis and co-authors also in this thesis work, independently by the calcination temperature, the XRD patterns were weaker, and so crystallites size of the vapour phase reconstructed samples was significantly smaller, than that of either the reconstructed in hydrothermal treatment ones, but disappearing of MgO phase suggested the vapour phase rehydration was successful.

4.2.4.3 N_2 Porosimetry

N_2 adsorption-desorption isotherms[25, 26] for the parent hydrotalcite and for CHT at 300 or 450 °C and rehydrated in aqueous vapour phase or in boiling water or in subcritical water can be seen in **Figure 4.16** and **Figure 4.17**. The isotherms have been offset for clarity.

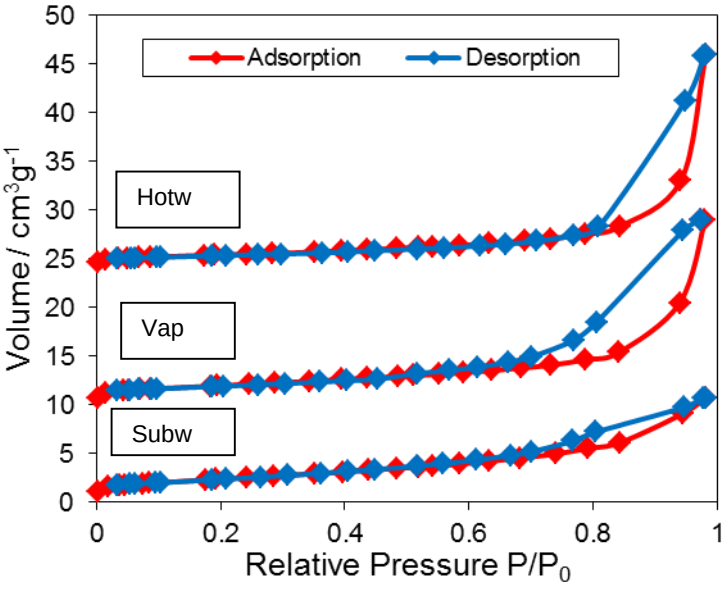

Figure 4.16: N_2 porosimetry isotherms for the series of 2 wt. % Au loading on CHT at 300 °C, then rehydrated at room temperature in aqueous vapour phase, at 120 °C in subcritical water or in boiling water at 100 °C.

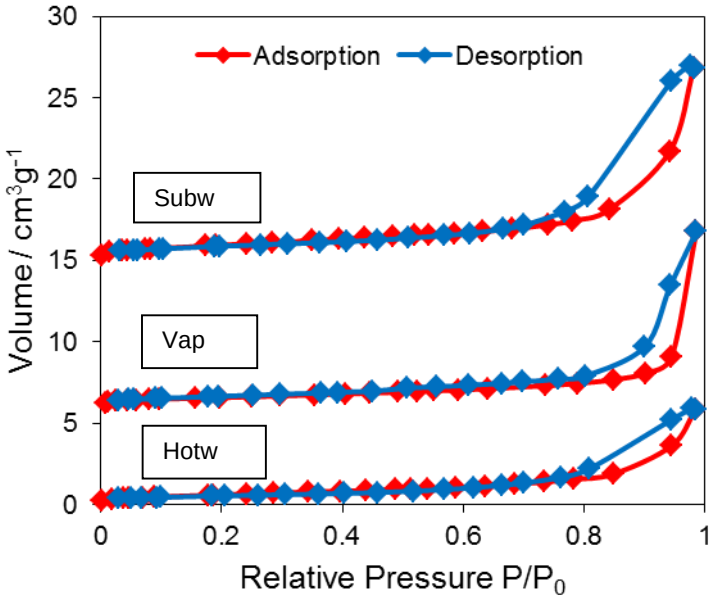

Figure 4.17: N_2 porosimetry isotherms for the series of 2 wt. % Au loading on CHT at 450 °C; then rehydrated at room temperature in aqueous vapour phase and under N_2 flow, at 120 °C in subcritical water or in boiling water at 100 °C.

The parent hydrotalcite shows type II H3 isotherm, consistent with microporous crystallites having interplatelet mesoporous voids and slit type pores[27, 50]. This

behaviour remains in each case after calcination and subsequent rehydration, regardless of the rehydration method followed. Surface area values are shown in **Table 4.8**, whereas it is possible to observe an increase in surface area when parent HT is calcined at 300 °C, due to the partial removal of carbonates from the interlayers and consequential formation of interplatelet voids[1].

When rehydration occurs, a minor reduction of surface area is visible and it is identical for all the less hydroxylated CHT treated at 300 °C, in the range of experimental error, while surface area shows a dramatic drop off when the treatment occurred at 450 °C and yields more hydroxylated materials. This loss in surface area after rehydration was previously reported by several authors[2, 10, 11] and described as a consequence of the closure of micropores and mesopores by agglomeration of platelets and subsequently formation of compact aggregates[6, 51].

Table 4.8: surface area values for parent HT and 2 wt. % gold loading on CHT at 300 or 450 °C and rehydrated in three different ways, as determined by N_2 porosimetry.

	BET surface area / m^2g^{-1}
Parent HT	95 ± 9.5
CHT300	122 ± 12.2
CHT300Vap	70 ± 7.0
CHT300Subw	74 ± 7.4
CHT300Hotw	76 ± 7.6
CHT450Vap	25 ± 2.5
CHT450Subw	24 ± 2.4
CHT450Hotw	32 ± 3.2

4.2.4.4 SEM of HT and CHTVap

SEM images were obtained for the parent HT and for the CHT450Vap meixnerite[4] materials without Au loaded on them and **Figure 4.18** shows an example of typical SEM image of the parent hydrotalcite.

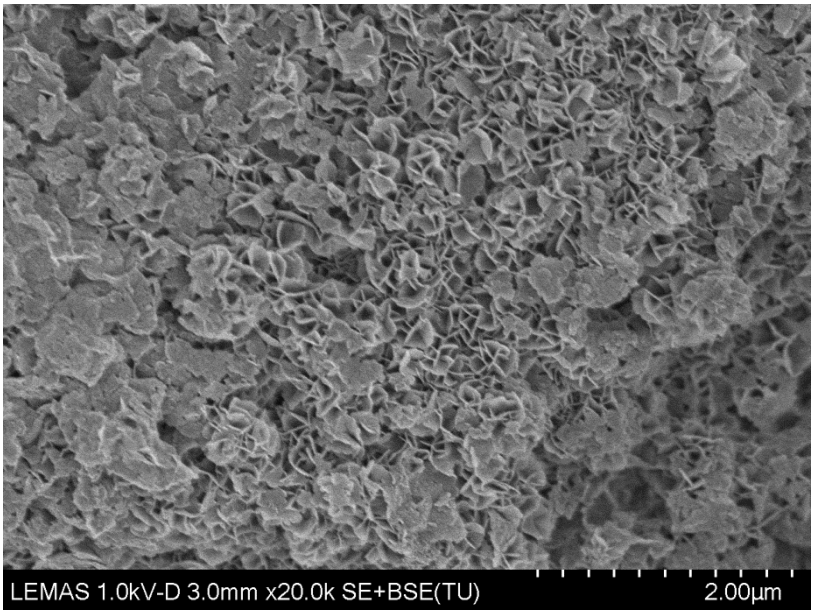

Figure 4.18: a representative SEM image of parent Mg_3Al HT, showing characteristic sand rose morphology.

The sample was calcined at 450 °C in oxygen for 4 hours and then rehydrated in aqueous vapour steam under wet nitrogen at room temperature for 48 hours, yielding meixnerite[4], as already discussed in **Chapter 4.2.3.2**; SEM analysis has shown a complete reconstruction of sand-rose structure after the CHT-RW process, as visible in **Figure 4.19** below.

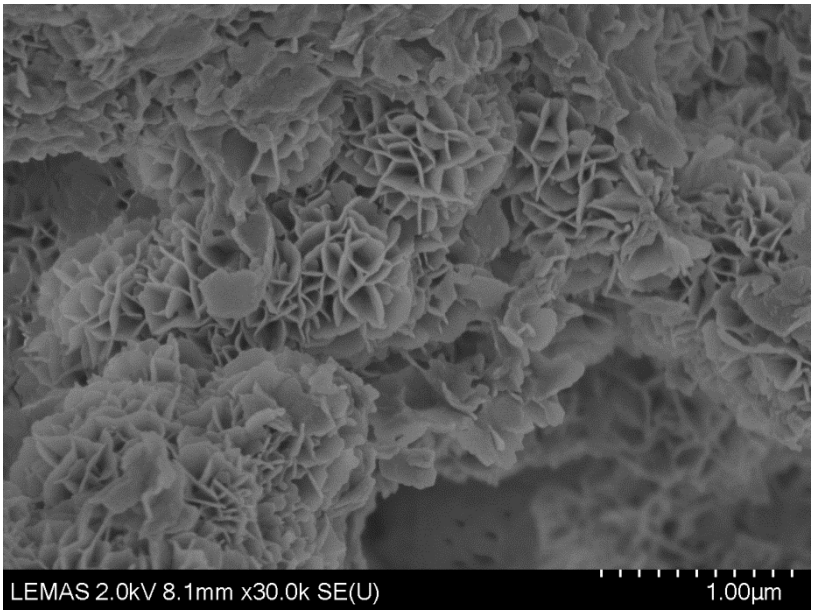

Figure 4.19: a representative SEM image of Mg_3Al meixnerite, showing the reconstruction of characteristic sand-rose morphology after calcination and rehydration.

Large and well-defined (around 200 nm up to 1 μm) compact particles[16], fused together, are clearly visible in both **Figure 4.18** and **4.19**, showing the characteristic sand-roses morphology and confirming the rombohedral 3R crystal system of hydrotalcite and meixnerite[4, 46].

4.2.4.5 Ex-situ DRIFT spectra

Ex situ DRIFT spectra **(Figure 4.20)** show the differences between parent hydrotalcite and 2 wt. % Au/CHT at 300 or 450 °C and rehydrated either in aqueous vapour phase, or in boiling water or in subcritical water; the peak attribution was made according to Meliàn-Cabrera and co-authors' paper[31] and according to Davis and co-authors' one[16].

For the parent HT, the OH stretching at 3800-2500 cm^{-1} is clearly visible for all the materials as a broad band, attributed to the stretching of the hydroxyl groups of the brucite-like sheets, while the shoulder at 3080 cm^{-1} is given by hydrogen bonding between the water molecules and CO_3^{2-} groups, both available in the interlayer region of a typical layered double hydroxide structure.

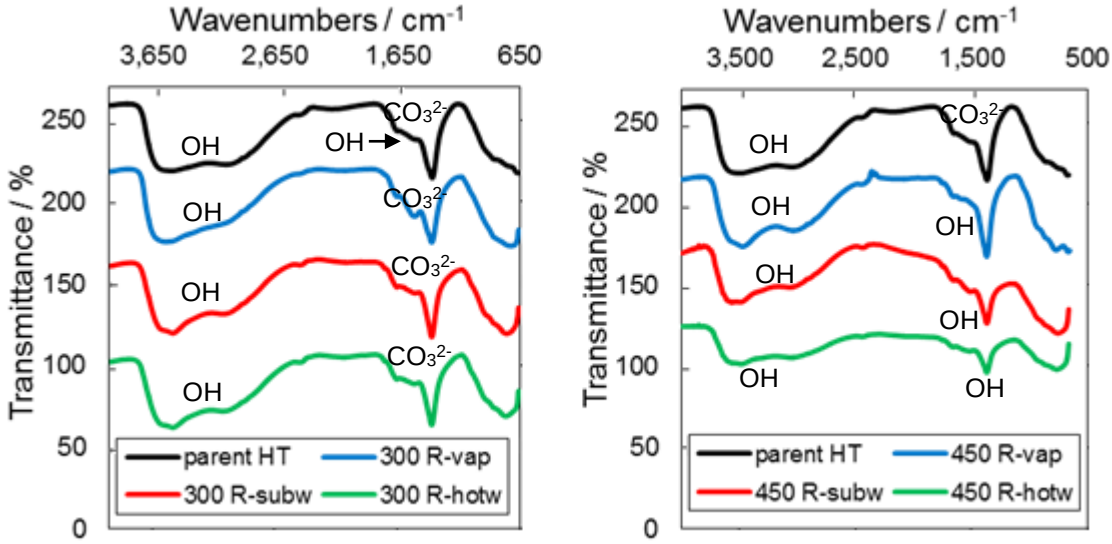

Figure 4.20: left – *ex-situ* DRIFT-IR spectra of parent uncalcined HT and 2 wt. % Au/CHT-RW series at 300 °C, right – *ex-situ* DRIFT-IR spectra of parent uncalcined HT and 2 wt. % Au/CHT-RW series at 450 °C, showing that hydrotalcite phase was successfully reconstructed.

In the case of meixnerite[4] materials, this shoulder band becomes more intense as the calcination temperature before the following rehydration increases, showing its highest intensity for CHT450Vap samples. This increase in intensity was attributed to partial replacement of CO_3^{2-} with –OH ions[31], suggesting the formation of stronger hydrogen bonds between vicinal –OH.

The OH bending of physisorbed water is visible at 1590 cm^{-1} for parent HT, while the two bands at 1497 cm^{-1} and 1331 cm^{-1} are due to the stretching of CO_3^{2-} in the interlayer region of the parent HT. As the calcination temperature before rehydration increases, the CO_3^{2-} band decreases, while the OH bending becomes sharper, confirming what observed for the stretching bands[16]. DRIFT-IR spectra did not show significant differences between CHT-RW at 300 or at 450 °C, being the reappearing of water and OH bands after rehydration the main information in each case. Differences between the two calcined and rehydrated materials at different temperatures could be observed in XRD patterns, **Chapter 4.2.4.2**, in surface areas, as observed in **Chapter 4.2.4.3** and after CO_2 TPD analysis, as it will be discussed in **Chapter 4.2.4.7.**

4.2.4.6 TGA and dTGA

TGA and dTGA profiles for 2 wt. % Au/CHT at 300 °C or at 450 °C and rehydrated in three different ways series can be seen below in **Figure 4.21**; dTGA peak areas were analysed using Origin software.

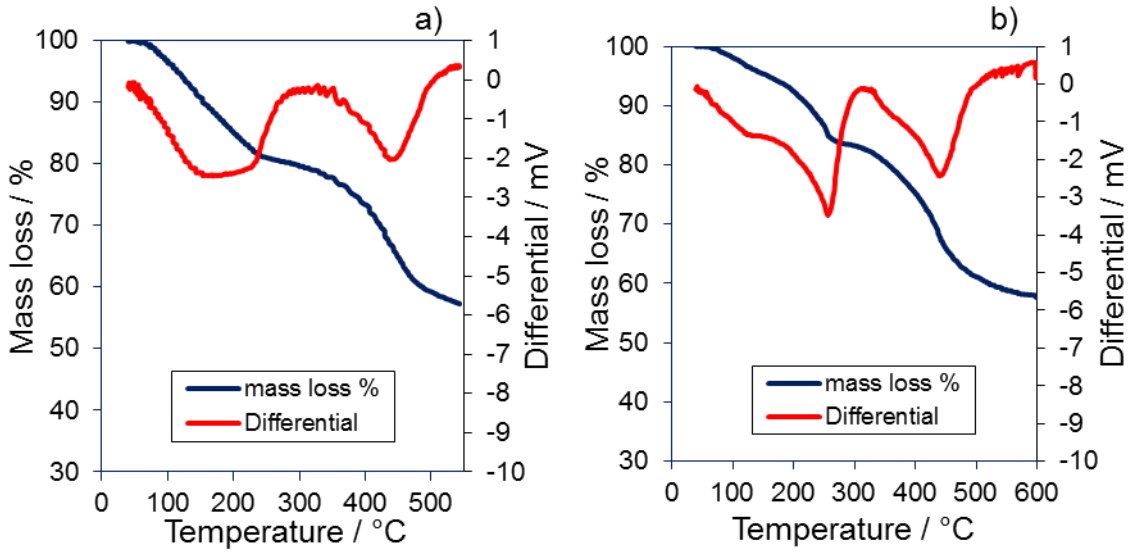

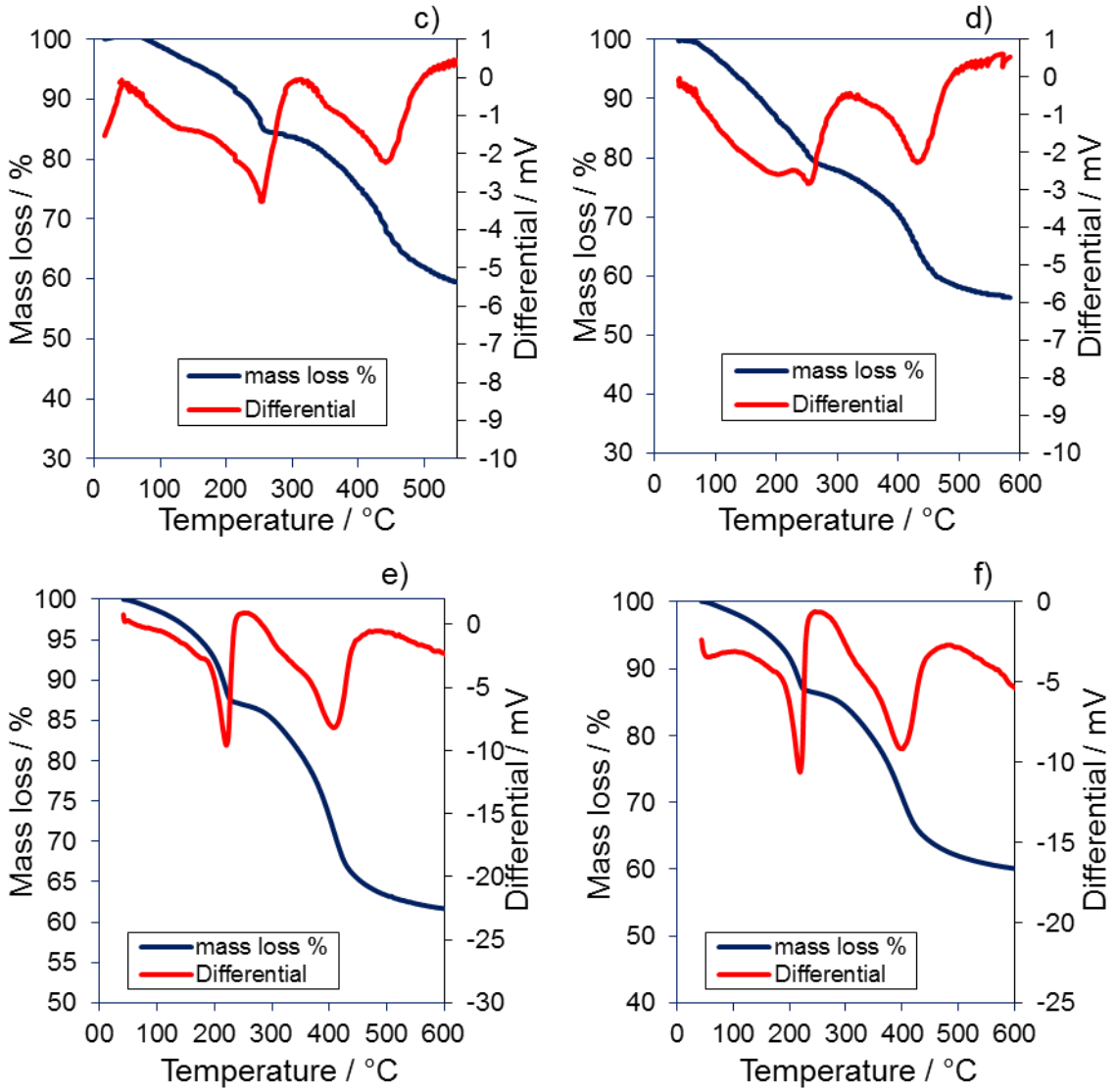

Figure 4.21: Thermogravimetric analysis (TGA) and dTGA of 2 wt. % Au on CHT a) calcined at 300 °C and rehydrated in aqueous vapour phase, b) calcined at 300 °C and rehydrated in subcritical water c) calcined at 300 °C and rehydrated in hot water d) calcined at 450 °C and rehydrated in aqueous vapour phase e) calcined at 450 °C and rehydrated in subcritical water f) calcined at 450 °C and rehydrated in boiling water.

The TGA analysis carried out on these materials has shown a two- or three-stage loss of weight[2, 20, 28, 52], typical of rehydrated hydrotalcites containing hydroxide as the interlayer anions[15]. The first weight loss, between about 70 ºC and 220 ºC, was attributed to the loss of water molecules adsorbed to the hydrotalcite surface, as well as interlayer water.

For CHT at 300 °C RW series, the loss of weight at higher temperatures, between 315 and 490 °C was attributed to the loss of hydroxide anions and carbonates from within the brucite-like layers, while for CHT at 450 °C RW is attributed to the loss of hydroxides anions, being the carbonates removed during the catalyst preparation; results are shown in **Table 4.9**.

Table 4.9: loss of weight values and their respective temperatures obtained by TGA and dTGA analysis for 2 wt. % Au on CHT-RW catalysts.

	Temperature 1st loss / °C	1st loss of weight (from total) / %	Temperature 2nd loss / °C	2nd loss of weight (from total) / %
CHT300Vap	205	19.4	428	19.5
CHT300Subw	252	16.7	430	21.3
CHT300Hotw	248	15.9	426	20.5
CHT450Vap	245	22.0	419	18.8
CHT450Subw	216	12.9	396	22.2
CHT450Hotw	214	13.7	388	23.2

It is already evident from values in **Table 4.9** that rehydration in vapour phase was capable of introducing more water than its analogue in hot water or in subcritical conditions, both for calcination at 300 and 450 °C, as it was carried out under aqueous nitrogen steam that prevented carbonates to go in the interlayers during the HT-phase reconstruction.

Further proof is given considering dTGA diagrams for catalysts series calcined at 300 °C, whereas the water region appears broader when the rehydration occurs in vapour phase, suggesting a major closure of micropores and mesopores by agglomeration of platelets, confirmed by N_2 porosimetry **(Chapter 4.2.4.3)**; while it is sharper in the other two cases, suggesting minor closure, due to the presence of carbonates. The OH and carbonates region shows, instead, the opposite behaviour. These differences are more evident when catalysts are calcined at 450 °C prior to rehydration, as the amount of removed carbonates at that temperature is higher.

While the desorption temperature minimum in the OH and carbonates region is almost always the same in the case of catalysts treated at 300 °C, in the range of experimental error, a shift at lower temperatures occurs for catalysts treated at 450 °C, suggesting a decrease in base strength[44] from CHTVap to CHTSubw or CHTHotw. These considerations will be confirmed with TPD analysis in **Chapter 4.2.4.7.**

4.2.4.7 Surface basicity

CO_2 pulse chemisorption and following TPD analysis were used to calculate the base site density and strength[1, 3, 15] for CHT calcined at 300 or 450 °C and rehydrated in vapour phase, boiling water or subcritical water. As already mentioned in **Chapter 3.2.3.7**, CO_2 is an acidic probe molecule and it is assumed that each molecule of CO_2 adsorbs onto one base site of the HT, or CHT, or CHT-RW materials, forming a bicarbonate species with the hydroxide anions, or surface hydroxyl groups, or surface oxides.

Known volumes of CO_2 were injected on an out-gassed sample of catalyst until saturation of the surface, then the sample was heated up to 550 ºC and the desorbing CO_2 measured using a TCD detector, to obtain the base site strength.

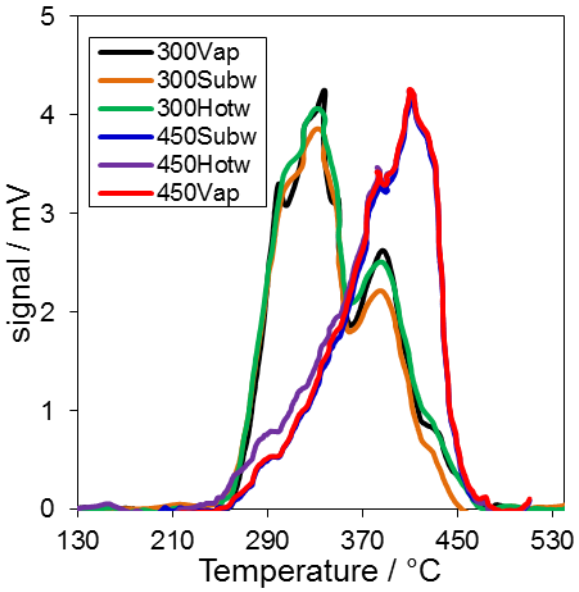

Figure 4.22: CO_2 TPD profiles for 300 vs. 450 °C CHT-RW series, in vapour phase or in boiling water or in subcritical water.

As shown in **Figure 4.22**, it is evident that all the CHT-RW at 450 °C were similar and show stronger base sites than the similar materials at 300 °C, the desorption temperature being higher for stronger bases. TPD data were therefore further analysed and areas were integrated using CASA software, to quantify the amount of weak, medium and strong base sites per catalyst, assuming that a molecule of CO_2 can bind as bicarbonate species on the surface hydroxyls in the lattice (weak sites), or as bicarbonate species on the interlayer anions (medium sites) or as mono- and bidentate species on strong oxides sites. Results are shown in **Table 4.10** for 2 wt. % Au/CHT-RW series.

Table 4.10: base site strength percentage distribution for 2 wt. % Au/CHT-RW series.

Catalyst	Weak sites / % (200-280 °C)	Medium sites / % (280-380 °C)	Strong sites / % (380-450 °C)
CHT200	-	92.8	7.2
CHT300	-	71.9	28.1
CHT300Vap	-	74.1	25.9
CHT300Subw	-	77.2	22.8
CHT300Hotw	-	79.2	20.8
CHT450Vap	-	59.7	40.3
CHT450Subw	-	62.2	37.8
CHT450Hotw	-	60.1	39.9

Table 4.11 shows, instead, normalised data per surface area, to obtain a significant comparison. The strength of the base sites increases as the temperature of calcination increases, as previously reported in the literature[36, 37] and as observed in **Chapter 4.2.3.5.**

Table 4.11: normalised number of strong sites per surface area of catalyst for 2 wt. % Au/CHT-RW series and maximum temperature for strong sites.

Catalyst	Strong sites / m^{-2}	T max for strong sites / °C
CHT200	1.26×10^{17}	390
CHT300	9.19×10^{17}	400
CHT300Vap	1.39×10^{17}	385
CHT300Subw	1.09×10^{17}	383
CHT300Hotw	1.03×10^{17}	383
CHT450Vap	6.88×10^{17}	410
CHT450Subw	4.52×10^{17}	408
CHT450Hotw	5.99×10^{17}	408

4.2.4.8 Surface chemical analysis

XPS analysis was run on the parent hydrotalcite, used as a fitting model, and then on 2 wt. % Au supported on CHT–RW series. **Figure 4.23** shows the Mg 2p region for a) CHT300Hotw and CHT450Hotw b) CHT300Vap and CHT450Vap c) CHT300Hotw and CHT450Hotw. Mg 2p was fitted by a double chemical environment containing the spin-orbit 2p doublet (separation = 0.28 eV), one with binding energies of 49.4 and 49.7 eV, attributed to Mg-OH in hydrotalcite-like phase after rehydration (NIST database[39] 50.40 eV for $MgAl_2O_4$ spinel, 49.50-49.90 eV for Mg hydrotalcite) and one at binding energies of 50.8 and 51.1 eV, attributed to loss of physisorbed water and loss of carbonates in the HT interlayers to form mixed oxides[14, 15], as observed in **Chapter 4.2.3.6.**

The presence of not rehydrated mixed oxides in all the catalysts suggested that the calcination-rehydration process was incomplete when the calcination temperature chosen was 300 °C.

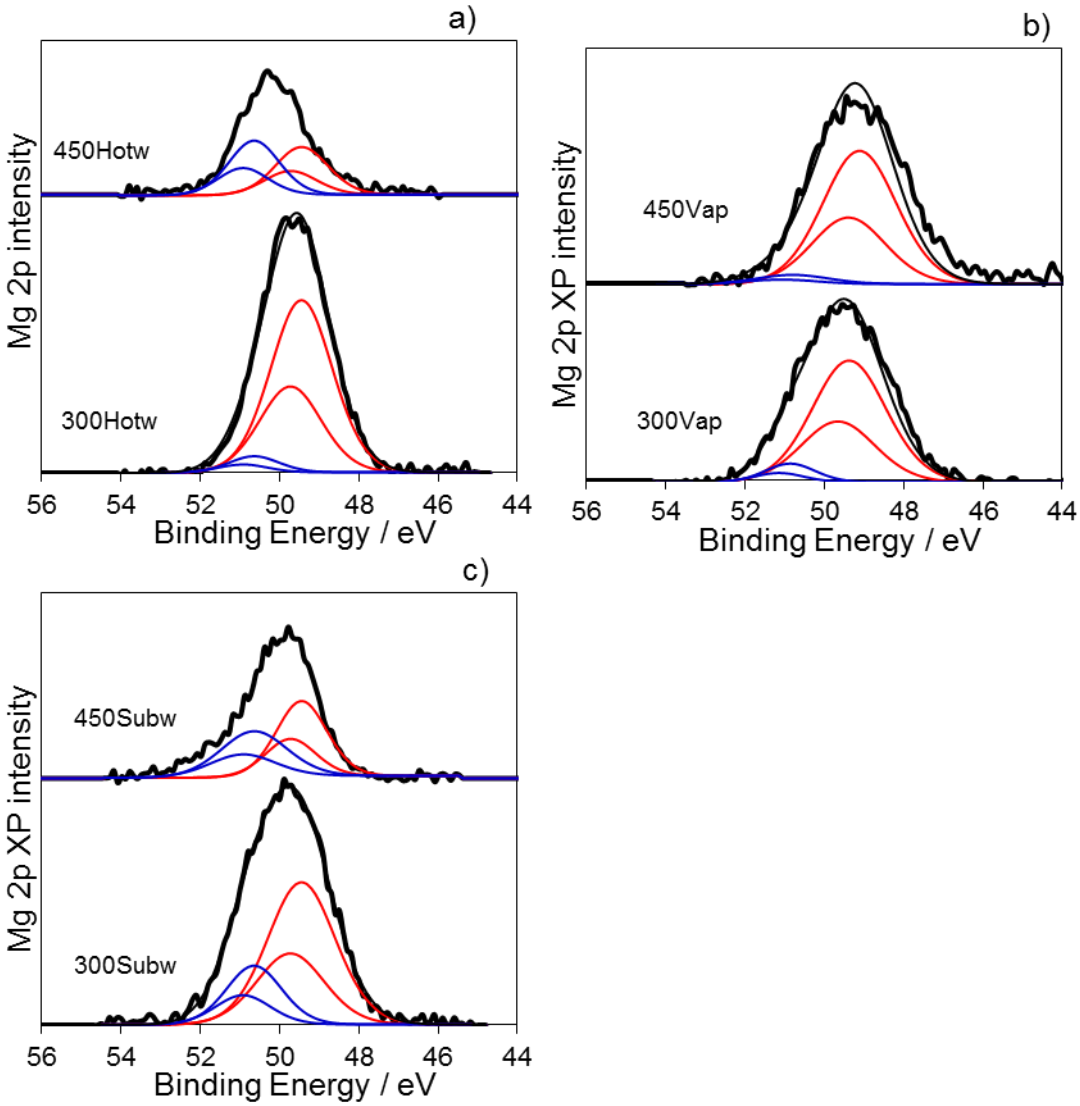

Figure 4.23: high resolution XP spectra**,** showing the Mg 2p chemical environment for a) CHT300Hotw and CHT450Hotw b) CHT300Vap and CHT450Vap c) CHT300Subw and CHT450Subw.

Table 4.12 reports all the exact measured maximum values for each CHT-RW; for the HT-phase, shifts in Mg 2p binding energy were observed between samples rehydrated under aqueous vapour phase (lower B. E.) and the ones rehydrated either in boiling water or in subcritical water (higher B. E.). This was attributed to a major CO_3^{2-} replacement by OH^- anions in the case of CHTVap, due to the presence of inert nitrogen atmosphere that prevented the formation of carbonates in the interlayers. The presence of a higher amount of carbonates was confirmed by elemental analysis, as discussed in **Chapter 4.2.4.1** and by TGA in **Chapter 4.2.4.6.**

An opposite trend, instead, was observed for mixed Mg_3Al oxides, meaning that for CHTVap the amount of available oxides (higher B.E.) was higher than the other two cases (lower B.E.), in which carbonates contaminate the formed oxides.

Table 4.12: measured Mg 2p maximum B. E. values for each CHT300 – RW.

CHT 300	Mg $2p_{1/2}$ / eV	Mg $2p_{3/2}$ / eV	Mg $2p_{1/2}$ / eV	Mg $2p_{3/2}$ / eV
Vap	49.66	49.38	51.14	50.86
Hotw	49.72	49.44	50.92	50.64
Subw	49.72	49.44	50.92	50.64

Analogous considerations should be done to explain the Mg 2p fitting for CHT450 – RW series shown in **Figure 4.23**, whereas the best HT-like phase reconstruction, yielding higher purity meixnerite materials, was achieved when aqueous vapour phase under nitrogen was chosen, confirming observations made in **Chapter 4.2.4.2. Table 4.13** reports all the exact measured maximum values for each CHT450 – RW, the discussion of which agrees with what previously observed for CHT300 – RW.

Table 4.13: measured Mg 2p maximum B. E. values for each CHT450 – RW.

CHT 450	Mg $2p_{1/2}$ / eV HT	Mg $2p_{3/2}$ / eV HT	Mg $2p_{1/2}$ / eV oxides	Mg $2p_{3/2}$ / eV oxides
Rvap	49.39	49.11	51.08	50.80
Rhotw	49.72	49.44	50.92	50.64
Rsubw	49.72	49.44	50.92	50.64

The Al 2s spectra **(Figure 4.24)** of CHT300 – RW series was likewise fitted by a double chemical environment; the binding energy of 118.2 eV was attributed to HT-like phase and the one of 120.2 eV was attributed to mixed Mg_3Al oxides (NIST database[39] 119.50 eV for Al_2O_3, 119.10 eV for $MgAl_2O_4$; 118.5 eV for HT-phase, Cantrell and co-authors[14]). Analogous considerations are valid for the Al 2s spectra of CHT450 – RW series.

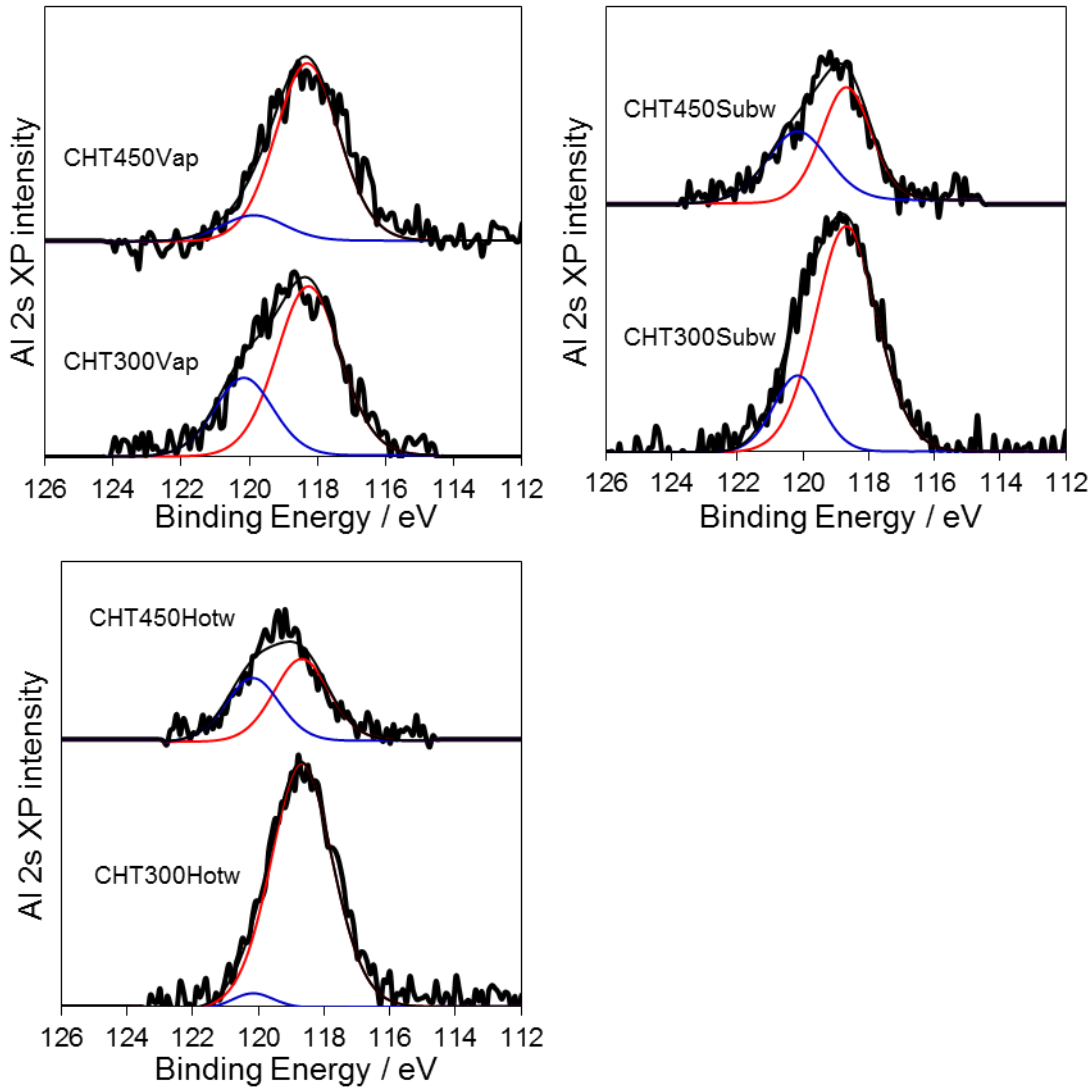

Figure 4.24: high resolution XP spectra, showing the Al 2s chemical environment for a) CHT300Vap and CHT450Vap, b) CHT300Subw and CHT450Subw c) CHT300Hotw and CHT450Hotw.

Table 4.14 reports all the exact measured maximum values for each CHT300 – RW and CHT450 – RW series. Shifts in Al 2s binding energy were observed between samples rehydrated under aqueous vapour phase (lower B. E.) and the ones rehydrated either in boiling water or in subcritical water (higher B. E.); these are more evident for samples calcined at higher temperatures. An opposite trend, instead, was observed for mixed Mg_3Al oxides, confirming all the considerations done for Mg.

Table 4.14: measured Al 2s maximum B. E. values for CHT300 – RW and CHT450 – RW series.

CHT 300	Al 2s HT-like / eV	Al 2s Mixed oxides / eV
Rvap	118.16	120.06
Rhotw	118.68	120.17
Rsubw	118.68	120.17
CHT 450	Al 2s HT-like / eV	Al 2s Mixed oxides / eV
Rvap	118.29	119.88
Rhotw	118.69	120.17
Rsubw	118.69	120.17

The analysis of O 1s spectra comprised two or three distinct chemical components, depending on the material. For CHT 300Vap **(Figure 4.25),** one was attributed to the O^{2-} of HT and carbonates, with a binding energy of 531.55 eV, (NIST database[39] 531.50 eV for $MgAl_2O_4$ spinel and for $MgCO_3$), the second one attributed to hydroxyls with a lower binding energy of 530.17 eV (NIST database[39] 530.90 eV for $Mg(OH)_2$, 529.3-530.9 eV for OH in hydrotalcite phase, Cantrell and co-authors[14]). The third chemical component, with a lower binding energy of 528.96 eV was attributed to O^{2-} in Mg_3Al oxides[41, 42]. (NIST database[39] 530.60-529.60 eV for MgO) This new component was visible only for CHT300Vap, confirming the presence of not rehydrated mixed oxides, but it was not detected for materials rehydrated in water **(Figure 4.25)**.

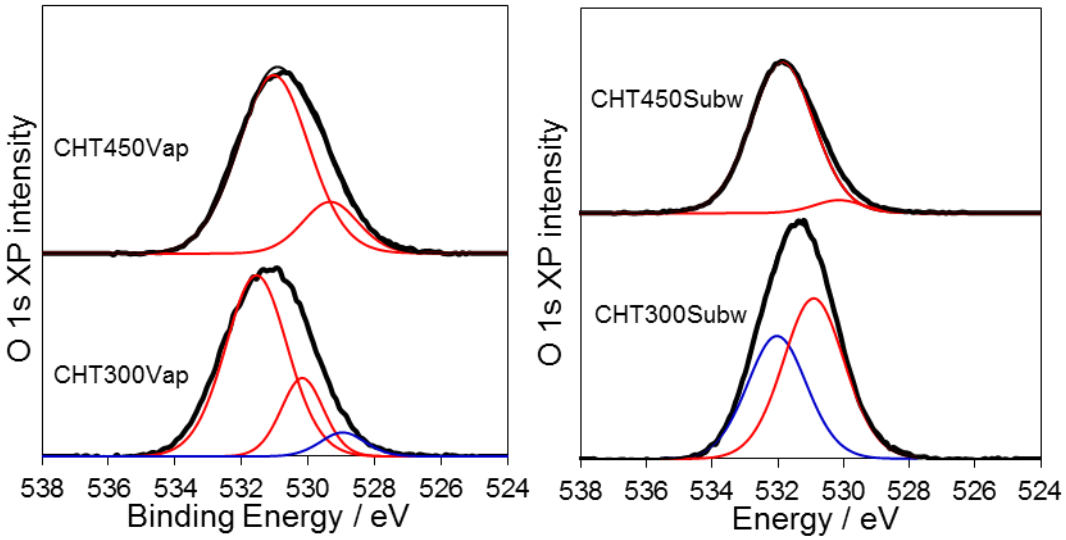

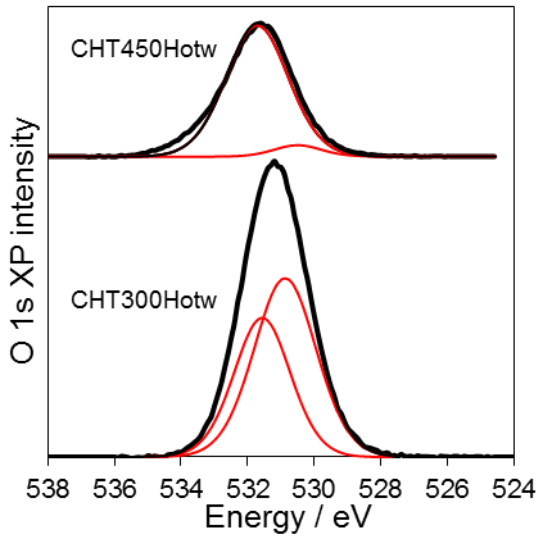

Figure 4.25: high resolution XP spectra, showing the O 1s chemical environment for a) CHT300Vap and CHT450Vap b) CHT300Subw and CHT450Subw c) CHT300Hotw and CHT450Hotw, highlighting the high binding energy CO_3^{2-}, the low binding energy OH^- and the lower binding energy O^{2-} states.

Similar considerations should be done for CHT450 – RW catalyst series, **(Figure 4.25)** even if, at this calcination temperature, no traces of mixed oxides were visible, suggesting a better rehydration and reconstruction of HT-like structure.

As already described in **Chapter 3.2.3.8**, the Au 4f region was fitted by creating three distinct chemical environments. The first one was fitted with two components for the doublet of Au 4f orbitals (doublet separation = 3.70 eV), then two others were necessary to subtract the Mg 2s contribution, that overlaps in the same region, respectively one for Mg in HT and one for Mg in CHT-RW phase. All the binding energy values for Au 4f are shown in **Table 4.15** and confirmed the presence of metallic gold (NIST database[39] $CsAuCl_4$ (Au^{3+}) 87.5-91.2 eV, Au foil 84.0-88.0 eV).

Table 4.15: Au 4f 7/2 and 5/2 binding energy for 2 wt. % Au on CHT 300 °C and rehydrated in three different ways.

2 wt. % Au supported on	Au 4f 5/2 B.E / eV	Au 4f 7/2 B.E / eV
CHT200	86.92	83.21
CHT300	86.65	82.95
CHT300Vap	86.46	82.76
CHT300Subw	86.88	83.18
CHT300Hotw	86.55	82.85

Figure 4.26 shows a comparison of XPS spectra for nominal 2 wt. % Au/CHT 300 or 450 °C and rehydrated in aqueous vapour phase, in boiling water or in subcritical water. Gold leaching for liquid phase rehydration protocols was discussed in **Chapter 4.2.4.1.**

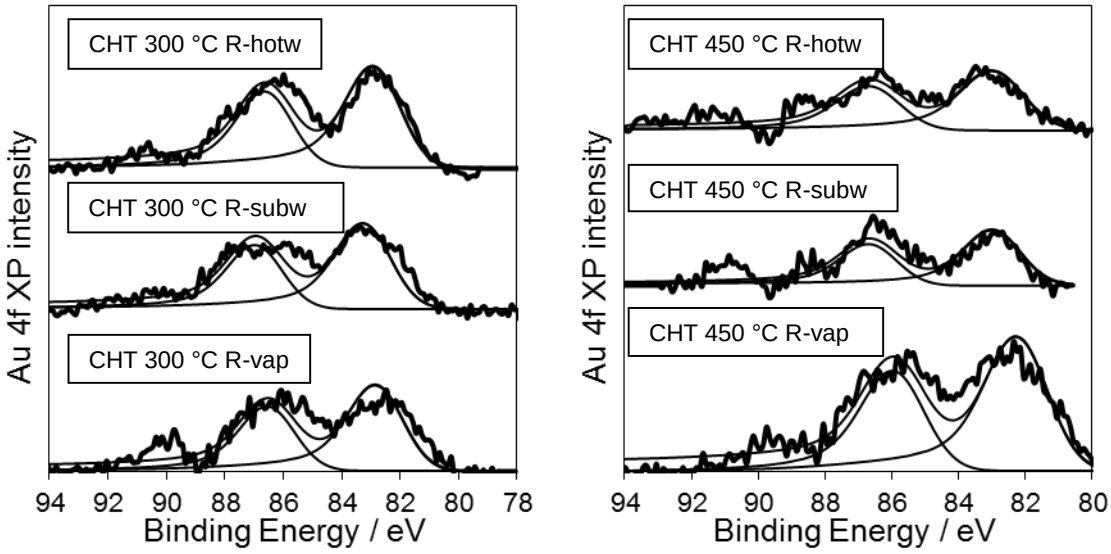

Figure 4.26: high resolution XP spectra, showing the Au 4f chemical environment for the 2 wt. % Au on CHT 300 °C R-vap, R-hotw or R-subw (left) and for their analogous at 450 °C (right).

4.2.5 Characterisation of different wt. % Au loadings on CHT450Vap

4.2.5.1 Elemental analysis

Five different Au loadings, respectively 0.5, 1, 2, 5 and 10 wt. %, were supported on HT *via* DP method[18] and calcined at 450 °C under O_2 flow, then rehydrated in aqueous vapour phase, under N_2 at room temperature. XPS surface and

XRF bulk analysis were run initially on the parent HT, then on the Au/CHTVap materials. **Table 4.16** shows bulk and surface values for gold elemental analysis.

Table 4.16: elemental analysis of different wt. % Au loaded on CHT450Vap, obtained by XPS (surface) and XRF (bulk) composition.

Nominal wt. % Au loading on CHT450Vap	XPS / wt. % (surface)	XRF / wt. % (bulk)
0.5	0.7	0.6
1	1.1	1.3
2	2.2	2.4
5	4.8	6.2
10	10.0	9.3

The nominal amount of gold was verified to agree with the effective expected one, XPS and XRF elemental analysis showing also a good agreement between bulk and surface composition in the range of experimental error, as shown in **Figure 4.27**.

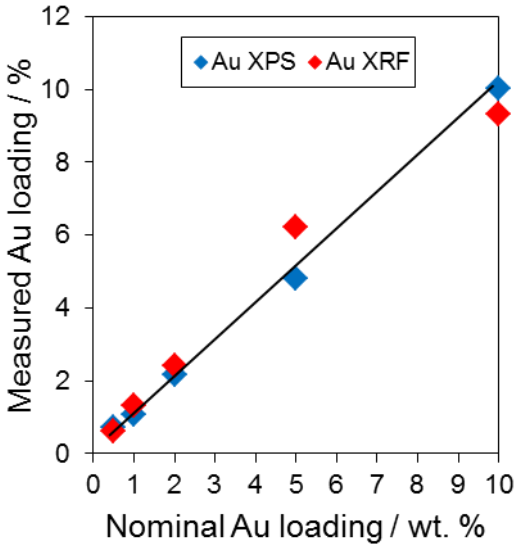

Figure 4.27: nominal vs. measured Au loading on CHT450Vap.

Table 4.17, instead, summarises XPS elemental analysis values for the same catalyst series, showing all the elements for an accurate characterisation. The average value of Mg/Al (atomic %) was found to be 3.4 ± 0.3.

Table 4.17: elemental analysis of different wt. % Au loaded on CHT450Vap, obtained by XPS (surface) composition, all elements shown.

0.5 wt.% Au CHT450Vap	Element / wt.%	1 wt.% Au CHT450Vap	Element / wt.%	2 wt.% Au CHT450Vap	Element / wt.%
Mg	27.6	Mg	27.3	Mg	28.4
Al	7.9	Al	8.0	Al	8.2
O	54.6	O	54.6	O	53.1
C	8.1	C	7.9	C	6.9
Cl	1.1	Cl	1.1	Cl	1.2
Au	0.7	Au	1.1	Au	2.2

5 wt.% Au CHT450Vap	Element / wt.%	10 wt.% Au CHT450Vap	Element / wt.%
Mg	26.9	Mg	23.3
Al	8.0	Al	7.6
O	51.6	O	50.8
C	7.4	C	6.7
Cl	1.3	Cl	1.5
Au	4.8	Au	10.0

4.2.5.2 XRD

Ex situ powder X-ray diffraction was run on the parent HT and on Au/CHTVap series **(Figure 4.28)** to study the reconstruction of hydrotalcite phase and to estimate the average gold particle size *via* Scherrer analysis[24]. The parent hydrotalcite exhibited a series of reflections at 11.2° (*d* 003), 22.4° (*d* 006), 34.2° (*d* 009), 38.3° (*d* 015), 44.6° (*d* 018), 60.1° (*d* 110), 61.3° (*d* 113) and 64.7° (*d* 116). As already discussed in **Chapter 4.2.3.2,** no impurities of Mg and Al oxides or carbonates were detected for this Mg_3Al hydrotalcite, showing a pure HT phase[2, 4, 19, 28, 43].

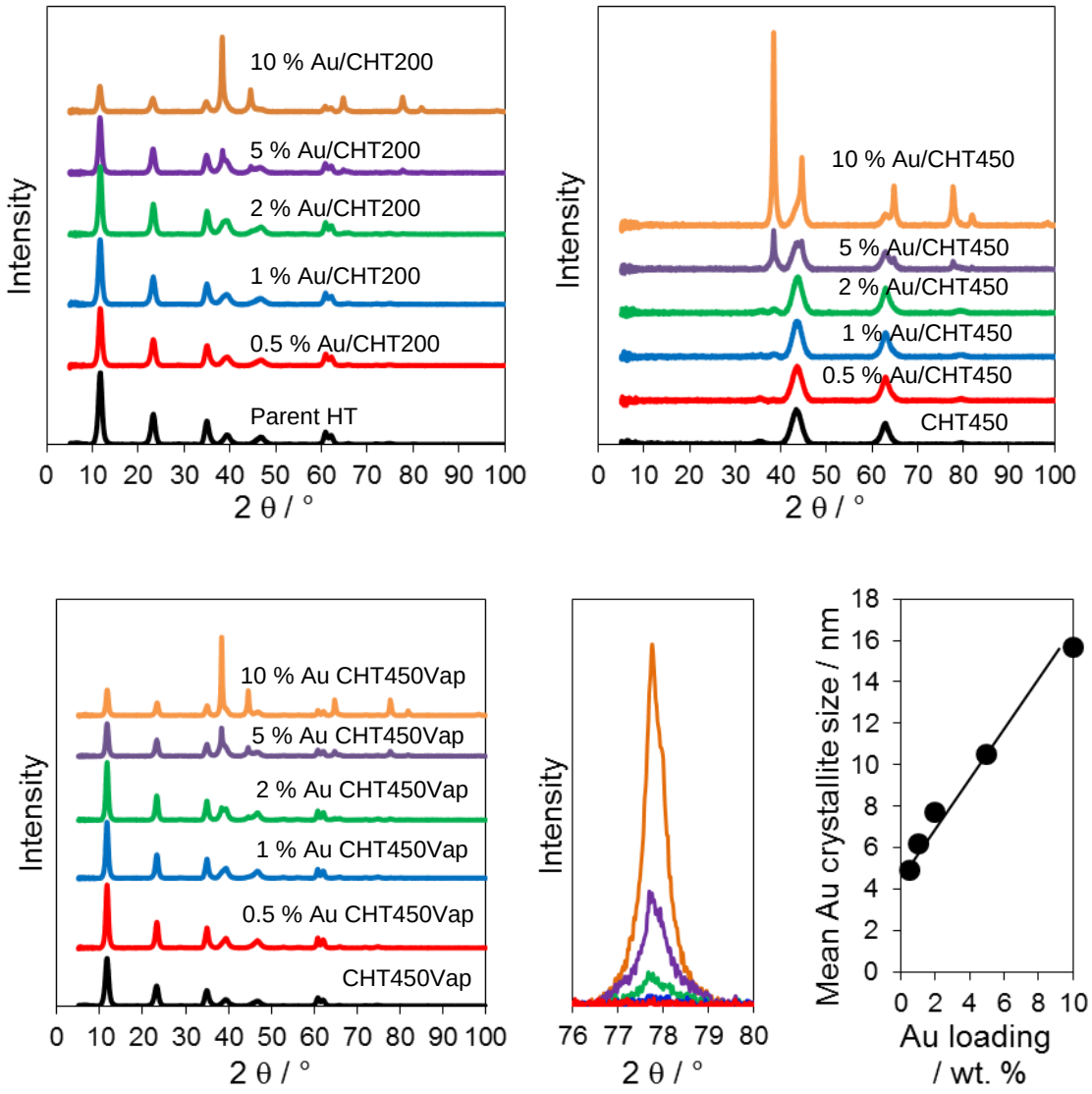

Figure 4.28: top left – XRD patterns of different gold wt. % loading on HT calcined at 200 °C, top right – after calcination at 450 °C, mixed MgAl oxides were formed; bottom left – after rehydration in aqueous vapour phase, HT-like structure was reconstructed successfully. Middle: evolution of Au reflections, bottom right – average Au particle size vs. Au loading.

As already observed in **Chapter 3.2.3.2**, gold peaks overlap with hydrotalcite ones and their intensity increases as the gold loading increases. After a calcination at 450 °C, all the hydrotalcites became mixed Mg_3Al oxides and this is evident because HT peaks disappeared; then, the vapour phase rehydration yielded a good reconstruction of the HT-like phase. As discussed in **Chapter 4.2.3.5**, after rehydration all the typical HT peaks were clearly visible again, being the overall result a replacement of carbonates with hydroxide species and the formation of meixnerite[4].

The intensity of Au peaks, that usually are visible at 38° (*d* 111), 44° (*d* 200), 65° (*d* 220) and 78° (*d* 311), increases with Au loading; nevertheless, these peaks overlap with HT ones and are not visible for low gold loading. Thus, a sample of parent CHT450Vap was used as the background and subtracted, to allow peaks at 78°, the less affected by HT contribute, to be fitted using CASA software and find the average Au particle size *via* Scherrer analysis, showing an increase of Au particle size as the gold loading increases **(Figure 4.28 – bottom right)**.

4.2.5.3 N_2 Porosimetry

N_2 adsorption-desorption isotherms for the parent HT and for CHT450Vap can be seen in **Figure 4.29,** while **Figure 4.30** shows isotherms for different gold loadings supported on CHT450Vap. The isotherms have been offset for clarity.

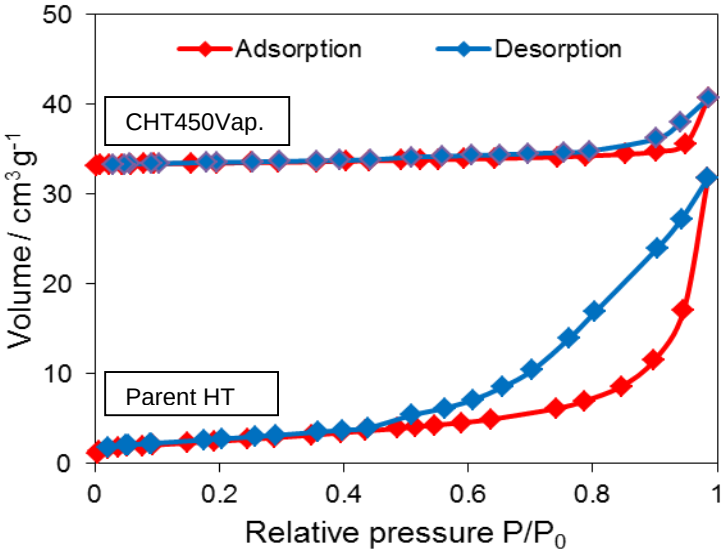

Figure 4.29: N_2 porosimetry isotherms for parent hydrotalcite vs. CHT450Vap. It is evident a minor hysteresis after CHT-RW process and a drop off in surface area.

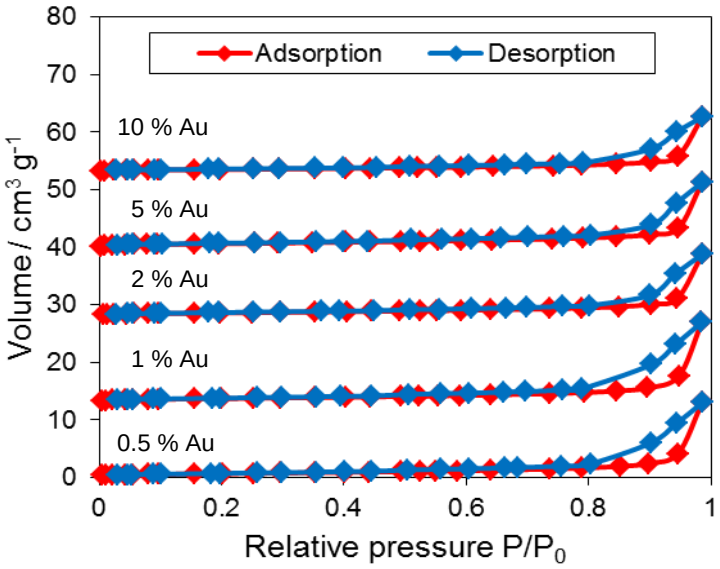

Figure 4.30: N_2 porosimetry isotherms for 0.5, 1, 2, 5 and 10 wt. % Au loading, supported on CHT at 450 °C and rehydrated at room temperature in aqueous vapour phase, under N_2 flow.

The parent hydrotalcite shows type II H3 isotherm, that remains before and after Au deposition-precipitation, consistent with microporous crystallites with interplatelet mesoporous voids and slit type pores[53]. All the considerations in **Chapter 4.2.4.3** are valid to explain this behaviour; **Table 4.18** shows surface areas for these materials.

Table 4.18: surface area values for parent HT and different wt. % gold loading on CHT at 450 °C and rehydrated in aqueous vapour phase, as determined by N_2 porosimetry.

	BET surface area / m^2g^{-1}
Parent HT	95 ± 9.5
CHT450Vap	20 ± 2.0
0.5 wt.% Au/ CHT450Vap	24 ± 2.4
1 wt.% Au/ CHT450Vap	27 ± 2.7
2 wt.% Au/ CHT450Vap	25 ± 2.5
5 wt.% Au/ CHT450Vap	27 ± 2.7
10 wt.% Au/ CHT450Vap	22 ± 2.2

No significant variations of surface areas were visible, in the range of the experimental error, for different Au loading on CHTVap series.

4.2.5.4 TEM and Au particle size distribution

Dark/bright field (S)TEM images of different Au loading on CHT 450°C-Rvap series are shown in **Figure 4.31**.

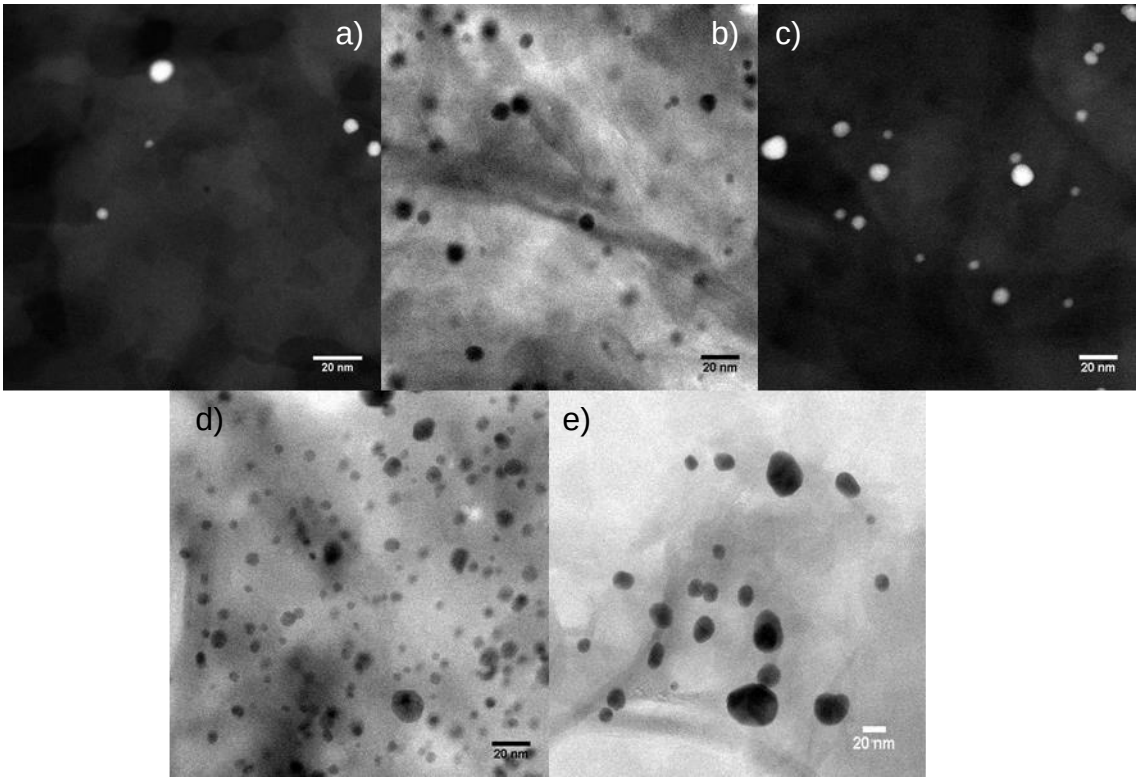

Figure 4.31: Dark/bright field (S)TEM images of (a) 0.5 wt. %, (b) 1 wt. %, (c) 2 wt. %, (d) 5 wt. % and (e) 10 wt% Au on CHT 450 °C R-vap catalysts.

ImageJ software was used to measure the particle size distribution for each material, and results are shown in **Figure 4.32**. The mean particle size increased with gold loading, resulting in a trend similar to that observed by XRD. Despite of what observed in **Chapter 3.2.3.4**, particles appear to be well dispersed for 0.5 and 1 wt. % Au loadings, growing and agglomerating at higher loadings to give a broad range of size. One of the possible explanations for this agglomeration is the minor space available, being the surface area of the support CHT-RW lower than the conventional HT one; the other is that, after thermal treatment at 450 °C, gold NPs start sintering, showing a growth.

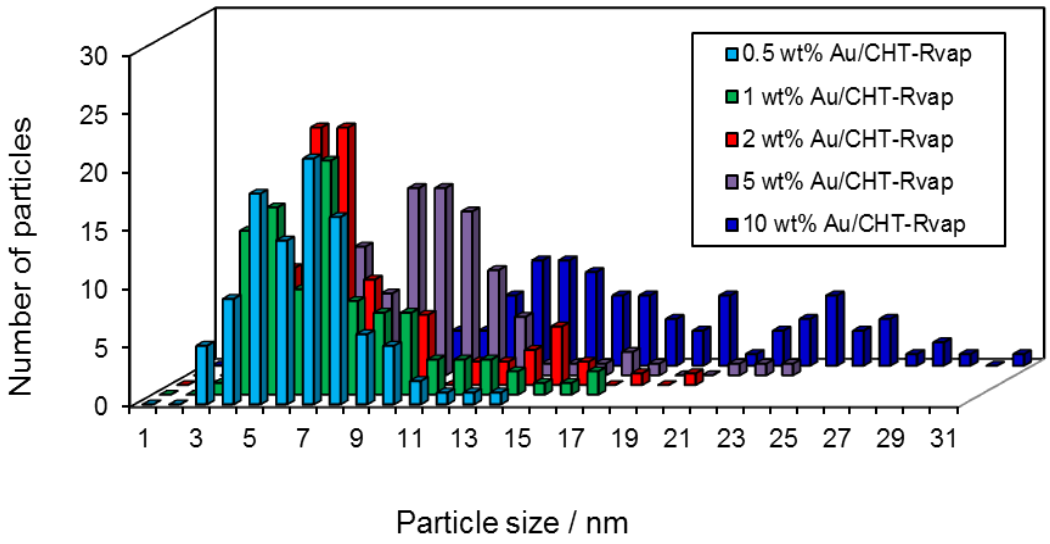

Figure 4.32: particle size distributions for different Au loadings supported on CHT450Vap; mean particle size increases with gold loading, showing broad distributions.

Figure 4.33 shows a comparison between average particle sizes obtained with Scherrer analysis and with TEM measurements.

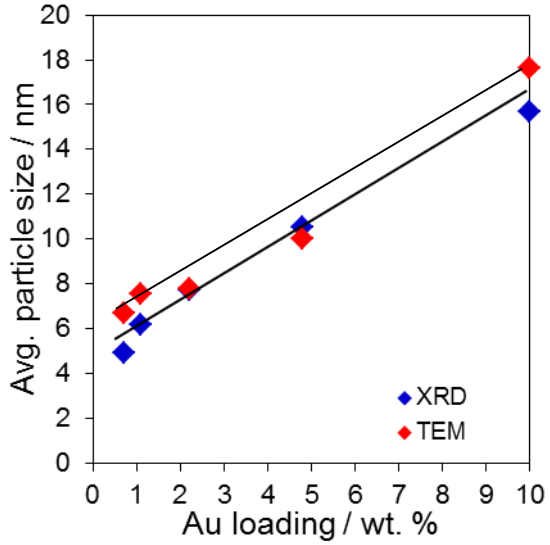

Figure 4.33: measured (TEM) and calculated (XRD) mean particle sizes for gold nanoparticles as a function of Au loading in Au/CHT450Vap. The fits look very similar, which shows good agreement between TEM and XRD measurements.

4.2.5.5 Ex situ DRIFT-IR spectra

Ex situ DRIFT-IR spectra shows differences between parent hydrotalcite, different gold loading on CHT at 450 °C **(Figure 4.34 - left)** and after rehydration in aqueous vapour phase; the peak attribution was made according to Meliàn-Cabrera and co-authors' paper[31] and according to Davis and co-authors' paper[16].

At 3800-2500 cm^{-1} the OH stretching is clearly visible for the parent hydrotalcite, the shoulder at 3080 cm^{-1} is characteristic of layered HT materials and is given by hydrogen bonding between the water molecules and CO_3^{2-} groups, both available in the interlayer region.

This band tends to disappear after calcination and becomes less intense, due to loss of OH from the interlayers; nevertheless, after rehydration of these materials, the band appears again and its intensity confirms the reconstruction of HT structure was successful, yielding meixnerite materials, for which this band is given by hydrogen bonding between water molecules.

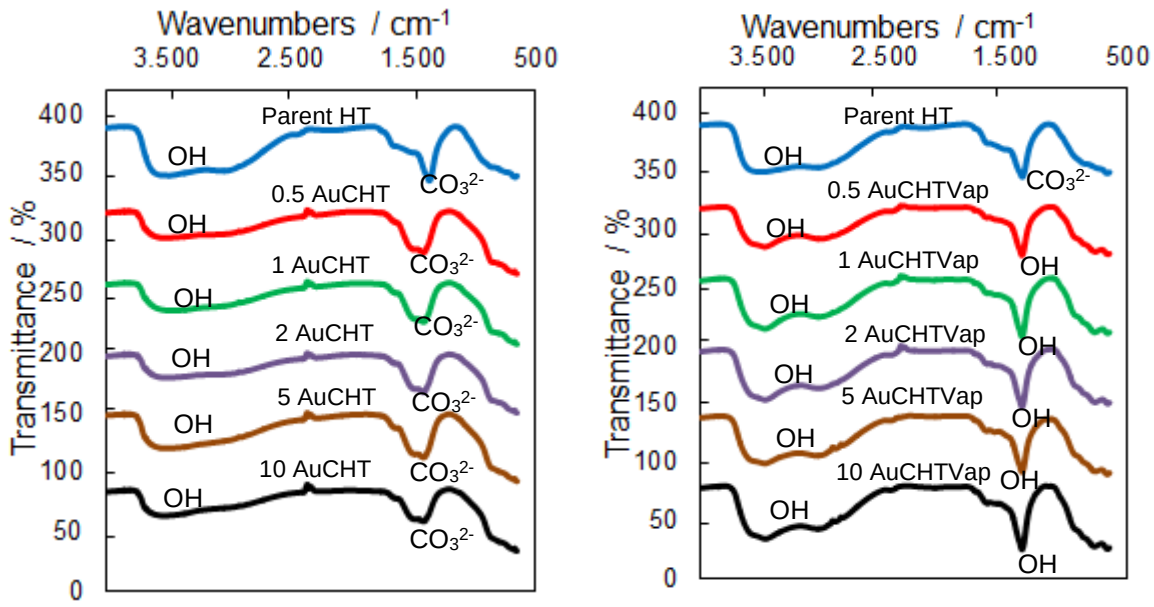

Figure 4.34: left – parent hydrotalcite and different gold loading on CHT450, right – the same samples after rehydration in aqueous vapour phase, under nitrogen and at room temperature.

For parent HT, the OH bending of physisorbed water is visible at 1590 cm^{-1}, while the two bands at 1497 cm^{-1} and 1331 cm^{-1} are due to the stretching of CO_3^{2-} in the interlayer region. The calcination caused an interlayer water removal and a carbonate rearrangement, justified by the absence of the previous shoulder in the OH region at 3080 cm^{-1} and the presence of a bending at 1590 cm^{-1}, then two new peaks appear, corresponding to C=O at 1508 cm^{-1} and to C-O at 1338 cm^{-1}, as previously observed in **Chapter 3.2.3.5.** No significant changes were visible across the different Au wt. % loading series on CHT and on CHTVap.

4.2.5.6 TGA and dTGA

TGA and dTGA profiles for different gold loading supported on CHT450Vap can be seen below in **Figure 4.35**; dTGA peak areas were analysed using Origin software.

The TGA analysis carried out on these materials has shown a two- or three-stage loss of weight[2, 20, 28, 52], typical of rehydrated hydrotalcites containing hydroxide as the interlayer anions[15]. For lower Au loading, the first weight loss between about 70 ºC and 220 ºC was a two-step, attributed to loss of physisorbed water (loss of water molecules adsorbed to the hydrotalcite surface), and to loss of interlayer water[54]; while a one-step

weight loss underwent for higher gold loading, showing a shift at slightly higher temperatures for the loss of interlayer water.

A loss of weight at higher temperatures, between 315 and 490 °C, was attributed to the loss of hydroxides anions, being the carbonates removed during the catalyst preparation, as already discussed in **Chapter 4.2.4.6.**

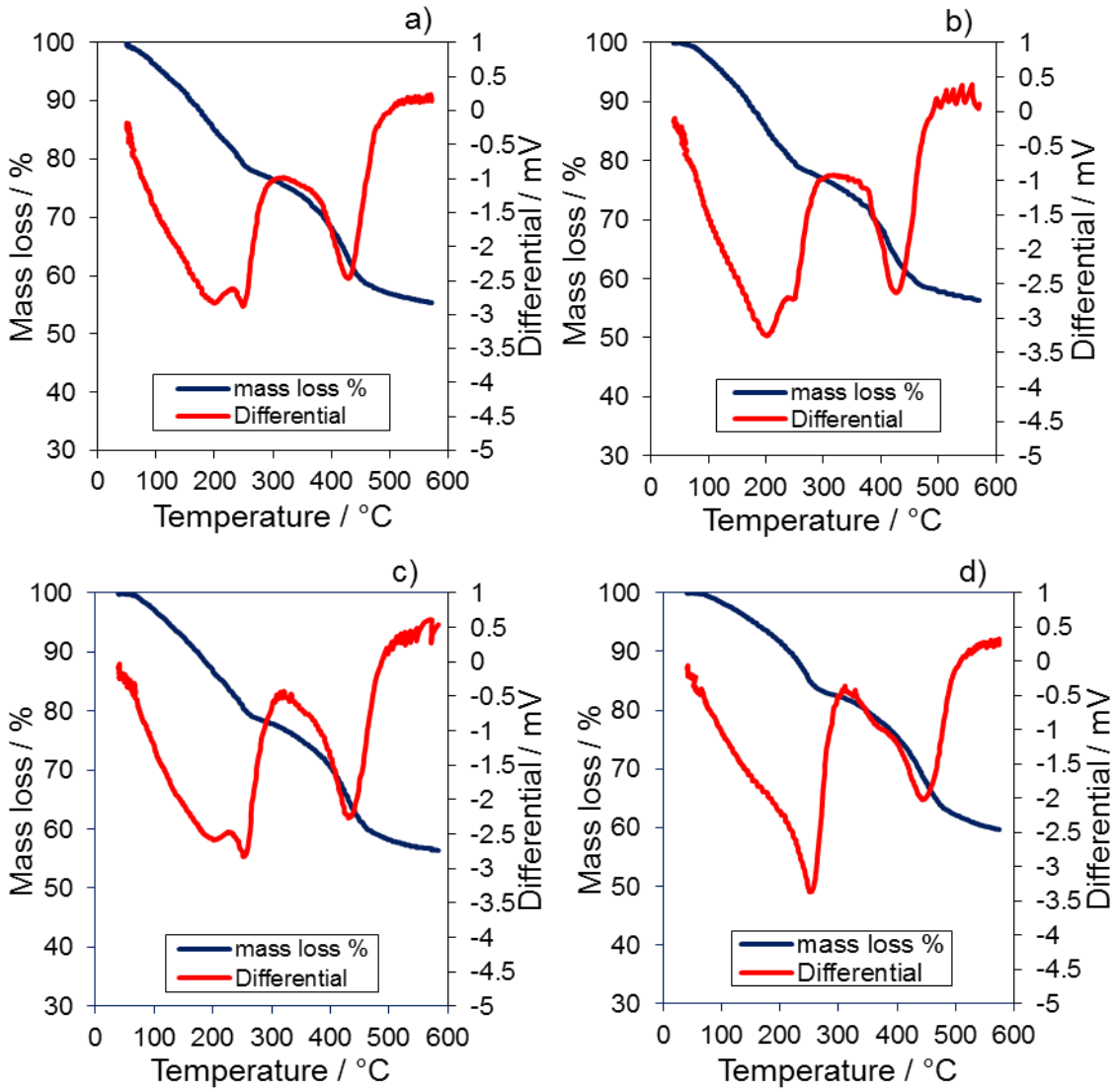

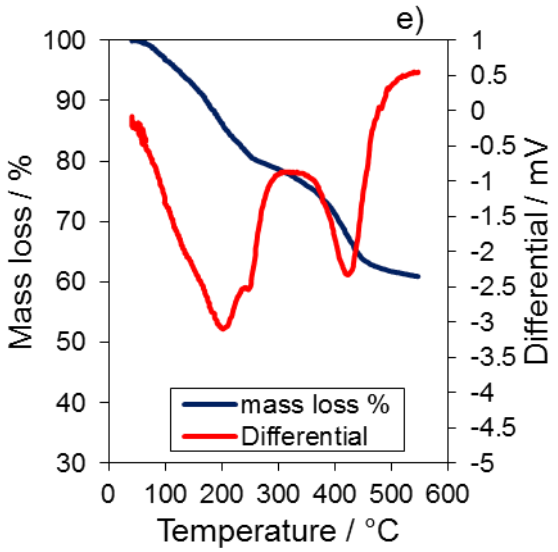

Figure 4.35: thermogravimetric analysis (TGA) and dTGA of different gold loadings on CHT 450 °C – Rvap. a) 0.5 wt. %, b) 1 wt. %, c) 2 wt. %, d) 5 wt. % and e) 10 wt. % Au.

Table 4.19 shows loss of weight values for Au/CHT 450 °C Rvap and temperatures. Similar considerations to what already explained in **Chapter 4.2.4.6** must be done to understand these data. An excess of gold per surface area might slow down water adsorption and the effect of rehydration, and so the reconstruction of HT-like structure.

Table 4.19: loss of weight values and their respective temperatures obtained by TGA and dTGA analysis for Au/CHT450Vap series.

Au CHT 450 °C Rvap / wt. % Au	Temperature 1st loss / °C	1st loss of weight (from total) / %	Temperature 2nd loss / °C	2nd loss of weight (from total) / %
0.5	179 - 243	20.3	419	16.8
1	188 - 238	18.2	416	15.7
2	183 - 237	22.0	419	18.8
5	246	17.5	435	19.9
10	190 -237	21.0	415	13.5

4.2.5.7 Surface basicity

CO_2 pulse chemisorption and following TPD analysis **(Figure 4.36)** were used to determine the base site density and strength for different Au/CHT-Rvap, as already described in **Chapter 4.2.3.5**[1, 3, 15].

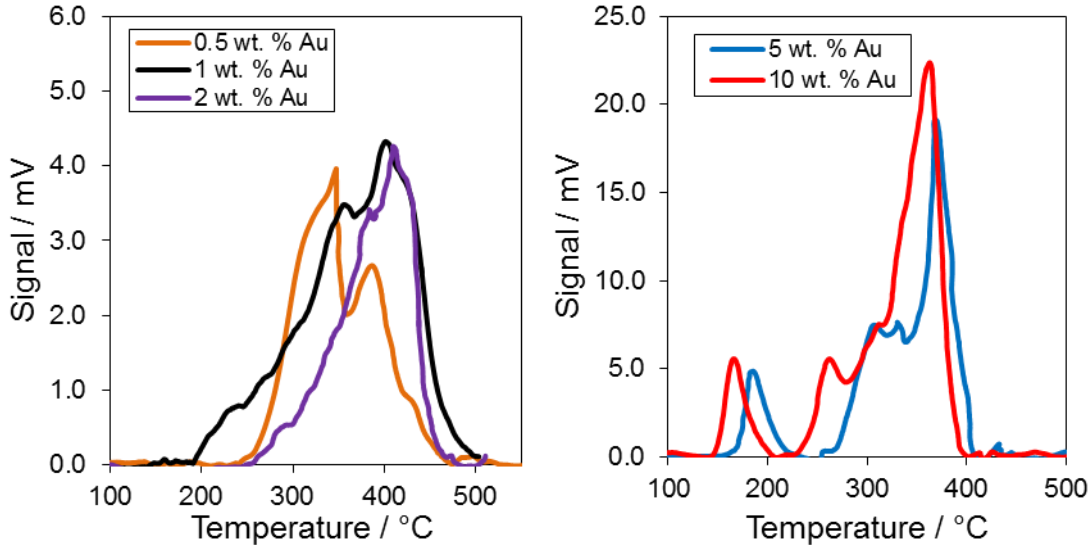

Figure 4.36: base site strength from CO_2 TPD as a function of Au loading in Au/CHT 450Vap catalysts.

The same calcination-rehydration in vapour phase procedure was followed in each case, but the resulting TPD profiles show similar results at lower gold loading. For 5 and 10 wt. % Au, a weaker site was detected, showing similarities with 10 wt. % Au/HT sample described in **Chapter 3.2.3.7. Table 4.20** summarises base site strength percentage values for these materials.

Table 4.20: base site strength percentage distribution for different wt. % Au/CHT - Rvap series.

Au/CHT Vap / wt. %	Weak sites / % (200-280 °C)	Medium sites / % (280-380 °C)	Strong sites / % (380-450 °C)
0.5	-	67.0	33.0
1	-	66.1	33.9
2	-	59.7	40.3
5	24.2	75.8	-
10	18.0	82.0	-

For high gold loading, 5 and 10 wt. % respectively, no strong sites were detected; this information was combined with TGA data in **Chapter 4.2.5.6** to support the hypothesis that, at high gold loading and low surface areas, Au blocks some base sites and slow down or even partially blocks the rehydration in vapour phase.

4.2.5.8 Surface chemical analysis

XPS analysis was run on the parent hydrotalcite, used as a fitting model, and then on 0.5, 1, 2, 5 and 10 wt. % Au/CHT450Vap materials; results for gold are shown in **Figure 4.37**. As already described in **Chapter 3.2.3.8** and **Chapter 4.2.4.8**, the Au 4f region was fitted by creating three distinct chemical environments; the first one was fitted with two components for the doublet of Au 4f orbitals (doublet separation = 3.70 eV) then other two were necessary to subtract the Mg 2s contribution, that overlaps in the same region, respectively one for Mg in HT and one for Mg in CHT-RW phase.

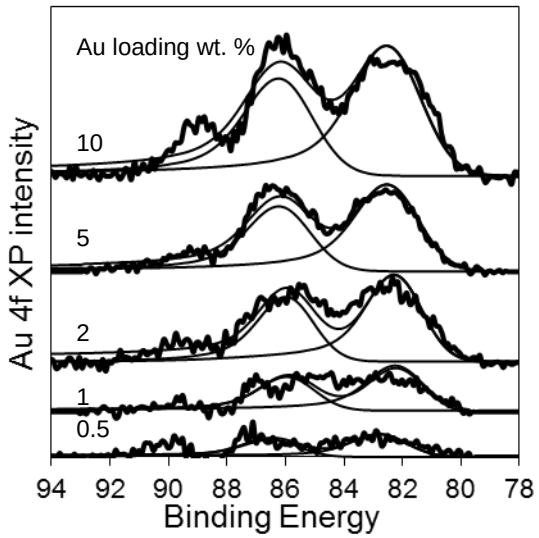

Figure 4.37: high resolution Au 4f XPS spectra of different Au loading series. A scale of 0.5 was applied to high loading (5 and 10 wt. %), in order to allow an optimal visualisation of the lower ones in the same scatter.

All the binding energy values for Au 4f are shown in **Table 4.21** and confirmed the presence of metallic gold (NIST database[39] $CsAuCl_4$ (Au^{3+}) 87.5-91.2 eV, Au foil 84.0-88.0 eV).

Table 4.21: Au 4f 7/2 and 5/2 binding energy for Au/CHT450Vap series.

Au loading / wt. %	Au 4f 5/2 B.E / eV	Au 4f 7/2 B.E / eV
0.5	85.85	82.15
1	85.85	82.15
2	85.88	82.18
5	86.12	82.41
10	86.12	82.41

4.2.6 Au/CHT and Au/CHT-RW catalysed aerobic selective oxidation of 5-HMF

4.2.6.1 The effect of calcination temperature on the selective oxidation of HMF

As already discussed through **Chapter 4.2.3**, the calcination of 2 wt. % Au/HT produced mixed Mg_3Al oxides, enhancing the base properties of the support. These catalysts were tested for the selective oxidation of HMF, in the same working conditions already described in **Chapter 3.2.4.4**, before or after the addition of NaOH 1M. **Scheme 4.1** recalls the reaction pathway for the aerobic selective oxidation of HMF to FDCA in the presence of Au nanoparticles supported onto hydrotalcite.

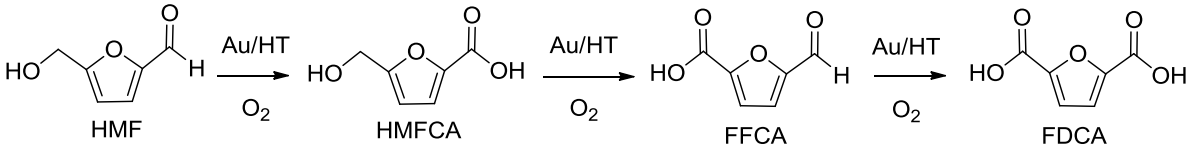

Scheme 4.1: the aerobic selective oxidation of 5-HMF to 2,5-FDCA.

Raw reaction profiles for the selective oxidation of HMF without addition of NaOH are shown in the Appendix, **Figure 4a.1.** A systematic kinetic study to follow the impact of NaOH 1 M (pH = 14) on the conversion of HMF was carried out using an excess of HMF (0.2 mmol instead of 0.1 mmol), in the same conditions previously described in **Chapter 3.2.4.**

As shown in **Figure 4.38**, the calcination at higher temperatures generated a new series of catalysts, that were found to be 12 – 25 times more active than the conventional 2 wt. % Au/HT activated at 200 °C; these results agree with the measured pH values, being 9 for the catalyst at 200 °C, 10 for the 300 °C, 10.5 for the 400 °C and

10.2 for the 500 °C. The new catalysts were capable to provide high conversions and FDCA yields without the need of added NaOH.

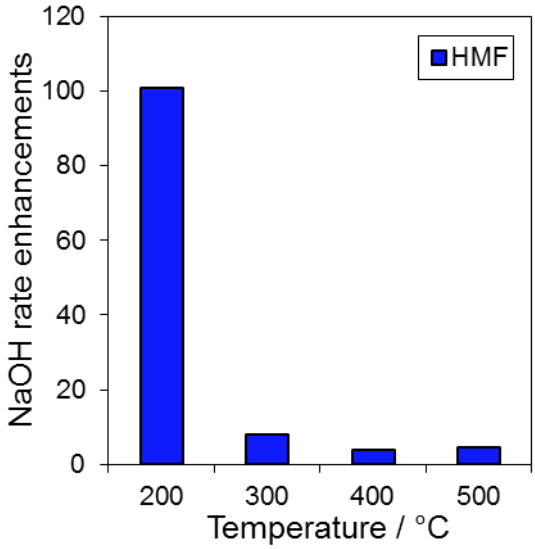

Figure 4.38: relative NaOH rate enhancements for the aerobic selective oxidation of HMF using 2 wt. % Au/CHT catalysts, calcined at different T. Reaction conditions: 25 mg of catalyst, 0.2 mmol of HMF, T = 90 °C, V = 6 ml H_2O and ν O_2 = 15 ml/min. Added NaOH = 6 mmol (1 M, pH = 14).

The most active catalyst, and consequentially the minor rate enhancement after the addition of NaOH 1M, was found to be 2 wt. % Au/CHT 400 °C, as shown in **Figure 4.39**, being the amount of gold identical for all these catalysts.

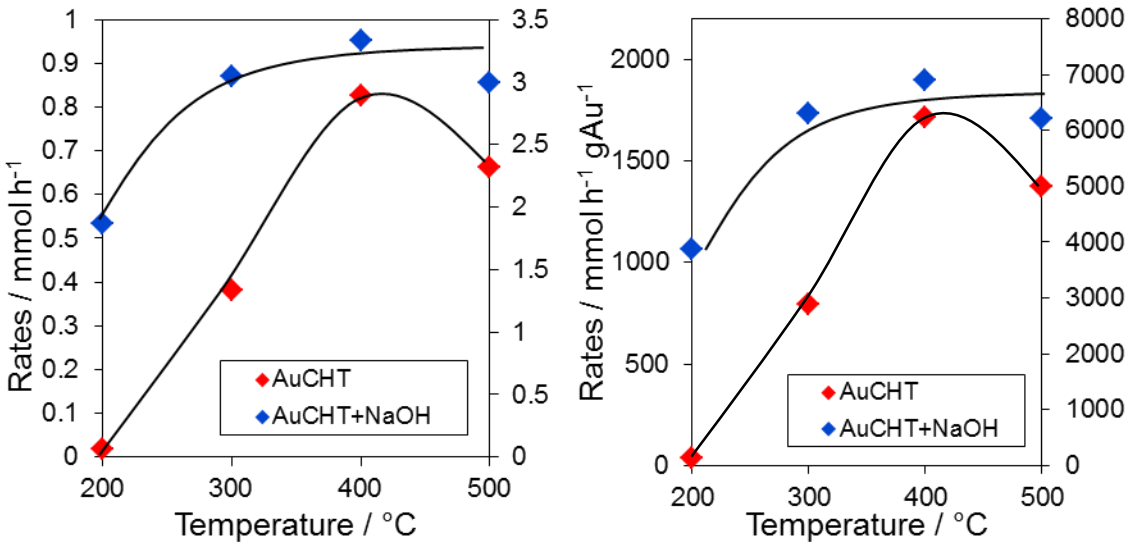

Figure 4.39: left – initial rate dependence HMF selox over 2 wt. % Au/CHT at different temperatures, with (in blue, right axis) and without (in red, left axis) NaOH 1M addition. Right – mass normalised initial rates of HMF selox over 2 wt. % Au/CHT at different calcination T, with (in blue, right axis) and without (in red, left axis) NaOH 1M addition. Reaction conditions: 25 mg of catalyst, 0.2 mmol of HMF, T = 90 °C, V = 6 ml H_2O and ν O_2 = 15 ml/min. Added NaOH = 6 mmol (1 M, pH = 14).

Based on results obtained by CO_2 TPD analysis (see **Chapter 4.2.3.5**), an explanation to attempt rationalising the enhanced FDCA production was given by plotting the normalised strongest base sites per m^2 vs. FDCA yields for 2 wt. % Au supported on HT or CHT vs. calcination temperature. **Figure 4.40** shows clearly the same trend between strong base sites and FDCA yield as a function of calcination temperature. These considerations, together with the characterisation already discussed through **Chapter 4**, underline the importance of strong base sites for the production of desired FDCA.

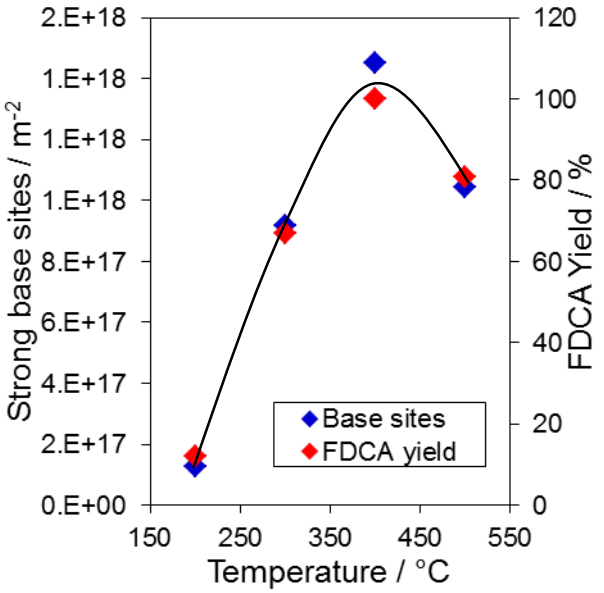

Figure 4.40: selox of HMF, strong base surface density from CO_2 TPD analysis (blue, left axis) and FDCA production (red, right axis) as a function of calcination temperature. Catalysts: 2 wt. % Au on HT or on CHT. Reaction conditions: 25 mg of catalyst, 0.1 mmol of HMF, T = 90 °C, V = 6 ml H_2O and ν O_2 = 15 ml/min.

4.2.6.2 The effect of CHT on lower gold loading for the selox of HMF

An attempt to promote the activity and FDCA yields for lower Au loading was carried out by calcining these catalysts, respectively 0.5 and 1 wt. % Au/HT, at 400 °C before testing for the selective oxidation of HMF**,** in reaction conditions already described in **Chapter 3.2.4.4.** The enhanced basicity of the CHT obtained improved also the two poorest catalytic systems, as shown in the Appendix, **Chapter 4.4, Figure 4a.2.**

The kinetic study was then carried out before and after the addition of NaOH 1M in reaction conditions already described in **Chapter 3.2.4.4. Figure 4.41** clearly shows a reduced impact of NaOH on the selective oxidation of HMF when CHT at 400 °C was used instead of HT at 200 °C, confirming that a solid base support can enhance also the poorest catalytic systems. As expected, the calcination temperatures of 400 °C enhanced the catalytic performances of lower gold loading and the best performances were achieved for 0.5 wt. % Au.

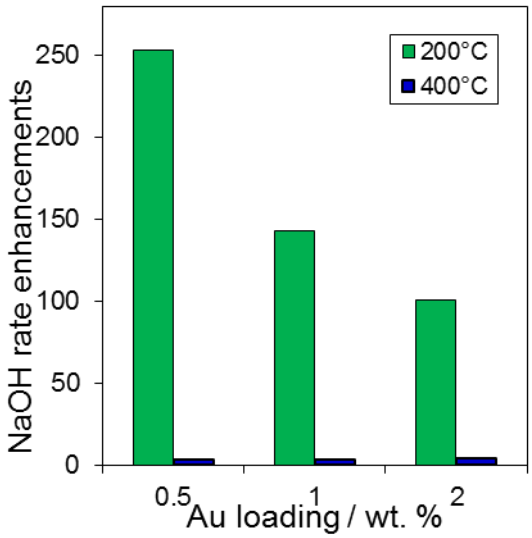

Figure 4.41: relative NaOH rate enhancements for the aerobic selective oxidation of HMF using different gold loading on HT at 200 °C (green) and on CHT at 400 °C (blue) catalysts. Reaction conditions: 25 mg of catalyst, 0.2 mmol of HMF, T = 90 °C, V = 6 ml H_2O and ν O_2 = 15 ml/min. Added NaOH = 6 mmol (1 M, pH = 14).

4.2.6.3 The effect of different calcination and rehydration methods on the aerobic selective oxidation of HMF and HMFCA

As already discussed through **Chapter 4.2.4** and **4.2.5**, the calcination of Au/HT materials produced mixed Mg_3Al oxides, which were then rehydrated following different protocols and reconstructing HT-like structure. Several systematic reaction tests were carried out in order to understand how these higher pH solid bases enhance the activity, yield and selectivity to FDCA for the aerobic selective oxidation of 5-HMF.

The catalysts used for this study were the 2 wt. % Au on a Na-free Mg_3Al hydrotalcite, calcined at 300 or at 450 °C and rehydrated following three different protocols described in **Chapter 4.2.2**, respectively CHTVap, CHTHotw and CHTSubw. Reaction conditions were chosen as follows: 25 mg of catalyst, 0.1 mmol of HMF in order to have HMF/Au = 40 (mol/mol), T = 90 °C, V = 6 ml H_2O and ν O_2 = 15 ml/min. These catalysts were tested alone or after the addition of a pre-determined amount of 1M NaOH, at pH = 14. Results for CHT300 – RW series are shown in the Appendix, **Chapter 4.4, Figure 4a.3** and **Figure 4a.4.**

The major impact on FDCA yield was obtained for the catalyst supported on CHTVap and two reasons were used to explain these results: at a first instance, as

observed in **Chapter 4.2.4.1,** when the rehydration was carried out in liquid water, gold leaching occurred, but the catalyst was stable when the rehydration took place in aqueous vapour phase. Furthermore, XRD and XPS analysis have underlined a higher content of mixed oxides for the material rehydrated in the vapour phase, and the formation of meixnerite instead of hydrotalcite, due to the absence of CO_2. The measured pH was 9.0 for all these catalysts, so the gold leaching must have a major impact in different performances of these materials.

The same reaction tests were carried out in identical conditions using 2 wt. % Au/CHT450 – RW series and raw reaction profiles are available in the Appendix, **Chapter 4.4, Figure 4a.5** and **Figure 4a.6.** Gold leaching occurred also when the catalysts were calcined at 450 °C prior to rehydration in liquid water, while they were stable when the aqueous vapour phase protocol was followed. The measured pH was 10.2 – 10.3 for these catalysts and this is one of the explanations of the higher performances achieved. XRD and XPS analysis have underlined a better reconstruction of HT-like phase than samples calcined at 300 °C prior to rehydration, and this justifies the observed enhancement.

A systematic kinetic study to follow the impact of NaOH on enhancing the conversion of HMF and FDCA yield was carried out using an excess of HMF (0.2 mmol instead of 0.1 mmol), in the same conditions previously described in **Chapter 3.2.4.** As shown in **Figure 4.42**, the highest performances were obtained for 2 wt. % Au/CHT calcined at 300 and 450 °C rehydrated in aqueous vapour phase, showing higher initial rates per g Au without extra base and a consequential lower impact of extra added NaOH and higher FDCA yields.

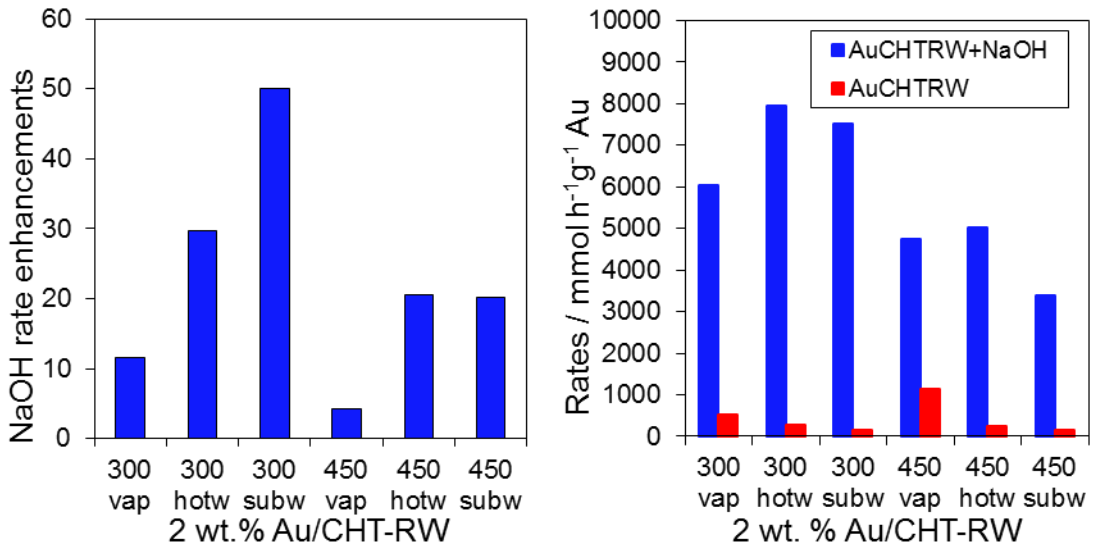

Figure 4.42: left – NaOH rate enhanchements for the selox of HMF using 2 wt. % Au on CHT calcined at two different temperatures (300 vs. 450 °C) and rehydrated in three different ways (aqueous vapour phase, boiling water or subcritical water). Right – normalised rates per g Au before and after the addition of NaOH. Reaction conditions: 25 mg of catalyst, 0.2 mmol of HMF, T = 90 °C, V = 6 ml H_2O and ν O_2 = 15 ml/min. Added NaOH = 6 mmol (1 M, pH = 14).

Data for the selective oxidation of HMFCA to FDCA were taken and analysed from the same reactions, considering the initial conversion of HMFCA to FFCA and then to FDCA; 2 wt. % Au/CHT450Vap was capable of giving the highest FDCA yield, showing better performances than the catalyst calcined at 300 °C in alcohol deprotonation and results are shown in **Figure 4.43**.

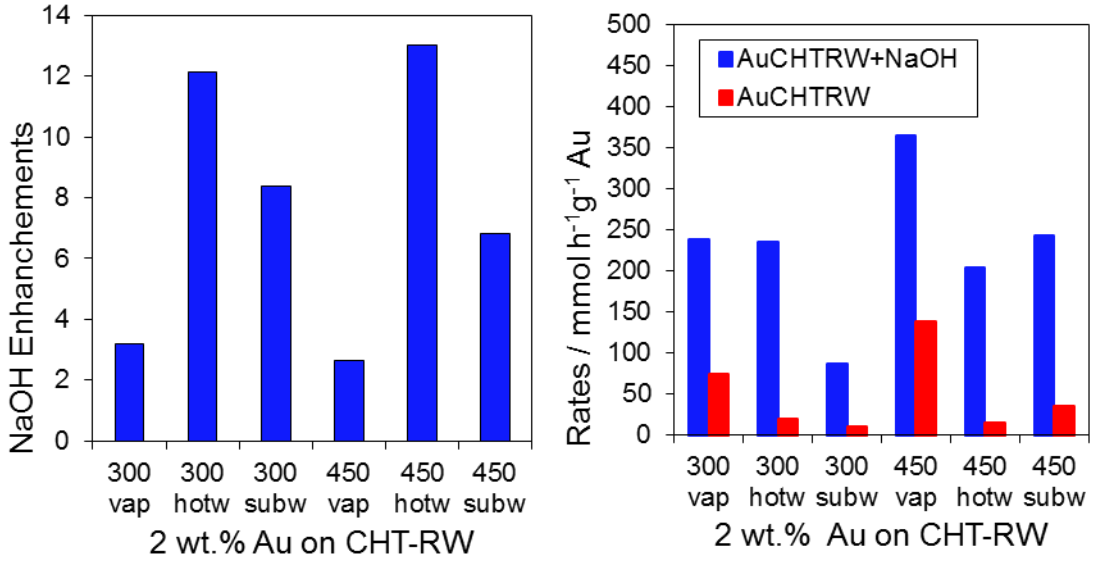

Figure 4.43: left – NaOH relative rate enhancements for the aerobic selox of HMFCA using 2 wt. % Au/CHT at two different temperatures (300 or 450 °C) and rehydrated in three different ways (aqueous vapour phase, boiling water or subcritical water). Right – normalised rates per g Au before and after the addition of NaOH for the same reactions. Reaction conditions: 25 mg of catalyst, 0.2 mmol of HMF, T = 90 °C, V = 6 ml H_2O and ν O_2 = 15 ml/min. Added NaOH = 6 mmol (1 M, pH = 14).

4.2.6.4 The effect of different gold loading on CHT450Vap on the aerobic selective oxidation of HMF and HMFCA

A series of different Au loading, respectively 0.5, 1, 2, 5 and 10 wt. %, were supported on CHT450Vap and several systematic reaction tests were carried out in order to understand the impact of different gold loading on the activity, yield and selectivity to FDCA for the aerobic selective oxidation of 5-HMF.

Reaction conditions were chosen as follows: 25 mg of catalyst, 0.1 mmol of HMF, T = 90 °C, V = 6 ml H_2O and ν O_2 = 15 ml/min. These catalysts were tested alone or after the addition of a pre-determined amount of 1M NaOH, at pH = 14. Raw reaction profiles are shown in the Appendix, **Figure 4a.7** and **Figure 4a.8.**

The measured pH for these catalysts was 10-10.5 and this was one of the factors that enhanced catalytic properties. As the amount of gold increases, HMF conversion and FDCA yields appear to increase, confirming the positive impact of higher gold loading already observed in **Chapter 3.2.4.4.**

A systematic kinetic study to follow the impact of NaOH on the conversion of HMF as the gold loading increases was then carried out using an excess of HMF (0.2 mmol instead of 0.1 mmol), in order to slow down the rapid oxidation of HMF to HMFCA; data about selective oxidation of HMFCA were obtained from the same reaction, considering the initial conversion of HMFCA to FFCA and then to FDCA. Results are shown in **Figure 4.44.**

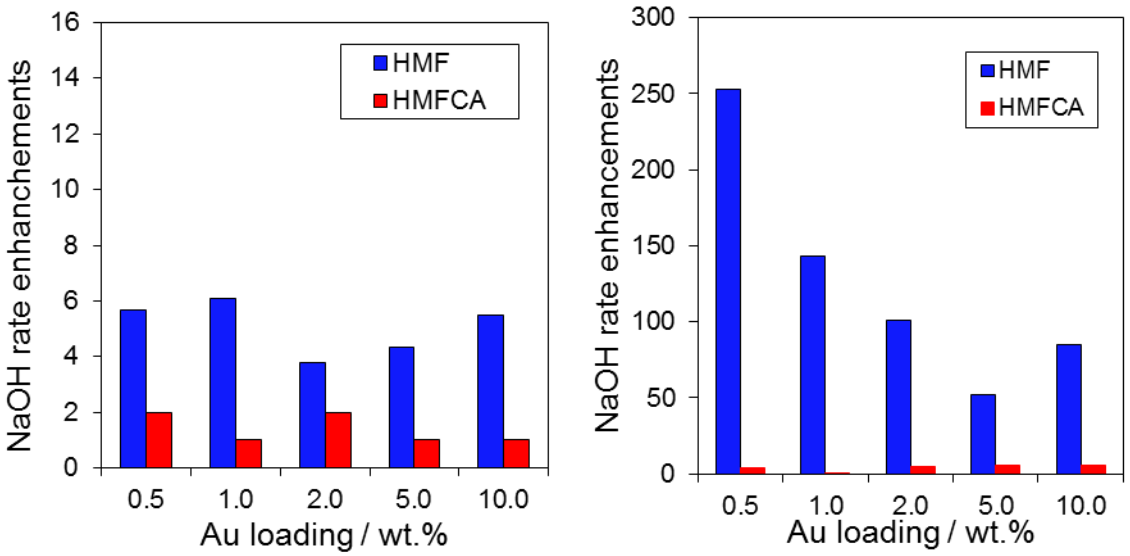

Figure 4.44: left – selox of HMF and HMFCA, NaOH relative rate enhancements for 5 different Au loading on CHT450Vap, highlighting a minor relative impact of NaOH on the HMF rates. Right – a recall of results for different Au loading on HT from Chapter 3, as a comparison. Reaction conditions: 25 mg of catalyst, 0.2 mmol of HMF, T = 90 °C, V = 6 ml H_2O and ν O_2 = 15 ml/min. Added NaOH = 6 mmol (1 M, pH = 14).

All the gold loadings have shown a similar NaOH enhancement (4-6 fold, in the range of the experimental error) and the rates per gram of gold increase until 2 wt. %, then decrease exponentially, either when the solid base is used alone or after the addition of NaOH 1M **(Figure 4.44 - left).**

Despite of previous results, obtained for Au on HT at 200 °C and recalled in **Figure 4.44 – right**, where lower loading had shown a higher enhancement, in this case the enhancement was constant for all of them. **Figure 4.45** shows, instead, raw and normalised initial rates per gram of gold of the same reactions.

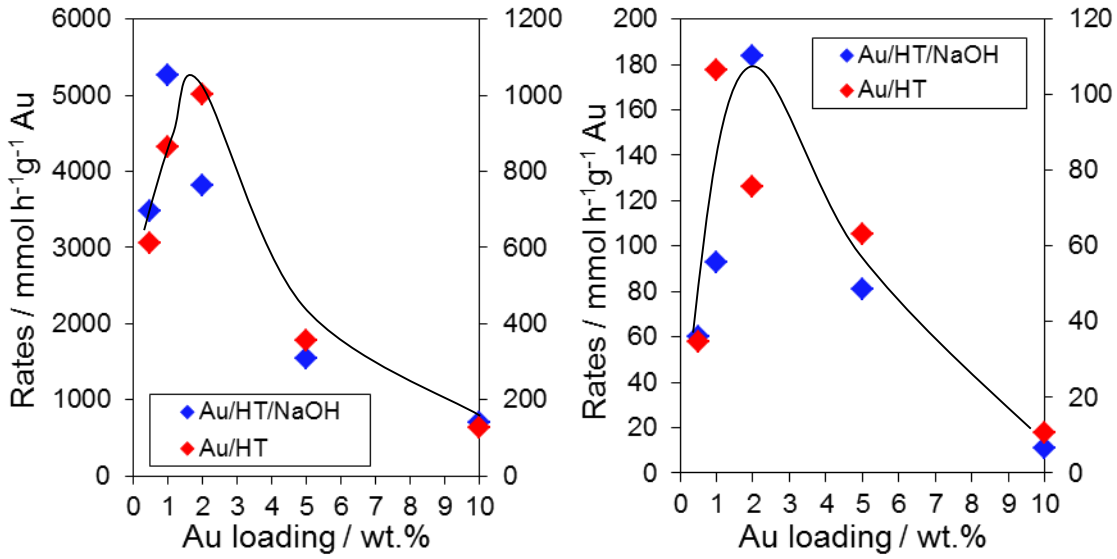

Figure 4.45: left – selox of HMF, normalised rates per g Au before and after the addition of NaOH. Right – the same data for the selox of HMFCA. Catalysts: different Au loadings on CHT 450 °C R-vap. Reaction conditions: 25 mg of catalyst, 0.2 mmol of HMF, T = 90 °C, V = 6 ml H_2O and ν O_2 = 15 ml/min. Added NaOH = 6 mmol (1 M, pH = 14).

An attempt to explain these differences was done, considering that when Au is loaded on HT and calcined at 200 °C, the presence of a consistent amount of CO_3^{2-} ions in the interlayer, as it appears observing all TPD and TGA graphs reported in **Chapter 3** and **Chapter 4**, blocks base sites needed for the formation of the reactive intermediate gem-diol. As the reaction, in absence of NaOH, occurs on the catalyst surface, for lower gold loading, respectively 0.5 and 1 wt. %, Au NPs are not always surrounded by ^{-}OH ions, but the higher is the loading, the higher is the chance for gold NPs to be surrounded by ^{-}OH ions.

When Au is loaded on CHT at 300 or, better, at 450 °C, the rehydration in aqueous vapour phase under N_2 replaces a high amount of CO_3^{2-} with ^{-}OH ions, so more Au particles, either at low or high loading, are surrounded by them and HMF activation occurs on the surface. This explains lower Au loadings benefit of a high enhancement (from poor to high activity) after the addition of NaOH when supported on conventional HTs and why this enhancement is lower (from moderate high to high activity) when NaOH is added on the rehydrated series. The neighbourhood between Au and OH appears to be important for the activation and following oxidation of HMF.

TOF values were therefore calculated using the method[55] already described in **Chapter 3.2.4.4;** results for HMF are shown in **Figure 4.46,** results for HMFCA are shown in **Figure 4.47,** showing surface gold as the active site and confirming what obtained in **Chapter 3:** the presence of more gold improved FDCA yields, but when normalised as surface gold, TOF values were constant in the range of experimental error.

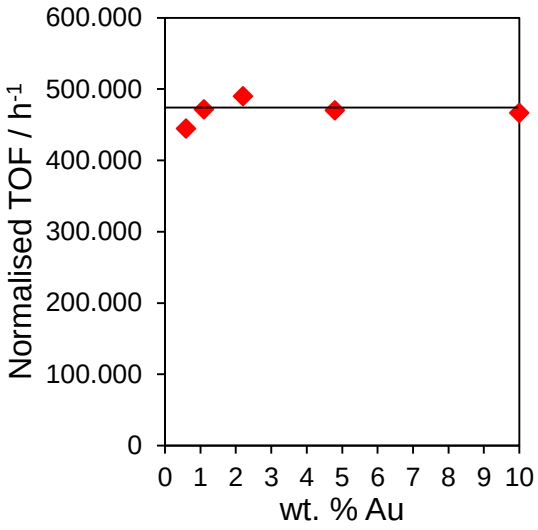

Figure 4.46: calculated TOF values for the aerobic selective oxidation of HMF as a function of gold loading. Reaction conditions: 25 mg of catalyst, 0.2 mmol of HMF, T = 90 °C, V = 6 ml H_2O and ν O_2 = 15 ml/min. Added NaOH = 6 mmol (1 M, pH = 14).

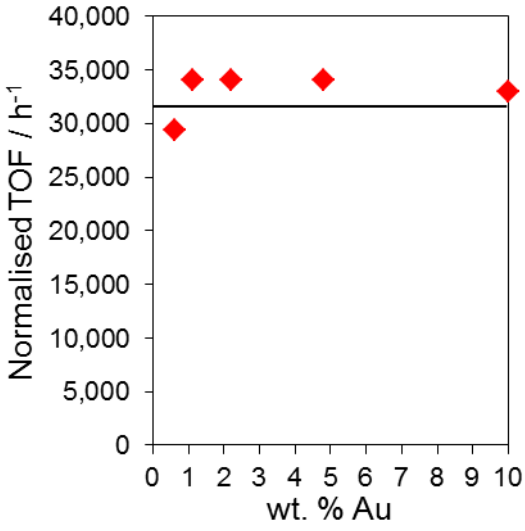

Figure 4.47: calculated TOF values for the aerobic selective oxidation of HMFCA as a function of gold loading. Reaction conditions: 25 mg of catalyst, 0.2 mmol of HMFCA,

T = 90 °C, V = 6 ml H_2O and ν O_2 = 15 ml/min. Added NaOH = 6 mmol (1 M, pH = 14).

4.3 Conclusions

Hydrotalcites having Mg/Al = 3 molar ratio were prepared using an alkali-free method *via* co-precipitation route. At a first instance, 2 wt. % Au was loaded on them using the deposition-precipitation method, the materials were calcined at different temperatures, respectively 300, 400 and 500 °C, to generate mixed Mg_3Al oxides.

Subsequently, a calcination – rehydration protocol was set up, in order to try optimising the calcination temperature and the preparation time, using an easy method: 2 wt. % Au/HT was calcined at 300 or at 450 °C, then the rehydration step was tested in aqueous vapour phase using N_2, or in subcritical water under pressure at 120 °C or in hot water at 100 °C.

Even if the vapour-phase rehydration required longer time, above two days, yielded not only a better reconstruction of meixnerite materials, being 450 °C the best temperature to remove CO_3^{2-}, but also no gold leach was detected during this preparation. Identified the most adequate temperature and rehydration protocol, five different gold loadings, respectively 0.5, 1, 2, 5 and 10 wt. % Au, were supported on the same materials and an accurate characterisation was done on them, to correlate morphology, base properties and their impact on reaction parameters.

All the catalysts were tested for the aerobic selective oxidation of HMF to FDCA before or after the addition of an excess of NaOH 1M solution. On increasing of solid basicity, the activity, the conversion and FDCA yields improved and the addition of an extra amount of NaOH 1 M was found to have a minor impact on all these parameters. Calcination at high temperatures enhanced dramatically the activity of low gold loadings and generates efficient catalysts.

The best catalyst, which has shown highest FDCA yield (100 %), was 2 wt. % Au/CHT 400 °C. This calcination temperature removes carbonates from the HT interlayers; then, a rehydration *in situ* occurs during the reaction, either generating ^-OH ions in water that activate HMF to 1,1 gem-diol or deprotonating easily the rate – determining step, the activation of R-OH group, for the selox of HMF and HMFCA.

TPD analysis, in **Chapter 4.2.3.5**, has shown this catalytic system possesses the strongest basicity and the highest base active sites density, while N_2 porosimetry has also shown the highest surface area. Therefore, no extra soluble base, NaOH, is needed to significantly enhance performances of this catalyst.

The combination of XRD, XPS, CO_2 TPD and detailed kinetic mapping has elucidated the nature of base sites, their role enhancing Au catalysed HMF aerobic selox to FDCA and any eventual deactivation, such as the formation of segregated oxides at high temperatures (500 °C) or gold leaching during liquid phase rehydration. Either mixed oxides or meixnerite solid bases can drive HMF selox even in concert with low concentrations of surface gold, a discovery that has important implications to enhance gold catalysis and cascade oxidations.

4.4 Appendix

Raw reaction profiles for the selox reactions described through **Chapter 4:**

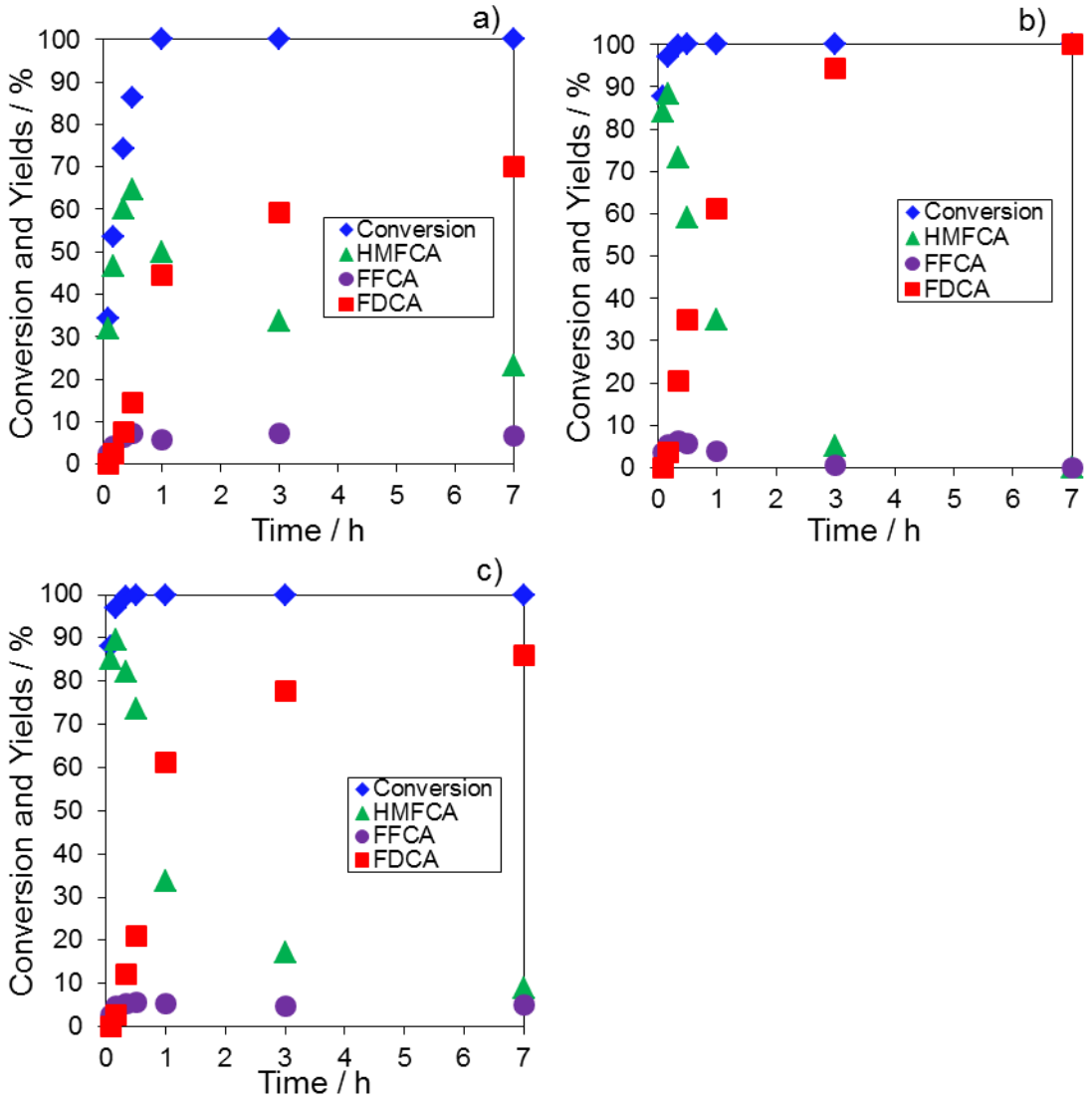

Figure 4a.1: reaction profiles for the aerobic selective oxidation of HMF, using 2 wt. % Au on CHT at different temperatures a) 300 °C b) 400 °C c) 500 °C. Reaction conditions: 25 mg of catalyst, 0.1 mmol of HMF in order to have HMF/Au = 40 (mol/mol), T = 90 °C, V = 6 ml H_2O and ν O_2 = 15 ml/min.

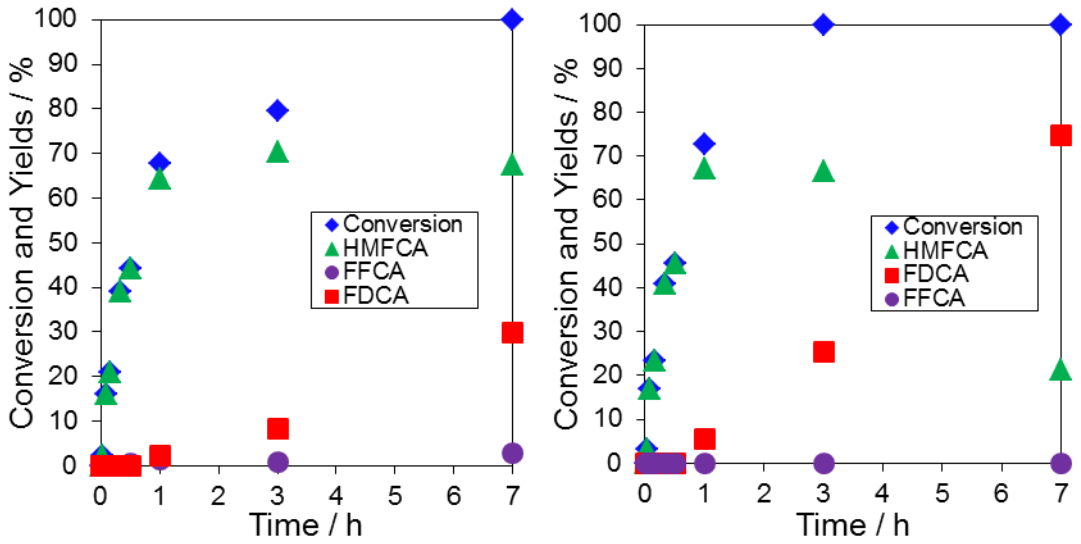

Figure 4a.2: left – aerobic selective oxidation of HMF using 0.5 wt. % Au/CHT 400 °C and right – using 1 wt. % Au on CHT 400 °C without added NaOH. Reaction conditions: 25 mg of catalyst, 0.1 mmol of HMF, T = 90 °C, V = 6 ml H_2O and ν O_2 = 15 ml/min.

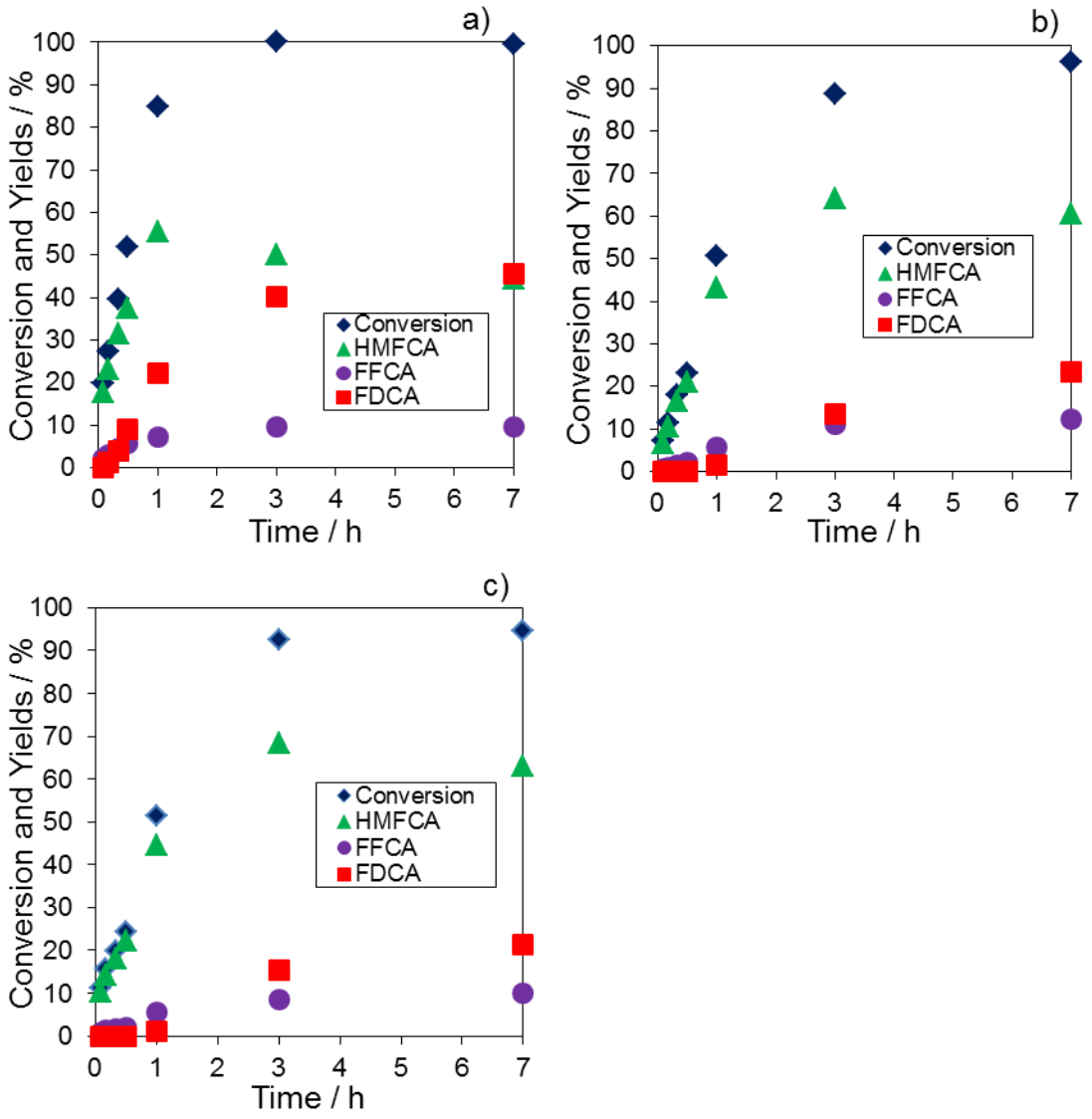

Figure 4a.3: reaction profiles for the aerobic selective oxidation of HMF, using 2 wt. % Au on CHT at 300 °C, rehydrated in different ways without extra added base a) at room temperature, in aqueous vapour phase, under N_2 flow, pH = 9.0 b) in subcritical water at 120 °C, pH = 9.0 c) in boiling water at 100 °C, pH = 9.0. Reaction conditions: 25 mg of catalyst, 0.1 mmol of HMF, T = 90 °C, V = 6 ml H_2O and ν O_2 = 15 ml/min.

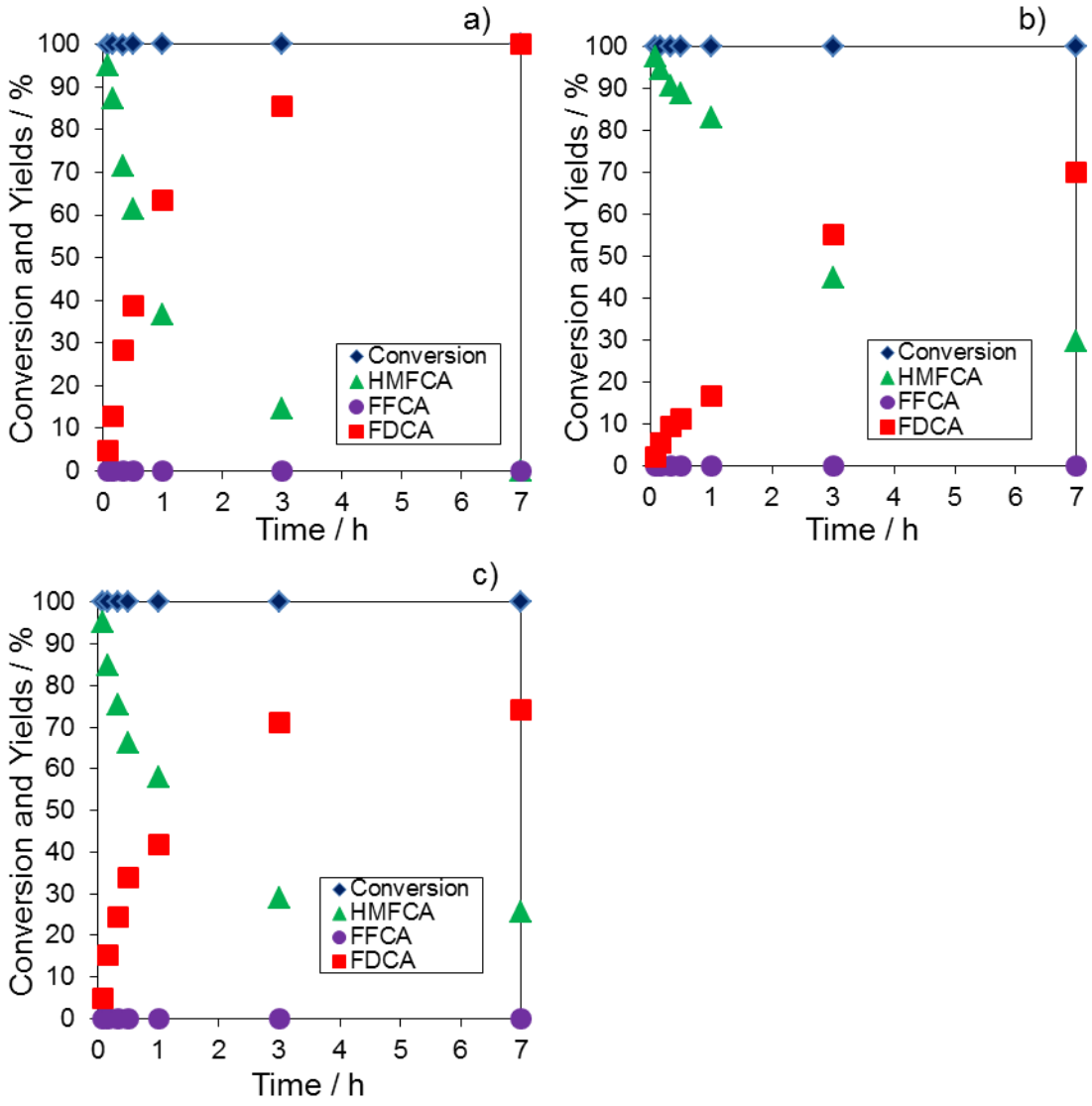

Figure 4a.4: reaction profiles for the aerobic selective oxidation of HMF, using 2 wt. % Au on CHT at 300 °C, rehydrated in different ways, after the addition of 6 mmol NaOH (1 M, pH = 14) a) at room temperature, in aqueous vapour phase, under N_2 flow b) in subcritical water at 120 °C c) in boiling water at 100 °C. Reaction conditions: 25 mg of catalyst, 0.1 mmol of HMF, T = 90 °C, V = 6 ml H_2O and ν O_2 = 15 ml/min.

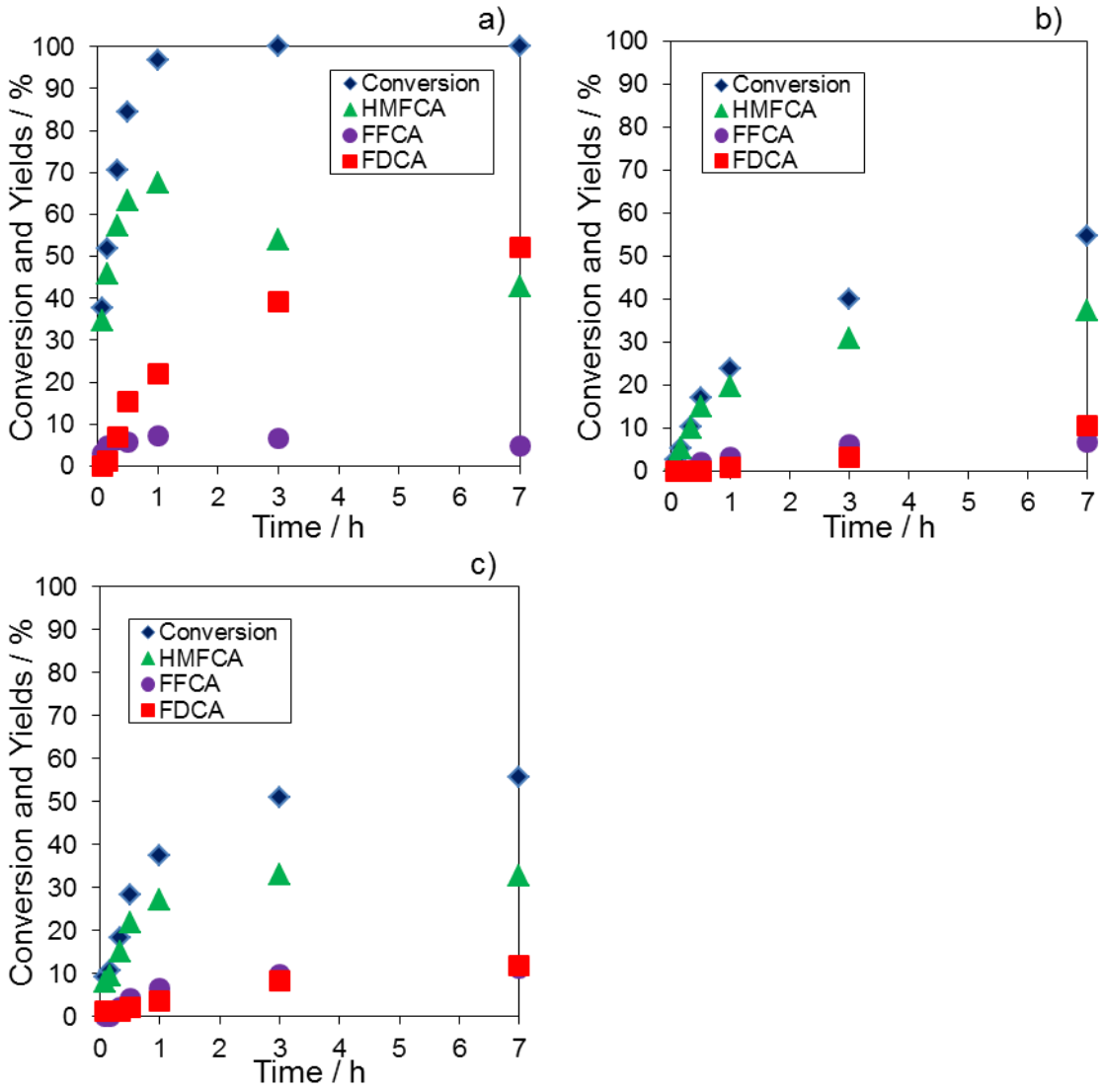

Figure 4a.5: reaction profiles for the aerobic selective oxidation of HMF, using 2 wt. % Au on CHT at 450 °C, rehydrated in different ways without extra added base. a) at room temperature, in aqueous vapour phase, under N_2 flow b) in subcritical water at 120 °C c) in boiling water at 100 °C. Reaction conditions: 25 mg of catalyst, 0.1 mmol of HMF, T = 90 °C, V = 6 ml H_2O and ν O_2 = 15 ml/min.

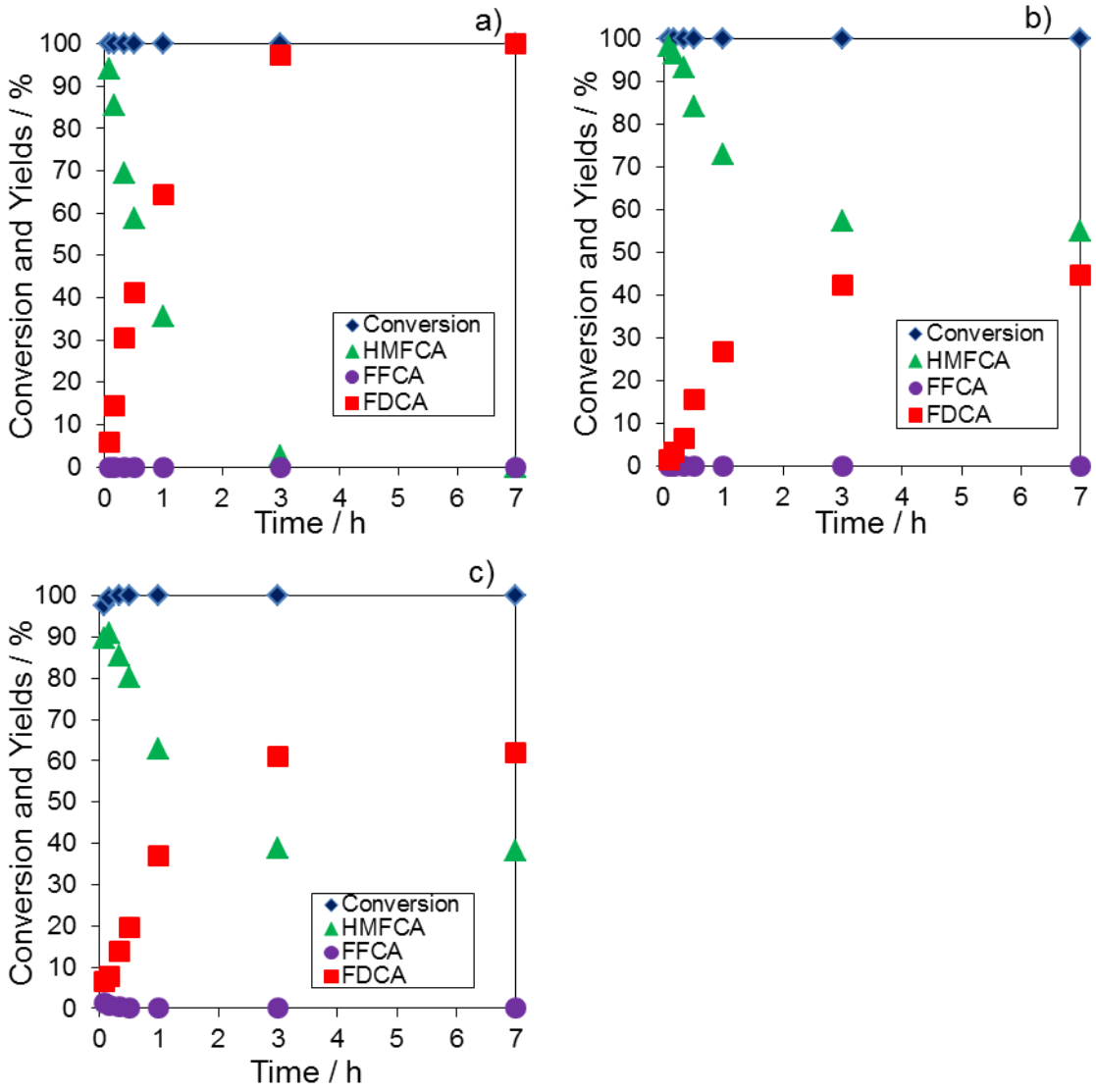

Figure 4a.6: reaction profiles for the aerobic selective oxidation of HMF, using 2 wt. % Au/CHT at 450 °C, then rehydrated in different ways, after the addition of 6 mmol NaOH (1 M, pH = 14) a) rehydrated at room temperature, in aqueous vapour phase, under N_2 flow b) in subcritical water at 120 °C c) in boiling water at 100 °C. Reaction conditions: 25 mg of catalyst, 0.1 mmol of HMF, T = 90 °C, V = 6 ml H_2O and ν O_2 = 15 ml/min.

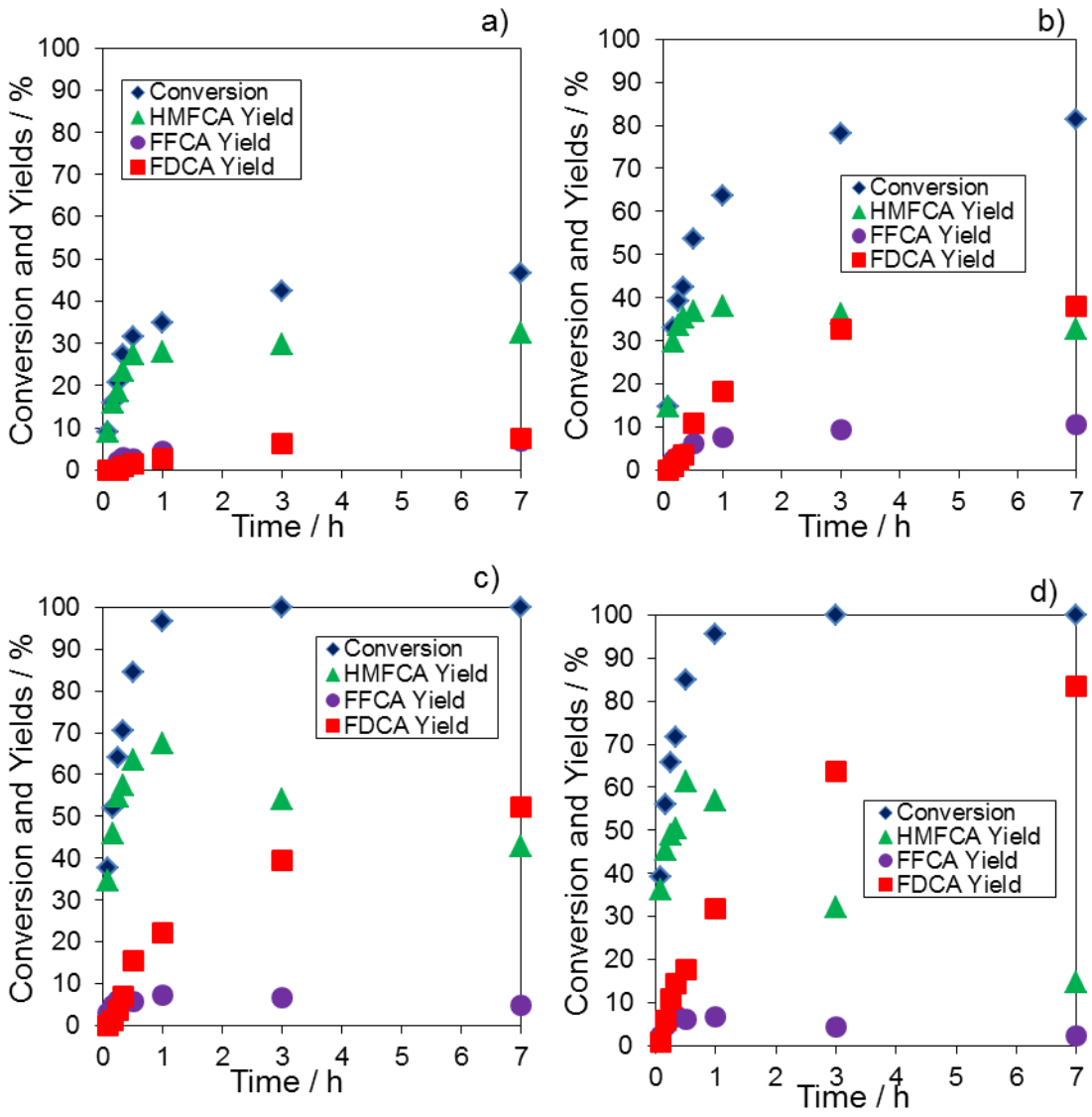
a)
b)
c)
d)
Conversion and Yields / %
Time / h
Conversion
HMFCA Yield
FFCA Yield
FDCA Yield

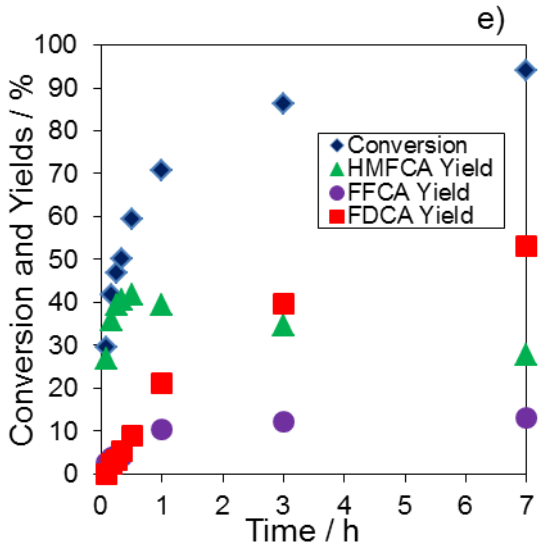

Figure 4a.7: reaction profiles for the aerobic selective oxidation of HMF, using different gold loading on CHT at 450 °C, rehydrated at room temperature, in aqueous vapour phase, under N_2 flow and without extra added base. a) 0.5 wt. % Au b) 1 wt. % Au c) 2 wt. % Au d) 5 wt. % Au and 3) 10 wt. % Au. Reaction conditions: 25 mg of catalyst, 0.1 mmol of HMF, T = 90 °C, V = 6 ml H_2O and ν O_2 = 15 ml/min.

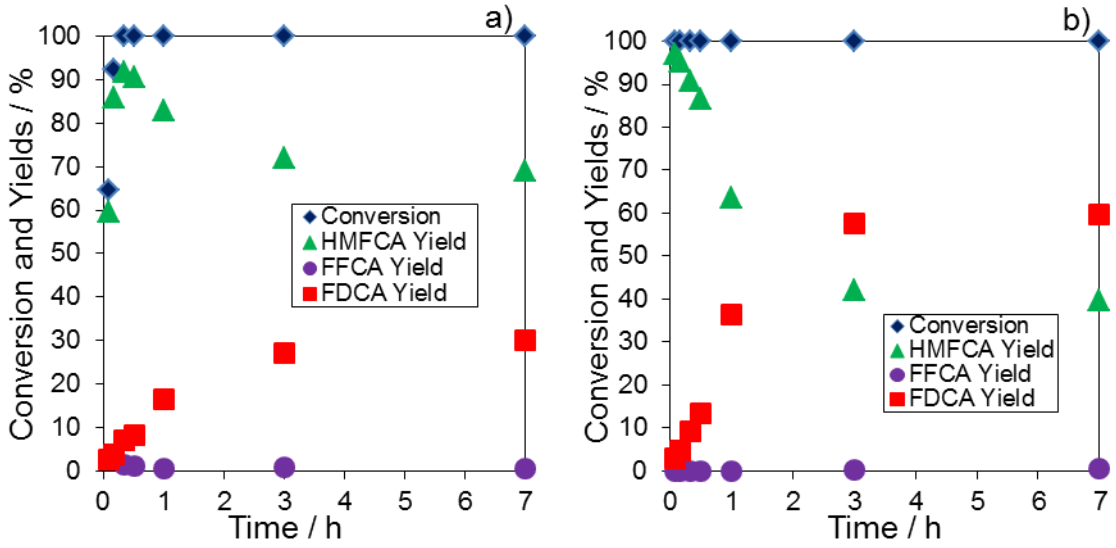

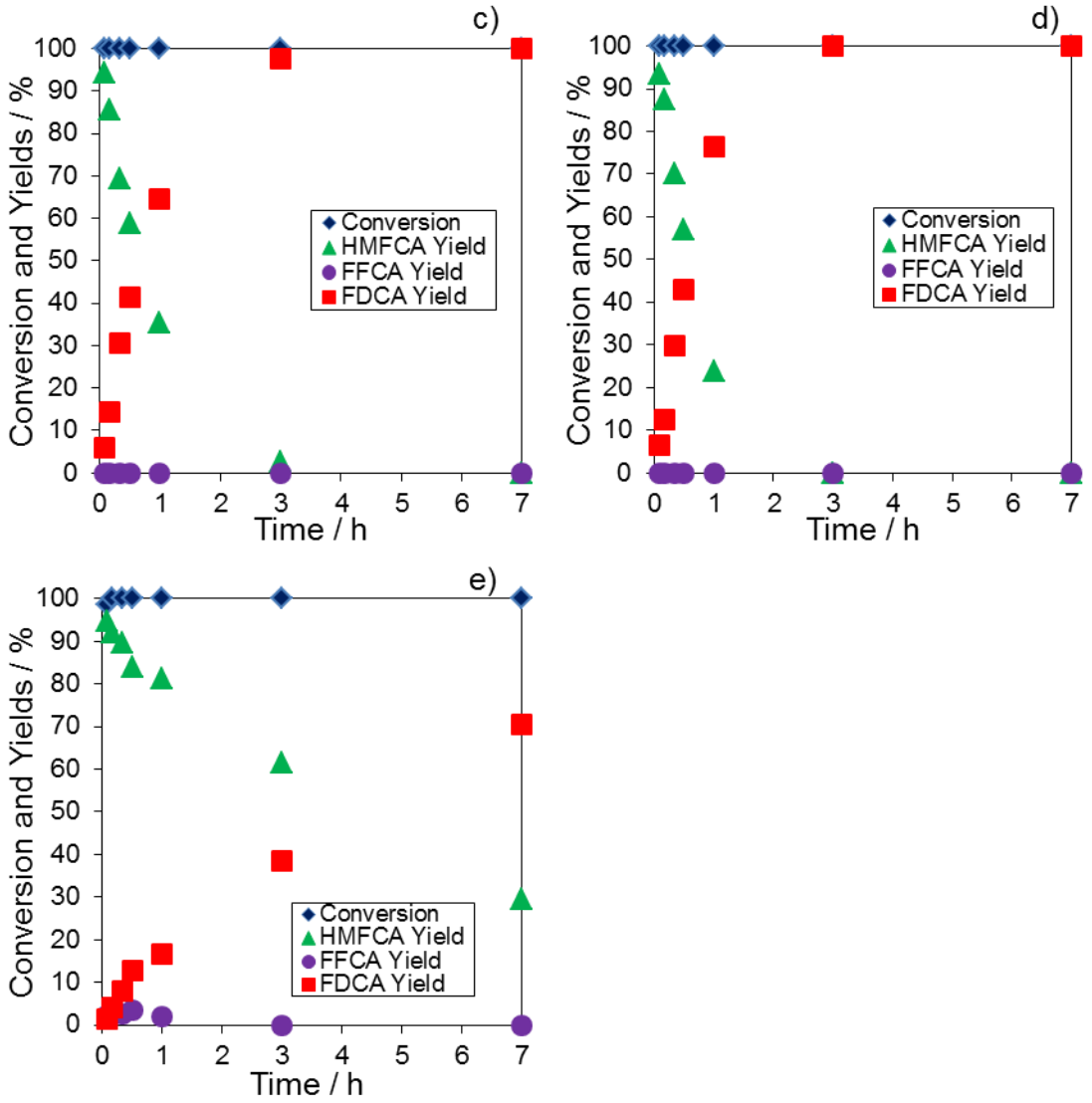

Figure 4a.8: reaction profiles for the aerobic selective oxidation of HMF, using different gold loading on CHT at 450 °C, rehydrated at room temperature, in aqueous vapour phase, under N_2 flow, after the addition of 6 mmol NaOH (1 M, pH = 14) a) 0.5 wt. % Au b) 1 wt. % Au c) 2 wt. % Au d) 5 wt. % Au and 3) 10 wt. % Au. Reaction conditions: 25 mg of catalyst, 0.1 mmol of HMF, T = 90 °C, V = 6 ml H_2O and ν O_2 = 15 ml/min.

4.5 References

1. J. I. Di Cosimo, V. K. Díez, M. Xu, E. Iglesia and C. R. Apesteguía, *Journal of Catalysis*, 1998, **178**, 499-510.
2. J. S. Valente, F. Figueras, M. Gravelle, P. Kumbhar, J. Lopez and J. P. Besse, *Journal of Catalysis*, 2000, **189**, 370-381.
3. S. Abelló, F. Medina, D. Tichit, J. Pérez-Ramírez, X. Rodríguez, J. E. Sueiras, P. Salagre and Y. Cesteros, *Applied Catalysis A: General*, 2005, **281**, 191-198.
4. F. Cavani, F. Trifirò and A. Vaccari, *Catalysis Today*, 1991, **11**, 173-301.
5. A. Vaccari, *Catalysis Today*, 1998, **41**, 53-71.
6. E. Angelescu, O. D. Pavel, R. Bîrjega, M. Florea and R. Zăvoianu, *Applied Catalysis A: General*, 2008, **341**, 50-57.
7. V. Dávila, E. Lima, S. Bulbulian and P. Bosch, *Microporous and Mesoporous Materials*, 2008, **107**, 240-246.
8. W. T. Reichle, S. Y. Kang and D. S. Everhardt, *Journal of Catalysis*, 1986, **101**, 352-359.
9. W. T. Reichle, *Journal of Catalysis*, 1985, **94**, 547-557.
10. M. J. Climent, A. Corma, S. Iborra, K. Epping and A. Velty, *Journal of Catalysis*, 2004, **225**, 316-326.
11. M. J. Climent, A. Corma, S. Iborra and A. Velty, *Journal of Catalysis*, 2004, **221**, 474-482.
12. A. Corma, S. B. A. Hamid, S. Iborra and A. Velty, *Journal of Catalysis*, 2005, **234**, 340-347.
13. M. J. Climent, A. Corma, S. Iborra and J. Primo, *Journal of Catalysis*, 1995, **151**, 60-66.
14. D. G. Cantrell, L. J. Gillie, A. F. Lee and K. Wilson, *Applied Catalysis A: General*, 2005, **287**, 183-190.
15. J. J. Woodford, J.-P. Dacquin, K. Wilson and A. F. Lee, *Energy & Environmental Science*, 2012, **5**, 6145-6150.
16. Y. Xi and R. J. Davis, *Journal of Catalysis*, 2009, **268**, 307-317.
17. T. Hibino and A. Tsunashima, *Chemistry of Materials*, 1998, **10**, 4055-4061.
18. N. K. Gupta, S. Nishimura, A. Takagaki and K. Ebitani, *Green Chemistry*, 2011, **13**, 824-827.
19. V. Rives, *Materials Chemistry and Physics*, 2002, **75**, 19-25.
20. S. Miyata, *Clays and Clay minerals*, 1980, **28**, 50-56.
21. JCPDS (1967) X-ray powder data file: card number 4-0829 and P. A.S.T.M., U.S.A.
22. A. Virnovskaia, S. Jørgensen, J. Hafizovic, Ø. Prytz, E. Kleimenov, M. Hävecker, H. Bluhm, A. Knop-Gericke, R. Schlögl and U. Olsbye, *Surface Science*, 2007, **601**, 30-43.
23. E. Kanezaki, *Solid State Ionics*, 1998, **106**, 279-284.
24. P. Scherrer, *Nachr. Ges. Wiss. Göttingen*, 1918, **26**, 98-100.
25. E. P. Barrett, L. G. Joyner and P. P. Halenda, *Journal of the American Chemical Society*, 1951, **73**, 373-380.
26. P. Kuśtrowski, L. Chmielarz, E. Bożek, M. Sawalha and F. Roessner, *Materials Research Bulletin*, 2004, **39**, 263-281.
27. K. S. W. Sing, D. H. Everett, R. A. W. Haul, L. Moscou, R. A. Pierotti, J. Rouquerol and T. Siemieniewska, in *Handbook of Heterogeneous Catalysis*, Wiley-VCH Verlag GmbH & Co. KGaA, 2008.

28. S. K. Sharma, P. K. Kushwaha, V. K. Srivastava, S. D. Bhatt and R. V. Jasra, *Industrial & Engineering Chemistry Research*, 2007, **46**, 4856-4865.
29. D. Evans and R. T. Slade, in *Layered Double Hydroxides*, eds. X. Duan and D. Evans, Springer Berlin Heidelberg, 2006, vol. 119, ch. 5, pp. 1-87.
30. G. Mascolo and O. Marino, *Thermochimica Acta*, 1980, **35**, 93-98.
31. I. Melian-Cabrera, M. Lopez Granados and J. L. G. Fierro, *Physical Chemistry Chemical Physics*, 2002, **4**, 3122-3127.
32. J. C. A. A. Roelofs, J. A. van Bokhoven, A. J. van Dillen, J. W. Geus and K. P. de Jong, *Chemistry – A European Journal*, 2002, **8**, 5571-5579.
33. Y. Xi and R. J. Davis, *Journal of Catalysis*, 2008, **254**, 190-197.
34. J. J. Creasey, A. Chieregato, J. C. Manayil, C. M. A. Parlett, K. Wilson and A. F. Lee, *Catalysis Science & Technology*, 2014.
35. S. Abelló, F. Medina, D. Tichit, J. Pérez-Ramírez, J. C. Groen, J. E. Sueiras, P. Salagre and Y. Cesteros, *Chemistry – A European Journal*, 2005, **11**, 728-739.
36. R. Bastiani, I. V. Zonno, I. A. V. Santos, C. A. Henriques and J. L. F. Monteiro, *Brazilian Journal of Chemical Engineering*, 2004, **21**, 193-202.
37. O. D. Pavel, D. Tichit and I.-C. Marcu, *Applied Clay Science*, 2012, **61**, 52-58.
38. R. Philipp and K. Fujimoto, *The Journal of Physical Chemistry*, 1992, **96**, 9035-9038.
39. A. K.-V. Alexander V. Naumkin, Stephen W. Gaarenstroom, and Cedric J. Powell, *NIST X-ray Photoelectron Spectroscopy Database, Version 4.1 (National Institute of Standards and Technology, Gaithersburg, 2012); http://srdata.nist.gov/xps/*.
40. S. Ardizzone, C. L. Bianchi, M. Fadoni and B. Vercelli, *Applied Surface Science*, 1997, **119**, 253-259.
41. J. M. Montero, D. R. Brown, P. L. Gai, A. F. Lee and K. Wilson, *Chemical Engineering Journal*, 2010, **161**, 332-339.
42. J. M. Montero, P. Gai, K. Wilson and A. F. Lee, *Green Chemistry*, 2009, **11**, 265-268.
43. P. Liu, Y. Guan, R. A. v. Santen, C. Li and E. J. M. Hensen, *Chemical Communications*, 2011, **47**, 11540-11542.
44. O. D. Pavel, R. Zăvoianu, R. Bîrjega, E. Angelescu, G. Costentin and M. Che, *Applied Clay Science*, 2015, **104**, 59-65.
45. F. Basile, G. Fornasari, M. Gazzano and A. Vaccari, *Applied Clay Science*, 2000, **16**, 185-200.
46. Q. Wang, Z. Wu, H. H. Tay, L. Chen, Y. Liu, J. Chang, Z. Zhong, J. Luo and A. Borgna, *Catalysis Today*, 2011, **164**, 198-203.
47. M. Rajamathi, G. D. Nataraja, S. Ananthamurthy and P. V. Kamath, *Journal of Materials Chemistry*, 2000, **10**, 2754-2753.
48. G. Thomas and P. V. Kamath, *J Chem Sci*, 2006, **118**, 127-133.
49. A. V. Radha, P. V. Kamath and C. Shivakumara, *The Journal of Physical Chemistry B*, 2007, **111**, 3411-3418.
50. J. W. McBain, *Journal of the American Chemical Society*, 1935, **57**, 699-700.
51. J. C. A. A. Roelofs, A. J. van Dillen and K. P. de Jong, *Catal Lett*, 2001, **74**, 91-94.
52. F. Li, X. Jiang, D. Evans and X. Duan, *J Porous Mater*, 2005, **12**, 55-63.
53. R. A. W. H. K. S. W. Sing, L. Moscou, R. A. Pierotti, J. Roquerol and T. Siemieniewska., *Pure Appl. Chem.*, 1985, **57**, 603-619.
54. W. Tongamp, Q. Zhang and F. Saito, *J Mater Sci*, 2007, **42**, 9210-9215.

55. A. Abad, A. Corma and H. García, *Chemistry – A European Journal*, 2008, **14**, 212-222.

Chapter 5

On the role of Pd in the AuPd/hydrotalcite catalysed oxidation of 5-HMF

Contents

5.1 Introduction

The oxidation of alcohols and polyols to carbonyls has been widely studied using supported heterogeneous Pd catalysts[1-9] in aqueous[1] and organic solvents[1, 10, 11]. Our research group has shown that high surface area (300 $m^2.g^{-1}$) mesoporous alumina[12] or mesoporous silica[11, 13, 14], such as surfactant-templated SBA-15 (a high surface area supports with hexagonally packed, p6mm, parallel mesopore channels (950 $m^2.g^{-1}$), and two high surface area cubic silica supports with three-dimensional interpenetrating mesopore networks, SBA-16, Im3m, ($m^2.g^{-1}$) and KIT-6, Ia3d, (940 $m^2.g^{-1}$), potentially linked *via* micropores[13, 14], were able to stabilise atomically highly dispersed Pd^{2+} centres, that exhibit exceptional activity toward the aerobic selox of allylic alcohols, being PdO the true active site for the oxidative dehydrogenation.

These materials were found to be highly selective (70-80 %) to the allylic aldehyde with the remaining products due to decarbonylation, breaking C-O bond and hydrogenation, due to surface hydrogen arising from the oxidative dehydrogenation mechanism. However, PdO can undergo *in situ* reduction to Pd^0 during alcohol selox[13-15] and does not carry on the second step required for HMF selox, the aldehyde to acid one.

To overcome these issues, AuPd bimetallic catalysts were tested for the selox of HMF. Our research group[10, 16] and several other authors[1, 17-19] have indeed tested bimetallic AuPd catalysts for the selox of different alcohols and polyols. Also, Hutchings and co-authors[18-20] found this alloy to be very active for direct synthesis of H_2O_2 from hydrogen and oxygen, either prepared *via* deposition-precipitation, *via* impregnation or *via* sol immobilisation.

Positive synergic effects,[21, 22] both geometric and electronic, between Au and Pd have been found to increase not only catalytic activity, yields and selectivity, but also catalytic lifetime under mild reaction conditions[1, 10]. Prati and co-authors reported in their works[1, 17] that, in the presence of a base, the activity of all these catalysts was enhanced, therefore in this chapter the use of HT as both the support and the solid source of base as a promoter will be explored, as well as it was for Au in previous chapters.

The main overarching goal is to verify if AuPd/HT can oxidise HMF at a lower pH = 9, without the need of extra added NaOH or without using high metal loadings, as it was the case for Au. The aim was to try use a cheaper and efficient catalyst, being the chosen total

amount of metal only 1 wt. % and being also Pd less expensive than Au. Kinetic studies will underscore the impact of Pd in enhancing Au catalytic properties and a HAADF-EDX study will provide more information about the AuPd alloy, to find correlations between its presence and dramatic increase in FDCA yield.

5.2 Results and discussion

5.2.1 Preparation of a Mg/Al = 3 hydrotalcite

Hydrotalcites were synthesised using the alkali-free co-precipitation method of Cantrell and co-workers[23], with some modifications, from diluted metal nitrate solutions, exactly as described in **Chapter 2.2.1.**

5.2.2 Typical preparation of AuPd/hydrotalcite catalysts

The deposition-precipitation method[24, 25] described in **Chapter 2.1.4** was used to prepare a series of AuPd/HT catalysts. The total amount of metal was chosen to be 1 wt. %, while the desired molar ratios were $Au_{95}Pd_5$, $Au_{90}Pd_{10}$, $Au_{80}Pd_{20}$, $Au_{70}Pd_{30}$ and $Au_{60}Pd_{40}$.

5.2.3 Characterisation of different AuPd loading on hydrotalcite

Bulk elemental analysis was performed to determine the actual AuPd content. Structural properties of materials were examined by powder X-ray diffraction (XRD) and N_2 porosimetry; IR was also performed to investigate any changes in HT structure after the deposition-precipitation and following reduction of AuPd nanoparticles. HAADF-STEM was used to measure the average AuPd particle size and EDX to accurately map the AuPd alloy.

5.2.3.1 Elemental analysis

EDX and ICP analyses were conducted on AuPd/HTs to quantify Au and Pd bulk and surface compositions. Gold and palladium loadings, obtained *via* EDX analysis, mapping accurately 100 single nanoparticles for each catalyst, are reported in **Table 5.1**, together with ICP bulk analysis for comparison. A slight discrepancy between nominal and determined AuPd ratio was found, nevertheless, all the catalysts have shown to be in a trend, as predicted; such discrepancy was observed also by Venezia and co-authors[26].

Table 5.1: elemental analysis of AuPd/HTs by EDX and by ICP.

Nominal AuPd loading / atomic %	Au / atomic % (EDX)	Pd / atomic % (EDX)	Alloy / atomic % (EDX)	Au / atomic % (ICP)	Pd / atomic % (ICP)
$Au_{95}Pd_5$	82	18	41	93	7
$Au_{90}Pd_{10}$	80	20	55	91	9
$Au_{80}Pd_{20}$	75	25	64	84	16
$Au_{70}Pd_{30}$	72	28	68	72	28
$Au_{60}Pd_{40}$	70	30	59	66	34

ICP bulk analysis allowed finding the exact molar ratio in the catalysts, so they were labelled as $Au_{93}Pd_7$, $Au_{91}Pd_9$, $Au_{84}Pd_{16}$, $Au_{72}Pd_{28}$, and $Au_{66}Pd_{34}$. **Figure 5.1** shows an example of co-existence of Au and Pd in a single metal particle obtained for $Au_{72}Pd_{28}$:

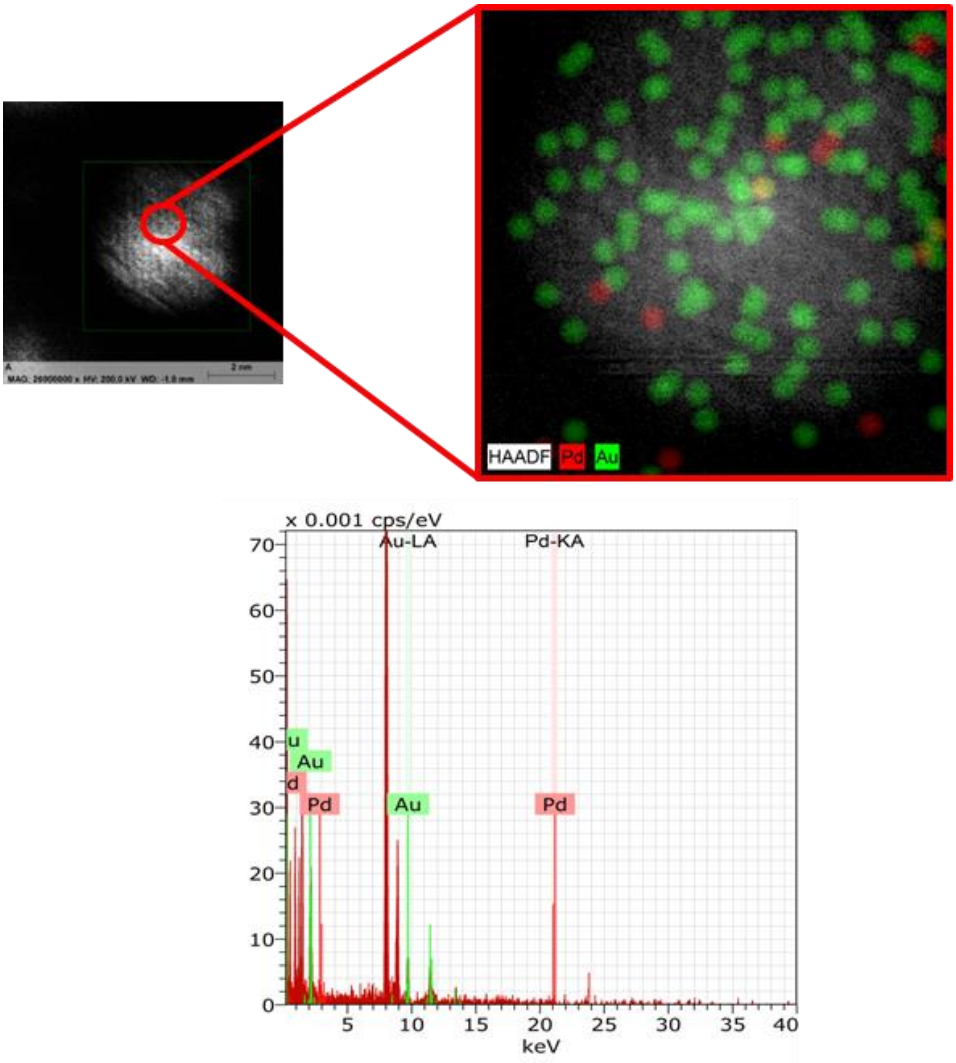

Figure 5.1: top – HR-TEM image of a single AuPd NP in Au $Au_{72}Pd_{28}$ and HAADF detail of Au and Pd mapping, bottom – EDX analysis showing Au – LA and Pd – KA spectral lines.

Figure 5.2 shows, instead, the Au and Pd average bulk distribution for all the catalysts, being the alloy itself a fraction of the total metal loading. Nishimura and co-authors[27] prepared protected Au/Pd-PVP supported on HT materials and declared a homogeneous alloy phase, but no accurate characterisation was done; in this thesis work, instead, the deposition-precipitation yielded a mixture of pure Au, pure Pd and AuPd alloy NPs, accurately mapped by EDX. No evidence of any core-shell structure was observed in the analysed particles, but pure Au, pure Pd or Au/Pd alloy were clearly detected.

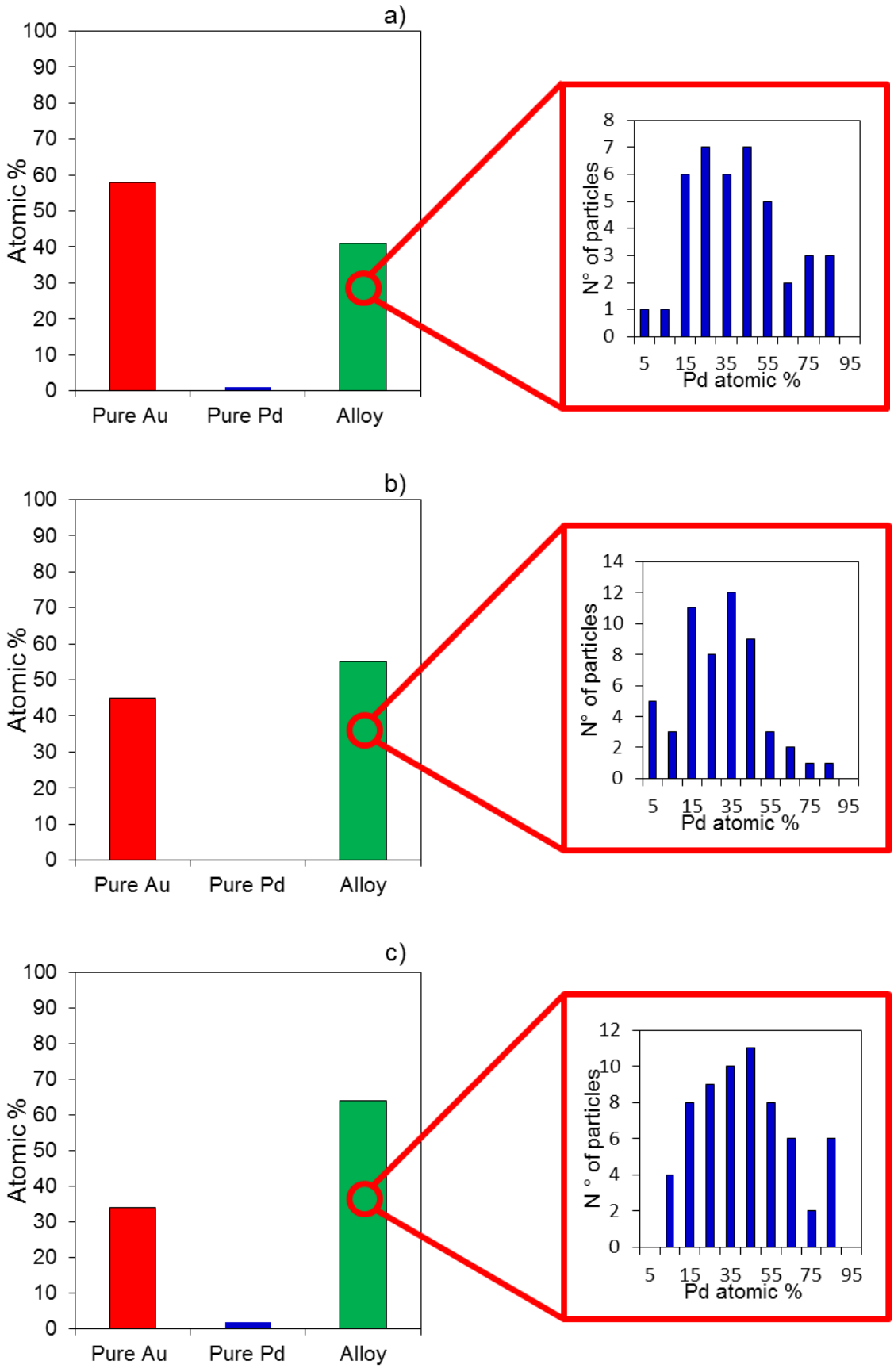
a)
Atomic %
100
90
80
70
60
50
40
30
20
10
0
Pure Au
Pure Pd
Alloy
N° of particles
8
7
6
5
4
3
2
1
0
5
15
35
55
75
95
Pd atomic %
b)
Atomic %
Pure Au
Pure Pd
Alloy
N° of particles
14
12
10
8
6
4
2
0
Pd atomic %
c)
Atomic %
Pure Au
Pure Pd
Alloy
N ° of particles
12
10
8
6
4
2
0
Pd atomic %

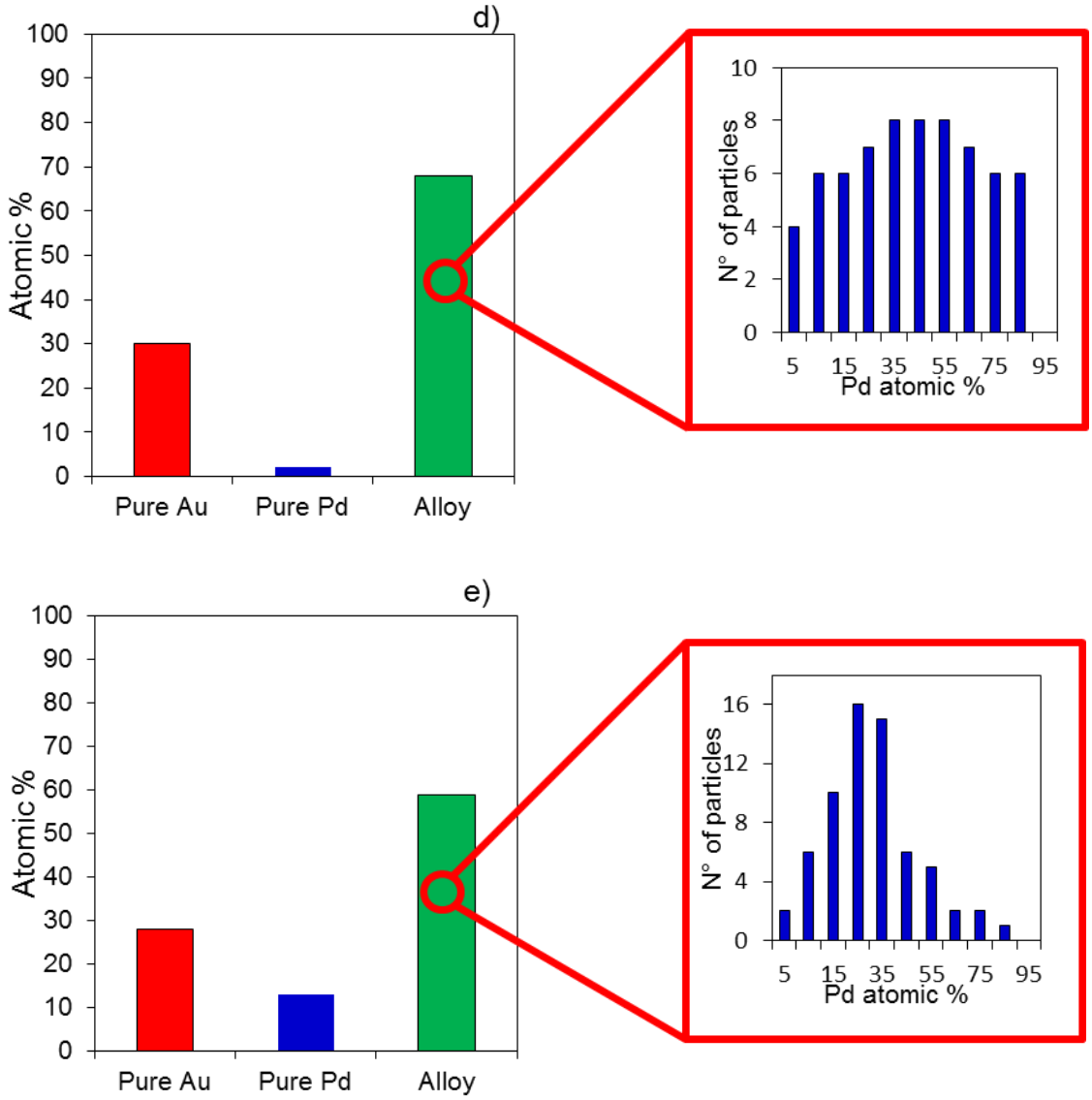

Figure 5.2: left parts – elemental analysis showing a broad distribution of pure Au, pure Pd and AuPd alloy in AuPd catalysts a) $Au_{93}Pd_7$, b) $Au_{91}Pd_9$, c) $Au_{84}Pd_{16}$, d) $Au_{72}Pd_{28}$, e) $Au_{66}Pd_{34}$. Right parts – insets show distributions of the Pd atomic % in the alloy.

XPS analysis was particularly difficult, as gold and palladium lines always overlap. The analysis of Au 4d and Pd 3d spectra has shown clear spectral contributions from both Au and Pd. As described by Hutchings and co-authors[25], an accurate analysis of the alloy and of eventual Pd/PdO species was difficult to achieve and, in order to estimate Au and Pd surface composition, the spectral envelope was deconstructed into its respective Pd 3d and Au 4d components. Au and Pd standard spectra were used and Pd contribution was subtracted, to allow find the composition shown in **Table 5.2.**

Table 5.2: bulk (ICP) vs. surface (XPS) composition of AuPd/HT series.

Nominal AuPd loading / atomic %	Au / atomic % (ICP) bulk	Pd / atomic % (ICP) bulk	Au / atomic % (XPS) surface	Pd / atomic % (XPS) surface
$Au_{95}Pd_5$	93	7	94	6
$Au_{90}Pd_{10}$	91	9	88	12
$Au_{80}Pd_{20}$	84	16	86	14
$Au_{70}Pd_{30}$	72	28	76	24
$Au_{60}Pd_{40}$	66	34	74	26

To summarise, **Figure 5.3** shows good agreement between these different bulk and surface averaging analytical methods.

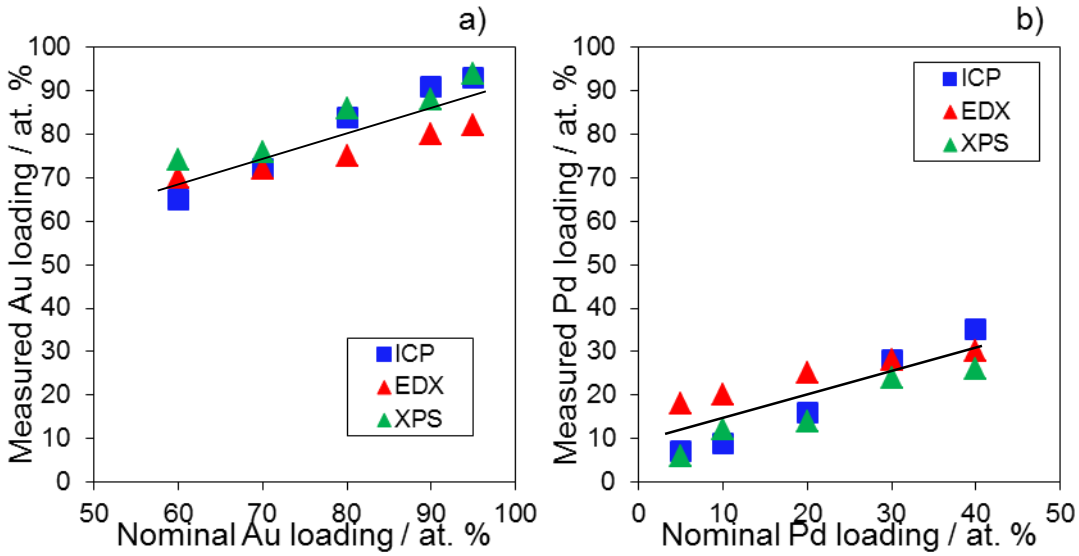

Figure 5.3: nominal vs. measured Au and Pd atomic %.

5.2.3.2 XRD

Ex situ powder XRD were run at room temperature on the parent HT and on AuPd/HT catalysts. The parent HT exhibited reflections at 11.2° (*d* 003), 22.4° (*d* 006), 34.2° (*d* 009), 38.3° (*d* 015), 44.6° (*d* 018), 60.1° (*d* 110), 61.3° (*d* 113) and 64.7° (*d* 116) **(Figure 5.4)**, consistent with literature values[28-30] for this material and as already discussed in **Chapter 3** and **Chapter 4**.

Volume-averaged crystallite sizes for hydrotalcite were determined as 7.4 nm from the 11.2° peak, applying the Scherrer equation[31]. These small crystallite sizes indicate that the extended porous network arises from agglomeration or fusion of these nanocrystalline platelets. The intensity of Au peaks[32, 33] are usually visible at 38° (*d* 111), 44° (*d* 200), 65° (*d* 220) and 78° (*d* 311), while the Pd ones[34-36] are visible at 40° (*d* 111), 46° (*d* 200), 68° (*d* 220) and 81° (*d* 311); nevertheless, these peaks overlap with HT ones and are not visible for low gold-palladium loadings, because of their weak intensity.

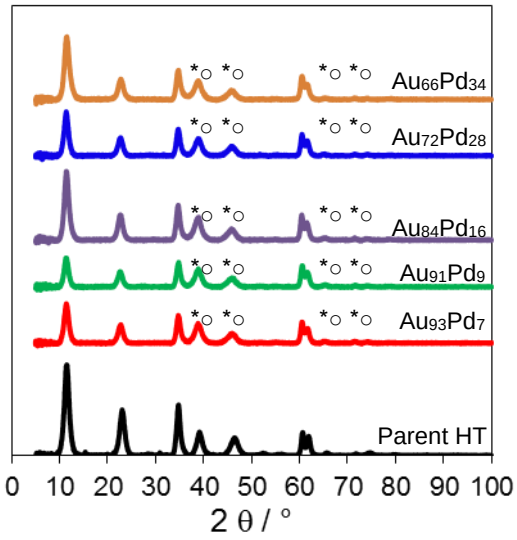

Figure 5.4: X-ray diffractograms of AuPd/HT catalysts, Au positions are marked with * and Pd ones with ○.

Due to HT and AuPd peaks overlapping, it was not possible to observe at room temperature any peak broadening at 38-40°, reported to be an indication of AuPd alloy formation by Venezia and co-authors[26]. For this reason, in order to follow any changes in the alloy composition with the temperature and to remove the contribute of HT structure, an *in situ* XRD experiment **(Figure 5.5)** was carried out on a $HAuCl_4$ + $PdCl_2$ precursor of $Au_{72}Pd_{28}$/HT, as this catalyst has shown the highest FDCA yield, (see **Chapter 5.2.4.1** and **5.2.4.2)**. Spectra were acquired as a function of calcination temperature, under O_2 atmosphere, between room temperature and 600 °C**.**

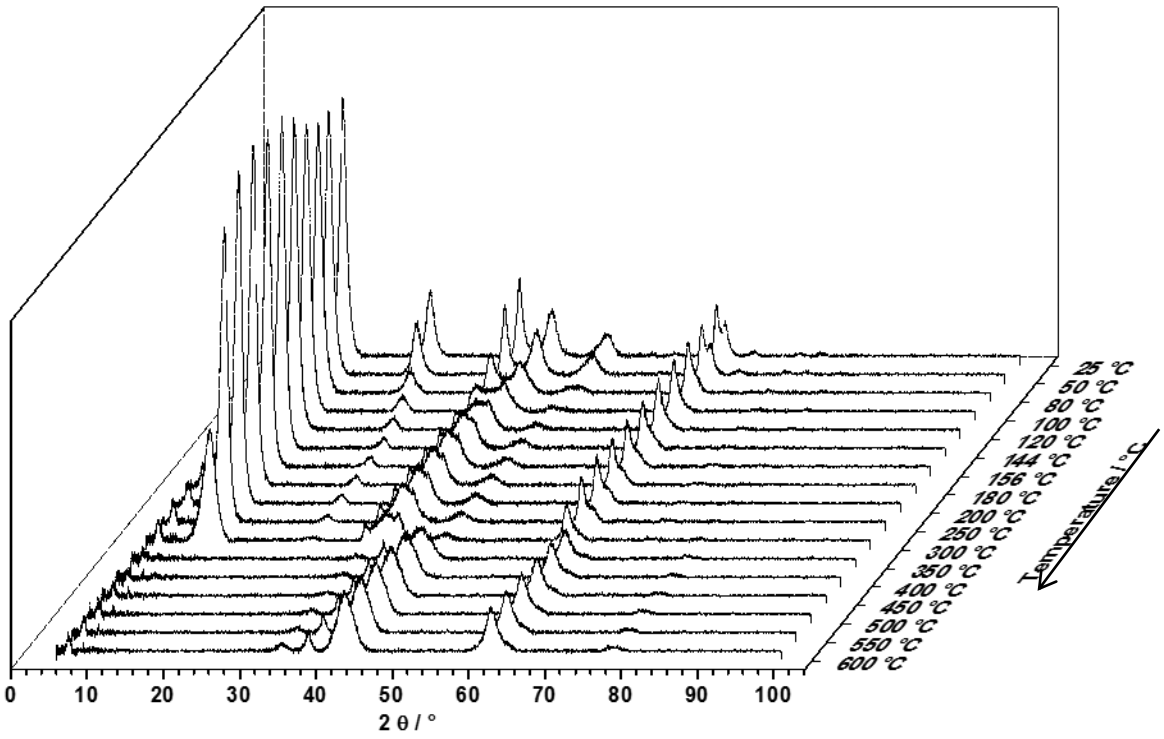

Figure 5.5: *in-situ* XRD patterns for $HAuCl_4$ + $PdCl_2$ deposited on HT as a function of calcination temperature.

As already explained in **Chapter 4.2.3.1**, the signals relative to characteristic hydrotalcite reflections[37, 38] became weaker at above 144 °C, although the HT structure is maintained until 200-250 °C, therefore Au and Pd peaks became visible and background subtractable, being a signal/noise distinction possible, only after 300 °C. Peaks at 38-40°, which resulted very broad confirming observations made by Venezia and co-authors[26], were fitted and deconvoluted to obtain an estimation of Au and Pd particle growth, as shown in **Figure 5.6**.

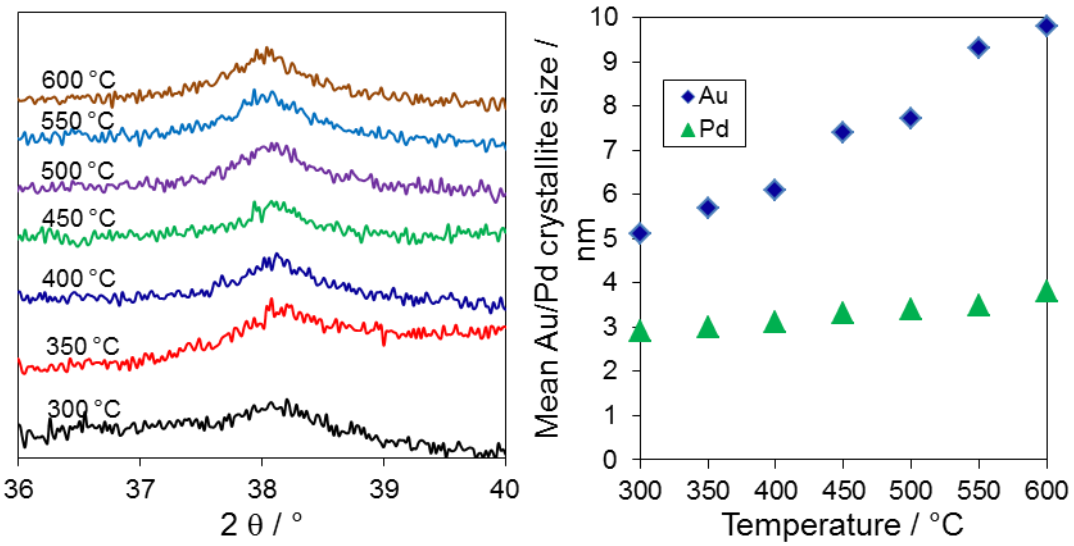

Figure 5.6: left - XRD patterns of $Au_{70}Pd_{30}$/CHT after subtraction of HT component as a function of calcination temperature; right – evolution of Au/Pd particle size with loading.

Au average particle size increased with the calcination temperature, as expected, because a similar trend was already observed in **Chapter 4.2.3.1.** Minor changes were observed for Pd, instead, and a similar result was already reported: Pd clusters are more highly dispersed for a given coverage and are known to be more sinter-resistant than Au ones[39]. Nevertheless, it is worth to remember that, at such low concentration and for their small dimensions, Pd particles were near to the limit detectable by XRD.

The *in situ* XRD experiment in this thesis work was compared with a previous work published by Lee, Lambert and co-authors[22], to underline differences between two preparation methods for AuPd alloy NPs having two different kind of structures. In Lee and Lambert's work, well-defined Au core – Pd shell structured NPs were prepared and then thermally treated during an *in situ* XRD experiment. Results described show an evolution of the Au core – Pd shell structure to a AuPd alloy as a function of annealing temperature and this was proved by an observed immediate decrease in measured lattice parameters, from 4.082 to 4.043 (± 20 %) in the interval between room temperature and 300 °C. After this temperature, relatively little change occurred, indicating that Pd/Au intermixing was essentially complete by 300 °C. Conversely, during this alloying phase, the particle diameter remained constant (5 nm) up to 300 °C, while it increased rapidly to 30 nm at 600 °C.

In this thesis work, instead, an almost constant lattice parameter of 4.085 ± 0.05 Å was observed, which is similar to 4.079 Å, the reported value in the JCPDS database[40] for

bulk fcc Au; for comparison, the reported value in the JCPDS database[41] for bulk fcc Pd is instead 3.890 Å. EDX analysis has shown, indeed, that the alloy is only a fraction of the catalyst, made of pure Au, pure Pd and AuPd particles. Changes in the alloy composition were observed by Lambert and co-authors[22] in the exact range of temperatures in which, in this thesis work, HT peaks overlaps with Au and Pd ones, therefore no changes could be detected during the AuPd formation and almost constant lattice parameters vs. temperature were found, as visible in **Figure 5.7**.

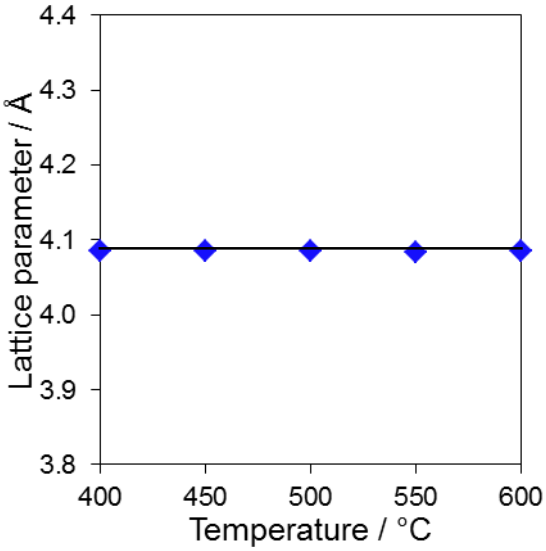

Figure 5.7: lattice parameters as a function of calcination temperature.

5.2.3.3 N_2 Porosimetry

N_2 adsorption-desorption isotherms[42, 43] for the parent hydrotalcite and Au/HTs are shown in **Figure 5.8**. The isotherms have been offset for clarity.

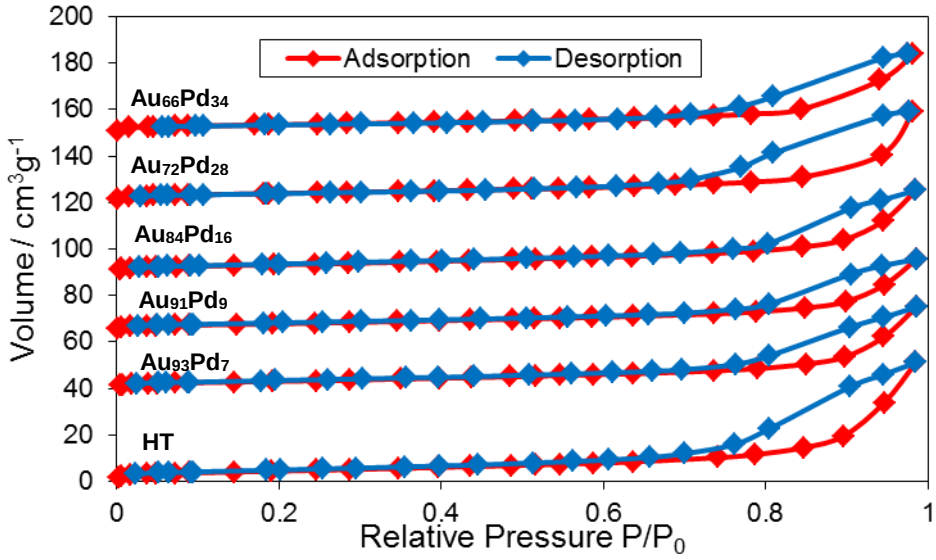

Figure 5.8: N_2 adsorption-desorption isotherms for AuPd/HTs.

The parent hydrotalcite exhibits a type II H3 isotherm, that is retained in all the Au/HTs, and is consistent with microporous crystallites with interplatelet mesoporous voids and slit type pores[44], as already discussed in **Chapter 3.2.3.3.** Following AuPd deposition and 200 °C calcination the Au/HTs exhibit smaller hysteresis loops than the parent HT. A reduction in the hysteresis may suggest that pores are more accessible[45] after calcination at 200 °C, due to an expansion of interplatelet mesoporous voids and a removal of water from interlayers[46, 47]. **Table 5.3** reports BET surface areas for the parent hydrotalcite and Au/HTs, with values in accordance with the literature[48].

Table 5.3: Surface areas of HT and Au/HTs determined by N_2 porosimetry.

	BET surface area / m^2g^{-1}
Parent HT	152 ± 15.2
$Au_{93}Pd_7$	149 ± 14.9
$Au_{91}Pd_9$	138 ± 13.8
$Au_{84}Pd_{16}$	143 ± 14.3
$Au_{72}Pd_{28}$	141 ± 14.1
$Au_{66}Pd_{34}$	140 ± 14.0

5.2.3.3 Ex situ DRIFT spectra

Ex situ DRIFT spectra **(Figure 5.9)** compare the uncalcined parent hydrotalcite and different AuPd/HT catalysts, calcined at 200 °C under oxygen and reduced under hydrogen at the same temperature; the peak assignment was made according to what reported by Meliàn-Cabrera and co-authors[49] and Davis and co-authors[47]. At 3800-2500 cm^{-1} the OH stretching is clearly visible for the parent hydrotalcite and the AuPd/HT as a broad band. The shoulder at 3080 cm^{-1} is characteristic of layered HTs, arising from hydrogen bonding between water molecules and CO_3^{2-} groups within the interlayer region. The OH bend of physisorbed water is visible at 1590 cm^{-1} for parent HT, as expected and as already described in **Chapter 3** and **Chapter 4**, while the two bands at 1497 cm^{-1} and 1331 cm^{-1} are due to the stretching of CO_3^{2-} in the interlayer region.

Deposition-precipitation[24] of AuPd on HT, followed by calcination and final reduction, caused interlayer water removal and a carbonate rearrangement, evidenced by the absence of the previous shoulder in the OH region at 3080 cm^{-1} and the 1590 cm^{-1} bend, and emergence of two new peaks corresponding to C=O at 1508 cm^{-1} and to C-O at 1338 cm^{-1} in **Figure 5.9.** No significant changes were seen as a function of AuPd loading and after following reduction under H_2.

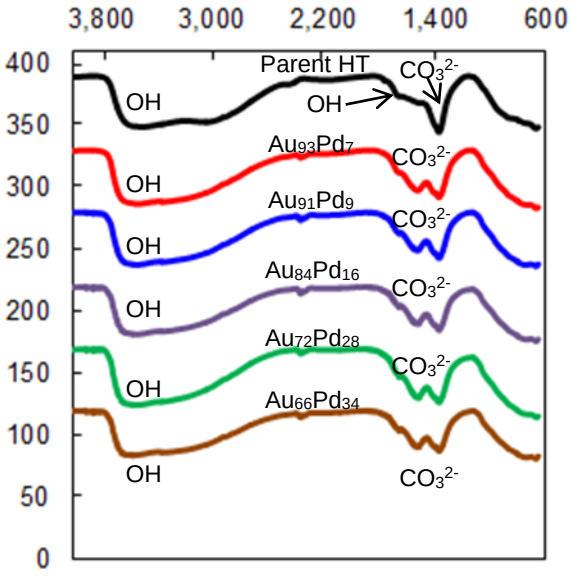

Figure 5.9: DRIFT spectra of parent uncalcined HT and of $Au_{93}Pd_7$/HT, $Au_{91}Pd_9$/HT, $Au_{84}Pd_{16}$/HT, $Au_{72}Pd_{28}$/HT, and $Au_{66}Pd_{34}$/HT, catalysts calcined at 200 °C under O_2, then reduced under H_2 at the same temperature.

5.2.3.4 TEM and AuPd particle size distribution

Dark/bright field (S)TEM images of the Au/HT series are shown in **Figure 5.10:**

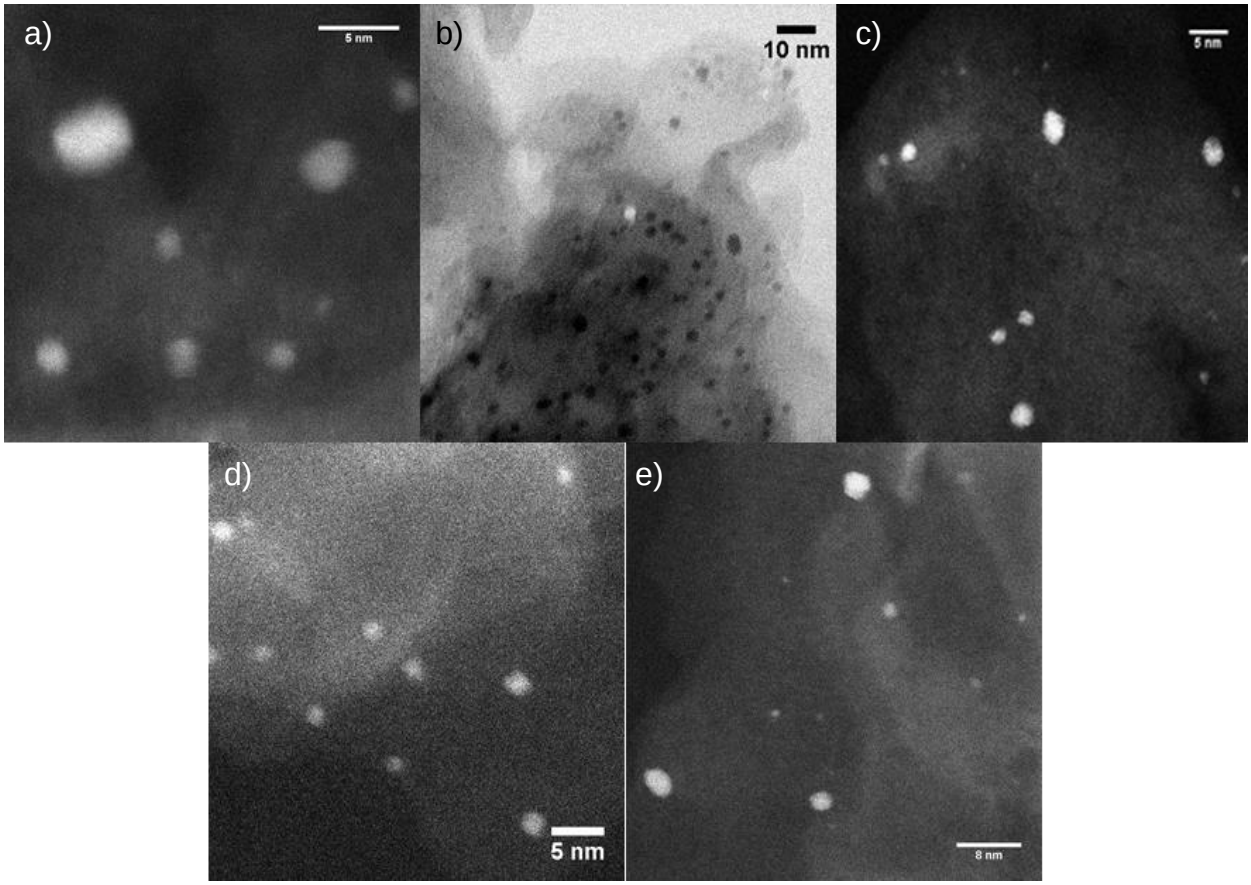

Figure 5.10: Dark and bright field (S)TEM images of 1 wt. % AuPd/HT catalysts a) $Au_{93}Pd_{7}$, b) $Au_{91}Pd_{9}$, c) $Au_{84}Pd_{16}$, d) $Au_{72}Pd_{28}$ and e) $Au_{66}Pd_{34}$.

ImageJ software was used to measure the particle size distribution for each material, and results are shown in **Figure 5.11**. Particles appear to be very well dispersed, small and of uniform size and shape for all the loadings, showing a narrow range of size between 2 and 6 nm, in agreement with XRD data fitting.

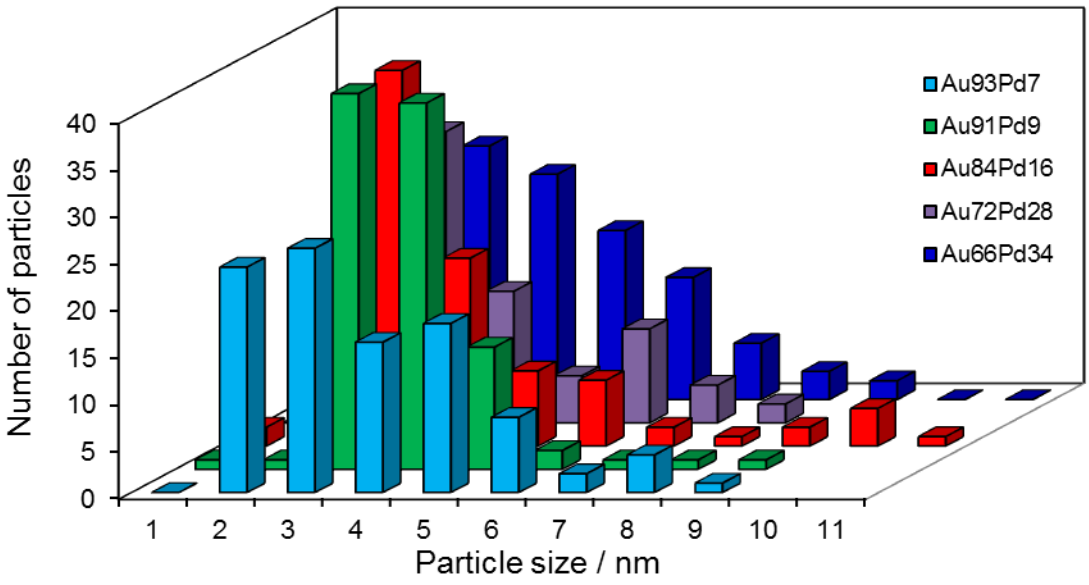

Figure 5.11: particle size distributions for AuPd/HT catalysts, 100 NPs counted for each sample.

5.2.4 Detailed studies on the aerobic selective oxidation of HMF

5.2.4.1 The effect of different AuPd atomic ratios on the aerobic selox of HMF

A series of different AuPd catalysts, respectively $Au_{93}Pd_7$, $Au_{91}Pd_9$, $Au_{84}Pd_{16}$, $Au_{72}Pd_{28}$ and $Au_{66}Pd_{34}$ were supported on HT at 200 °C and activated under H_2, following the previously described deposition-precipitation procedure[24] (see **Chapter 5.2.2**) and being 1 wt. % the total amount of metal; reactions were carried out with or without extra added NaOH**,** following a protocol, here described, and named standard reaction conditions: 25 mg of catalyst, 0.1 mmol of HMF, T = 90 °C, V = 6 ml H_2O, 500 rpm and ν O_2 = 15 ml/min. When required, NaOH 1 M (6 mmol, pH = 14) was added for high pH reactions.

No reaction occurred when 1 wt. % Pd/HT catalyst was used as a control test in H_2O, with or without NaOH. The raw and complete reaction profiles without extra added base at pH = 9 are shown in **Figure 5.12** below:

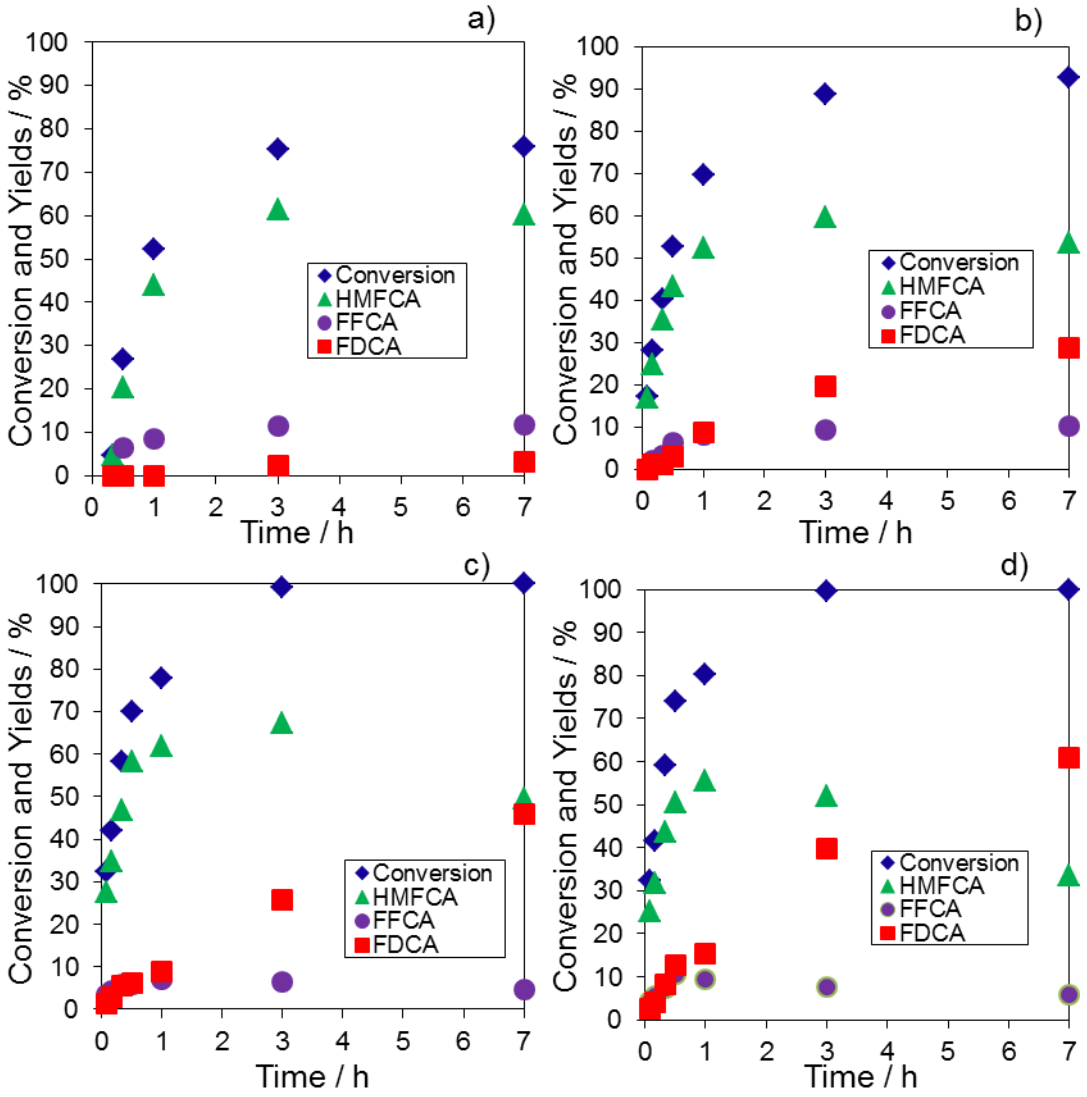
a)
b)
c)
d)
Conversion and Yields / %
Time / h
Conversion
HMFCA
FFCA
FDCA

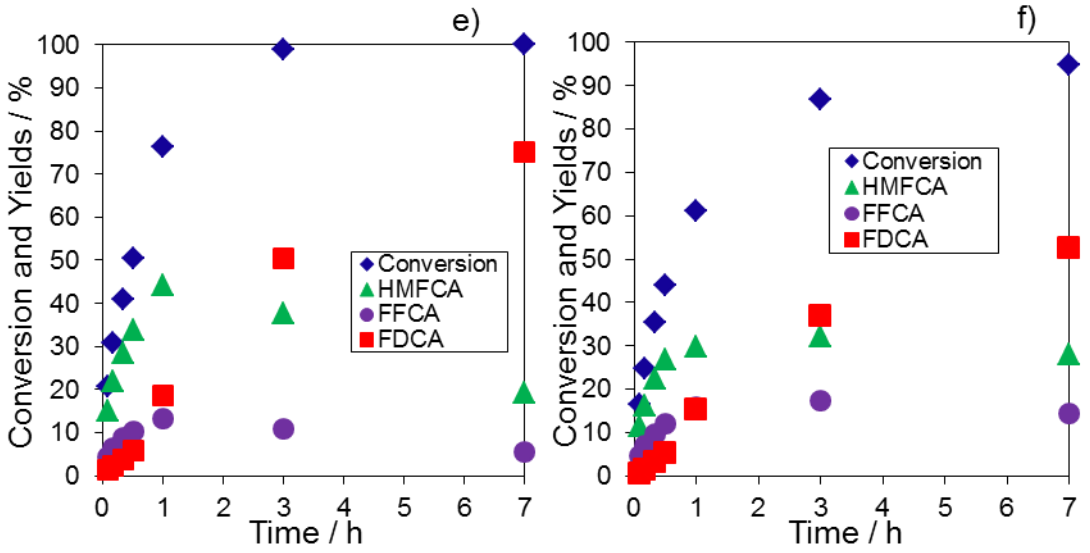

Figure 5.12: reaction profiles for the aerobic selox of HMF, using different 1 wt. % AuPd/HT catalysts and without extra added base at pH = 9. a) 1 wt. % Au, b) $Au_{93}Pd_7$, c) $Au_{91}Pd_9$, d) $Au_{84}Pd_{16}$, e) $Au_{72}Pd_{28}$ and f) $Au_{66}Pd_{34}$. Standard reaction conditions followed.

As the amount of palladium in the catalyst increases, conversion and FDCA yields appear to increase, showing a maximum in FDCA yield for $Au_{72}Pd_{28}$. Reactions were then repeated in the presence of 6 mmol of NaOH (pH = 14) and all the raw complete reaction profiles are shown in **Figure 5.13**.

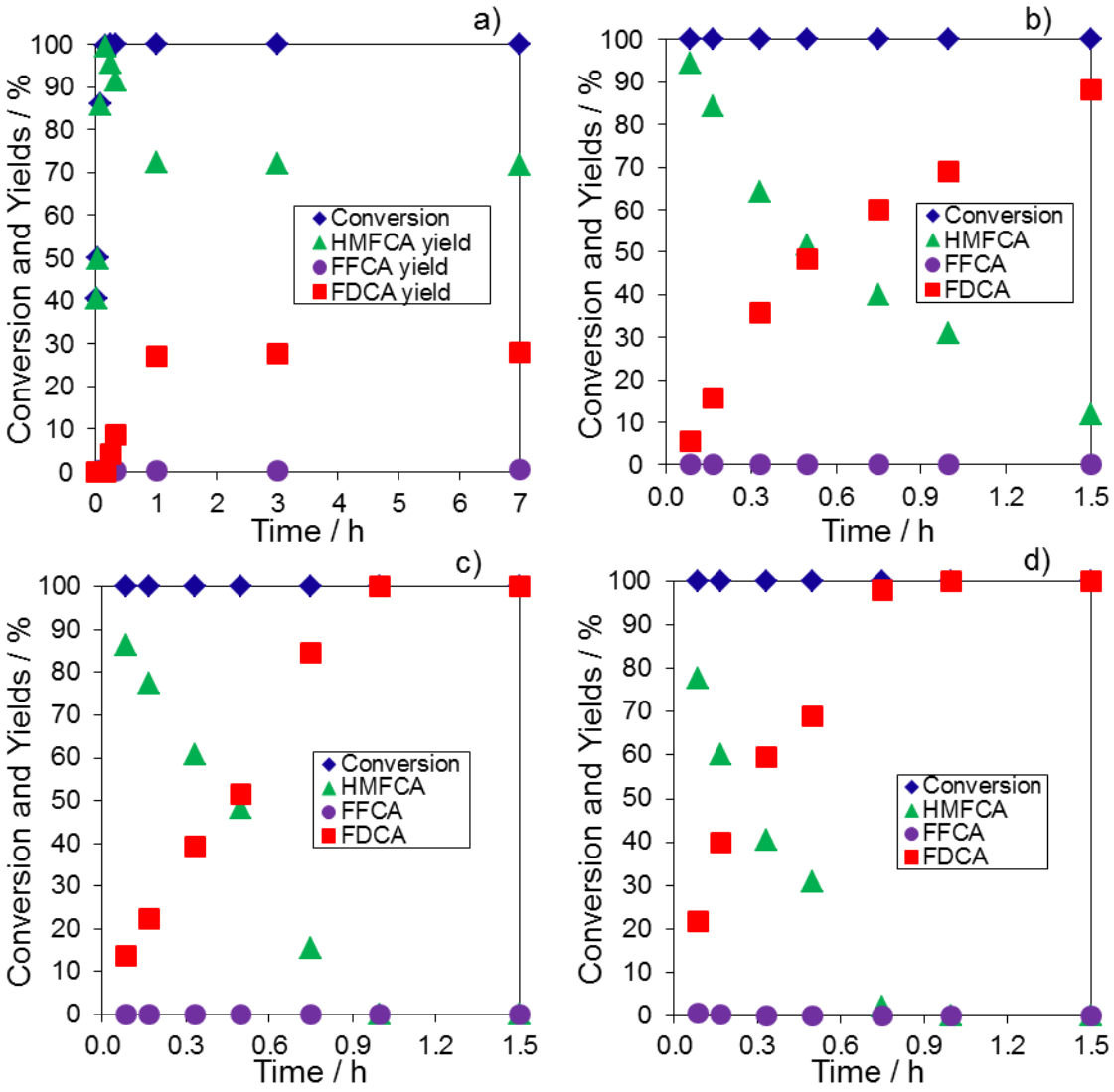
a)
Conversion and Yields / %
Time / h
Conversion
HMFCA yield
FFCA yield
FDCA yield
b)
Conversion and Yields / %
Time / h
Conversion
HMFCA
FFCA
FDCA
c)
Conversion and Yields / %
Time / h
Conversion
HMFCA
FFCA
FDCA
d)
Conversion and Yields / %
Time / h
Conversion
HMFCA
FFCA
FDCA

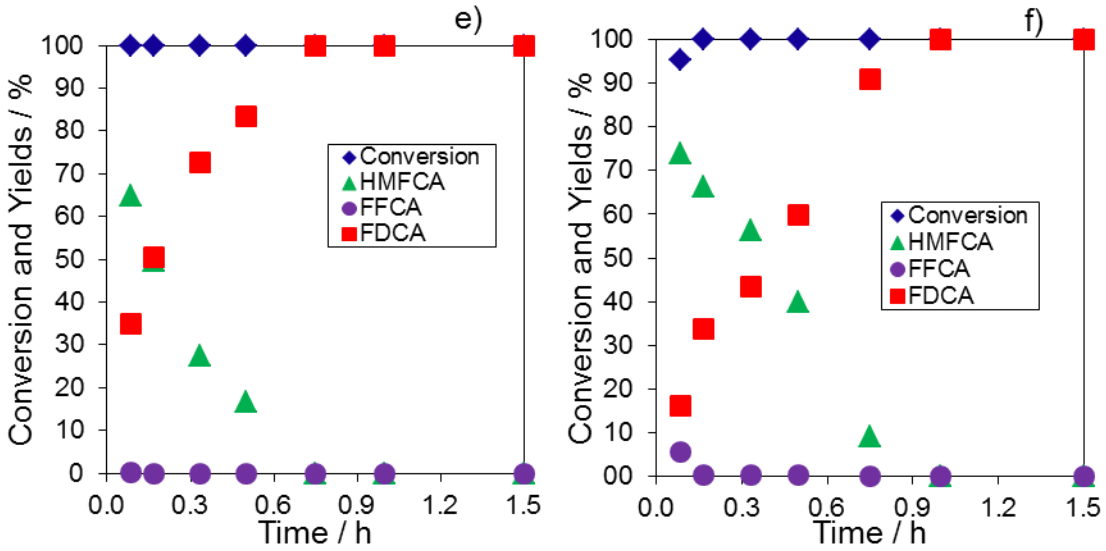

Figure 5.13: reaction profiles for the aerobic selox of HMF, using different 1 wt. % AuPd/HT catalysts at pH = 14 a) 1 wt. % Au, b) $Au_{93}Pd_7$, c) $Au_{91}Pd_9$, d) $Au_{84}Pd_{16}$, e) $Au_{72}Pd_{28}$ and f) $Au_{66}Pd_{34}$. Reaction were performed under standard conditions + NaOH = 6 mmol, 1M.

Based on these experimental results, it appears that AuPd/HT are high efficient catalysts for the selox of HMF to FDCA even in the absence of NaOH, showing minor pH dependence that what observed in **Chapter 3.2.4.2** for pure Au.

A systematic kinetic study to follow the exact impact of NaOH on the conversion of HMF as the palladium loading increases was then carried out using an excess of HMF (0.5 mmol instead of 0.1 mmol), in order to slow down the rapid oxidation of HMF to HMFCA. Results are shown in **Figure 5.14**, being $Au_{93}Pd_7$ the most active catalyst per Pd atomic % in the absence of NaOH 1M; high catalytic performances were achieved even when a minor amount of Pd was added to Au, as shown plotting normalised reaction rates per gram of gold vs. Pd atomic %.

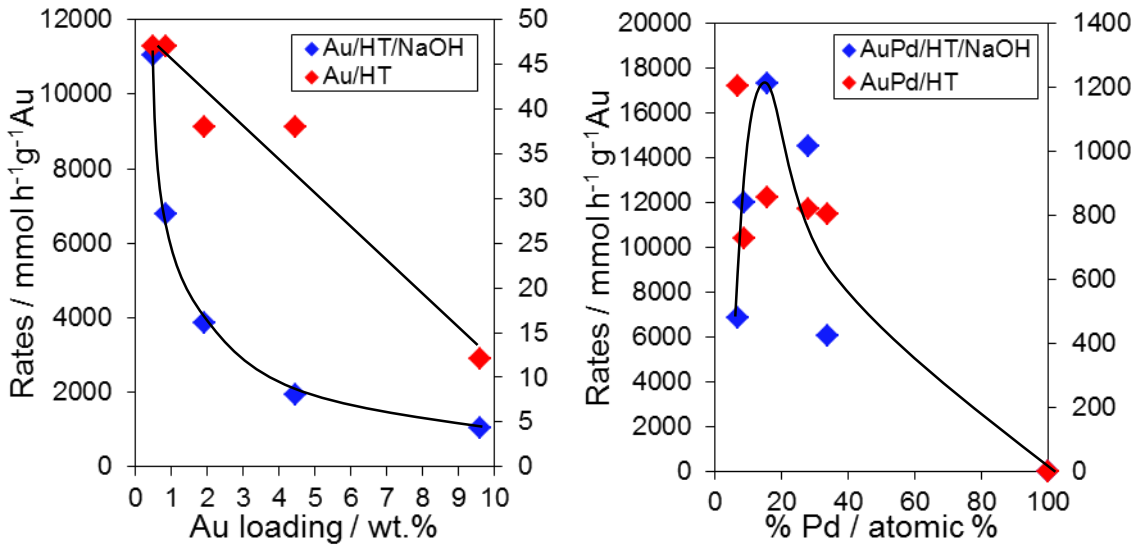

Figure 5.14: left – mass normalised rates of HMF selox as a function of Au loading without (in red, right axis) and with NaOH (in blue, left axis); right – mass normalised rates of HMF selox per g Au as a function of Pd atomic % without (in red, right axis) and with NaOH addition (in blue, left axis). Reaction conditions: 0.2 mmol of HMF for Au/HT catalyst, 0.5 mmol of HMF for AuPd/HT ones, all the rest identical to standard conditions. When added, NaOH = 6 mmol (pH = 14).

All the AuPd catalysts have shown a similar NaOH enhancement for HMF selox (6-20 folds, in the range of the experimental error), that is significantly lower compared to the 143 folds obtained for 1 wt. % Au (having the same wt. % metal amount of the AuPd/HT series), suggesting that Pd is capable to enhance Au catalytic activity even at pH = 9. It is interesting to observe in **Figure 5.15** that NaOH addition has shown a minor impact on $Au_{93}Pd_7$ and $Au_{66}Pd_{34}$ (6 and 8 folds, respectively) than on $Au_{91}Pd_9$, $Au_{84}Pd_{16}$ and $Au_{72}Pd_{28}$ (17, 20 and 18, respectively) for the oxidation of R-CHO.

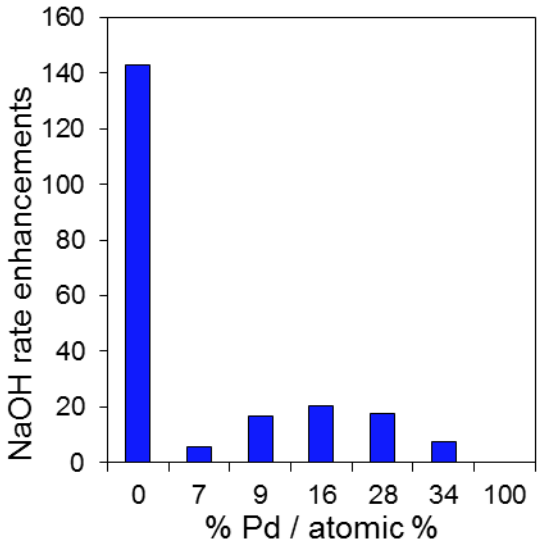

Figure 5.15: comparative NaOH rate enhancements for the aerobic selective oxidation of HMF, using 1 wt. % Au or different AuPd loadings. Standard reaction conditions followed, but 0.2 mmol of HMF for Au and 0.5 mmol for AuPd catalysts. When added, NaOH = 6 mmol, 1M, pH = 14.

5.2.4.2 The effect of different AuPd atomic ratios on the aerobic selox of HMFCA

In order to better decouple the influence of palladium contribute in enhancing gold performances on the selective oxidation of the aldehyde from the alcohol function in HMF, reactions were carried out on HMFCA with or without extra added NaOH**,** following a protocol, here described, and named standard reaction conditions: 25 mg of catalyst, 0.1 mmol of HMFCA, T = 90 °C, V = 6 ml H_2O, 500 rpm and ν O_2 = 15 ml/min. When required, NaOH 1 M (6 mmol, pH = 14) was added for high pH reactions. Raw and complete reaction profiles are shown in **Figure 5.16.**

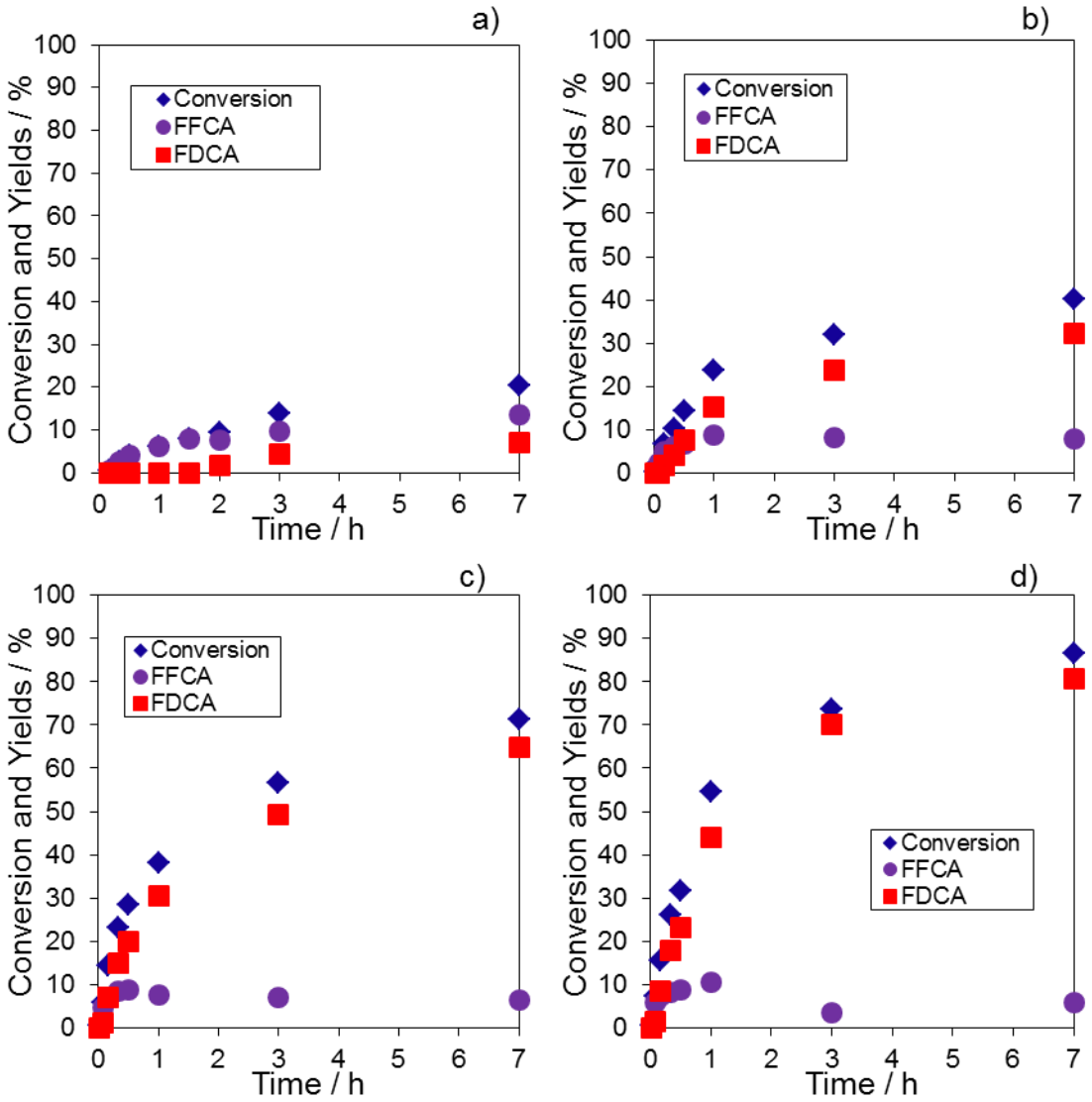
a)
b)
c)
d)
Conversion
FFCA
FDCA
Conversion and Yields / %
Time / h

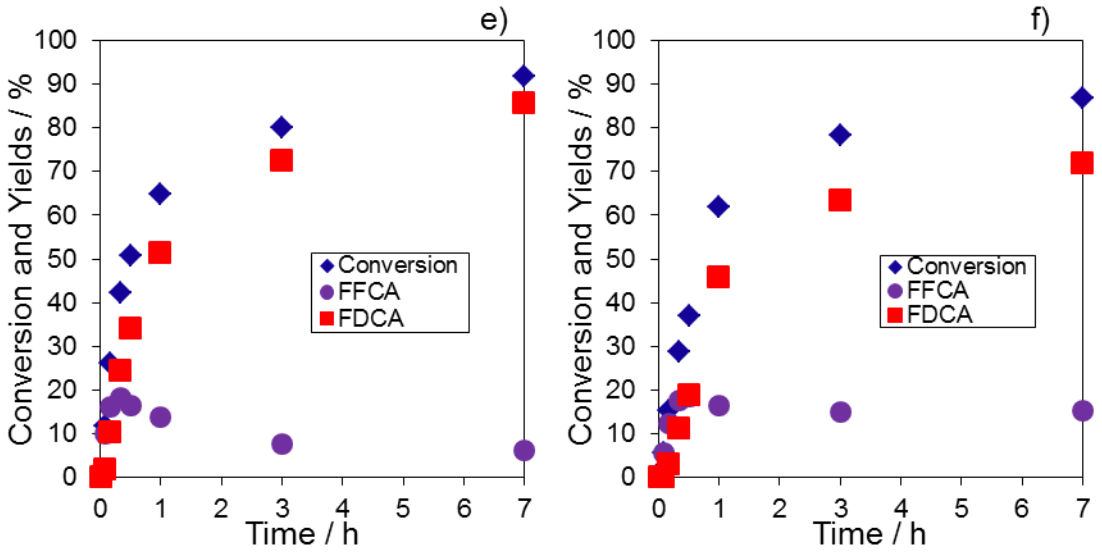

Figure 5.16: reaction profiles for the aerobic selox of HMFCA, using different 1 wt. % AuPd/HT catalysts at pH = 9 a) 1 wt. % Au, b) $Au_{93}Pd_7$, c) $Au_{91}Pd_9$, d) $Au_{84}Pd_{16}$, e) $Au_{72}Pd_{28}$ and f) $Au_{66}Pd_{34}$. Standard reaction conditions followed.

Also for HMFCA, as the amount of palladium increases, conversion and FDCA yields appear to increase, showing a maximum in FDCA yields for $Au_{72}Pd_{28}$. The reactions were then repeated in the presence of 6 mmol of NaOH at pH = 14 and all the raw complete reaction profiles are shown in **Figure 5.17.**

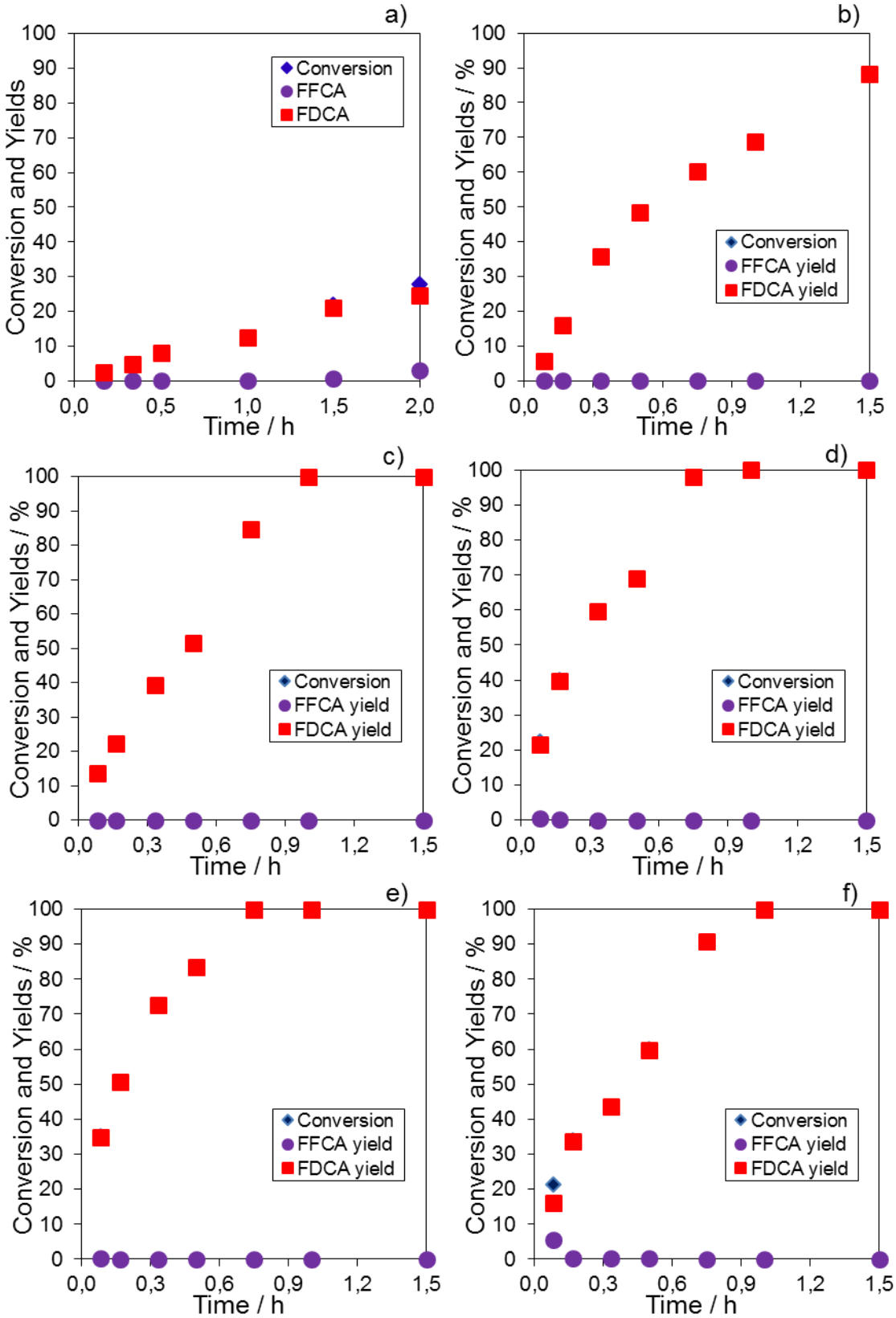

Figure 5.17: reaction profiles for the aerobic selox of HMFCA, using 1 wt. % Au/HT or 1 wt. % AuPd/HT catalysts at pH = 14 a) 1 wt. % Au, b) $Au_{93}Pd_7$, c) $Au_{91}Pd_9$, d) $Au_{84}Pd_{16}$, e) $Au_{72}Pd_{28}$ and f) $Au_{66}Pd_{34}$. Standard reaction conditions followed + NaOH = 6 mmol, 1M.

A systematic kinetic study to follow the impact of NaOH on the conversion of HMFCA as the palladium loading increases was then carried out. Results are shown in **Figure 5.18 - right**, being $Au_{72}Pd_{28}$ the most active catalyst per Pd atomic % in the absence of NaOH 1M and underlining the effect of Pd in enhancing gold rates and catalytic properties; also, the effect and the importance of Pd are more evident for R-OH than for R-CHO. It is interesting to observe that such AuPd ratio was found to be the optimal also for the synthesis of H_2O_2 by Hutchings and co-authors[25]. **Figure 5.18 – left** shows the same reaction using different wt. % Au/HT, for comparison (see **Chapter 3.2.4.4).**

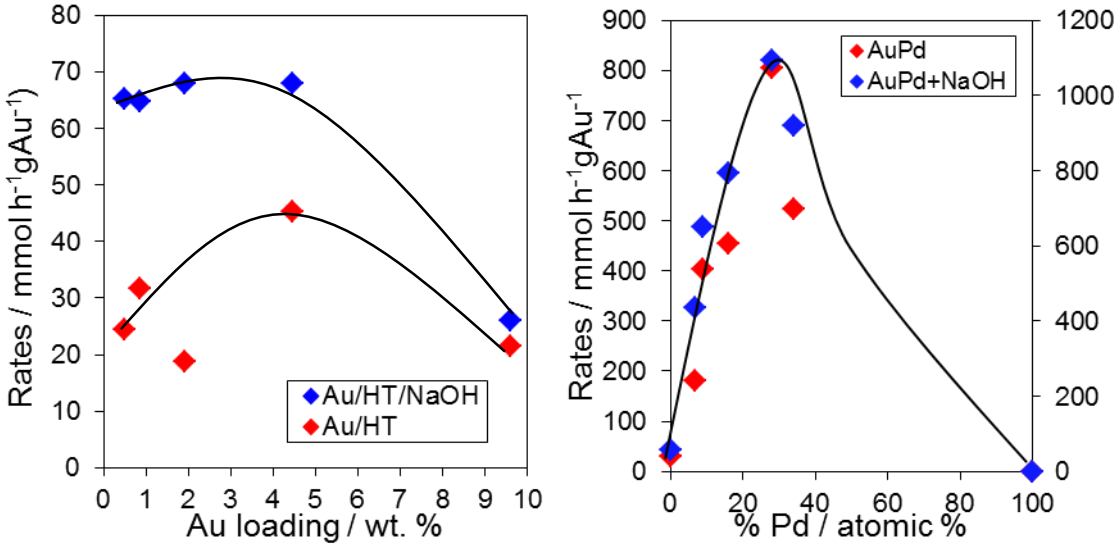

Figure 5.18: left – mass normalised rates of HMFCA selox as a function of Au loading without (in red) and with NaOH (in blue) as comparison; right – mass normalised rates of HMFCA selox per g Au as a function of Pd at.% without (in red, left axis) and with NaOH addition (in blue, right axis). Reaction conditions: 0.1 mmol of HMFCA for both the catalysts, all the other parameters identical to standard conditions. When added, NaOH = 6 mmol (pH = 14).

Rates of reaction for the selox of the alcohol were at least 10-20 times faster on AuPd than on pure Au. All the AuPd/HT catalysts (being 1 wt % the total amount of metal) and also 1 wt. % Au/HT have shown a similar NaOH enhancement for HMFCA selox (1-2 folds), in the range of the experimental error, as shown in **Figure 5.19.**

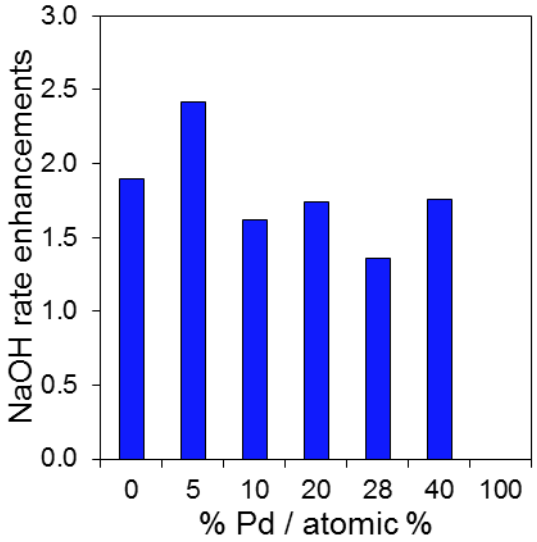

Figure 5.19: comparative NaOH rate enhancements for the selective aerobic oxidation of HMFCA using 1 wt. % Au or different AuPd loadings. Reaction conditions: 25 mg of catalyst, 0.1 mmol of HMFCA for Au/HT and for AuPd/HT catalysts, T = 90 °C, V = 6 ml H_2O and ν O_2 = 15 ml/min, NaOH = 6 mmol, 1M at pH = 14.

An attempt to rationalise results for the selox of HMF, since the true active site in this reaction is not known yet, was made either plotting FDCA yields vs. the amount of Pd atomic % in the catalysts or vs. the amount of bulk average AuPd/(Au+Pd) alloy composition, as determined by EDX analysis **(Figure 5.20).** A linear correlation, in the range of experimental error, was found between FDCA yields after 7 hours and the bulk average AuPd/(Au+Pd) composition, so the alloy was proposed as responsible to enhance catalytic properties and as the active species for HMF selox. It is worth remembering from EDX analysis, that also pure Au NPs are present in the catalysts, playing a role in the selective oxidation of both the alcohol and the aldehyde function, as already widely discussed in **Chapter 3.**

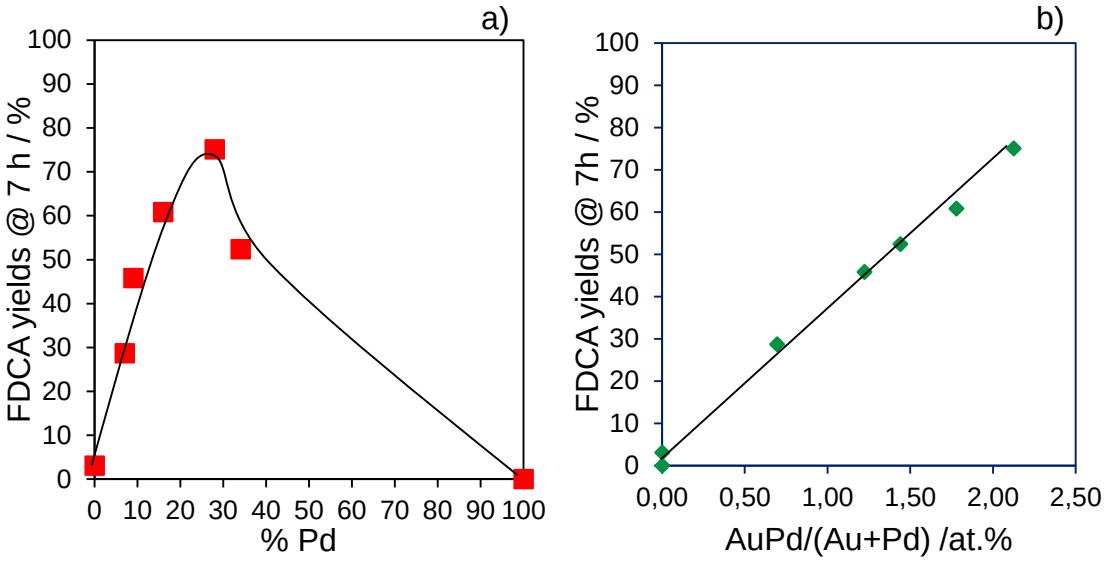

Figure 5.20: left – raw FDCA yields vs. Pd atomic %, showing a volcano plot and right – a linear correlation between raw FDCA yields and normalised AuPd/(Au+Pd) alloy atomic %. Standard reaction conditions for HMF selox.

5.2.4.3 Proposed explanation for AuPd alloys in enhancing the selox of HMF

For Au shell – Pd core NPs, our previous group's works[10] and also Hsu and co-authors ones[34], concluded that both Au-induced Pd ensembles' geometric effects, yielding disruption of continuous Pd ensembles by Au sites, and electronic effects are responsible for the enhanced catalytic activity of Au after Pd addition for a single well-defined bimetallic catalyst[50]. When an Au-Pd alloy was formed after thermal treating of Au shell – Pd core NPs, the Au-rich structure benefitted from dramatic enhancements in the rate of selective oxidation for the selox of crotyl alcohol, both for the activity and the selectivity. Pd intermixing with Au was proposed to yield stronger O_2 adatom adsorption, and so higher O_2 coverage and availability over AuPd alloy, rather than over pure Au.

Rebelli and co-authors[21] prepared higher AuPd metal loadings (above 2 wt. %) and were able to monitor Au $4f_{7/2}$ and Pd $3d_{3/2}$ XPS peaks. They observed a negative shift, from 83 eV to 82.3 eV, with decreasing Au loading that was most likely due to electronic interactions[51] and not to particle size, with a net transfer of electron density from Pd to Au. Nevertheless, this net charge transfer must be small for the electro neutrality required by metallic systems, according to the charge-compensation model[52, 53].

Prati and co-authors observed, as in this thesis work, that the nature of the metal and the Au–Pd ratio play the main role in determining the catalytic activity. The addition of

NaOH enhanced the activity of all the catalysts, the effect on Pd and Pd-rich catalyst being considerably lower than that for gold and gold-rich composition. It has been reported that in a AuPd catalyst, Au acted as promoter to isolate Pd monomer[54] and that AuPd could create bifunctional sites[55]. Different effects of the base on different AuPd ratios were observed also in this thesis work, being minor for the richest catalyst in AuPd alloy and when the alloy was richer in Pd content. As observed in both Prati's works and here, it can be stated that different alloy composition works differently, with the following difference: in this thesis work catalysts resulted made of Au and AuPd alloy. In the gold-rich composition a gold-type mechanism is observed, where the rate determining step is represented by the H abstraction (highest effect of NaOH) whereas in the palladium-rich composition the rate determining step is represented by the H transfer from Pd–H species (negligible effect of the NaOH). Nevertheless, it is not clear or there are not definitive proves if the effect of Au in alloys isolates Pd sites, which act as PdO species[13] for alcohol oxidation to aldehyde and then gold oxidises the aldehyde to acid.

5.3 Conclusions

Hydrotalcites having Mg/Al = 3 molar ratio were prepared using an alkali-free method *via* co-precipitation route. A series of different AuPd catalysts were supported on HTs using the deposition-precipitation method and calcined at 200 °C.

Catalysts were tested for the aerobic selective oxidation of HMF to FDCA before or after the addition of an excess of NaOH 1M solution. Our previous conclusions have shown that hydroxide ions facilitate both the activation of the aldehyde function and the initial deprotonation of alcohols on Au, which are well-known to be weak acids (pKa = 14–18), since a gold catalyst, by itself, cannot deprotonate the hydroxyl group of alcohols. Herein, the addition of Pd to Au was an excellent alternative route of increasing Au catalytic properties, already at pH = 9 provided by HT surface, yielding a maximum of FDCA above 75 % and without the need of extra added NaOH.

Based on kinetic studies' results, this chapter proposes and claims, as well, benefits of bulk average alloy as responsible of the observed enhancements for the selective oxidation of both the R-CHO and the R-OH function of HMF, without furan-ring opening or other side reactions, such as Cannizzaro disproportion. To the best of our knowledge, AuPd alloy might promote the oxidation of alcohol to aldehyde, deprotonating the alcohol, the crucial rate

determining step; while Au NPs, also present in the prepared catalysts, can drive the selox of aldehyde to carboxylic acid at pH 9, as discussed in **Chapter 3**.

As a further explanation, geometric and electronic effects[52] were previously proposed to be important to explain the enhanced performances: Au is the most electronegative metallic element, so after alloying with Pd, a charge transfer[21] from the Pd site to the Au site is expected. Further investigations *via operando* XAS[56] might help to clarify what is the true active site, if there are any changes in the AuPd alloy with the reaction on-going, to definitively understand the synergic effect of these two metals in enhancing the selox of R-CHO and R-OH.

5.4 References

1. N. Dimitratos, A. Villa, D. Wang, F. Porta, D. Su and L. Prati, *Journal of Catalysis*, 2006, **244**, 113-121.
2. M. Besson and P. Gallezot, *Catalysis Today*, 2000, **57**, 127-141.
3. A.-B. Crozon, M. Besson and P. Gallezot, *New Journal of Chemistry*, 1998, **22**, 269-273.
4. T. Mallat and A. Baiker, *Catalysis Today*, 1994, **19**, 247-283.
5. P. Vinke, D. d. Wit, A. T. J. W. de Goede and H. v. Bekkum, in *Studies in Surface Science and Catalysis*, eds. P. Ruiz and B. Delmon, Elsevier, 1992, vol. Volume 72, pp. 1-20.
6. P. Gallezot, *Catalysis Today*, 1997, **37**, 405-418.
7. S. E. Davis, A. D. Benavidez, R. W. Gosselink, J. H. Bitter, K. P. de Jong, A. K. Datye and R. J. Davis, *Journal of Molecular Catalysis A: Chemical*, 2014, **388–389**, 123-132.
8. S. E. Davis, B. N. Zope and R. J. Davis, *Green Chemistry*, 2012, **14**, 143-147.
9. S. E. Davis, L. R. Houk, E. C. Tamargo, A. K. Datye and R. J. Davis, *Catalysis Today*, 2011, **160**, 55-60.
10. A. F. Lee, C. V. Ellis, K. Wilson and N. S. Hondow, *Catalysis Today*, 2010, **157**, 243-249.
11. C. M. A. Parlett, L. J. Durndell, A. Machado, G. Cibin, D. W. Bruce, N. S. Hondow, K. Wilson, A. F. Lee, C. M. A. Parlett, L. J. Durndell, A. Machado, G. Cibin, D. W. Bruce, N. S. Hondow, K. Wilson and A. F. Lee, *Catalysis today*, 2014, **229**, 46-55.
12. S. F. J. Hackett, R. M. Brydson, M. H. Gass, I. Harvey, A. D. Newman, K. Wilson and A. F. Lee, *Angewandte Chemie International Edition*, 2007, **46**, 8593-8596.
13. C. M. A. Parlett, D. W. Bruce, N. S. Hondow, A. F. Lee and K. Wilson, *ACS Catalysis*, 2011, **1**, 636-640.
14. C. M. A. Parlett, A. F. Lee, K. Wilson, D. W. Bruce, N. S. Hondow and M. A. Newton, *Chem.Cat.Chem.*, 2013, **5**, 939-950.
15. A. F. Lee and K. Wilson, *Green Chemistry*, 2004, **6**, 37-42.
16. J. Naughton, A. F. Lee, S. Thompson, C. P. Vinod and K. Wilson, *Physical Chemistry Chemical Physics*, 2010, **12**, 2670-2678.
17. A. Villa, N. Janjic, P. Spontoni, D. Wang, D. S. Su and L. Prati, *Applied Catalysis A: General*, 2009, **364**, 221-228.

18. G. L. Brett, Q. He, C. Hammond, P. J. Miedziak, N. Dimitratos, M. Sankar, A. A. Herzing, M. Conte, J. A. Lopez-Sanchez, C. J. Kiely, D. W. Knight, S. H. Taylor and G. J. Hutchings, *Angewandte Chemie*, 2011, **123**, 10318-10321.
19. S. Meenakshisundaram, E. Nowicka, P. J. Miedziak, G. L. Brett, R. L. Jenkins, N. Dimitratos, S. H. Taylor, D. W. Knight, D. Bethell and G. J. Hutchings, *Faraday Discussions*, 2010, **145**, 341-356.
20. J. K. E. D. I. Enache, P. Landon, B. Solsona-Espriu, A. F. Carley, A. A. Herzing, and C. J. K. M. Watanabe, D. W. Knight and G. J. Hutchings, *Science*, 2006, **311**, 362.
21. J. Rebelli, M. Detwiler, S. Ma, C. T. Williams and J. R. Monnier, *Journal of Catalysis*, 2010, **270**, 224-233.
22. A. F. Lee, C. J. Baddeley, C. Hardacre, R. M. Ormerod, R. M. Lambert, G. Schmid and H. West, *The Journal of Physical Chemistry*, 1995, **99**, 6096-6102.
23. D. G. Cantrell, L. J. Gillie, A. F. Lee and K. Wilson, *Applied Catalysis A: General*, 2005, **287**, 183-190.
24. N. K. Gupta, S. Nishimura, A. Takagaki and K. Ebitani, *Green Chemistry*, 2011, **13**, 824-827.
25. J. K. Edwards, B. E. Solsona, P. Landon, A. F. Carley, A. Herzing, C. J. Kiely and G. J. Hutchings, *Journal of Catalysis*, 2005, **236**, 69-79.
26. A. M. Venezia, V. La Parola, G. Deganello, B. Pawelec and J. L. G. Fierro, *Journal of Catalysis*, 2003, **215**, 317-325.
27. S. Nishimura, Y. Yakita, M. Katayama, K. Higashimine and K. Ebitani, *Catalysis Science & Technology*, 2013, **3**, 351-359.
28. S. K. Sharma, P. K. Kushwaha, V. K. Srivastava, S. D. Bhatt and R. V. Jasra, *Industrial & Engineering Chemistry Research*, 2007, **46**, 4856-4865.
29. P. Liu, Y. Guan, R. A. v. Santen, C. Li and E. J. M. Hensen, *Chemical Communications*, 2011, **47**, 11540-11542.
30. F. Cavani, F. Trifirò and A. Vaccari, *Catalysis Today*, 1991, **11**, 173-301.
31. P. Scherrer, *Nachr. Ges. Wiss. Göttingen*, 1918, **26**, 98-100.
32. C. Shimou, L. Yaodong and W. Guozhong, *Nanotechnology*, 2005, **16**, 2360.
33. E. Genty, R. Cousin, C. Gennequin, S. Capelle, A. Aboukaïs and S. Siffert, *Catalysis Today*, 2011, **176**, 116-119.
34. C. Hsu, C. Huang, Y. Hao and F. Liu, *Nanoscale Research Letters*, 2013, **8**, 1-7.
35. R. K. Petla, S. Vivekanandhan, M. Misra, A. K. Mohanty and N. Satyanarayana, *Journal of Biomaterials and Nanobiotechnology*, 2012, **Vol.03No.01**, 6.
36. A.-X. Yin, X.-Q. Min, W. Zhu, H.-S. Wu, Y.-W. Zhang and C.-H. Yan, *Chemical Communications*, 2012, **48**, 543-545.
37. A. Virnovskaia, S. Jørgensen, J. Hafizovic, Ø. Prytz, E. Kleimenov, M. Hävecker, H. Bluhm, A. Knop-Gericke, R. Schlögl and U. Olsbye, *Surface Science*, 2007, **601**, 30-43.
38. S. Miyata, *Clays and Clay minerals*, 1980, **28**, 50-56.
39. K. Luo, T. Wei, C. W. Yi, S. Axnanda and D. W. Goodman, *The Journal of Physical Chemistry B*, 2005, **109**, 23517-23522.
40. A. S. T. M. JCPDS (1967) X-ray powder data file: card number 4-784, Philadelphia, U.S.A.
41. A. S. T. M. JCPDS (1967) X-ray powder data file: card number 46-1043, Philadelphia, U.S.A.
42. E. P. Barrett, L. G. Joyner and P. P. Halenda, *Journal of the American Chemical Society*, 1951, **73**, 373-380.
43. P. Kuśtrowski, L. Chmielarz, E. Bożek, M. Sawalha and F. Roessner, *Materials Research Bulletin*, 2004, **39**, 263-281.

44. K. S. W. Sing, *Pure Appl. Chem.*, 1985, **57**, 603-619.
45. J. W. McBain, *Journal of the American Chemical Society*, 1935, **57**, 699-700.
46. A. Vaccari, *Catalysis Today*, 1998, **41**, 53-71.
47. Y. Xi and R. J. Davis, *Journal of Catalysis*, 2009, **268**, 307-317.
48. J. I. Di Cosimo, V. K. Díez, M. Xu, E. Iglesia and C. R. Apesteguía, *Journal of Catalysis*, 1998, **178**, 499-510.
49. I. Melian-Cabrera, M. Lopez Granados and J. L. G. Fierro, *Physical Chemistry Chemical Physics*, 2002, **4**, 3122-3127.
50. R. M. Ormerod, C. J. Baddeley and R. M. Lambert, *Surface Science*, 1991, **259**, L709-L713.
51. D. L. Weissman-Wenocur, P. M. Stefan, B. B. Pate, M. L. Shek, I. Lindau and W. E. Spicer, *Physical Review B*, 1983, **27**, 3308-3317.
52. Y.-S. J. Lee, Y.; Chung, Y-D.; Lim, K-Y.; Whang, C-N.; Oh, S-J., *Journal of the Korean Physical Society*, 2000, **37**, 451-455.
53. N. Mårtensson, R. Nyholm, H. Calén, J. Hedman and B. Johansson, *Physical Review B*, 1981, **24**, 1725-1738.
54. M. K. Chen, D.; Yi, C.W. and Goodman, D.W., *Science*, 2005, **310**, 291.
55. D. Wang, A. Villa, F. Porta, D. Su and L. Prati, *Chemical Communications*, 2006, 1956-1958.
56. F. Liu, D. Wechsler and P. Zhang, *Chemical Physics Letters*, 2008, **461**, 254-259.

Chapter 6

Conclusions

Contents

6.1 Conclusions

The overarching goals at the beginning of this thesis project were to investigate the use of Au NPs, supported on hydrotalcite as the heterogeneous catalyst, for the selective oxidation of HMF to FDCA; to understand if this catalytic system[1] is really heterogeneous or partially homo- and partially heterogeneous, to study what the true[1-3] Au active site is, what is the effect of a solid base as the support[4] and the pH-dependence of this selox over Au.

The selox of HMF was found to be pH-sensitive (**Figure 6.1** – left, taken from **Chapter 3**) and, in accordance with the literature, which holds that alcohols are oxidised more slowly than aldehydes over gold, HMFCA / FFCA (**Scheme 6.1**, step 2) exhibited the slowest rate with/without additional NaOH and the highest activation energy (40 kJ mol^{-1}). However, the aldehyde oxidations in steps 1 and 3 surprisingly exhibited the strongest NaOH dependencies, equating to 100-fold (HMF / HMFCA) and 66-fold (FFCA / FDCA) rate enhancements respectively[5]. These far exceed the comparatively small four-fold enhancement observed for step 2 (HMFCA/FFCA) and appears a general phenomenon for Au catalysed aldehyde versus alcohol oxidation. High FDCA yields were found to be achievable either by using low concentrations of Au in conjunction with a strong soluble base, or high concentrations of Au on a moderate strength solid base[5].

The proposed explanation[5] for the loading dependence of these two catalytic regimes (soluble base ≤ 2 wt. % Au ≤ solid base) is the competitive adsorption between HMF and HMFCA. The HMF:surface Au molar ratio approaches 60:1 for the 0.5 wt. % Au/HT catalyst, hence it is unlikely that the low concentration of gem-diol formed without NaOH can effectively compete for adsorption sites over gold nanoparticles.

NaOH addition promotes and accelerates gem-diol formation[2, 6, 7] from HMF in solution, displacing the HMF adsorption equilibrium and liberating reactive gold surface site for both geminal diol dehydrogenation to HMFCA, and subsequent OH^- mediated oxidative dehydrogenation of HMFCA to FFCA and FFCA hydration/dehydrogenation to FDCA.

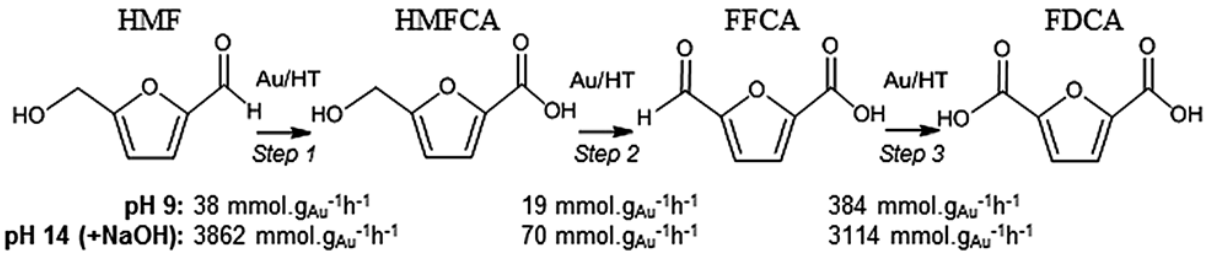

Scheme 6.1: impact of NaOH on kinetics of HMF oxidation over 2 wt. % Au/HT taken from **Chapter 3.**

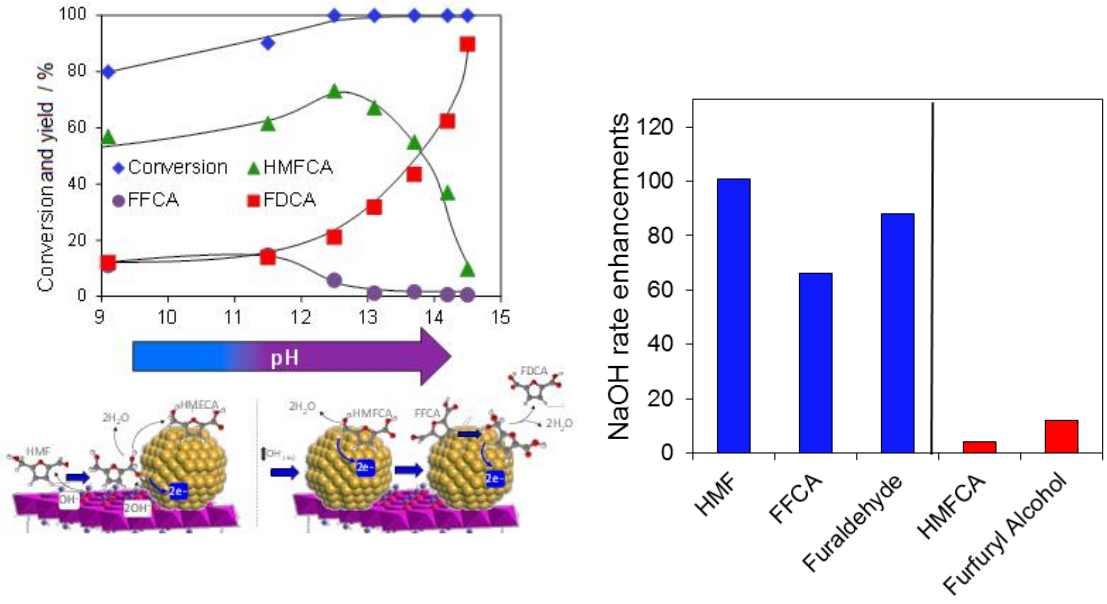

Figure 6.1: left - influence of pH on the aqueous phase selox of 5-HMF by 2 wt. % Au/HT after 7 h, and postulated pH dependent reaction mechanism, from **Chapter 3.** Right – the comparative NaOH rate enhancements for the selective aerobic oxidation of furanic aldehydes versus alcohols over a 2 wt. % Au/HT catalyst, from **Chapter 3.**

Thermal evolution of the gold precursor was investigated[5] by *in situ* Au L_{III} X-ray absorption near edge spectroscopy (XANES) (**Figure 6.2**, from **Chapter 3**). Heating to 65 °C under flowing air initiated precursor decomposition and the concomitant appearance of Au_2O_3, which remained stable to ~110 °C before decomposing to metallic Au. Complete

decomposition of both the $Au(NH_3)_4(OH)_3$ precursor and Au_2O_3 to metallic gold required calcination > 170 °C.

An *operando in situ* XAS study (**Figure 6.3** from **Chapter 3**) was subsequently performed of the thermally processed 2 wt.% Au/HT material, in order to identify the nature of the gold active sites during 5-HMF oxidation, in the reaction conditions described in **Chapter 3**, before and after the addition of NaOH. Despite such high pH, the XANES spectra remained unperturbed following NaOH or 5-HMF addition confirming that gold remained in its metallic form during the selective oxidation of 5-HMF, with no evidence of $Au(OH)_3$ or Na-Au intermetallics detected as might arise due to either gold leaching or Na chemisorption and alloying[5]. These results confirm that gold nanoparticles do not sinter or leach even after 16 h reaction and that NaOH directly promotes oxidation without influencing the electronic or structural properties of gold, showing that the active site is Au^0.

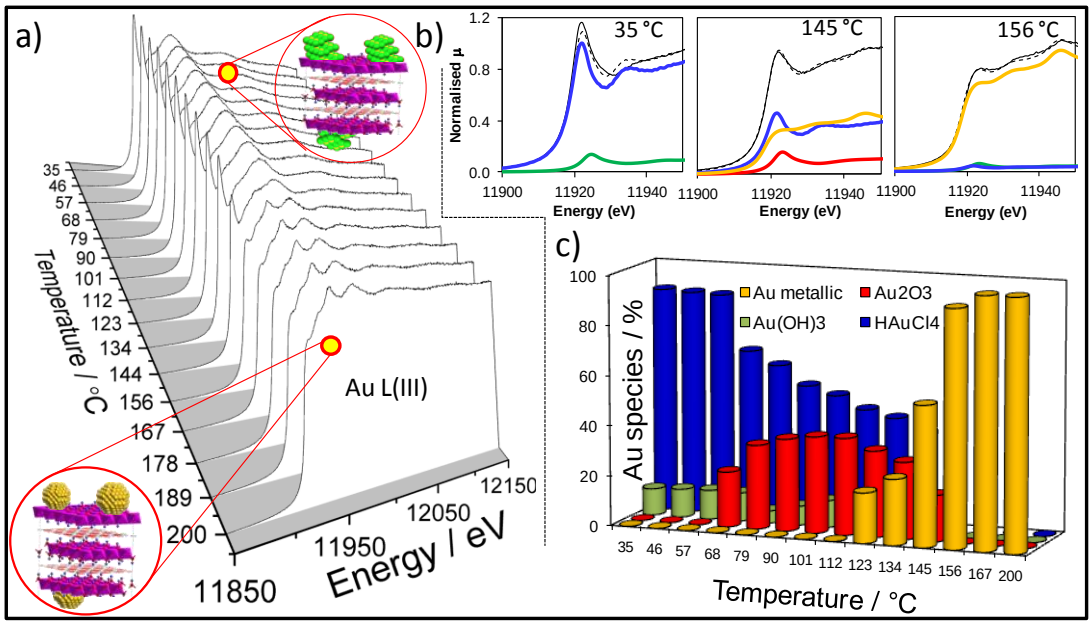

Figure 6.2: *In-situ* Au L_{III} XANES during thermal processing of the $HAuCl_4$/Mg-Al HT precursor a) waterfall plot showing thermal evolution of normalised XANES spectra; b) representative least squares fitted XANES spectra to reference gold species; c) quantitative thermal evolution of fitted Au species, taken from **Chapter 3.**

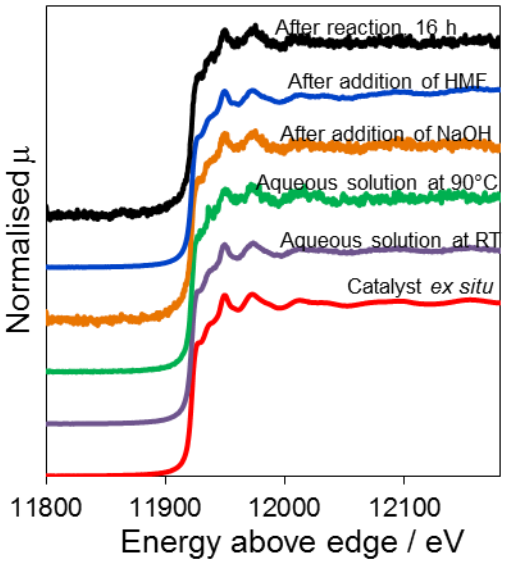

Figure 6.3: Au L_{III} edge (11.9 keV) *in situ* XANES spectra for the aerobic selective oxidation of HMF, as a function of reaction conditions. No changes were visible in the Au^0 oxidation state.

The impact of the calcination temperature of different Au loadings/HT on the base site distribution and on the base strength of hydrotalcites were studied, to generate a stronger basic support that enhances Au/HT catalytic properties without the need of extra added NaOH or high Au loading, being this a waste of expensive precious metal; a comparison between different protocols for calcination and calcination rehydration was carried out. At a first instance, 2 wt. % Au was loaded on HT using the DP method, then the materials were calcined at different temperatures, respectively 300, 400 and 500 °C, to generate mixed Mg_3Al oxides. Subsequently, a calcination – rehydration protocol was set up, in order to try optimising the calcination temperature and the preparation time: the material Au/HT was calcined at 300 or at 450 °C, then the rehydration step was tested in aqueous vapour phase using N_2, in subcritical water under pressure at 120 °C or in hot water at 100 °C.

The best catalyst, which has shown highest FDCA yield (100 %), was 2 wt. % Au/CHT400 °C without subsequent rehydration. This calcination temperature removes carbonates from the HT interlayers, then a rehydration *in situ* occurs during the reaction, either generating ^-OH ions in water that activate HMF to 1,2 gem-diol or deprotonating easily the rate – determining step, the activation of R-OH group, for the selox of HMF and HMFCA. TPD analysis, (**Figure 6.4** from **Chapter 4**), has shown this catalytic system possesses the strongest basicity and the highest base active sites density, while N_2 porosimetry has also shown the highest surface area.

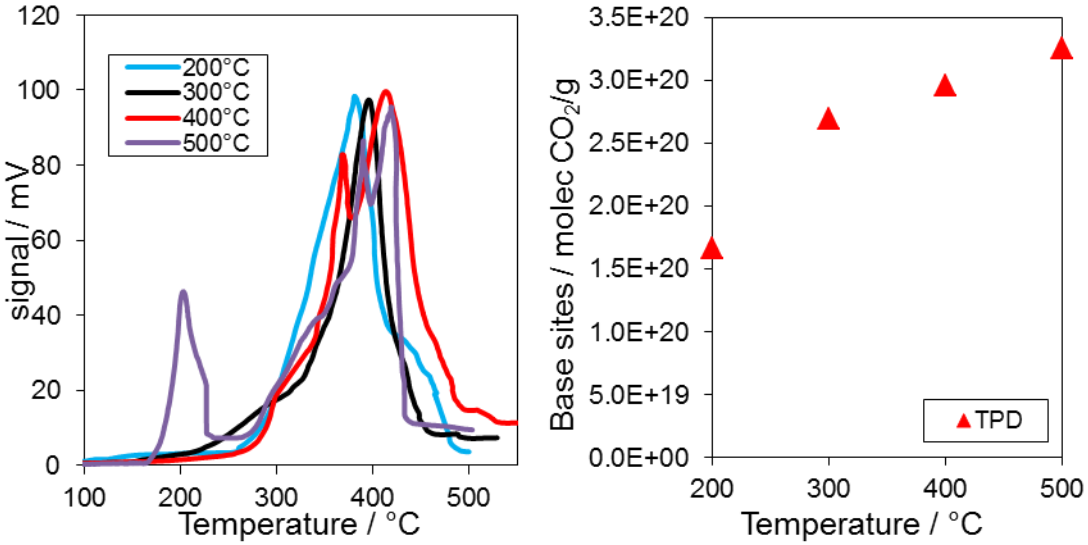

Figure 6.4: left –CO_2 TPD spectra, and right - surface base density determined for 2 wt. % Au/CHT materials as a function of calcination temperature, from **Chapter 4.**

The addition of Pd to Au **(Figure 6.5)** was an excellent alternative route of increasing Au catalytic properties, already at pH = 9 provided by HT surface, yielding a maximum of FDCA above 75 % and without the need of extra added NaOH. To the best of our knowledge, AuPd alloy might promote the oxidation of alcohol to aldehyde, deprotonating the alcohol, the crucial rate-determining step; while Au NPs, also present in the prepared catalysts, can drive the selox of aldehyde to carboxylic acid at pH 9. Both geometric and electronic effects were proposed and discussed to be responsible of the catalytic enhancement but, to date, the true mechanism and active site is not well known yet.

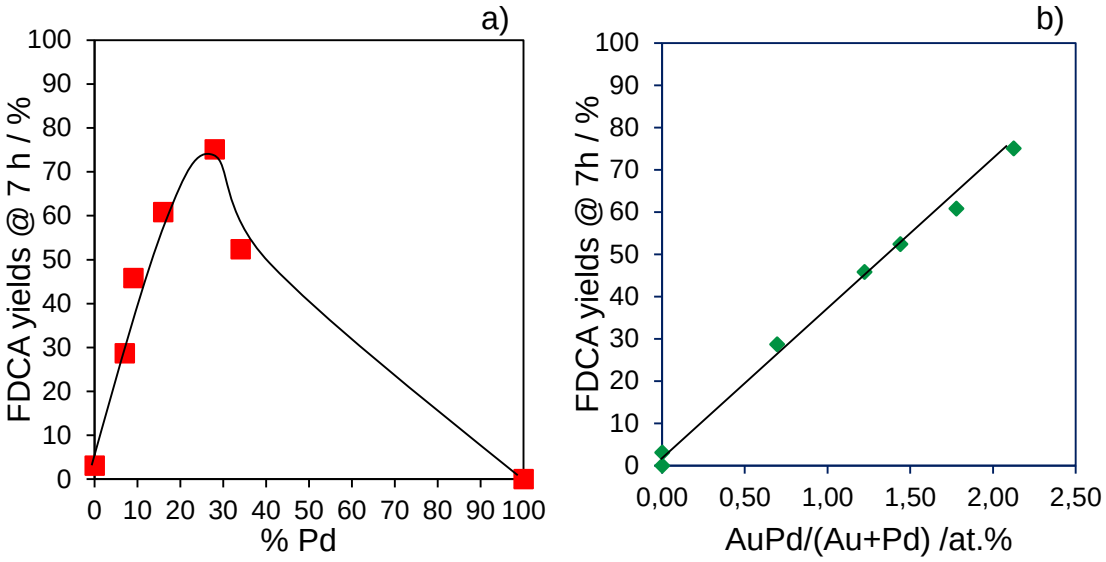

Figure 6.5: left – raw FDCA yields vs. Pd atomic %, showing a volcano plot and right – a linear correlation between raw FDCA yields and normalised AuPd/(Au+Pd) alloy atomic %. Standard reaction conditions for HMF selox.

Further investigations *via operando* XAS[8] might help to clarify what is the true active site, if there are any changes in the AuPd alloy with the reaction on-going, to definitively understand the synergic effect of these two metals in enhancing the selox of R-CHO and R-OH. An attempt to titrate Pd active sites with CO or H_2 titration/TPD, followed by *in-situ* DRIFT-IR study might help find the number of Pd active sites and estimate TOF values with more accuracy. *In-situ* NMR might help understand better the reaction mechanism and follow the 1,1-gem-diol formation, both for Au/HT and for AuPd/HT catalytic systems, in the presence and in the absence of base.

6.2 References

1. N. K. Gupta, S. Nishimura, A. Takagaki and K. Ebitani, *Green Chemistry*, **13**, 824-827.
2. C. Della Pina, E. Falletta, L. Prati and M. Rossi, *Chemical Society Reviews*, 2008, **37**, 2077-2095.
3. C. D. Pina, E. Falletta and M. Rossi, *Chemical Society Reviews*, 2012, **41**, 350-369.
4. W. Fang, J. Chen, Q. Zhang, W. Deng and Y. Wang, *Chemistry – A European Journal*, 2011, **17**, 1247-1256.
5. L. Ardemani, G. Cibin, A. J. Dent, M. A. Isaacs, G. Kyriakou, A. F. Lee, C. M. A. Parlett, S. A. Parry and K. Wilson, *Chemical Science*, 2015.
6. S. E. Davis, B. N. Zope and R. J. Davis, *Green Chemistry*, **14**, 143-147.
7. S. E. Davis, A. D. Benavidez, R. W. Gosselink, J. H. Bitter, K. P. de Jong, A. K. Datye and R. J. Davis, *Journal of Molecular Catalysis A: Chemical*, 2014, **388–389**, 123-132.
8. F. Liu, D. Wechsler and P. Zhang, *Chemical Physics Letters*, 2008, **461**, 254-259.